Correlation of optical anisotropy with structural changes in $Ge_2Sb_2Te_5$

Janaki Shanmugam

Department of Materials

Linacre College

University of Oxford

A thesis submitted in partial fulfilment of the requirements

for the degree of *Doctor of Philosophy*

Hilary 2018

Abstract

$Ge_2Sb_2Te_5$ (GST) is an established phase-change material that undergoes fast reversible transitions between amorphous and crystalline states with a high electro-optical contrast, enabling applications in non-volatile optical and electronic memories and optically-switchable structured metamaterials. This work demonstrates that optical anisotropy can be induced and recorded in pure and doped GST thin films using circularly polarised light (CPL), opening up the possibility of controlled induction of anisotropic phase transition in these and related materials for optoelectronic and photonic applications. While the amorphous-to-crystalline phase transition in GST has generally been understood to proceed via a thermal mechanism, significant optical anisotropy (measured by circular dichroism (CD) spectroscopy in this work) strongly suggests that there is an electronic athermal component of the phase change induced by the handedness of circularly polarised nanosecond laser pulses and implies the existence of chiral structures or motifs. Optically active and inactive regions in the films have also been studied using X-ray and electron diffraction and spectroscopic techniques in order to obtain a structural picture that can be correlated to the optical changes observed and the findings offer surprising evidence of the nature of the phase transition. Regions exhibiting higher CD signal intensities were found to be mostly amorphous with elemental phase separation observed within modified surface features. Several mechanisms are proposed for the observed phenomena, including the retention of chiral crystalline fragments in laser-irradiated and melt-quenched amorphous regions, which could explain the results of CD spectroscopy. This may be extended to other material systems and harnessed in potential metamaterials, plasmonics, photonics or chiroptical applications.

Statement of authorship

Parts of the work presented in Chapters 3, 4, and 5 of this thesis are of a collaborative nature and the contributions that are not my own are detailed below.

1. Thin film deposition (Section 3.1) was performed at Optoelectronics Research Centre, University of Southampton. I performed initial testing and determination of deposition parameters for different targets under the supervision of Mr. Chris Craig, operating the RF sputter equipment for the first batch of samples (Pure GST, Ti-GST, In-GST, Se-GST, Cr-GST) with a 20nm thick silica capping layer. Deposition of Au-GST and Ce-GST films and subsequent deposition runs (pure GST and Cr-GST films of different thicknesses on both silica and LiF substrates, with and without a 5nm thick capping layer) were carried out by Mr Chris Craig as per my requirements.
2. Laser irradiation (Section 3.2) was performed at the Clarendon Laboratory, Department of Physics, University of Oxford with the assistance of Prof Paul Ewart, Prof Benjamin Williams and Dr Andrew Luers.
3. Circular dichroism spectroscopy (Section 3.3) was performed at B23 beamline, Diamond Light Source, Harwell Campus with the help of beamline scientists Prof Giuliano Siligardi, Dr Rohanah Hussain and Dr Tamas Javorfi.
4. High resolution powder X-ray diffraction (Section 3.5) was performed at I11 beamline, Diamond Light Source. Beamline scientists Dr Stephen Thompson and Dr Sarah Day helped with the experimental setup.
5. The scanning electron microscope JEM-7600F images (Section 3.6) were acquired with the help of Dr Tjiu Weng Wei at the Institute of Materials, Science and Engineering (IMRE), A*STAR, Singapore.
6. TEM sample preparation by focused ion beam (FIB) milling (Section 3.7.1) was performed by Ms June Ong Lay Ting and Ms Hui Hui Kim at IMRE, A*STAR, Singapore.
7. STEM pencil beam diffraction experiments (Section 3.7.4) on the JEOL ARM300CF at the electron Physical Science Imaging Centre (ePSIC), Harwell Campus, were performed with the assistance of Dr Chris Allen and Dr Mohsen Danaie.
8. Dual EELS and EDX spectrum image acquisition (Section 3.7.5) on the JEOL ARM200F at the National University of Singapore was performed with the assistance of Dr Michel Bosman.
9. eRDF Analyser software (Section 3.8.2) was written with the help of Dr. Konstantin Borisenko. Mr Yu-Jen Chou contributed to testing of the software.
10. Liquid quench simulations of pure and Cr-doped GST (Section 3.8.3) were performed by Dr Konstantin Borisenko.

List of publications

The following is a list of original publications containing parts of the work done during the course of my DPhil and presented in this thesis:

1. Borisenko, K. B., **Shanmugam, J.**, Williams, B. A. O., Ewart, P., Gholipour, B., Hewak, D. W., Hussain, R., Javorfi, T., Siligardi, G., & Kirkland, A. I. (2015). Photo-induced optical activity in phase-change memory materials. *Sci. Rep.*, *5*, 8770. https://doi.org/10.1038/srep08770

2. **Shanmugam, J.**, Borisenko, K. B., Chou, Y.-J., & Kirkland, A. I. (2017). eRDF Analyser: An interactive GUI for electron reduced density function analysis. *SoftwareX*, *6*, 185–192. https://doi.org/10.1016/j.softx.2017.07.001

Acknowledgements

I would like to express my sincere gratitude and appreciation to my supervisors Professor Angus Kirkland and Dr. Konstantin Borisenko at the Department of Materials, University of Oxford, and Dr. Michel Bosman at the Institute of Materials Research and Engineering (IMRE), Agency for Science, Technology and Research (A*STAR), Singapore for their invaluable guidance, advice and doses of inspiration and encouragement during the course of my DPhil research.

I thank our collaborators Dr. Andrew Luers, and Prof. Paul Ewart at the Clarendon Laboratory, Prof. Benjamin Williams at the Department of Engineering, Mr. Christopher Craig and Prof. Daniel Hewak at the University of Southampton Optoelectronics Research Centre, and Prof. Giuliano Siligardi, Dr. Rohanah Hussain and Dr. Tamas Javorfi at the B23 beamline at Diamond Light Source (DLS), Harwell Campus, Oxford for the research opportunities and insightful discussions. I would also like to thank Mr. Yu-Jen Chou, Dr. Christopher Allen, Dr. Mohsen Danaie and other post-doctoral fellows of the Electron Microscopy Image Analysis group, the support scientists at the David Cockayne Centre for Electron Microscopy and the Oxford Materials Characterisation Service, Dr. Tjiu Weng Weei, Ms. Ong Lay Ting June and Ms. Hui Hui Kim at the IMRE Analysis & Characterisation department and others at DLS for their assistance in various research endeavours.

I am grateful for the funding and generous stipend provided by the A*STAR Graduate Academy (A*GA), Singapore, without which I would not have been able to embark on this incredible journey. I thank my scholarship officers as well as the IT support staff and other administrative staff at the Department of Materials and Linacre College for their support.

Last but not least, my friends and family. You have given me the encouragement and strength to persevere but most importantly, thank you for always believing in me.

Contents

Chapter 1

Introduction

1.1. Background

Phase transformations in inorganic materials, such as metals, glasses, alloys and ceramics, have formed the basis of many vital technological applications in diverse disciplines. These phase transformations may involve structural and compositional changes under external stimuli, such as temperature, pressure, mechanical stress or electrical bias, that may occur through atomic diffusion, alteration of phase type and composition and production of metastable intermediate phases. Metastable states are not shown in equilibrium phase diagrams since they do not correspond to a global minimum Gibbs free energy for a given composition and their phase transformations are usually reversible at standard conditions. Examples of metastability include supercooled or superheated liquids where the relaxation of these liquids to a stable equilibrium involves a phase transformation (Debenedetti, 1996) and martensite in steel whose transformation occurs (almost) at the speed of sound (Nishiyama, 1978).

Chalcogenides typically contain one or more chalcogens, i.e. the elements sulphur (S), selenium (Se) and tellurium (Te) in group 16 of the periodic table (excluding oxygen (O) and the highly radioactive polonium (Po)), as a major constituent in a binary or multi-component system. While binary chalcogenides (including transition metal dichalcogenides) such as MoS_2 have a two-dimensional layered structure with weak van der Waals bonding between layers (Lee, Shin, Lee, & Lee, 2016), the addition of network formers introduces cross-linking that increases

network rigidity and the glass-liquid transition (or glass transition for short) temperature region (in which a supercooled liquid melt transitions to an amorphous solid) (Kolobov & Tominaga, 2012). Network formers, named for their ability to covalently bond with O in conventional oxide glasses, typically have high valence states and include e.g. four-fold coordinated Ge and Si and three-fold coordinated As and Sb.

Chalcogenide solids can exist in both crystalline and amorphous states. The glass forming ability (or the ability to form an amorphous solid without homogenous crystal nucleation by rapidly cooling a melt to a temperature above the glass transition temperature) decreases with increasing molar weights of the constituent chalcogens (S > Se > Te) (Kolobov & Tominaga, 2012). Although GeTe-based phase-change alloys are marginal glass formers due to rapid crystallisation (in tens of nanoseconds) above the glass transition temperature, an amorphous phase still can be achieved with very high quenching rates ($>10^8$K/s). Such phase-change alloys are semiconducting and undergo a reversible transition between the amorphous and crystalline phases distinguished by a high optical contrast.

The ternary chalcogenide $Ge_2Sb_2Te_5$ was originally discovered as a pseudo-binary ($2GeTe:Sb_2Te_3$) alloy on the GeTe-Sb_2Te_3 tie-line (Figure 1.1) and subsequently developed for applications in optical non-volatile memory (NVM) (Yamada et al., 1987). It surpassed many challenges for practical applications in data storage with its fast crystallization rate (of the order of tens of nanoseconds), high amorphous state stability and excellent electro-optical contrast between the amorphous and crystalline states.

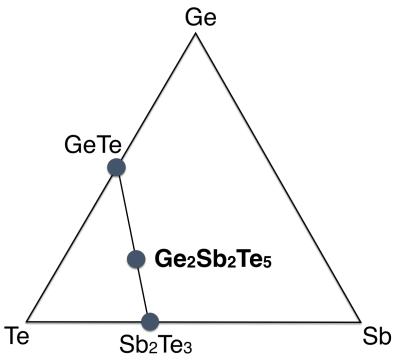

Figure 1.1: Phase diagram for the Ge:Te:Sb ternary system. $Ge_2Sb_2Te_5$ is a pseudo-binary alloy that falls on the GeTe-Sb_2Te_3 tie-line.

Optical NVM devices such as rewriteable CD/DVDs and Blu-ray discs exploit the optical contrast and reversible transition between the amorphous and metastable crystalline states to store and erase data. Laser pulses are used to switch states, between amorphous regions encoding "zero" bits and crystalline regions encoding "one" bits. These bits are then read out by the contrast in reflectivity, where the crystalline state has a higher optical reflectivity than the amorphous state. $Ge_2Sb_2Te_5$ has subsequently been applied in electronic NVM (phase change random access memory (PCRAM)) devices, which operate using a change in electrical conductivity, switching between a high resistance state (HRS) (amorphous phase) and a low resistance state (LRS) (conducting crystalline phase) with current pulses. The reversible phase transition in both NVM applications is accomplished by employing pulses of varying intensity and duration.

Although phase-change appears to be a binary operation, multi-level memory devices based on intermediate resistive states corresponding to different amorphous-to-crystalline fractions in the material have been practically realised recently (Ríos et al., 2015). $Ge_2Sb_2Te_5$ has also been successfully used in other applications including metamaterials (Cao, Zhang, Simpson, Wei, & Cryan, 2013), photonic waveguides

(Pernice & Bhaskaran, 2012), plasmonic and optoelectronic devices (Gholipour, Zhang, MacDonald, Hewak, & Zheludev, 2013), nanophotonic circuits (Lu et al., 2017) and even as artificial neurons in neuromorphic computing systems (Tuma, Pantazi, Le Gallo, Sebastian, & Eleftheriou, 2016).

1.2. Motivation and objectives

Although $Ge_2Sb_2Te_5$ is a material system that has been studied extensively (Kolobov et al., 2005; Lencer, Salinga, & Wuttig, 2011; Raoux, Ielmini, Wuttig, & Karpov, 2012; Raoux, Xiong, Wuttig, & Pop, 2014) the details of the mechanism of the fast and reversible phase change between its amorphous and metastable crystalline states are still not fully understood. While this phase change has been generally accepted to occur via a thermal mechanism (Wuttig & Yamada, 2007), growing experimental evidence (Kolobov, Fons, & Tominaga, 2014; Li, Liu, Han, & Zhang, 2012) suggests that non-thermal effects are also at play, leading to transient solid-state phase transitions that do not occur via melting.

Due to their transient nature, these athermal effects rarely manifest in persistent structural changes. However, the possibility of creating additional structural states in $Ge_2Sb_2Te_5$ differentiated by athermal effects holds great promise as an alternative means of increasing the storage capacity of phase change memory to meet the increasing technological demands for compact data storage in today's society. Due to the helicity and chiral nature of circularly polarised light (CPL), where opposite handed (left and right CPL) waves are non-superimposable, this work will explore the possibility of using CPL as an athermal factor in inducing an amorphous-to-crystalline phase change in $Ge_2Sb_2Te_5$ thin films.

By measuring the optical anisotropy of the laser-irradiated regions, it will be shown that the handedness of CPL can be recorded in the films and result in optical anisotropy, as quantified by circular dichroism measurements. The effect of doping and influence of various laser irradiation parameters on the optical anisotropy will also be investigated for further understanding of this photo-induced phenomenon. Structural analysis of the laser-irradiated and as-deposited regions in the thin films will examine differences in morphology, composition and local order through X-ray and electron scattering and diffraction studies. It is expected that the correlation of the optical anisotropic properties with the structural differences, complemented by theoretical simulations, will provide insight into the origin of observed chirality and the influence of polarisation on the photo-induced phase transition in $Ge_2Sb_2Te_5$ thin films.

1.3 Thesis Outline

In this thesis, Chapter 2 provides an overview of the $Ge_2Sb_2Te_5$ material structure and the phase change phenomenon that occurs between its amorphous and crystalline phases, as well as photo-induced optical anisotropy in other chalcogenide systems. Characterisation techniques typically used to study these materials are also briefly described, while the experimental methods used in this work are detailed in Chapter 3. Chapter 4 deals mainly with the experimental observation and study of optical anisotropic properties, specifically in the form of circular dichroism (CD), in pure and doped $Ge_2Sb_2Te_5$ films while structural characterisation and analysis of these films carried out to investigate the origin of the observed CD signals is discussed in Chapter 5. The concluding Chapter 6 summarises the work presented in this thesis and discusses potential avenues of further research.

Chapter 2

Phase change in $Ge_2Sb_2Te_5$

2.1. The structure of $Ge_2Sb_2Te_5$

The mechanism of phase transformation between crystalline and amorphous states in $Ge_2Sb_2Te_5$ has been debated in the literature, due to a lack of agreement on the structures of the different phases as well as a lack of agreement on the pathways in which they transform reversibly between the phases. The atomic structures of the phases and the structural changes during phase transitions are discussed in more detail below, while the mechanism of phase change will be dealt with in a subsequent section.

2.1.1. Crystalline phases

Crystalline $Ge_2Sb_2Te_5$ is known to exist in two forms: a metastable phase and a stable phase. Structural models derived from X-ray (Matsunaga, Yamada, & Kubota, 2004; Yamada & Matsunaga, 2000) and electron (Kooi & De Hosson, 2002; Petrov, Imamov, & Pinsker, 1968) diffraction data, as well as from *ab-initio* molecular dynamics (MD) simulations (Sun, Zhou, & Ahuja, 2006) are described below.

Hexagonal phase

Petrov et al. (1968) described the stable hexagonal structure as a nine-layered stacking sequence (Te-Sb-Te-Ge-Te-Te-Ge-Te-Sb-Te) along the c-axis or [0001] direction (primitive rhombohedral space group $P\bar{3}m_1$, a = b = 4.2Å, c = 16.96Å). Kooi & De Hosson (2002) expressed a similar stacking sequence based on electron diffraction measurements, but with exchanged Ge and Sb layers (Te-Ge-Te-Sb-Te-Te-Sb-Te-Ge-Te) (a = b = 4.25Å, c = 17.27Å). This sequence was confirmed to be the

most stable stacking order in the hexagonal configuration through density functional theory (DFT) calculations (Sun et al., 2006). However, Matsunaga et al. (2004) argued that Ge and Sb were distributed randomly across the same layer (Te-Ge/Sb-Te-Sb/Ge-Te-Te-Sb/Ge-Te-Ge/Sb), with a difference in Ge/Sb ratio between alternate layers. These models are illustrated in Figure 2.1.

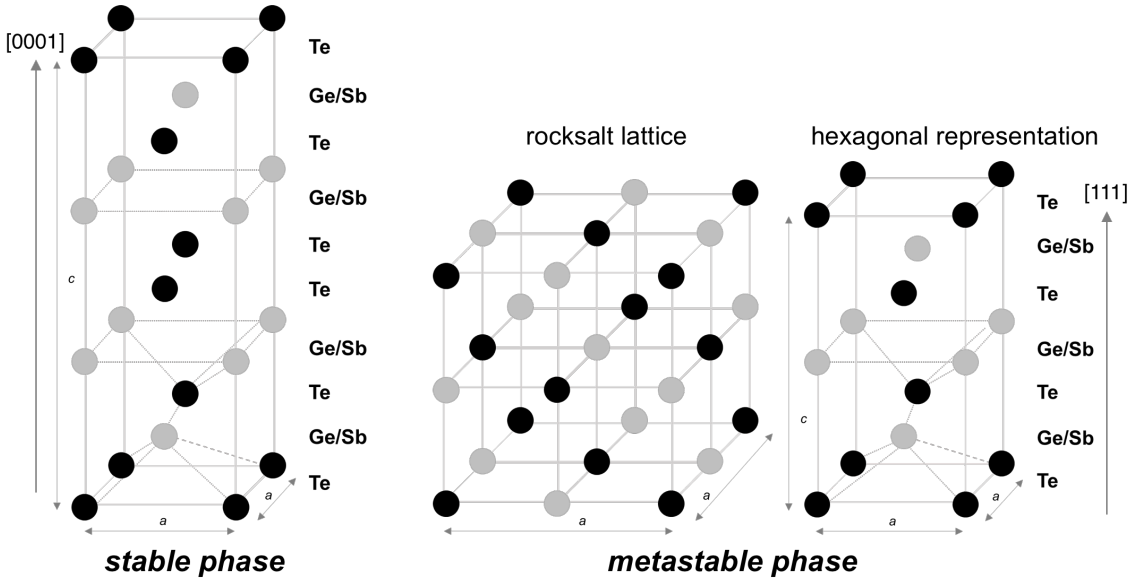

Figure 2.1: Schematic representation of the lattice structures of crystalline $Ge_2Sb_2Te_5$ phases. The stable phase has a nine-layered hexagonal stacking sequence whereas atoms in the metastable phase occupy a rocksalt lattice (equivalent to a six-layered stacking sequence in the hexagonal configuration also shown). Te atom positions are in black and Ge / Sb sub lattice positions (variable concentrations of Ge and Sb) are in grey.

Metastable cubic phase

Yamada & Matsunaga (2000) described the metastable phase as a rocksalt (NaCl-type) structure (a = 6.02Å), in which Te atoms occupy all Cl sites while Ge and Sb randomly occupy Na sites with intrinsic vacancies. This may also be considered as a six-layered stacking sequence (Te-Ge/Sb-Te-Ge/Sb-Te-Ge/Sb) along a <111> direction of a face-centred-cubic (fcc) structure that corresponds to the [0001] direction in the hexagonal configuration, as illustrated in Figure 2.1. Sun et al. (2006)

proposed a slightly modified metastable structure with two alternatively bonded repeat units in a rocksalt structure: (I) Te-Ge-Te-Sb-Te and (II) Te-Sb-Te-Ge, with vacancy layers between the two units (Figure 2.2).

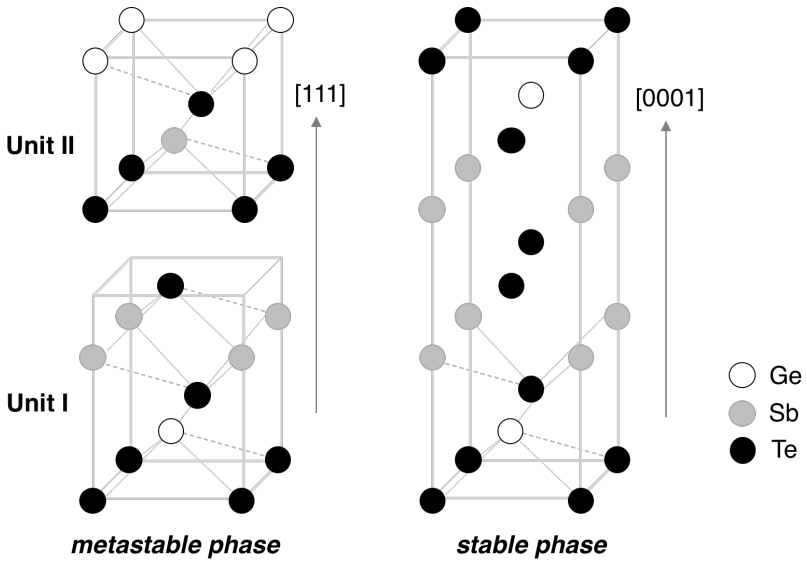

Figure 2.2: Schematic representation of the structures of crystalline $Ge_2Sb_2Te_5$ phases proposed by Sun et al., (2006).

The vacancies observed in the Ge/Sb sub-lattice in the metastable crystalline phases (as well as in the amorphous phase) are intrinsic defects whose distribution strongly impacts functional properties. It has been suggested that these vacancies may serve to absorb lattice expansion, thereby reducing volume expansion and stress during melting and subsequent amorphisation, as discussed below.

Although Sun et al. (2006) predicted that Ge/Sb vacancies should be highly ordered, the structural models discussed above assume a random distribution of these vacancies. Recent aberration-corrected electron microscopy analyses of metastable $Ge_2Sb_2Te_5$ (Lotnyk et al., 2016; Ross, Lotnyk, Thelander, & Rauschenbach, 2014) validate this assumption, where vacancy layers were observed in the Ge/Sb sub-lattice with a stacking sequence similar to, but with greater disorder than that of, the

Matsunaga model (2004). This increased disorder was attributed to a random distribution of Ge and Sb atoms and vacancies (with local concentration varying between 20 and 35 atomic percent) within the sub-lattice.

Ab-initio MD simulations and calculations of X-ray absorption near-edge structure (XANES) spectra by Liu et al. (2011) showed that Ge/Sb vacancies may play a crucial role in stabilizing tetrahedral coordination by forming clusters of tetrahedral Ge atoms surrounding the vacancies. However, this tetrahedral cluster formation was challenged by Raty et al. (2012), based on MD simulations (Da Silva, Walsh, Wei, & Lee, 2009) where the displacement of Ge atoms from octahedral to tetrahedral sites near intrinsic vacancies resulted in an unstable high-energy intermediate configuration. The authors concluded that the metastable phase in $Ge_2Sb_2Te_5$ is exclusively characterized by a distorted octahedral (six-fold) atomic arrangement. This agrees with the experimental results of Lotnyk et al. (2016) who reported no evidence of tetrahedral Ge atoms and proposed the distorted octahedral arrangement as the main structural motif.

In contrast, other experimental observations and first principle calculations support the coexistence of octahedral and tetrahedral environments. Liu et al. (2011) performed radial distribution function (RDF) analysis of electron diffraction measurements and identified that only 35% of Ge atoms were in a tetrahedral environment. DFT and MD simulations have produced similar results independently (Akola & Jones, 2007; Caravati, Bernasconi, Kühne, Krack, & Parrinello, 2007), showing a third of Ge atoms in tetrahedral geometry and the remaining Ge, Sb and Te atoms mostly three-fold coordinated in distorted octahedral sites.

Despite these variations in the local geometry, bond length measurements using experimental extended X-ray absorption fine structure (EXAFS) and simulated XANES data (Kolobov et al., 2004) support a distorted rocksalt model of the metastable phase of crystalline $Ge_2Sb_2Te_5$, with displacement of Ge and Sb atoms from their ideal to off-centre positions (Krbal et al., 2012), instead of an ideal rocksalt structure.

2.1.2. Amorphous phase

The amorphous phase in phase-change materials characteristically lacks long-range order and translational periodicity but has a high degree of short-range order (SRO) with well-defined structure at the atomic scale. The structure of the amorphous phase has been studied primarily by experimental techniques sensitive to local atomic environments, including probing of short-range order by X-ray absorption (Kolobov et al., 2004; Krbal et al., 2011), X-ray scattering (Kohara et al., 2006) and electron diffraction (Borisenko, Chen, Song, Nguyen-Manh, & Cockayne, 2009; Lang, Song, Nguyen-Manh, & Cockayne, 2007), medium-range order by fluctuation microscopy (Kwon et al., 2007; Li, Darmawikarta, & Abelson, 2013), as well as molecular dynamics simulations (Akola, Larrucea, & Jones, 2011; Hegedüs & Elliott, 2008).

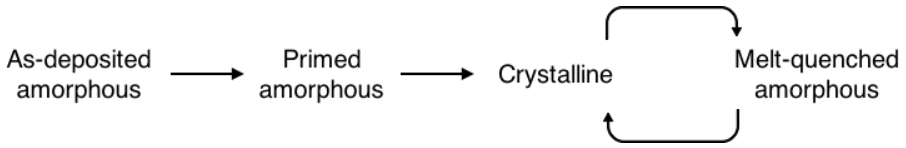

Figure 2.3: Schematic order of phase transitions in non-volatile memory (NVM) applications involving various amorphous phases.

Practical applications of reversible switching between the metastable crystalline and amorphous phases usually involve the melt-quenched amorphised form

as opposed to the as-deposited form (Figure 2.3). During annealing, the as-deposited amorphous phase requires a longer incubation time to reach a primed amorphous state (Coombs, Jongenelis, van Es-Spiekman, & Jacobs, 1995; Khulbe, Wright, & Mansuripur, 2000), in which seeding (or formation of critical nuclei) occurs without triggering crystallisation. Since crystallisation in $Ge_2Sb_2Te_5$ is nucleation-driven, this leads to longer crystallisation onset times in the as-deposited state (at least by an order of magnitude) (Weidenhof, Friedrich, Ziegler, & Wuttig, 2001) as compared to the melt-quenched state.

Raman spectroscopy and EXAFS studies (Krbal et al., 2011) have found that the melt-quenched amorphous state still retains crystalline characteristics on a local scale after a phase transition. Similarly, the ultrafast crystallization of $Ge_2Sb_2Te_5$ has been attributed to the persistence of nanoscale order and the presence of motifs such as ring structures (Figure 2.4) in the amorphous phase, that enable a quick transition to a similarly locally ordered metastable crystallisation phase via atomic rearrangement (discussed further in the next section).

Although the existence and dominance of such structural motifs was challenged by Jóvári et al. (2008), based on the fitting of atomistic models using reverse Monte Carlo simulations to simultaneous X-ray and neutron diffraction data and EXAFS measurements, Kohara et al. (2006) concluded from an X-ray diffraction study that the amorphous phase is characterised mainly by even-membered ring structures. Such even-membered rings were found to have a strong preference for heteropolar Ge-Te and Sb-Te bonds, as opposed to odd-membered ring structures induced by the formation of homopolar Ge-Ge bonds (that are predominant in GeTe but less likely to occur in $Ge_2Sb_2Te_5$). This was in agreement with the low probability

of occurrence of "wrong" bonds described by Jóvári et al. (2008), i.e. Ge-Ge and Ge-Sb bonds as well as an insignificant number of Sb-Sb and Te-Te bonds that are missing in the crystalline state.

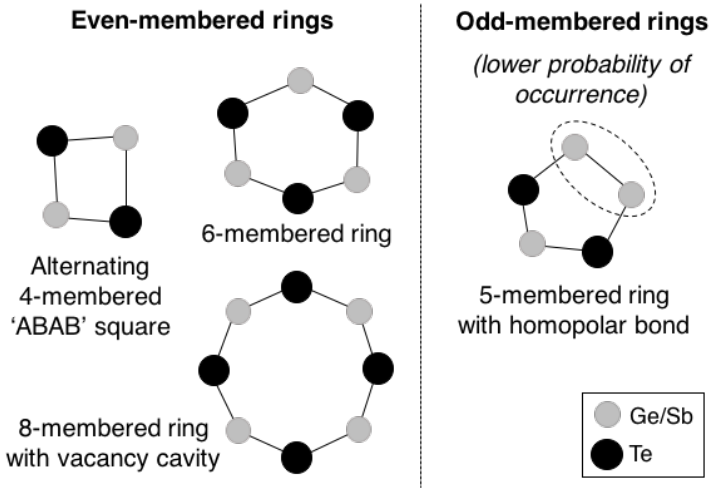

Figure 2.4: Illustrations of irreducible (shortest closed) ring structures observed in models of amorphous $Ge_2Sb_2Te_5$.

A distorted planar eight-membered ring surrounding a vacancy was also proposed by Lang, Song, Nguyen-Manh, & Cockayne (2007) as the structural motif in the amorphous phase. While their electron diffraction radial density function analysis results agreed with previous EXAFS data (Kolobov et al., 2004) on interatomic distances, evidence for the transfer of alternating four-membered ring fragments (with bond angles of *ca.* 90 degrees) from metastable to amorphous states is prolific in the literature (Akola & Jones, 2007; Borisenko, Chen, Song, Nguyen-Manh, et al., 2009; Hegedüs & Elliott, 2008; Kwon et al., 2007).

2.2. Thermal mechanism of phase change

Phase changes are typically induced in $Ge_2Sb_2Te_5$-based NVM devices using either light or current pulses of different intensities and durations, resulting in the transition from an amorphous to a crystalline state (crystallisation) or vice versa (amorphisation). This transition has been commonly believed to occur via a thermal mechanism (Wuttig & Yamada, 2007), as described further below.

2.2.1. Laser-induced thermal phase change

Nanosecond laser pulses in the visible wavelength range used to induce a reversible phase change in $Ge_2Sb_2Te_5$ films and devices can be approximated as a thermal source, and the operational principle of such a phase change is illustrated in Figure 2.5.

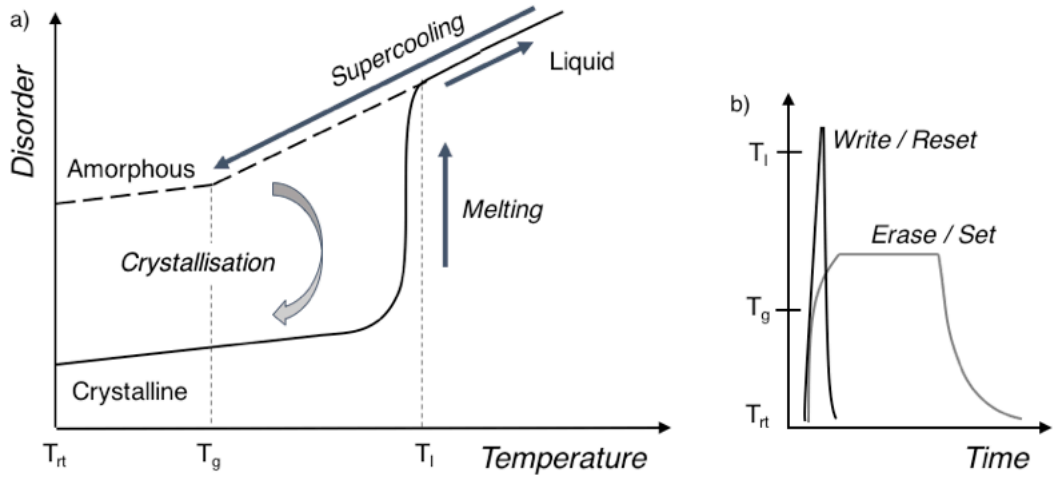

Figure 2.5: a) Illustration of a phase change induced by thermal heating. Crystallisation is represented by the curved arrow and amorphisation is represented by straight arrows. b) Comparison of typical pulse durations and intensity used for crystallisation (erase / set) and amorphisation (write / reset). T_{rt} is the room temperature, T_g is the glass transition temperature, and T_l is the liquidus temperature. (Adapted from Wuttig & Yamada (2007))

Amorphisation of crystalline $Ge_2Sb_2Te_5$ can be achieved with a short intense pulse which heats the material above the liquidus temperature T_l (~900K) (Kosyakov, Shestakov, Shelimova, Kuznetsov, & Zemskov, 2000) followed by rapid quenching below the glass transition temperature. On the typical timescale within the laser pulse duration (of the order of 10^{-9}s), light is absorbed by the material and the excess energy of the photo-excited electrons is transferred to lattice vibrational modes. Heating of the lattice above T_l by phonon emission leads to melting of the crystalline material. With extremely high cooling rates (>10^9K/s), disorder in the liquid melt is frozen in the resulting amorphous solid.

Crystallisation of the amorphous phase is usually achieved with a longer pulse of lower intensity, by annealing the material at a temperature above T_g, but below T_l. In contrast to the rapid quenching in amorphisation, slow cooling allows the formation and growth of nuclei into a highly ordered crystalline structure, with the highest crystallisation speeds occurring at temperatures between T_g and T_l (Kolobov & Tominaga, 2012). A range of temperatures have been reported for the phase transitions from amorphous to metastable crystalline phase and from metastable to stable crystalline phases (around 400K and 600K respectively) (Friedrich, Weidenhof, Njoroge, Franz, & Wuttig, 2000; Kooi, Groot, & De Hosson, 2004; Song, Zhang, Sik Jeong, Kim, & Kim, 2008) as well as for T_g (within 10K of the crystallisation temperature) (Kalb, Wuttig, & Spaepen, 2007; Lankhorst, 2002).

2.2.2. Structural transformations during phase transitions

The fast and reversible nature of phase switching (of the order of tens of nanoseconds) in $Ge_2Sb_2Te_5$ between amorphous and metastable crystalline states (activation energy of crystallisation (E_A) ~ 2.2 eV (Friedrich et al., 2000)) suggests

that no large scale atomic rearrangements occur. Similarly, the ease of transformation between metastable and stable phases (E_A ~ 3.6 eV (Friedrich et al., 2000)) is also attributed to structural similarities.

For example, in the model proposed by Sun et al. (2006) (Figure 2.2), the transition from metastable to stable phase is explained through slipping of unit II along a [210] direction while unit I remains intact. Matsunaga et al. (2004) also noted that their reported stable and metastable phases were similar, with the only major differences being a lack of adjacent Te-Te layers and the existence of Ge/Sb vacancies (up to 20 atomic percent in the Ge/Sb sub lattice) in the metastable phase. Observation of the appearance and disappearance of such vacancy layers along a <111> direction under the influence of the electron beam led Lotnyk et al. (2016) to propose that phase transformation occurs via the movement of Ge and Sb atoms along the same direction.

As described earlier, relics or fragments from the crystalline state may be preserved in the amorphous state after phase switching. Theoretical calculations by Akola & Jones (2007) suggested reorientation of alternating four-membered rings (or ABAB squares) during the phase transition. Hegedüs & Elliott (2008) also reported similar transient connected square rings appearing in melt simulations and acting as nucleation centres, reminiscent of the nanoscale order (1–2nm) observed in the fluctuation electron microscopy study by Kwon et al. (2007). DFT optimisation of electron diffraction reduced density function analysis by Borisenko et al. (2009) supported this theoretical model. The authors rationalised the phase transition through a mechanism similar to a Rubik's cube rotation involving a relative rotation of the layers of the four-membered rings so as to preserve some short-range and medium-range order between the amorphous and metastable phases.

In contrast, Kolobov et al. (2004) proposed an umbrella-flip model of amorphisation (Figure 2.6), where Ge atoms flip from an octahedral coordination (in a metastable crystalline phase) to a predominantly tetrahedral coordination (in an amorphous phase). Based on EXAFS measurements and XANES simulations, the authors argued that this diffusionless phase transformation could occur without complete structural relaxation (where some bonds are still preserved). Wełnic et al. (2005) also proposed a transition from a distorted rocksalt structure to an energetically similar spinel structure (a = 6.30Å) with Ge atoms in a tetrahedral environment in the amorphous phase, based on DFT calculations for $Ge_1Sb_2Te_4$. Calculations of changes in Ge coordination due to amorphisation in $Ge_2Sb_2Te_5$ (Da Silva, 2011) have shown that the reduction in average effective coordination number is actually smaller than the symmetric six-fold to four-fold coordination due to the presence of distorted octahedral sites in the metastable crystalline phase.

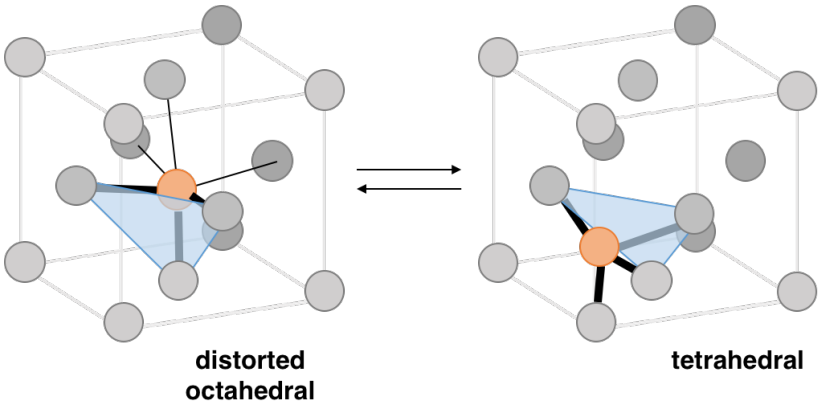

Figure 2.6: Illustration of umbrella-flip model proposed by Kolobov et al. (2004) where Ge atom (in orange) switches from a distorted octahedral environment in the metastable crystalline phase to tetrahedral coordination in the amorphous phase. Neighbouring Te atoms are shown in grey.

Atomic displacements from high-symmetry lattice positions in the metastable crystalline state have been described as local Peierls-like distortions. The simplest

Peierls distortion in a one-dimensional chain of equally-spaced atoms is illustrated in Figure 2.7, where a periodic distortion of the lattice leading to longer and shorter bonds decreases the energy of occupied electron states and creates an additional energy band gap (Lencer et al., 2011).

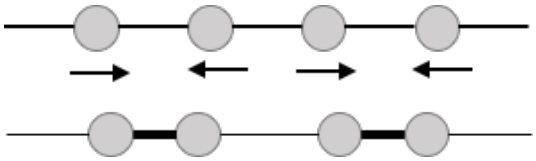

Figure 2.7: Illustration of a periodic Peierls distortion in a one-dimensional lattice resulting in a system of longer and shorter bonds instead of identical bonds.

Similar local distortions in the crystalline phase of phase-change alloys such as GeTe and $Ge_2Sb_2Te_5$ results in the breaking of octahedral symmetry of six identical bonds into three short and three long Ge-Te and Sb-Te bonds (e.g. as illustrated in Figure 2.6 with the thicker and thinner lines representing the short and long Ge-Te bonds respectively). This has also been described as bonding energy hierarchy between the short (stronger) and long (weaker) bonds (Kolobov, Krbal, Fons, Tominaga, & Uruga, 2011).

2.2.3. Role of resonance bonding

Although resonance was first used to describe chemical bonding in benzene rings and graphitic systems, Lucovsky & White (1973) extended the concept to describe sharing of electrons within high symmetry structures in solids such as crystalline IV-VI compounds and Group VI elemental semiconductors, which switch to amorphous states with vastly different optical and electronic properties.

Resonance bonding is characterised by pronounced electron delocalisation where a single, half-filled π-band forms two bonds from the same atom, i.e. more than

that allowed by the octet or '8 - *N*' rule (where the coordination of an atom with *N* valence electrons in a covalent bonding configuration equals (8 – *N)*), resulting in more bond positions than there are electron pairs. Electron density is redistributed among the unsaturated bonds via a resonance configuration, which requires longer range order (with alignment of higher-order neighbours) than conventional covalent bonding that only requires nearest-neighbour ordering for an electron bond pair.

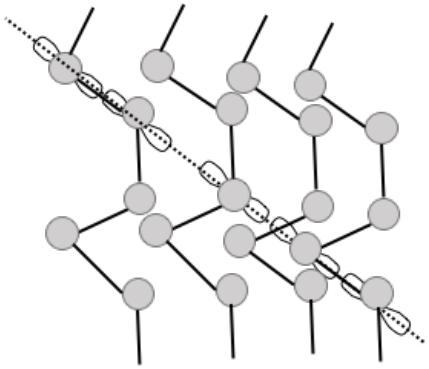

Figure 2.8: Projected view of the alignment of p-orbitals across helix-like chains of trigonal crystalline selenium, imparts long-range order and electron delocalisation leads to a resonance configuration. Covalent intra-chain bonds are in solid lines while the inter-chain bonds are dashed.

In the crystalline phase of elemental chalcogens such as trigonal Se (t-Se) and Te (t-Te), resonance bonding is achieved through the alignment of *p*-orbitals (Figure 2.8) of covalently bonded atoms in chain structures that contributes to long-range ordering between or across adjacent chains (Robertson & Huang, 2012; Shportko et al., 2008). In the amorphous phase, this alignment is disrupted by displacement and disordering of the chains, destroying long-range order and resonance while preserving the covalent backbone (intra-chain bonds). This system of strong intra-chain bonds and weak inter-chain bonds has been considered analogous to resonant bonding in crystalline GeTe-based phase-change alloys such as $Ge_2Sb_2Te_5$. However, Peierls-like

lattice distortions increase electron localisation and weaken the resonance effect in these materials.

Such resonance bonding is considered a unique characteristic of the crystalline phase of chalcogenide phase-change materials and is thought to be responsible for the large optical contrast observed between the crystalline and amorphous phases. These resonance effects have been quantified by measurements of increased electronic polarizability in the crystalline compared to amorphous phases (e.g. 70-200% increase in the dielectric constant of the crystalline phase from that of amorphous $Ge_2Sb_2Te_5$ (Shportko et al., 2008), which is comparable to that of an undoped covalent semiconductor such as Si or Ge).

2.3. Evidence of athermal mechanisms

Although the loss of long-range order during amorphisation destroys resonance bonding in crystalline phase-change materials, it has been shown that amorphisation via melting is not necessary for the large optical contrast observed between the crystalline and amorphous phases (Kolobov, Fons, & Tominaga, 2014; Kolobov et al., 2011). It has also been suggested that a change in the local bonding character, e.g. angular disorder (or loss of next-nearest neighbour angular order) irrespective of coordination number (Huang & Robertson, 2010), instead of a complete loss of long-rage order could be responsible for the drastic change in optical properties.

While sp^3-hybridised orbitals in tetrahedrally-bonded semiconductors such as Si or Ge split into bonding and anti-bonding states (that broaden and overlap to form valence and conduction bands respectively), only *p*-orbitals are involved in the splitting of molecular states in chalcogenides. In addition, chalcogenides which are

also known as lone-pair semiconductors (Kastner, 1972), have non-bonding electrons in lone-pair states which form the top of the valence band. Optical and electronic transitions can thus occur from bonding to anti-bonding states (intra-chain bonds) and from the lone-pair to anti-bonding states (inter-chain or resonant bonds).

2.3.1. Transient changes at sub-nanosecond timescales

Evidence of direct solid-state crystallisation of $Ge_2Sb_2Te_5$ films has been observed under low power laser irradiation (Friedrich, Weidenhof, Lenk, & Wuttig, 2001; Zhang et al., 2012). Real-time optical reflectivity measurements carried out by Zhang et al. (2012) during laser-induced crystallisation of $Ge_2Sb_2Te_5$ films using nanosecond pulse durations (with heating rates of approximately 10^9K/s) suggest the occurrence of solid-state crystallisation at low fluence followed by melting then ablation with increasing laser fluence ($T_c < T_m < T_{ablation}$). However, when shorter pulse durations were used (such as picosecond-pulse irradiation with heating rates of 10^{12}K/s), ablation occurred before melting ($T_c < T_{ablation} < T_m$). This lack of melting-involved laser-induced phase change (as also observed by Fons et al. (2010)) appears to lead to faster solid-state crystallisation by an order of magnitude.

Upon laser irradiation with nanosecond pulses, the excess energy of the photo-excited electrons is transferred to lattice phonons within the timescale of excitation. With an overlap of electron-hole pair recombination events, there is sufficient time for thermal equilibrium to be achieved in this regime, leading to heating of the material and a melting transition. However, this thermalisation process (which takes several picoseconds) cannot account for the transitions that occur under ultrashort laser pulse excitation at sub-picosecond timescales.

The faster speed of phase transitions in $Ge_2Sb_2Te_5$ that occur without melting has been attributed to structural changes that proceed via a photo-excited state instead of a molten or liquid state (as in the case of the slower thermal melting) and the role of electronic excitation in these phase transitions has been emphasised in recent literature (Kolobov, Fons, Tominaga, & Hase, 2014; Kolobov et al., 2011; Li et al., 2012). According to the non-thermal electronic excitation model (Sundaram & Mazur, 2002), when a significant fraction of the valence electrons is excited into the conduction band at a sub-picosecond timescale and the rate of phonon emission is slower than the timescale of excitation, the photo-excited electrons and the lattice are no longer in thermal equilibrium. Disordering of the lattice thus allows non-thermal transient transitions to occur without an increase in temperature.

There has been great interest in studying the non-equilibrium excited state properties within these ultrashort timescales with time-resolved optical pump-probe, electron and X-ray measurements or MD simulations. Recently, Waldecker et al. (2015) reported the decoupling of optical changes from the much slower structural changes in $Ge_2Sb_2Te_5$. Miller, Rudé, Pruneri, & Wall (2016) also differentiated the behaviour of the photo-excited electrons in amorphous and crystalline phases. Such optical dissociation studies are only achievable under strictly controlled conditions and are especially complicated for resonant bonding materials as noted by Kolobov, Fons, Tominaga, & Hase (2014). While a significant fraction (above 10%) of valence electrons need to be excited for detectable optical effects (Sundaram & Mazur, 2002), high excitation levels (that may be caused by high laser fluence) will lead to a rise in temperature, making it a challenge to distinguish purely electronic effects from thermal effects. Therefore, although large ultrafast optical changes without structural switching

may be an important step towards achieving faster speeds in photonic devices and switches, this comes at the cost of structural permanence.

2.3.2. Polarisation-dependent athermal transitions

Apart from optical dissociation studies on $Ge_2Sb_2Te_5$ discussed above, experimental evidence of athermal melting, amorphisation and crystallisation has also been observed during phase transitions induced by polarised light in other chalcogenides (such as glasses based on good glass formers e.g. selenium and sulphur). Linear anisotropy observed in otherwise macroscopically isotropic chalcogenides was attributed to the preferential orientation and growth of microscopic anisotropic crystallites perpendicular to the polarisation vector (Elliott & Tikhomirov, 1996; Fritzsche, 1995).

Using Raman scattering, Poborchii, Kolobov, & Tanaka (1998) found a preferential orientation of trigonal crystalline selenium (c-Se), where the direction of the *c*-axis was dependent on the linear polarisation of light used to induce the crystallisation of amorphous selenium (a-Se) films. This polarisation dependence suggests a non-thermal mechanism of photo-crystallisation, which has been an argument favoured by other similar studies where strong optical anisotropy was also observed in photo-crystallised selenium (Lyubin, Klebanov, Mitkova, & Petkova, 1997; Tikhomirov, Hertogen, Glorieux, & Adriaenssens, 1997). Melting of both a-Se and c-Se solids at room temperatures was described as a purely athermal phenomenon, involving the photo-excited rupture of the weaker inter-chain bonds (Poborchii, Kolobov, & Tanaka, 1999). Similar observations have also been made in layered As_2S_3 structures (Frumar, Firth, & Owen, 1995).

While polarisation dependence may be considered as unambiguous evidence for non-thermal effects, Poborchii et al. (1998) put forward a simple alternative thermal mechanism of crystallisation. The authors proposed differential absorption of the illumination by different c-Se crystallites oriented randomly in the amorphous film, such that photo-induced heating would promote preferential growth and orientation of the crystallites absorbing more of the linearly polarised light. The seeming contradiction in the ordering of chains during photo-crystallisation being disrupted by the photo-excited rupturing of inter-chain bonds was resolved by a two-stage process in which athermal photo-melting is followed by thermal crystallisation (Poborchii et al., 1999).

The observation of polarisation dependence offers an alternative means of determining whether thermal effects are purely responsible for phase transitions and associated electro-optical changes or if electronic excitation also plays a part (as suggested by Lyubin et al. (1997)). Indeed, Fons et al. (2010) suggested that the use of linearly polarised light may lead to spatially selective rupture of bonds in $Ge_2Sb_2Te_5$ and a polarisation-dependent crystalline state. This was exemplified in a study (Kitamura, Katsumata, Morita, Hira, & Saiki, 2012) where amorphous $Ge_2Sb_2Te_5$ films excited with linearly-polarised femtosecond laser pulses underwent an athermal phase-change and displayed anisotropy in the form of a large optical rotation.

2.3.3. Chirality and circular dichroism

Historically, photo-induced optical anisotropy was used to refer to linear anisotropy (linear dichroism and linear birefringence, that are associated with linearly polarised light) while the term gyrotropy referred to circular dichroism and circular birefringence (associated with circularly polarised light). In this thesis, however,

optical anisotropy is used broadly and interchangeably to denote both linear and circular anisotropies. Dichroism arises due to a difference in absorption of light, depending on the polarisation of the light passing through the medium; similarly, birefringence results from a difference in refraction. In addition to optical anisotropy, photo-darkening (an isotropic effect attributed to creation of colour centres) has also been observed in chalcogenides.

While the use of linearly polarised light to induce phase transitions and anisotropy was discussed earlier, the use of circularly polarised light has been rarely discussed in the phase change chalcogenide literature, e.g. the extension of Fritzsche's model (1995) to the use of circularly polarised light to induce optical anisotropy. An earlier theoretical model proposed by DiVincenzo (1988) predicted the effect of photo-induced gyrotropy in amorphous semiconductors, based on the difference in absorbance coefficients between left and right chiral domains. This involved time-sensitive diffusion of highly excited carriers from one domain to the other as first observed in As_2S_3 glasses (Lyubin & Tikhomirov, 1991).

DiVincenzo hypothesised that local chirality in bonds characterised by dihedral angles e.g. in twisted even-membered rings that persisted across atom clusters could contribute to medium-range ordering in continuous random network models. It was proposed that non-linear optical experiments could be used to probe such chiral ordering in amorphous materials. There have subsequently been experimental studies reported on the optical activity of gyrotropic single crystals (Goulon et al., 2000), chiral sculptured thin films (Robbie, Brett, & Lakhtakia, 1996) and self-assembling monolayers of metal oxides (Moshe et al., 2013) which typically involve optical rotation dispersion (a manifestation of circular birefringence) or circular dichroism in

the X-ray wavelength range using solution-based spectroscopy. However, investigations of phase change chalcogenide solid thin films are non-existent.

Circular dichroism spectroscopy

Gyrotropy is typically 10^3-10^5 times smaller than linear anisotropies and therefore much more difficult to observe and measure reliably (Kaminsky, 2000). Accordingly, circular dichroism (CD) measured in naturally occurring molecules tends to be in the order of millidegrees, as compared to artificial metamaterials with enhanced chirality exhibiting CD responses of a few degrees (Cao et al., 2013). The small chiral effect observed is attributed to the smaller helical pitch of the naturally occurring molecules or crystallites compared to that of the circularly polarised light in the UV-visible range.

Circular dichroism arises from a difference in absorbance between left and right circularly polarised light passing through an optically active chiral sample (Equation 2.1) and is commonly expressed in terms of the historical units of ellipticity (in millidegrees), although the differential absorbance can be measured directly in modern instruments. The proportional relationship between absorbance and ellipticity θ (in degrees) is given in Equation 2.2 (Schellman, 1975).

$$CD\ (\lambda) = \Delta\ ABS\ (\lambda) = \ ABS_{LCPL}(\lambda) - ABS_{RCPL}(\lambda) \qquad (2.1)$$

$$\theta\ (deg) \cong 33\ \Delta\ ABS(\lambda) \qquad (2.2)$$

CD spectroscopy is traditionally used in biology to study the structural and conformational chirality of proteins and other biological molecules. The technique is often termed natural circular dichroism spectroscopy, to differentiate it from magnetic

circular dichroism spectroscopy that is carried out in the presence of magnetic fields to determine spin and orbital magnetic moments and anisotropies.

Chirality

Since observation of CD indicates evidence of chirality, it may be instructive to examine the symmetry groups of chiral structures. Figure 2.9 illustrates the classification of the 230 known three-dimensional space groups, which are split into three classes depending on the type of operations permitted; either proper (simple rotations, translations and screw rotations) or improper (inversion, reflection, glide and rotoinversion) operations.

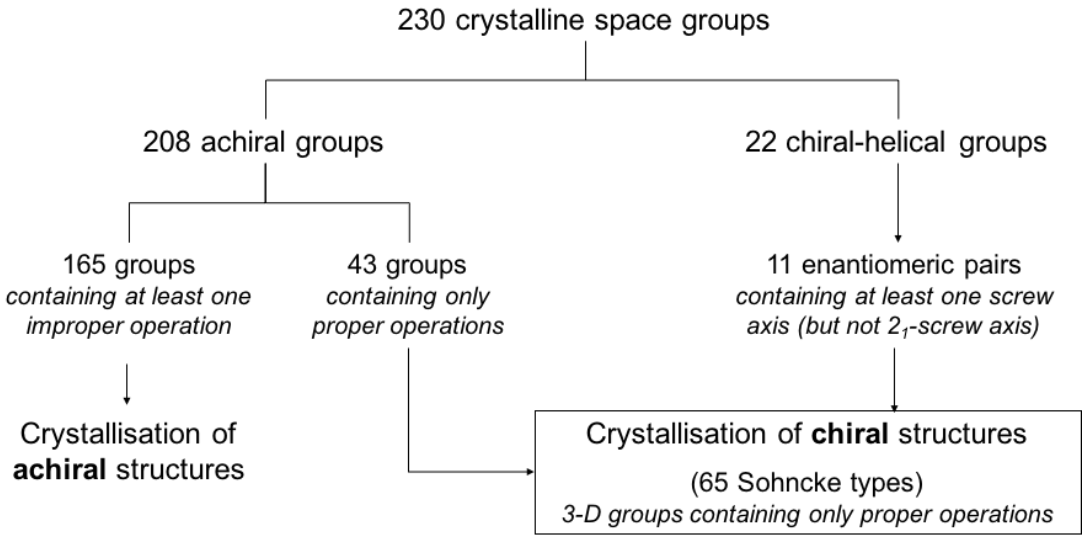

Figure 2.9: Classification of crystalline space groups in which chiral crystals can adopt one out of the 65 Sohncke space group types.

An object is defined as being chiral or having chirality if it "cannot be superposed by pure rotation or translation on its image formed by inversion through a point" (Müller, 2016). Thus, the symmetry group of such a chiral object would not contain improper operations. Although there are only 22 chiral-helical space groups, chiral structures are known to crystallise in both chiral and achiral space groups

containing only proper operations (65 Sohncke space group types) (Flack, 2003; Müller, 2016), as listed in Appendix A.

2.4. Doping of $Ge_2Sb_2Te_5$

A wide variety of dopants, including p-block elements (e.g. C, N, O, Si, In, Sn, Bi), some rare-earth metals and first-row transition metals (TM) have been investigated in relation to the crystallisation behaviour and enhancement of optoelectronic properties of $Ge_2Sb_2Te_5$. For example, N doping has been found to suppress crystallisation and grain growth, resulting in higher crystallisation temperatures (Caravati et al., 2011; Kim et al., 2008), which has important implications for increased temperature stability of phase-change devices. An increase in the mobility gap for conduction also showed increased resistivity in N-incorporated films (Privitera, Rimini, & Zonca, 2004).

Skelton & Elliott (2013) proposed that suitable dopants should be able to integrate into the host structure with minimal distortion, and found that first-row TM dopants generally occupy both vacancy and interstitial sites but tend to be located near voids when there is a mismatch of bond lengths or coordination. This matches the phase segregation of nitrogen to grain boundaries as observed in N-doped $Ge_2Sb_2Te_5$ (Caravati et al., 2011), with preferential binding to Ge to form a nitride involving a *p*-orbital hybridisation that can be related back to resonance bonding effects. Borisenko and co-workers (Borisenko, Chen, Cockayne, Song, & Jeong, 2011; Borisenko, Chen, Song, & Cockayne, 2009) also investigated the metastable and amorphous phases of nitrogen- and carbon-doped $Ge_2Sb_2Te_5$ and proposed similar ring motifs as in pure $Ge_2Sb_2Te_5$.

First-principles simulations by Skelton & Elliott (2013) with first-row TM dopants in a $Ge_2Sb_2Te_5$ host have shown that the elements V, Cr, Mn and Fe may have magnetic ground states in both amorphous and crystalline phases, allowing a potential additional parameter that may be utilized in spintronic applications. Interestingly, they also reported that while most of the TM dopants caused an increase in optical contrast at 780 nm (the operational wavelength of compact discs read/write lasers), optical contrast was generally reduced at shorter wavelengths of 405 nm and 650 nm.

Based on Raman spectroscopy of $Ge_2Sb_2Te_5$ doped with varying concentrations of Bi, Sn and In, Kozyukhin, Veres, Nguyen, Ingram, & Kudoyarova (2013) also reported that the incorporation mechanisms and bonding configurations may differ depending on the dopant concentration. Doping and the subsequent local distortions can thus be expected to significantly affect the phase transformations in $Ge_2Sb_2Te_5$ as well as its electronic and optical properties.

2.5. Structural characterisation techniques

The choice of experimental techniques for probing and characterising thin films requires careful consideration of the experimental objectives. Much of the literature on $Ge_2Sb_2Te_5$ discussed in earlier sections has used non-destructive surface techniques such as Raman scattering, X-ray absorption and fluorescence measurements, as well as potentially destructive ones including powder diffraction, transmission electron microscopy (TEM) imaging, diffraction and related spectroscopic techniques. Atomic modelling and simulations can complement and enhance these experimental studies. Some relevant techniques, practical concerns and challenges will be briefly explored in this section.

2.5.1. Sample preparation

Thin film preparation

While bulk glasses are usually prepared by melt-quenching or annealing into glassy amorphous states, thin films of amorphous alloys or compounds are more commonly prepared by vapour deposition. Simple thermal evaporation may result in films with varying compositions especially when the melting points of the constituent elements differ, whereas physical vapour deposition (PVD) such as conventional sputtering in the presence of an inert gas (e.g. argon) or chemical vapour deposition (CVD) can be used to obtain films with a stoichiometry similar to that of the target.

Sputter deposition involves ablation of the target by bombardment with charged particles from a plasma created from the sputtering gas, followed by deposition and growth of the vaporised material on a substrate. Since sputtering does not require heating of the target to high temperatures, it is especially useful for compounds whose elements would otherwise evaporate at different rates. Sputtering is typically carried out by applying a negative DC (direct current) voltage to the target (cathode), which attracts positively charged ions from the plasma that sputter the target surface. However, DC sputtering only works for conductive materials that can act as an electrode. Poorly conductive targets lead to charge build-up on the surface, which can be avoided by applying an AC field (usually at a radio frequency (RF) of 13.56MHz) between the targets and a grounded electrode in a process known as RF sputtering.

Magnetrons are also often employed in sputtering to increase the deposition rate; magnets placed behind the cathode create a strong magnetic field that traps charged particles in a dense plasma near the target surface, increasing the frequency

of collision between the charged particles and the target instead of the substrate. Other variations include pulsed laser deposition, where a pulsed laser is used to ablate material for plasma generation and reactive sputtering involving a chemical reaction between the sputtering gas and sputtered material before deposition. CVD processes, in which a reaction between volatile precursors leads to deposition of the desired product on substrate surface, are often used for increased purity, stoichiometry control and conformal coverage of high-aspect ratio feature surfaces.

The choice of technique, deposition conditions and substrates used can influence growth modes. For example, molecular beam epitaxy, pulsed laser deposition and CVD processes are favoured for the growth of epitaxial films due to the ability to control crystallinity of the films. While crystalline substrates are often chosen for the growth of polycrystalline or single crystal thin films via lattice matching, the choice of substrates is less important for amorphous film growth. It is also quite common for films to be deposited in an amorphous state and then annealed into a crystalline phase. Predominantly, parameters such as the deposition temperature, power applied to target, gas flow and pressure can be controlled precisely to achieve desired characteristics, including material properties that are influenced by the film microstructure.

Transmission electron microscopy sample preparation

Thin films are frequently deposited directly onto mesh grids for plan-view analysis in transmission electron microscopy (TEM) studies. Planar specimens can also be prepared by depositing thin films on substrates with high solubility in water or other solvents (e.g. NaCl) that can then be floated and picked up directly onto TEM mesh support grids. However, there is a tendency for the disintegration of these

floated-off films due to surface tension, rendering site-specific preparation difficult. Epoxy coatings can be applied for structural rigidity but this can pose problems when removing the epoxy layer, especially if the material is sensitive to heat or the chemical solvents used.

Another challenge that may be posed by the support film coating on the mesh grids during TEM analysis is the potential complication in sensitive analysis of amorphous thin films. Although these ultra-thin coatings (of a few nanometres of evaporated carbon or formvar) are electron-transparent and offer support for the thin film specimen, their presence may interfere with the structural analysis of amorphous materials (especially where diffused diffraction rings from both materials cannot be differentiated easily). As such, holey carbon support films are favoured over evaporated support films that cover the entire grid.

Furthermore, when *ex-situ* measurement of optical properties of the thin films is required before TEM analysis, the substrates would have to be optically transparent in the wavelength regime of interest. In contrast to the direct growth of films on TEM grids, the preparation of very thin samples for TEM analysis would require different techniques. Traditional dimpling, grinding and polishing can be used to prepare plan-view and cross-section samples but focused ion beam (FIB) milling, in particular, can be used for fast, site-specific cross-section sample preparation.

In modern FIB instruments, a finely focused primary beam of high-energy gallium ions (30kV accelerating voltage) is used to sputter the sample surface and mill site-specific specimen lift-outs while a secondary low-energy electron beam (5kV accelerating voltage) is used for imaging without causing further damage to the sample. Gas-assisted deposition of sacrificial metals such as tungsten or platinum is

often carried out to protect the sample from destructive sputtering, especially for $Ge_2Sb_2Te_5$ samples which can be sensitive to heating under the electron and ion beams. Gallium ion implantation and amorphisation of the lifted-out specimen surfaces can occur but gentle ion milling at low voltage can remove most of the damaged surface layer, leaving about 2nm of amorphised material on each side of a 20-30nm thick lamella.

2.5.2. Electron microscopy

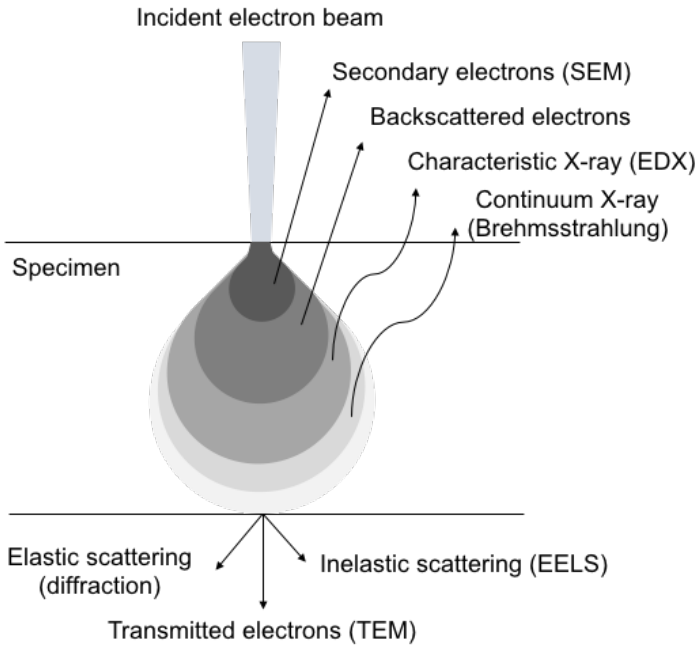

Figure 2.10: A simplified illustration of electron-matter interactions

When an electron beam is incident on a specimen, the electron-matter interaction (Figure 2.10) results in scattering and transmission of electrons through the specimen as well as emission of secondary electrons and characteristic X-rays. Imaging of low-energy secondary electrons and high-energy backscattered electrons in the scanning electron microscope (SEM) gives topographical and compositional information about the specimen close to the surface. Transmitted and forward-

scattered electrons can be used to measure information in the TEM, by combining electron diffraction with direct high-resolution imaging and a range of other techniques. In particular, electron energy loss spectroscopy (EELS) is the result of inelastic scattering and can be used to give chemical information on composition and bond states, while elemental composition can also be characterised using energy dispersive X-ray (EDX) spectroscopy which measures the energy of characteristic X-rays emitted during electron excitation.

While these versatile and complementary techniques are well established, the use of electron diffraction techniques to perform radial distribution or reduced density function (RDF) analysis is less common. The latter is a powerful technique that has been used to characterise local order in amorphous materials such as silicon (Treacy & Borisenko, 2012), oxide thin films (Yan et al., 2012) and glasses (Mu, Wang, Feng, & Kübel, 2016).

Reduced density function (RDF) analysis

The RDF is an effective way of describing average local structure in terms of the probability of finding a pair of atoms separated by a distance ***r***. This function is experimentally accessible through diffraction experiments using X-rays, neutrons or electrons and enables characterisation of structural order in polycrystalline and nanoparticulate materials and short-range order in amorphous materials or glasses.

Considering a system of N particles occupying points at $r = R_i$, a two-particle distribution function,

$$n^{(2)}(r_1, r_2) = n^{(1)}(r_1)n^{(2)}(r_2)g^{(2)}(r_1, r_2)\ , \qquad (2.3)$$

describes the probability of two particles existing simultaneously at r_1 and r_2. Although higher-order functions can be defined similarly, only the pair correlation function $g^{(2)}(r_1, r_2)$ (or simply $g(r)$) can be measured experimentally. Placing the origin on an atom, the average number of atoms in a spherical shell of thickness dr at distance r is given by

$$n(r) = 4\pi r^2 \rho g(r) dr, \tag{2.4}$$

where $\rho = \frac{N}{V}$ is the average number density of N atoms in a shell volume $V \approx 4\pi r^2 dr$. The radial distribution function $J(r)$ is defined as;

$$J(r) = 4\pi r^2 g(r) , \tag{2.5}$$

where $g(r)$ is the pair distribution function directly related to the local density of atoms at a distance $\boldsymbol{r}$ from the central atom.

For a perfect crystal with a periodic arrangement of atoms, this distribution can be represented as a series of sharp peaks (which may be broadened by thermal vibrations), whereas for an ideal dilute gas with a completely random arrangement, where the atom position does not influence the distribution around it, $g(r)$ equals 1 for all r and $J(r) = 4\pi r^2$. The distribution function for amorphous solids at short distances lies in between these two cases (Figure 2.11). The first peak position giving the average interatomic distances between nearest-neighbours is typically clearly defined but as r increases, increased disorder leads to a spread of bond angles and lengths, resulting in peak broadening and a decrease in peak intensity.

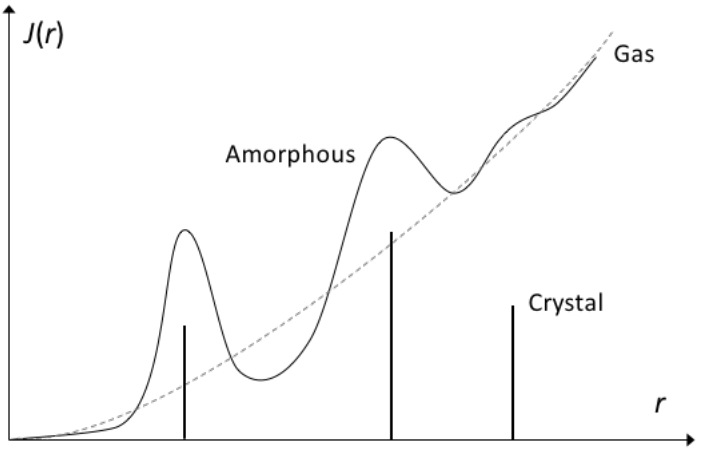

Figure 2.11: Sketch of the general forms of the radial distribution function J(r) for a perfect crystal (vertical lines), amorphous solid (solid curve) and ideal dilute gas (dotted curve) systems.

It should be noted that $J(r)$ as plotted in Figure 2.11 is a rotationally averaged one-dimensional representation of a three-dimensional structure. Although the distribution is influenced by higher-order correlation functions, the pair correlation function $g(r)$ can be studied through a reduced density function (RDF),

$$G(r) \equiv 4\pi r[g(r) - \rho_0] , \qquad (2.6)$$

where ρ_0 is the macroscopic average density. The relationship between $J(r)$ and $G(r)$ can be expressed as Equation 2.7 and bond angles and coordination numbers can also be extracted from these two functions and $g(r)$.

$$J(r) = r(G(r) + 4\pi r\rho_0) \qquad (2.7)$$

While diffraction data from X-rays, particularly with synchrotron radiation and neutrons has been widely used, the probe size of X-ray and neutrons is typically too large for the study of short-range order within nanovolumes of materials. Electron diffraction, however, is particularly powerful in this regard, especially using aberration corrected probes. The procedure for extraction of the reduced density function (RDF) $G(r)$ from experimental electron diffraction patterns (recorded using selected area or

nano beam diffraction under parallel illumination in a TEM) was first developed by Cockayne & McKenzie (1988) and this implementation is detailed in Chapter 3.

Since the RDF is only sensitive to first-order (two-body or pair) correlations, the analysis describes short-range order of up to about 1nm. Accurate interpretation of the raw data and partial distribution functions of alloys and compounds are accessible through refinement of theoretical models (Cockayne, Chen, Li, & Borisenko, 2010), which is further described in a subsequent section.

However, fluctuation electron microscopy (FEM) (Voyles, Gibson, & Treacy, 2000), which is a hybrid method combining imaging and diffraction, has been suggested to be more sensitive to higher-order correlation functions than the RDF technique (Treacy, Gibson, Fan, Paterson, & McNulty, 2005; Yan et al., 2012). FEM quantifies the extent of medium order (roughly 1–3nm) by measuring the angular dependence of scattering fluctuations (diffracted intensity variance) from nanovolumes, which is manifested as "speckled" contrast, in hollow-cone dark-field images (Treacy & Gibson, 1996) or a series of nanobeam diffraction patterns (Voyles & Muller, 2002). FEM analysis is dependent on higher-order (three and four-body) correlations than RDF techniques, although sensitivity to medium-range order is maximised when the image resolution is of the characteristic size of the ordered regions being studied.

These techniques for extracting an averaged statistical description of amorphous material structures are still evolving and alternative methods for RDF analyses (Cockayne et al., 2010; Koch & Garofalini, 2006; Petersen, McBride, McCulloch, Snook, & Yarovsky, 2005) and methods for improving the resolution and

accuracy (Chen, Cockayne, Borisenko, & Song, 2011) for medium-range order sensitivity have been proposed.

Details of RDF analysis using electron diffraction data are discussed further in Chapter 3. Most commonly, this technique involves the use of selected area electron diffraction (SAED), which is suited to averaging of structural information over large areas. However, recent advancements in electron optics enable the formation of smaller probes in nanobeam diffraction (NBD) in TEM and Scanning TEM (STEM) for characterising smaller volumes.

Focusing a convergent probe on the specimen can produce atomic sized beams in STEM mode. However, RDF studies of defects and structures without long range periodicity usually require parallel illumination with small beam convergence to form discrete spots in the diffraction pattern. This can be achieved by setting up a quasi-parallel probe with approximately 1mrad convergence semi-angles. Similar techniques have been developed to achieve near-parallel probe diameters of 1–2nm on a JEOL 2010F microscope (D-STEM technique) (Ganesh, Kawasaki, Zhou, & Ferreira, 2010) and 15–50nm probes on a Tecnai F-30 microscope (Kolb, Gorelik, Kübel, Otten, & Hubert, 2007).

2.5.3. Structural modelling

Molecular dynamics

Molecular dynamics (MD) is a simulation method that is frequently used to examine the dynamics of atomic-level phenomena, to refine atomic or molecular structures and to examine and/or predict their physical properties. MD requires definition of a potential function (interatomic potential) that describes the interactions

between particles in a system. Classical MD treats the atoms as classical particles and uses semi-empirically derived potentials (such as the Born-Oppenheimer approximation) to represent their ground state, while system properties dependent on quantum effects are not considered. Atomic forces, the system energy and properties can be approximated more accurately from first principles using a combination of quantum mechanical methods, such as density functional theory (DFT) calculations, coupled to molecular dynamics. This derivation from first principles which is independent of empirical parameters, including the calculation of the system evolution with time, is referred to as *ab-initio* MD simulation.

DFT reduces the many-electron problem of the quantum mechanical ground state to a single electron form, through the self-consistent-field Kohn-Sham equations (Kohn & Sham, 1965). Practical solutions of these equations are performed by approximations of the exchange-correlation energy functional e.g. the local density approximation (LDA) where the functional based on a uniform electron gas is only dependent on the local density. However, the electron correlation in molecules and solids can be overestimated by LDA due to large bond strengths. The use of functionals that also depend on the gradient of the local density (general-gradient approximation (GGA)) and the second-derivative of the local density (meta-GGA), or hybrid functionals (that mix Hartree-Fock exchange energy with other approximations as above) (Becke, 1993) improve upon LDA and can lead to more accurate approximations.

Structural models of amorphous phase change materials are often created with *ab-initio* MD simulations for complementary theoretical investigations. This involves simulating the melt-quench procedure using an initial model in which the simulation

cell is heated to high temperature to randomize the atom positions, equilibrated above the melting point and subsequently rapidly quenched in a series of temperature reduction steps and annealed to give an amorphous model. DFT energy optimisation of the models can result in optimisation of atom geometries corresponding to local or global energy minima.

As mentioned earlier, there are differences between as-deposited and melt-quenched amorphous structures and the corresponding calculated models for $Ge_2Sb_2Te_5$ show different amounts of tetrahedral arrangements and homopolar / heteropolar bond distributions (Akola et al., 2011). It has been suggested that homopolar (Ge-Ge, Sb-Sb, Te-Te) bonds and Ge-Sb bonds (often referred to as "wrong" bonds) are more common in as-deposited structures, reducing the occurrence of even-numbered ABAB square rings which leads to less nucleation sites and slower crystallisation speeds. However, simulating the as-deposited amorphous structure (Akola et al., 2011) is a more complex procedure than melt-quench simulation which requires knowledge of the layered or clustered deposition of the material.

Simulating the crystallisation of phase change materials also requires *ab-initio* MD to capture the complex structural rearrangements. Although crystallisation occurs in nanoseconds, this timescale is too long for computationally intensive *ab-initio* simulations which are typically limited to hundreds of picoseconds. Standard methods also restrict the simulation cell size to an upper limit of 1-2nm (< 800 atoms), although recent developments have shown extended capability for handling larger models (GeTe (Sosso, Miceli, Caravati, Behler, & Bernasconi, 2012), $Ge_2Sb_2Te_5$ (Sebastiano Caravati, Sosso, Bernasconi, & Parrinello, 2013)) over timescales of a few nanoseconds.

Reverse Monte Carlo modelling

The MD simulated model is often subsequently refined to arrive at a structure that has greatest consistency with experimental data. This is accomplished by Reverse Monte Carlo (RMC) modelling, where atoms in a starting configuration are displaced randomly, subject to a set of constraints, over an iterative process until the data generated from the model matches the input experimental data (usually the measured structure factor or its Fourier transform, the radial (pair) distribution function or its associated reduced density function in the case of electron diffraction). RMC was primarily developed to study liquid and amorphous materials (McGreevy & Pusztai, 1988) and it continues to be popular in these applications. The method has also been extended to the study of disordered crystalline materials.

Starting with the initial configuration obtained from MD simulations, normal periodic boundary conditions are applied and the radial distribution function $g_s(r)$ of the model is computed. A new configuration is created by random movement of an atom within a specified distance, for which a new radial distribution function $g'_s(r)$ is calculated. The change in radial distribution function is then compared against the corresponding experimental data $g_e(r)$ using a standard χ^2 test;

$$\chi^2 = \sum_{i=1}^{m} \left(g_e(r_i) - g_s(r_i)\right)^2 / \sigma_e^2(r_i) \qquad (2.8)$$

$$\chi'^2 = \sum_{i=1}^{m} \left(g_e(r_i) - g'_s(r_i)\right)^2 / \sigma_e^2(r_i) \qquad (2.9)$$

where m is the number of r points and σ_e is the experimental error. If $\chi' < \chi$, the new configuration is accepted, or if $\chi' > \chi$, it is accepted with a probability that follows normal distribution with width σ, then serving as the starting configuration for the next random motion. Otherwise, the initial configuration is retained. This process is

repeated until χ^2 decreases to and oscillates about a minimum value for each atom in the model. The structure factor can also be compared instead of the radial distribution function or the reduced density function and software programs typically compute just the subsequent changes in the functions due to atomic motion.

RMC is an improvement upon the traditional Metropolis Monte Carlo (MMC) method which minimises a potential energy function instead of the differences in the radial distribution function but lacks consistency with experimental data. A significant issue that RMC modelling faces is the lack of a unique solution of the atomic structure, since multiple configurations can result in the same structure factor used in the fitting. Starting with *ab-initio* simulations instead of random models may alleviate this problem but use of multiple experimental datasets (neutron, X-ray, electron scattering and EXAFS data) (e.g. RMCProfile[1]) is considered essential to arrive at a unique atomic model that is consistent with all available data. Since RMC tends to create the most disordered systems consistent with the data, an appropriate choice of constraints such as closest distance of approach of two atoms, coordination numbers and bond angles are usually also included to reduce the number of possible configurations. The RMC method also tends to produce unphysical local bonding configurations when fitting the experimental data but this may be overcome by hybrid RMC methods (e.g. HRMC (Opletal, 2017)) which minimise both the potential energy and discrepancies between experimental and simulated data.

[1] RMCProfile. v6.7.0. July 2017. http://www.rmcprofile.org/

2.6. Summary

This chapter has provided a background history describing the significance of $Ge_2Sb_2Te_5$, including structural models of the different phases observed and debated in the literature. Various mechanisms of the fast and reversible phase change between amorphous and metastable crystalline states have also been discussed, relating resonance bonding in the system to the large optoelectronic contrast observed between the phases. While a thermal route for the phase transition is still required for permanent structural change, there is also strong evidence of the involvement of athermal effects. Such polarisation-dependent effects and the optical anisotropic properties may lead to new possibilities in applications for $Ge_2Sb_2Te_5$. This places great importance on characterisation techniques used to investigate these properties as well as theoretical calculations and computational models.

Chapter 3

Experimental Methods

3.1. Thin Film Deposition

Pure and doped amorphous GST thin films were deposited by magnetron radio frequency (RF) sputtering (Kurt J. Lesker NANO 38) at the Optoelectronics Research Centre, University of Southampton. Films of varying thicknesses were deposited on 25mm diameter fused silica (1mm thick) and lithium fluoride (2mm thick) disk substrates. These substrates were chosen for their optical transparency between 180nm and 600nm, making them suitable for subsequent optical measurements in the same wavelength range.

The fused silica substrates were cleaned before deposition as follows: sonication using acetone in an ultrasonic bath for about 3 minutes, washing with deionised (DI) water then methanol, immediate drying with compressed air, then baking on a hot plate at 140°C for about 5 minutes to remove any remaining moisture on the substrate surface. This cleaning procedure was however, not performed on samples on lithium fluoride substrates due to possible degradation of the substrates from exposure to aqueous environments.

Thin film deposition was carried out in an argon environment (using a gas flow of 20 standard cubic centimetres per minute (sccm); up to $1E^{-5}$ Torr vacuum pressure), with the substrates supported on a rotating stage to give an even film thickness across the substrate surface. Pure GST films were deposited using a $Ge_2Sb_2Te_5$ sputter target; 3 and 7 atomic percent (at%) chromium doping (Cr-GST) was achieved by tuning the

power density of an additional Cr target relative to the $Ge_2Sb_2Te_5$ target. Adjusting the power density of the sputter targets affects the deposition rate and therefore, trials were conducted on glass slides to determine the required target powers and exposures needed to achieve a desired film thicknesses (as measured with a KLA Tencor Profiler). In addition, doped GST films using dopants including gold, cerium, selenium, indium and titanium with a concentration of 10 at% were similarly prepared by RF sputtering. Nitrogen doped GST (N-GST) films (10 at%) prepared by plasma nitriding of GST films were obtained from a commercial source.

Film thicknesses were selected to give an optical absorption of *ca.* 1 in the 180nm to 600nm wavelength range after phase transition and photo-darkening of the film. This was determined by trial and error to be approximately 30nm for pure GST, 45nm for N-GST and 40nm for Cr-GST. Films with all other dopants were also deposited at a thickness of 40nm.

As-deposited GST and N-GST samples were coated with a 20nm thick capping layer of silica by RF sputtering to prevent oxidation during long-term storage. However, subsequent laser irradiation caused damage to the capping layer (peeling and formation of surface dendritic structures), exposing the underlying GST film. Hence, another set of GST and Cr-GST films were prepared with a thinner 5nm capping layer together with a corresponding set of uncapped samples to aid studies of the effects, if any, of the capping layer.

3.2. Laser irradiation

The as-deposited amorphous thin films were irradiated with left or right circularly or linearly polarized light (L-CPL or R-CPL or LPL, respectively) to induce a phase transition or crystallisation. These laser excitations were carried out at the Clarendon Laboratory, Department of Physics, University of Oxford. Nanosecond laser pulses (8ns FWHM (full width half maximum) pulse width, 10Hz repetition rate) were generated using a frequency-doubled Nd:YAG laser light at a wavelength of 532nm (second harmonic).

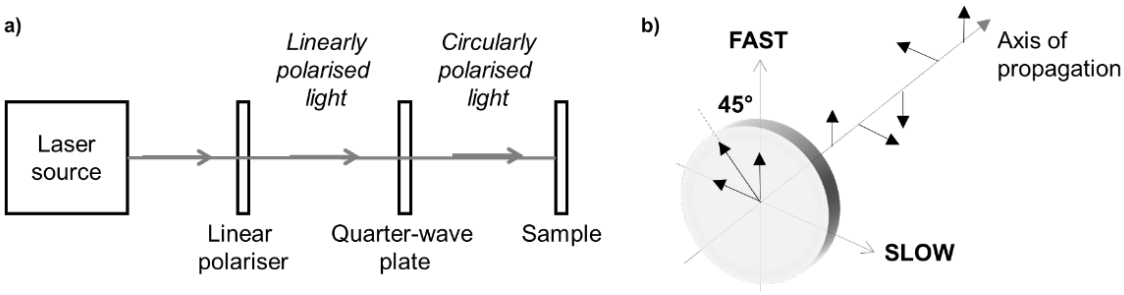

Figure 3.1: a) Simplified diagram of the optical setup used for laser irradiation of thin films and b) a quarter-wave plate that produces right-hand CPL (tips of the arrows showing maximum components of slow and fast axes trace out a right-handed helix).

Circularly polarised light (CPL) is a superposition of two linearly polarised plane waves with equal amplitude and a 90° phase difference. The most common means of generating CPL is to pass linearly polarised light (LPL) through a quarter-wave plate (Figure 3.1(a)). A linear polariser (Glan-Taylor prism) was first used to ensure a 100% plane polarised wave incident on the quarter-wave plate. The axis of polarisation of the incident electromagnetic wave was chosen such that it makes a 45° angle with respect to the fast (or slow) axis of the quarter-wave plate (Figure 3.1(b)), which divides the light into two equal perpendicular electric field components where one is retarded by a quarter wavelength, producing a circularly polarised wave. The

corresponding magnetic field component is similarly affected. The other handedness of circularly polarised light was produced by rotating the quarter-wave plate (equivalent to rotating plane of polarisation of incident light) by 90°.

The samples were mounted with the film facing the beam and were irradiated with average laser powers varying between 3mW and 20mW. For each power chosen, three polarised irradiations were carried out: L-CPL, R-CPL, and LPL (Figure 3.2). Preliminary investigations were carried out with varied exposures guided by visual changes in the film (photo-darkening indicating a phase transformation), but longer exposures or higher powers resulted in optical damage to the film (ablation of material from the centre of the irradiated spot where the Gaussian profile laser beam (Figure 3.3) is most intense). On this basis, the exposure duration was standardised at 20s for all samples in order to achieve uniform photo-darkening of the film while minimising laser-induced damage.

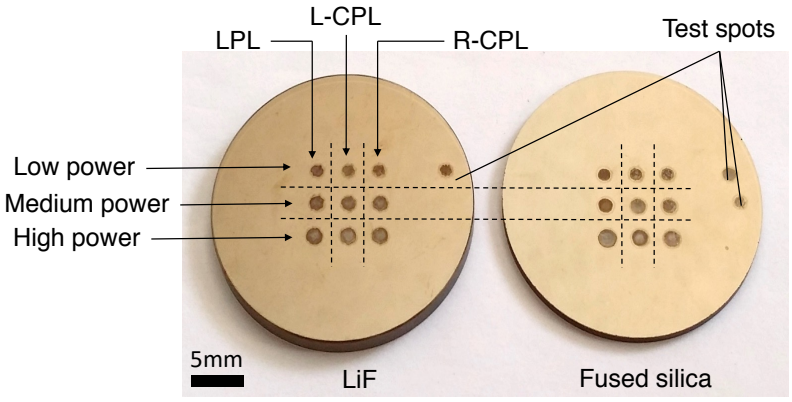

Figure 3.2: Laser-irradiated spots on thin film samples (on 25mm diameter substrates) with varying power and polarisation.

The average optical power of the laser (measured at the sample position using a laser energy meter) was prone to minor fluctuations. Where it was immediately obvious (e.g. if an irradiated spot was not darkened or shaped similar to other spots in

the set), this was rectified by measuring and adjusting the power and repeating that irradiation at another position. However, while this ensured that each row of spots on a film were irradiated with approximately the same power, spots on different films irradiated during different sessions were not easily comparable. The effective beam area also differed slightly between different irradiation sessions. The laser fluence or energy density (pulse energy per unit effective area) was therefore calculated as a more useful parameter for comparison.

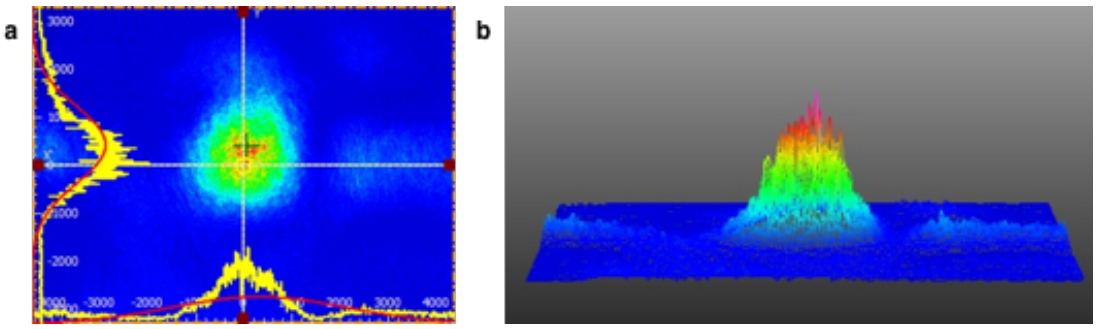

Figure 3.3: Gaussian profile of the laser beam measured using a CCD camera beam profiler at the sample position.

For a measured average power of the laser beam, P_{avg}, and a repetition rate, R_{rep}, the average pulse energy is given by;

$$\mathrm{E}_{pulse} = \frac{\mathrm{P}_{avg}}{\mathrm{R}_{rep}} \qquad (3.1)$$

The effective beam diameter and area (corrected for a Gaussian intensity by calculating an equivalent circular area within which pixel intensities exceed $1/e^2$ or 13.5% of the peak intensity) was measured using a ThorLabs CCD camera beam profiler at the sample position (Figure 3.3). This effective beam area A_{eff} was then used to calculate the pulse energy density U_{Pulse} (Equation 3.2). A more accurate total energy density U_{Total} can also be calculated using Equation 3.3. However, since the exposure duration t was constant for all samples, the proportional quantity U_{Pulse} was used for simplicity.

$$U_{Pulse} = \frac{\mathrm{E}_{pulse}}{\mathrm{A}_{eff}} \quad (3.2)$$

$$U_{Total} = \mathrm{U}_{Pulse} \times \mathrm{R}_{rep} \times t \quad (3.3)$$

3.3. Circular Dichroism (CD) Spectroscopy

Circular dichroism (CD) spectroscopy was performed at beamline B23 at Diamond Light Source (Hussain, Jávorfi, & Siligardi, 2012) located at the Harwell Science and Innovation Campus in Oxfordshire, UK. Synchrotron radiation is two to three orders of magnitude brighter than in conventional bench-top CD spectrometers, providing a much higher spectral signal-to-noise ratio especially at shorter wavelengths. The highly-collimated beam with a small cross section (about 0.6 mm in diameter) leads to a higher photon flux density that significantly reduces measurement time and the amount of chiral material required for successful detection of a CD signal.

3.3.1. Experimental setup

Measurements were carried out using the module B spectrograph (Figure 3.4) at the B23 beamline. A $MgCl_2$ Rochon polarising prism installed in the module splits the incident (elliptically polarised) synchrotron radiation that has passed through a monochromator (with an exit slit size of 1mm) into two orthogonal linearly polarised beams. A fused silica photo-elastic modulator (PEM) acts as a quarter-wave plate, resulting in two circularly-polarised beams that are constantly modulated between left and right handedness at 50kHz frequency. Thin film samples were mounted on a customised vertical mounting stage in the chamber with the film facing the beam. Due to the divergence of the extraordinary ray (2-3mm apart from the ordinary ray on the sample), the dual-beam mode is only suitable for probing homogeneous samples.

Hence, CD measurements on the thin films were performed in single-beam mode (by blocking the extraordinary ray before the sample).

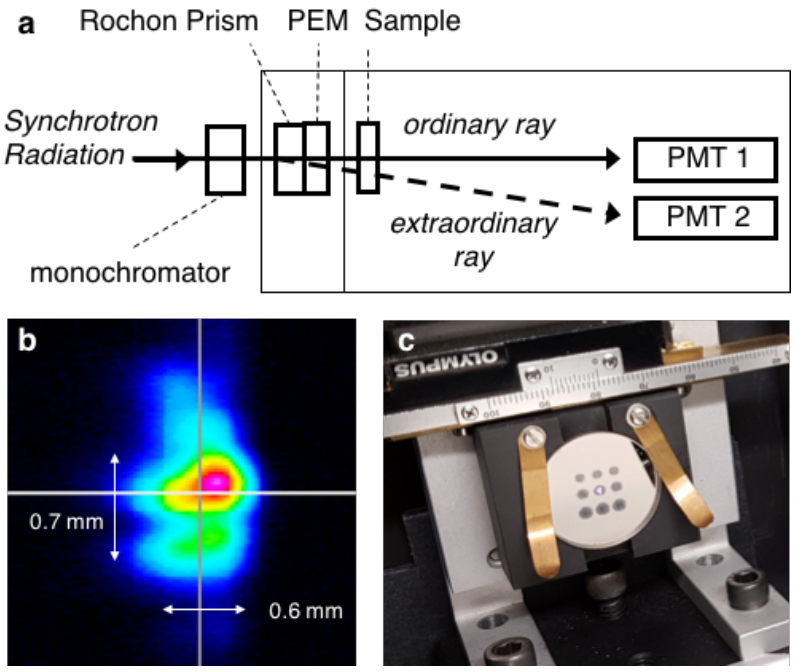

Figure 3.4: (a) Simplified schematic of the spectrometer at the beamline user-end station showing paths of both the ordinary and extraordinary rays. (b) A typical beam profile of a single beam, which is shown in (c) passing through the central laser-irradiated spot of a thin film sample on a customized mounting stage.

Alternating left (L-CPL) and right circularly polarised light (R-CPL) transmitted through the film is detected by a photomultiplier tube (PMT 1). The PMT generates voltage signals representing the time-dependent intensity of the light detected, which are then digitised into a 50kHz AC signal, a time-averaged DC level and noise components. Since the CD is calculated from the 50kHz AC component relative to the DC component (the difference between L-CPL and R-CPL absorbance measurements), there is no need for independent amplification of each component and calibration using a chemical standard. This is in contrast to conventional CD instruments based on a lock-in amplifier (where the DC component is kept constant via a PMT high tension (HT) voltage feedback loop such that the changing

wavelength-dependent gain factor requires calibration). All the above computations were digitally processed on the backend using the direct subtraction method developed by On-Line Instrument Systems, OLIS and only the final CD spectra and corresponding PMT voltage data were accessible to the end user at the beamline station.

By rotating the Rochon prism between two orthogonal positions (R1 and R2), the alternating handed circularly polarised light incident on the sample was rotated by 90°. CD spectra were collected using both prism rotations (the significance of which is explained in the following section), from an as-deposited amorphous (reference) region and laser-irradiated regions (irradiated by L-CPL, R-CPL and LPL) for each thin film. Alignment of the beam at different sample positions was performed using white light with the Rochon prism at the R1 position. Corresponding spectra at the R2 position were then recorded by rotating the prism only, without any change in the sample position. Each spectrum was averaged over four scans, where each scan was recorded using 5nm steps between 180nm and 600nm (near-UV–visible spectral range) with an integration time of one second at each data point. Since the recorded spectra were characteristically broad and lacking fine features, a step size of 5nm was considered reasonable within the time constraints of the experimental sessions.

3.3.2. Spectral analysis

Since the synchrotron source radiation is elliptically polarised, the intensity of the incident CPL beam on the sample is dependent on the relative orientation of the axis of the ellipse and the Rochon prism. When the Rochon prism is rotated, the ordinary beam achieved at the R2 position has a lower intensity than that at the R1 position. This is reflected in the PMT voltage spectra (Figure 3.5), where lower

transmission intensities lead to higher noise and higher voltage values at the R2 prism position compared to R1. Higher PMT voltages are also recorded when detecting the beam transmitted through a reference amorphous region as compared to the laser-irradiated (crystalline) regions at both prism rotations (R1 and R2). The PMT voltage data can thus be used to determine the accuracy of the beam alignment on a region of the sample. However, when the voltage level approaches the saturation limit of the detector (700V), the low signal-to-noise ratio could also result in spectral artefacts, particularly at either end of the wavelength range. Hence, the CD spectra need to be interpreted in tandem with the corresponding PMT voltage spectra.

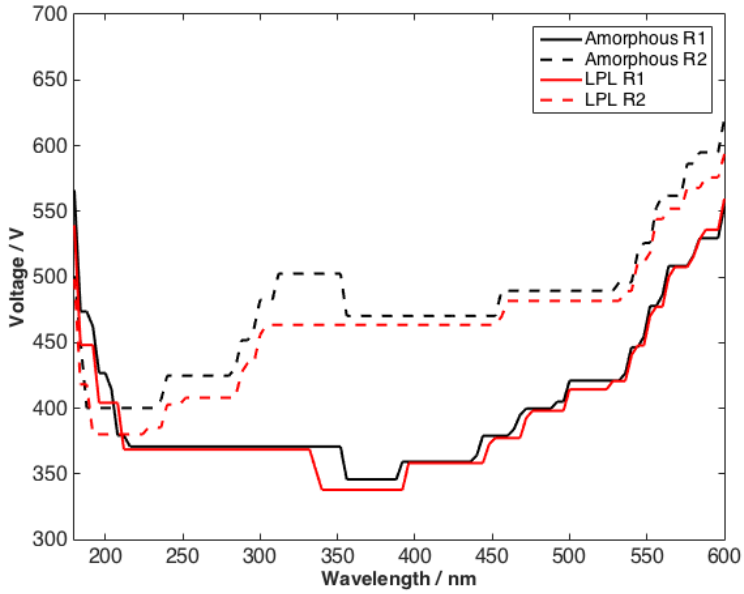

Figure 3.5: PMT voltage data showing higher values when detecting lower beam intensities, such as that achieved at the R2 Rochon prism position (dotted lines) compared to R1 (solid lines). Higher transmitted intensity through reference amorphous regions (in black) is also reflected in higher voltage values than laser-irradiated regions e.g. with linearly polarized light (LPL in red).

In the absence of linear dichroism, rotating the Rochon prism (and hence the polarised beam) by 90° leads only to a sign reversal of the CD signal spectrum from one position to the other and vice versa. Figure 3.6 shows typical plots of the mean

spectral values computed from repeated scans of an amorphous region (Figure 3.6(a)) and a laser-irradiated spot (Figure 3.6(d)) measured at both R1 and R2 positions. In order to rule out linear dichroic effects due to laser-induced sample effects, summation of the spectra at R1 and R2 from the reference amorphous region (Figure 3.6(b)) should ideally be equal to a similar summation of spectra from a laser-irradiated region (Figure 3.6(e)). Conversely, calculating the difference between spectra measured using R1 and R2 effectively doubles the CD signal (Figure 3.6(c) and (f)) measured at a specific region, which is especially useful when the CD signal is weak.

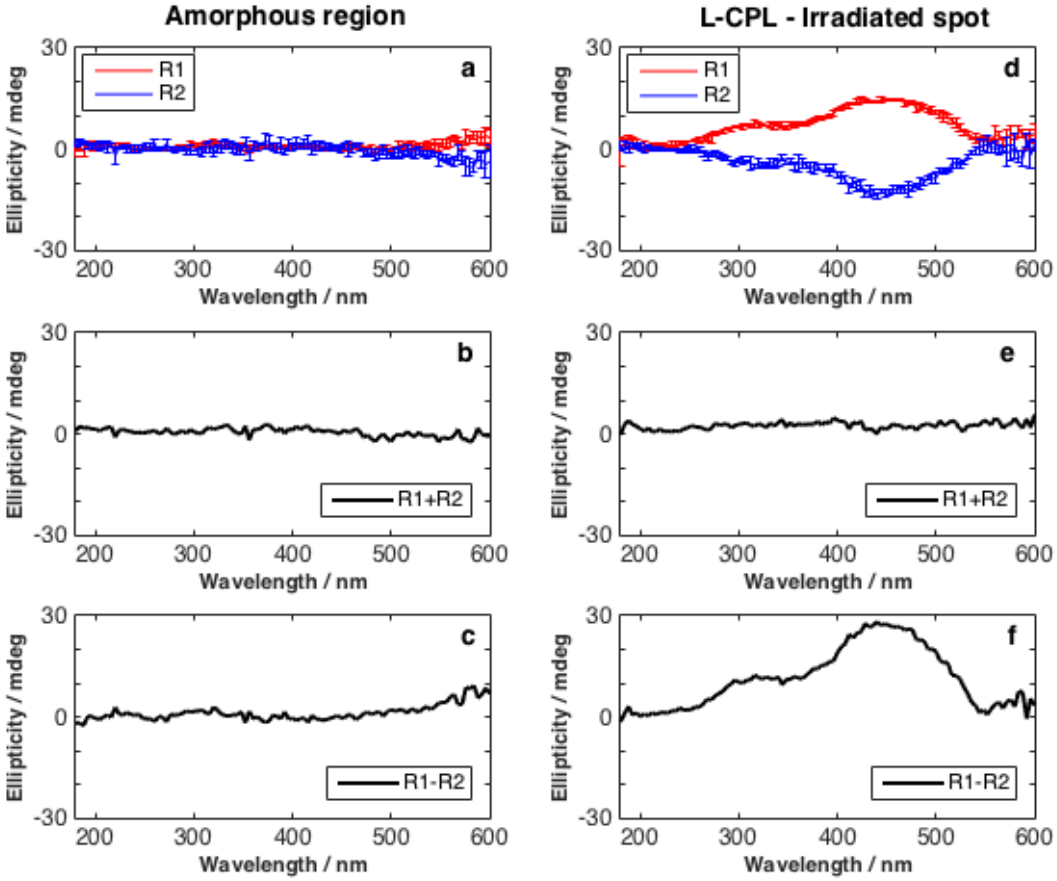

Figure 3.6:CD signals measured from (a) an amorphous region and (d) a left circularly polarized laser-irradiated spot using both R1 (red) and R2 (blue) prism positions, with symmetric error bars showing standard deviation of multiple scans from the mean. The sum of R1 and R2 spectra from both regions (corresponding to (a) and (d)) are shown in (b) and (e), while the differences (R1-R2) are shown in (c) and (f) respectively. All x-axes range from 180 to 600 nm.

The symmetric error bars in Figures 3.6(a) and (d) define the standard deviation of the repeated scans from the computed mean at each data point. The standard deviation was calculated using normalisation by n-1 instead of n, where n is the sample size, which is the default normalisation used in the MATLAB computations used for all spectral analysis. In subsequent calculations, such as summation or difference of spectra R1 and R2, the error is propagated by computing the square root of the sum of squared standard deviations from both spectra. It was found that the difference between the summation of R1 and R2 from amorphous and laser-irradiated regions (corresponding to Figure 3.6(b) and (e)) is typically within the margins of experimental error (twice the standard deviation averaged across the wavelength range), as illustrated in Figure 3.7. Any large deviations from the averaged experimental error tend to occur at either end of the wavelength range, which is close to the sensitivity limit of the PMT detector. The linear dichroism contribution within the investigated wavelength range (180nm to 600nm) was thus assumed to be negligible in subsequent analyses.

The summed spectra (R1+R2) from the reference region (Figure 3.6(b)) also serve as a baseline to ensure reproducibility of measurements using suitable prism rotations and PMT detector conditions. Subsequent normalisation of the doubled CD spectra (R1-R2) from the laser-irradiated spots against the amorphous spectra from the same sample normalises this baseline (as shown in Figure 3.8). This procedure; subtracting the amorphous spectral values from the laser-irradiated spectral values at corresponding wavelengths for each sample such that amorphous spectral values are normalised to zero, allows CD spectra to be compared across different samples to systematically investigate the effects of various experimental factors on the CD signal.

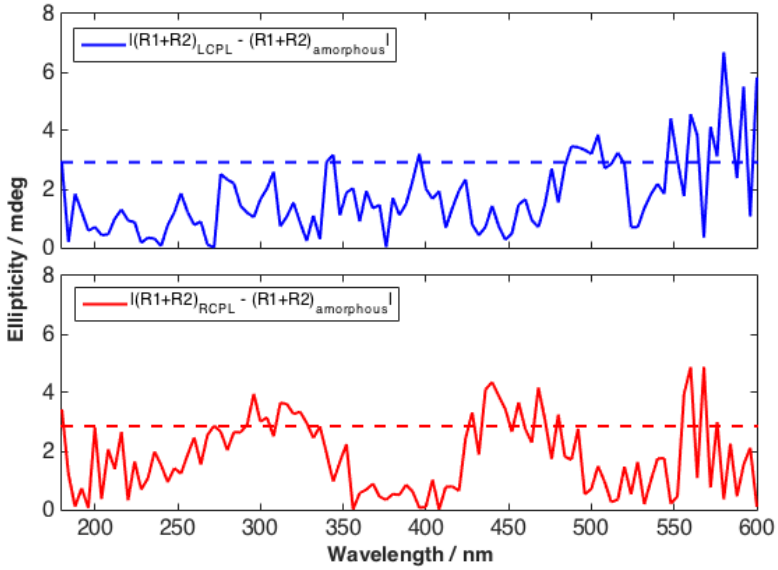

Figure 3.7: Absolute deviation in R1+R2 summed spectra (from Figures 3.6 (b) and (e)) between laser-irradiated spots (top: L-CPL in blue, bottom: R-CPL in red) and the amorphous region. Horizontal dotted lines in both plots refer to the average experimental error (twice the propagated standard deviation, or 2σ, averaged across the wavelength range of 180-600 nm) of R1+R2 spectra from the respective laser-irradiated spots.

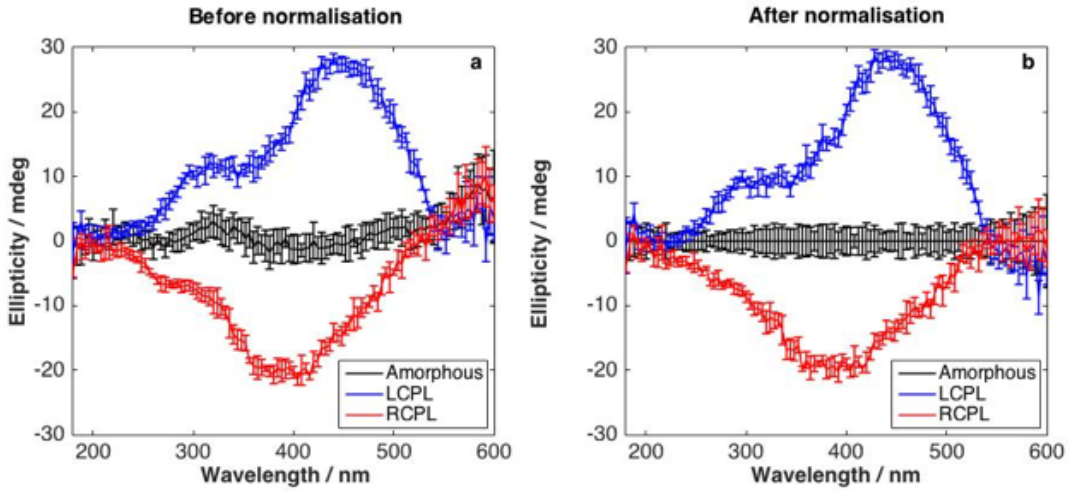

Figure 3.8: Doubled CD spectra (R1-R2) (a) before and (b) after normalization against the amorphous spectrum (black). Spectra recorded from LCPL-irradiated regions are shown in blue; RCPL-irradiated regions are shown in red. The symmetric error bars in (a) represent the square root of the sum of squared standard deviations of individual R1 and R2 spectra, and are carried over to (b) after normalization of the spectral values.

3.4. Raman spectroscopy

When intense monochromatic laser light is incident upon a sample, scattering of the light can occur either at the same wavelength (elastic Rayleigh scattering) or at different wavelengths (inelastic Raman scattering). Raman scattering at characteristic frequencies is associated with vibrational, rotational and electronic level transitions, which are specific to chemical bonds and symmetry of molecules. This information provides a unique structural fingerprint that allows rapid identification of material structures using a non-destructive technique. Raman spectra are typically reported in terms of wavenumber shift, $\Delta\omega = \frac{1}{\lambda_0} - \frac{1}{\lambda_1}$, in units of inverse length (commonly cm^{-1}), where λ_0 is the excitation wavelength and λ_1 is the Raman spectrum wavelength.

Raman spectra were acquired from different regions in the thin film samples on a JY HORIBA LabRAM ARAMIS imaging confocal Raman microscope (at Begbroke Science Park, Oxford) to confirm crystallisation of the laser-irradiated spots. A frequency doubled Nd:YAG laser source with wavelength of 532nm was used with a 300 μm confocal hole diameter, slit size of 150μm and 1800 lines/mm grating. A neutral density filter level was adjusted to ≤1% of the total laser power (*ca*. 50mW) to avoid phase transitions being induced by the Raman laser and the laser/grating combination was calibrated using a silicon wafer (with a well-defined characteristic Raman shift at $520.7cm^{-1}$). A 100X objective lens was used to focus the beam to about 5μm diameter on the sample. Spectra were recorded by accumulating 3 scans acquired with an integration time of 30 seconds each over a spectral range of $100cm^{-1}$ to $600cm^{-1}$. Cosmic spikes were removed in the acquisition software (LabSpec 6 Spectroscopy

Suite), while any further baseline corrections and peak fitting analyses were carried out using OriginPro (Origin Lab, Northampton, MA).

3.5. X-ray diffraction (XRD)

When an incident beam of monochromated X-rays interact with a material, diffraction of X-rays (undergoing constructive and destructive interference) by ordered crystals in the target material can be described by Bragg's Law. For materials composed of randomly oriented crystallites instead of a single large crystal, powder diffraction is the principal technique used to determine its structure.

High-resolution X-ray diffraction (XRD) experiments were performed in transmission mode with a parallel beam at beamline I11 at Diamond Light Source in the Long Duration Beamtime Hutch (experimental hutch 2), with a beam size of 0.8mm and 25keV energy (λ = 0.493Å). The synchrotron radiation provides more intense X-rays than conventional lab-based sources, giving a higher flux on the sample and hence better sensitivity to the diffracted reflections. Since the collimated beam is insensitive to sample geometry and displacement errors, minimal sample preparation is required.

Thin film sample discs on various crystalline and amorphous substrates were loaded in a custom holder on the sample stage (Medium Slider 4) and the X/Y positions of various target regions were recorded. An automated script was written to acquire diffraction maps (3-by-3 grid scans) from various laser-irradiated spots as well as amorphous regions and a scratched region with the substrate exposed (Figure 3.9). Calibration data was acquired from a polycrystalline ceria (CeO_2) sample.

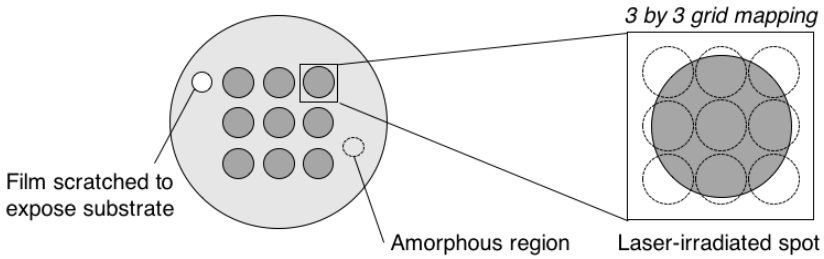

Figure 3.9: Illustration of regions on sample disc probed with an X-ray beam and the 3-by-3 grid mapping at each spot.

Data recorded with the Pixium detector (2880 by 2881 pixels) were rendered in the native NEXUS (*.nxs*) file format. These datasets were calibrated and processed using the open source software package DAWN Science (version 2.5) (Filik et al., 2017). Diffraction patterns as well as radially averaged intensity profiles were then converted into text files for further analysis.

3.6. Scanning electron microscopy (SEM)

After initial visual inspection of the laser-irradiated regions using optical microscopy, their surface morphology was studied by scanning electron microscopy, on two Schottky field emission gun scanning electron microscopes (FE-SEM): a JEOL JSM-6500F (at Begbroke Science Park, Oxford) and a JSM-7600F (at the Institute of Materials Research and Engineering (IMRE)).

Electron beam interaction with atoms at different depths of the sample leads to various signals in the SEM, including backscattered electrons, secondary electrons and characteristic X-rays. The most common mode used in SEM analysis is secondary electron imaging (SEI), where the detection of low energy secondary electrons emitted as a result of inelastic scattering close to the specimen surface (within a few

nanometres) leads to high-resolution imaging of the surface morphology with a large depth of field.

Electron irradiation of non-conducting samples can cause accumulation of static electric charge on the sample surface which can lead to image distortions. To reduce this charging effect, samples were mounted on holders using electrically conductive carbon tape and adhesive aluminium tape was used to create an electrical discharge bridge from the sample to a grounded holder. SEI was also performed in the Gentle Beam (GB) mode, using an accelerating voltage of 1kV. In this mode, incident electrons are decelerated immediately before the specimen such that the interaction volume and charge build up are reduced, enabling high-resolution imaging of the surface with less damage to the sample at lower accelerating voltages (Figure 3.10).

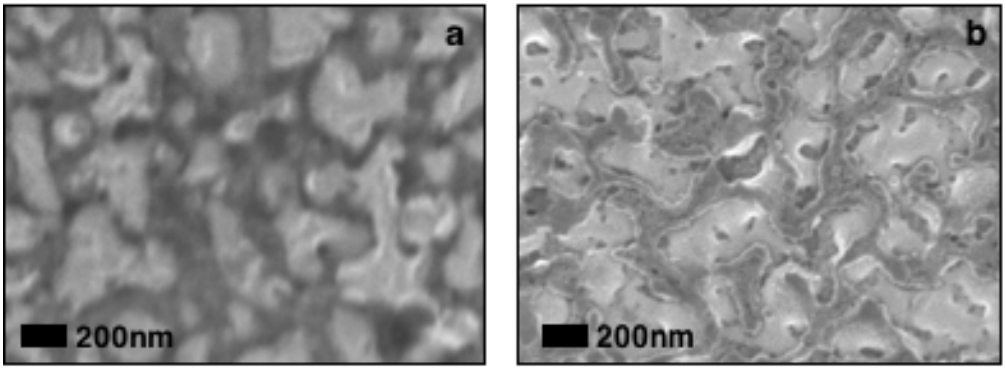

Figure 3.10: SEM images of an irradiated GST film surface obtained using secondary electron imaging at 1kV accelerating voltage in (a) normal mode and (b) Gentle Beam (GB) mode. The latter mode is useful in reducing charging effects in the sample and allows higher resolution imaging of the surface morphology.

Energy dispersive X-ray (EDX) spectroscopy was also performed in the FE-SEM equipped with an OXFORD X-Max50 silicon drift detector. An accelerating voltage of 15 kV was used to probe the samples and acquire EDX point and line spectra as well as image mapping for elemental compositional analysis.

3.7. Transmission electron microscopy (TEM)

3.7.1. Sample preparation

Planar TEM specimens of amorphous thin films were initially prepared by the floating method. Amorphous GST (pure and doped) thin films of 20nm thickness deposited on sodium chloride (NaCl) substrates were dipped in water at room temperature. While the substrates dissolved, the thin films floated off and could be picked up directly onto 3mm mesh copper grids coated with lacey carbon. Films on LiF substrates were also floated off either in water heated close to its boiling point or dilute inorganic acids (e.g. hydrochloric acid). For both methods however, the thin film tended to disintegrate due to surface tension. Hence, these methods were not suitable for site-specific preparation of the laser-irradiated spots that had been examined in previous experiments.

In order to prepare electron-transparent cross section specimens from specific regions within the laser-irradiated spots for analysis in the TEM, the samples were coated with protective capping layers; a thin layer of gold or carbon evaporated using a coater followed by platinum layers deposited with the gas injection system (GIS). A dual-beam focused ion beam (FIB) system (FEI Helios NanoLab 460S) was used to prepare TEM lamellae from laser-irradiated as well as amorphous regions using a standard lift-out procedure; ion milling at 30kV, followed by low voltage milling at 5kV and 2kV. Milling of the lamellae to electron-transparency was challenging due to the beam sensitivity of the substrates, which often caused lamellae to detach from the Omniprobe grid post prematurely or during subsequent TEM experiments and required repeated sample preparation.

3.7.2. TEM imaging and nanobeam diffraction

Imaging and diffraction experiments were carried out on a monochromated FEI Titan Analytical TEM/STEM (scanning transmission electron microscope) operated at 200kV. Selected area electron diffraction (SAED) experiments were also carried out on a JEOL JEM-2100 microscope at 200kV.

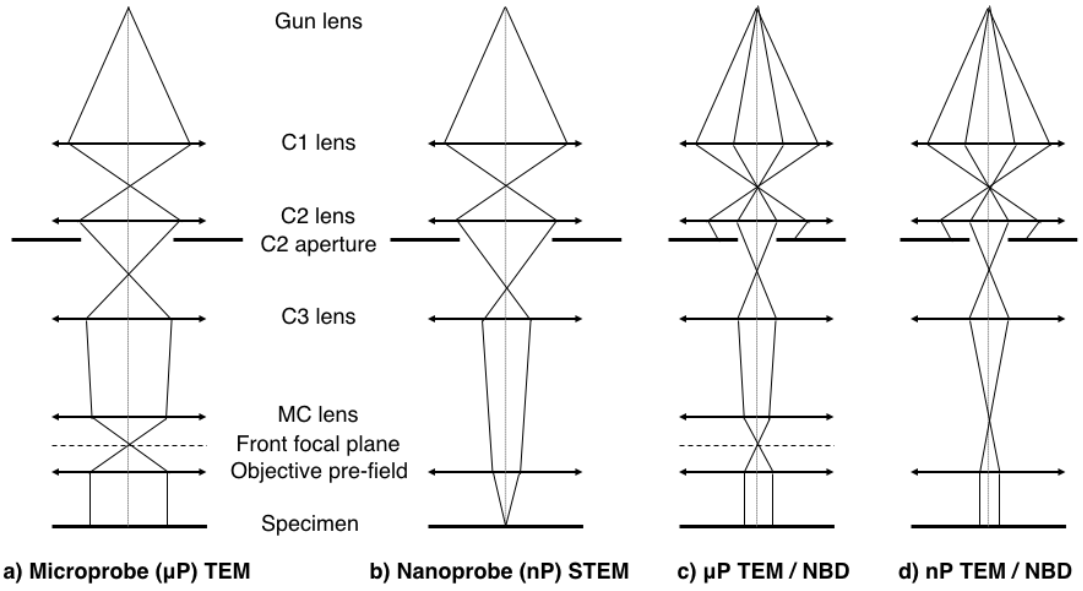

Figure 3.11: Ray diagrams of the condenser lens configuration for (a) conventional TEM, (b) convergent STEM and (c) TEM nanobeam electron diffraction (NBD) modes in the Titan.

The TITAN microscope illumination system consists of a gun lens, three condenser lenses (C1, C2, C3), a minicondenser lens (MC) and an objective lens. The condenser column has two basic settings: parallel illumination for conventional TEM (Figure 3.11(a)) and probe illumination for STEM (Figure 3.11(b), where the convergence of the beam can be adjusted by fine-tuning the C3 lens. The TEM mode normally uses a microprobe setting, while the STEM mode uses a nanoprobe setting. This setting is controlled by the MC lens situated above the front focal plane of the objective lens. When the MC is on (microprobe setting), the illuminated area is five

times larger (and probe convergence angle is five times smaller) than when it is off (nanoprobe setting).

In nano-area electron diffraction (NED, or nano beam diffraction (NBD)) in TEM mode, the electron beam is limited by the C2 aperture and focused to the front focal plane of the objective pre-field, forming parallel illumination at the specimen (Figure 3.11(c)). In contrast to selected area electron diffraction (SAED) where a selected area aperture is inserted at the intermediate image plane of the objective lens, resulting in a (typically micron-sized or smaller) virtual aperture at the specimen plane, NBD is capable of acquiring diffraction data from smaller areas of the specimen (<100nm).

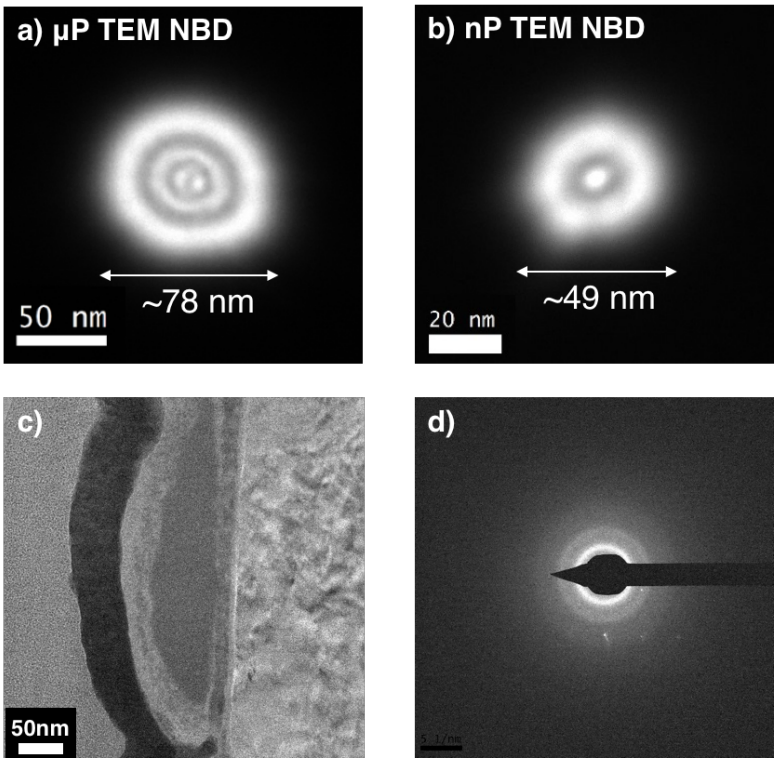

Figure 3.12: Images of the electron beam in TEM nano beam diffraction (NBD) mode using (a) microprobe and (b) nanoprobe settings. A TEM image of a cross-sectional sample taken using the nanoprobe setting is shown in (c), together with (d) a corresponding diffraction pattern recorded with the probe centered on the image field of view. Diffraction from the substrate are visible in this pattern, illustrating the difficulty in probe positioning and

switching between imaging and diffraction modes while attempting to avoid contributions from surrounding layers.

The smallest available 10μm C2 aperture gives a beam less than 80 nm in diameter (as shown in Figure 3.12(a)). However, this beam size was not suitable for probing the structure of the thin films (<60nm thick) in the cross-sectional specimens due to diffraction contributions from adjacent layers. Switching to the nanoprobe setting (Figure 3.11(d)) produced a smaller beam of less than 50nm in diameter (Figure 3.12(b)), but diffraction patterns obtained under this condition still showed contributions from the substrate or the protective capping layer, especially at narrower regions of the film (Figure 3.12(c), (d)).

3.7.3. Quasi-parallel STEM probe illumination

In order to obtain smaller probe sizes, formation of a quasi-parallel STEM probe was attempted in the Titan. The optical setting providing the most parallel beam condition (Figure 3.13(a)) was used following a procedure in the FEI True Crystal Strain analysis manual (FEI, 2010) as described in Appendix B. This quasi-parallel beam condition can be recognised when the diffraction discs formed by a convergent probe collapse into spots.

For a convergence semi-angle, α = 1mrad and for an electron wavelength of λ ~ 2.7pm at 200kV, the probe diameter can be estimated at the diffraction limit ($d = 0.6\frac{\lambda}{\alpha}$) as approximately 1-2nm. The most parallel condition (minimum possible convergence semi-angle of 0.12mrad with a 10μm C2 aperture), where the optics are essentially the same as those in the TEM mode with the same aperture except for the use of separate beam tilts and shifts in the two modes, gives a probe size of roughly

15nm as estimated from the resolution of HAADF-STEM images of polycrystalline aluminium film.

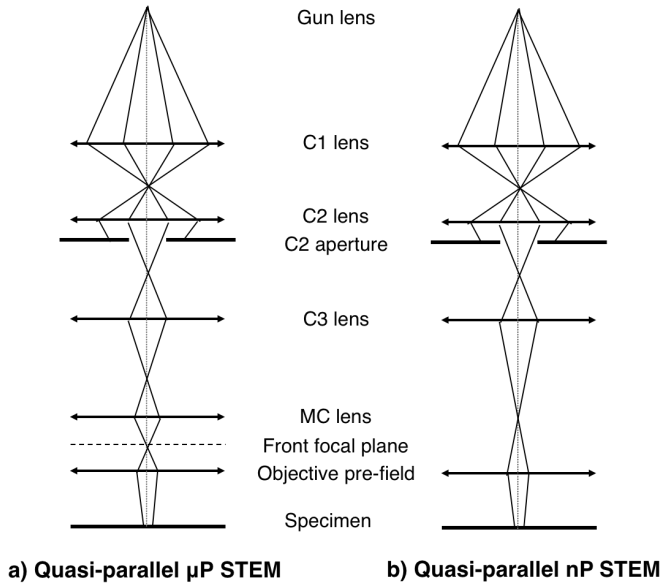

Figure 3.13: Ray diagrams of the pre-specimen lens system configuration in STEM mode, forming quasi-parallel beam in the Titan with (a) microprobe setting and (b) nanoprobe setting.

However, re-loading saved alignment files did not recall the optical settings accurately. In particular, the beam condition seemed to change between experiments, possibly due to the source nearing the end of its lifetime, resulting in a shadow of a probe-forming aperture and a cut-off in diffraction patterns beyond scattering angles of $q \sim 6\text{Å}^{-1}$ (Figure 3.14). Since information at higher scattering angles (at least up to $q = 15\text{Å}^{-1}$) are required for subsequent analysis, the instability of the alignment renders this method of probe formation unreliable for a controlled series of experiments.

A quasi-parallel STEM probe formation was then attempted using the default nanoprobe setting (Figure 3.13(b)) and the convergence semi-angle was similarly adjusted using free lens control. Although only basic beam alignments were performed, diffraction patterns were easily acquired with this probe (probe sizes for

different convergence semi-angles are given in Table B.1 in Appendix B) and recorded using the Gatan OneView camera on the Titan.

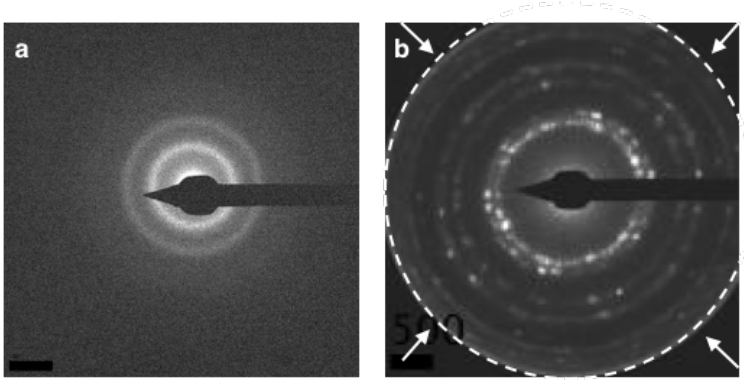

Figure 3.14: Diffraction patterns recorded from (a) amorphous GST and (b) a platinum protective layer using quasi-parallel STEM probe (0.12mrad convergence angle in microprobe setting) on the TITAN. There is a shadow of the probe-forming aperture and wrap-around of electrons beyond scattering angles of q ~ 6Å^{-1} in (b) (marked by a dotted line and arrows) whereas these are absent in (a) obtained during a different session. This is attributed to an incorrect alignment of the lenses and instability in recalling the alignments.

The ability to correlate diffraction data with the actual specimen region is a major advantage of using a STEM probe, as opposed to TEM nanobeam diffraction which requires switching between imaging and diffraction modes to position the beam. However, the much smaller quasi-parallel probe necessitates numerous diffraction pattern acquisitions for averaged volume diffraction studies. Tecnai Imaging & Analysis (TIA), which is part of the Titan microscope software and user interface, was used to acquire HAADF-STEM images of the specimens as well as to position the probe on regions of interest and collect multiple diffraction patterns.

The camera length for diffraction patterns of the floated GST films was calibrated using polycrystalline diffraction patterns obtained from an evaporated aluminium standard under similar probe conditions. HAADF-STEM images of this polycrystalline aluminium film were also used to estimate the size of probes with different convergence semi-angles. Diffraction patterns from the polycrystalline

platinum protective layer on the FIB-prepared lamellae were used to calibrate diffractions patterns from the cross-sectional specimens.

Both LiF and fused silica substrates in the cross-sectional samples were found to be beam sensitive; prolonged beam exposure caused damage to the substrate and led to breaking of specimens from the grid post. Hence, the exposure was minimised by reducing the beam current (<1nA) and blanking the beam between acquisitions. Reducing the beam current further (<1pA) led to very low counts and extremely long exposures for diffraction pattern acquisition. Although organic contamination is a common problem in STEM, the use of low beam current in addition to plasma cleaning prior to sample loading was found to alleviate this issue.

3.7.4. Analytical spectroscopy

EDX analysis was performed with a beam current of 1nA on the TITAN using an Oxford EDAX detector and spectra were collected up to 20keV with an energy resolution of 134eV. Dual EDX and EELS spectrum imaging was also performed on a C_s-corrected JEOL Atomic Resolution Microscope (JEM-ARM200F at the National University of Singapore) operated at 200kV. EELS spectra were collected with a GIF Quantum ER using a 30mrad probe-defining condenser aperture, and a 5mm EELS aperture in the range of 400eV to 1400eV.

3.8. Reduced Density Function (RDF) Analysis

There are a few open source packages that can be used for reduced density function and/or radial distribution function analysis of electron diffraction patterns: notably, the Digital Micrograph (DM) plugins RDFTools (Mitchell & Petersen, 2012) and PASAD (Gammer, Mangler, Rentenberger, & Karnthaler, 2010). However, these

plugins are dependent on the host acquisition software Gatan Microscopy. Hence, an in-house program, *eRDF Analyser* was developed independently on an alternative platform (a MATLAB graphical user interface (GUI) that is also accessible as a standalone package).

Although the executable form of the *eRDF Analyser* software eliminates dependence on version compatibility, the source code (written on MATLAB version 2015b) has also been made backward compatible. There has also been another MATLAB-based standalone program published recently, SUePDF (Tran, Svensson, & Tai, 2017), which differs in the underlying implementations of the analysis procedure; e.g. modelling of the atomic scattering background contribution to the scattering intensity is performed by an empirical background fitting including correction for inelastic scattering in SUePDF, while it is based on the physically accurate elastic atomic scattering intensities in *eRDF Analyser*.

The theory of RDF extraction from electron diffraction patterns and its implementation in the *eRDF Analyser* software is based upon the work of Cockayne & McKenzie (1988) and an in-house implementation in Microsoft Excel which is detailed in the following sections. Both the executable and source code files of the *eRDF Analyser* software are available for download on a public Github repository (Shanmugam, Borisenko, Chou, & Kirkland, 2017).

3.8.1. Theory of RDF extraction from electron diffraction data

Assuming elastic single scattering, the extraction of the RDF from an electron diffraction pattern recorded under parallel illumination conditions involves a

numerical conversion of $I(\boldsymbol{q})$, the azimuthally (or radially) averaged scattered intensity recorded in the diffraction pattern as a function of the scattering vector $\boldsymbol{q}$;

$$\boldsymbol{q} = 4\pi sin\theta/\lambda \tag{3.4}$$

where θ is the scattering half-angle and λ is the electron wavelength. The scattering vector is frequently expressed in the form $\boldsymbol{s} = \boldsymbol{q}/2\pi$. The scattered intensity $I(\boldsymbol{q})$ is given by the Debye formula which, when neglecting small scattering angles, can be expressed as;

$$I(\boldsymbol{q}) = Nf^2(\boldsymbol{q}) + 4\pi Nf^2(\boldsymbol{q}) \int_0^\infty [g(\boldsymbol{r}) - \rho_0] \frac{\boldsymbol{r}}{\boldsymbol{q}} \sin(\boldsymbol{qr})\, d\boldsymbol{r} \tag{3.5}$$

where $\boldsymbol{r}$ is the distance between neighbouring atoms.

Defining a reduced intensity function or scattering factor as;

$$\varphi(\boldsymbol{q}) = \left[\frac{I(\boldsymbol{q})_{experimental} - \sum_i N_i \langle f_i{}^2(\boldsymbol{q})\rangle}{\sum_i N_i \langle f_i(\boldsymbol{q})\rangle^2}\right] \boldsymbol{q}, \tag{3.6}$$

where N_i is the number of atoms of type i and $f_i(\boldsymbol{q})$ is the elastic electron atomic scattering factor, gives information about the local order expressed as the deviation of total scattered intensity $I(\boldsymbol{q})$, dependent on both individual and atomic pair contributions from the atoms in the material.

Numerical solutions of the electron scattering factors $f_i(\boldsymbol{q})$ have been computed by different methods (e.g. Doyle & Turner, 1968; Kirkland, 1998). In order to reduce the amount of data required as input for such simulation programs, parameterisation of the electron scattering factors is often achieved by fitting a combination of functions to the tabulated electron scattering data using a non-linear least-squares fitting. The choice of basic functions, such as Gaussians (to empirically fit behaviour at small scattering angles) and Lorentzians (for asymptotic behaviour at large angles), enables

the required Fourier transforms to be computed analytically to derive other quantities such as the atomic potential.

Although the set of electron scattering factors for all neutral atoms tabulated by Kirkland (1998, 2010) is widely used in simulations of electron diffraction and high-resolution imaging, Lobato & van Dyck (2014) noted drawbacks in Kirkland's parameterisation (1998), including the use of the Levenberg-Marquardt algorithm (LMA) that is sensitive to local minima. They proposed an alternative parameterisation of electron scattering factors, using a modified simulated annealing (SA) global optimisation algorithm, that is more accurate.

Experimentally, the contribution from individually scattered atoms can be accounted for by a background intensity $I(\boldsymbol{q})_{fitted}$,

$$I(\boldsymbol{q})_{fitted} = N \sum_i p_i \langle f_i^{\,2}(\boldsymbol{q}) \rangle + C \qquad (3.7)$$

that is fitted from the oscillations of the experimental total scattering intensity $I(\boldsymbol{q})_{experimental}$, as described in the following section. In this analysis, N is the dose-dependent scaling factor reflecting the total number of atomic formula units, p_i is the atomic fraction of atomic species of type i, and C is a correction for the dark current in the recorded diffraction pattern. Equation 3.6 thus reduces to;

$$\varphi(\boldsymbol{q}) = \left[\frac{I(\boldsymbol{q})_{experimental} - I(\boldsymbol{q})_{fitted}}{\sum_i N_i \langle f_i(q) \rangle^2}\right] \boldsymbol{q}. \qquad (3.8)$$

The RDF, $G(\boldsymbol{r})$, is obtained by Fourier transformation of $\varphi(\boldsymbol{q})$ (Equation 3.9). However, due to practical limitations, such as masking of the central beam, finite detector sizes and camera lengths, there is a finite minimum and maximum cut-off in the $\boldsymbol{q}$ values. These can lead to a truncation of the Fourier series, which can cause spurious or unphysical peaks. Hence, a damping function of form $exp(-b\boldsymbol{q}^2)$, where

b is a damping factor, is multiplied with $\varphi(\boldsymbol{q})$ before the Fourier Transform to reduce the effects of a limited $\boldsymbol{q}$-range and high frequency noise (at high $\boldsymbol{q}$). The truncated *G(r)* is then computed as in Equation 3.10.

$$G(\boldsymbol{r}) = 4\int_0^{\infty} \varphi(\boldsymbol{q}) \sin(\boldsymbol{qr})\, d\boldsymbol{q} \tag{3.9}$$

$$\cong 4\int_{q_{min}}^{q_{max}} [\varphi(\boldsymbol{q}) \cdot exp(-b\boldsymbol{q}^2)] \sin(\boldsymbol{qr})\, d\boldsymbol{q} \tag{3.10}$$

3.8.2. Implementation in eRDF Analyser software

Electron diffraction data was input into the eRDF Analyser software (GUI shown in Figure 3.15) in the form of either a two-dimensional pattern or a one-dimensional radially averaged intensity profile. Calibration of the camera length and the scattering vector $d\boldsymbol{s} = d\boldsymbol{q}/2\pi$ (in inverse Angstroms per pixel) and the selection of a suitable data range ($\boldsymbol{q}_{min}$ and $\boldsymbol{q}_{max}$) is required before the atomic scattering background $I(\boldsymbol{q})_{fitted}$ can be fitted to the experimental scattering intensity $I(\boldsymbol{q})_{experimental}$. An example of the fitting output functions from the software is also shown in Figure 3.15.

For an automated fit, an analytical solution for the coefficients *N* and *C* (in Equation 3.7) was derived by minimising the weighted functional in Equation 3.11 with weights w_j, where the summation runs over all data points *j*. Weights were implemented in the software by selecting either the entire range or the tail end (higher angle scattering) of the experimental data to perform the fitting.

$$\sum_j w_j (I(q_j)_{experimental} - I(q_j)_{fitted})^2 = min \tag{3.11}$$

Defining $F(q_j) = \sum_i p_i \langle f_i^2(q_j) \rangle$, $I(\boldsymbol{q})_{fitted}$ takes the form given in Equation 3.12. If the intersection between $I(\boldsymbol{q})_{fitted}$ and $I(\boldsymbol{q})_{experimental}$ occurs at a point q_k, the solution is given by the system of Equations 3.13 (rewritten in 3.14).

$$I(q)_{fitted} = NF(q) + C \tag{3.12}$$

$$\begin{cases} \sum_j w_j \left(I(q_j)_{exp} - NF(q_j) - C \right)^2 = min \\ I(q_k)_{exp} - NF(q_k) - C = 0 \end{cases} \tag{3.13}$$

$$\sum_j w_j \left(I(q_j)_{exp} - NF(q_j) - I(q_k)_{exp} + NF(q_k) \right)^2 = min \tag{3.14}$$

$$\frac{d\left(\sum_j w_j \left(I(q_j)_{exp} - NF(q_j) - I(q_k)_{exp} + NF(q_k) \right)^2 \right)}{dN} = 0 \tag{3.15}$$

Since the resulting functional (Equation 3.14) is a variable in N, a solution for N can be found by equating the first derivative of the functional by N to zero (Equation 3.15). The computed value of N (Equation 3.16) can then be used to obtain C (Equation 3.17).

$$N = \frac{\sum_j w_j F(q_j) I(q_j)_{exp} - \sum_j w_j F(q_k) I(q_j)_{exp} - \sum_j w_j F(q_j) I(q_k)_{exp} + \sum_j w_j F(q_k) I(q_k)_{exp}}{\sum_j w_j F(q_j)^2 - 2 \sum_j w_j F(q_j) F(q_k) + \sum_j w_j F(q_k)^2} \tag{3.16}$$

$$C = I(q_k)_{exp} - NF(q_k) \tag{3.17}$$

A choice between Kirkland's (2010) and Lobato & van Dyck's (2014) parameterised forms of the elastic electron atomic scattering factors $f_i(\boldsymbol{q})$ is available in the software. Although the latter parameterisation is more accurate in fitting of the tabulated data (Kirkland, 1998) up to $\boldsymbol{q} = 12$Å^{-1}, the difference observed in the resultant RDF curves was only appreciable at $\boldsymbol{r} < 1$Å (Figure 3.16), where no contribution from interatomic distances is expected. Therefore, Kirkland's parameterised forms were used in all fitting for consistency with subsequent model refinement analysis.

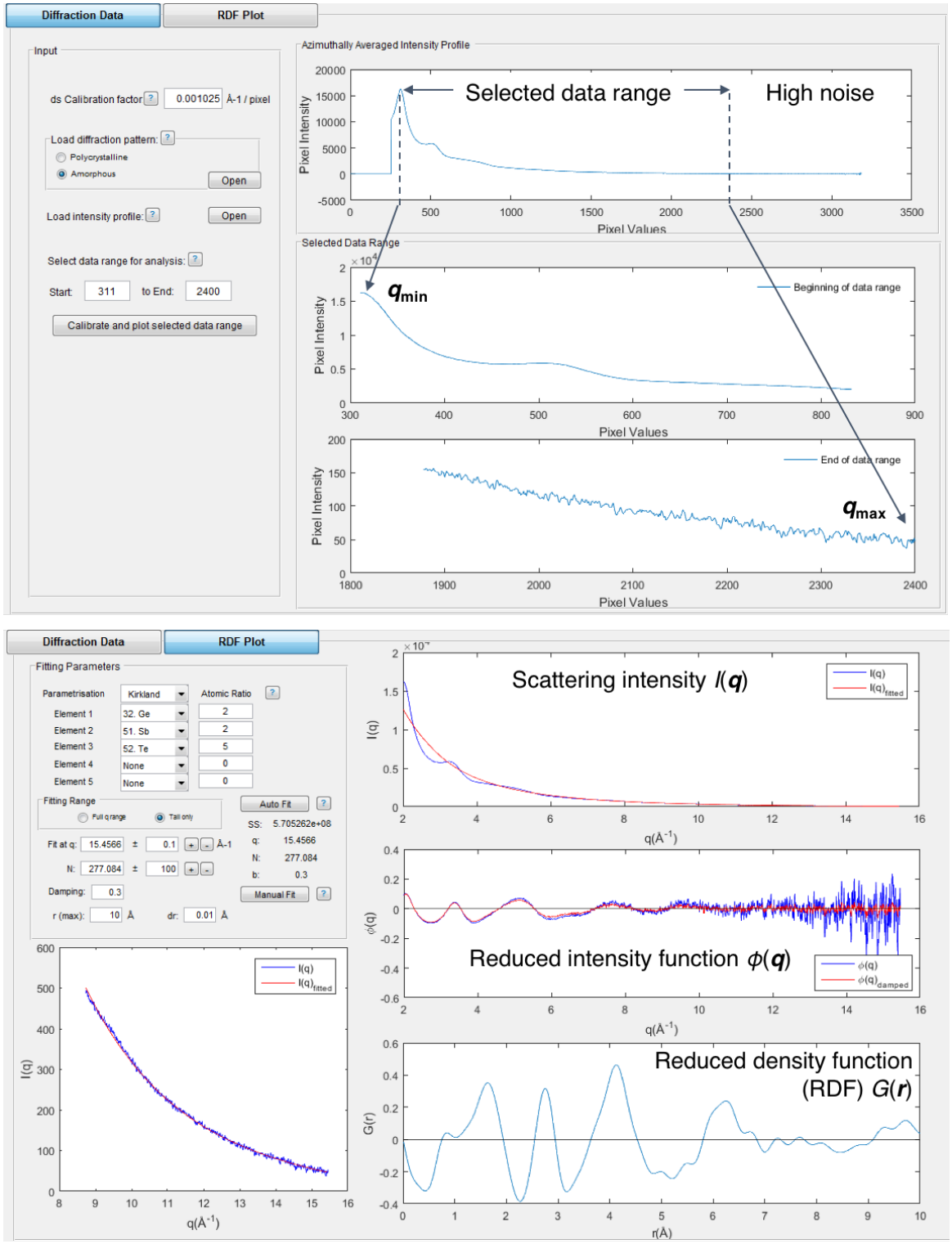

Figure 3.15: Scattering intensity data selection, fitting and output functions visualised in the eRDF Analyser software graphical user interface. Data shown is from a 20nm amorphous GST film.

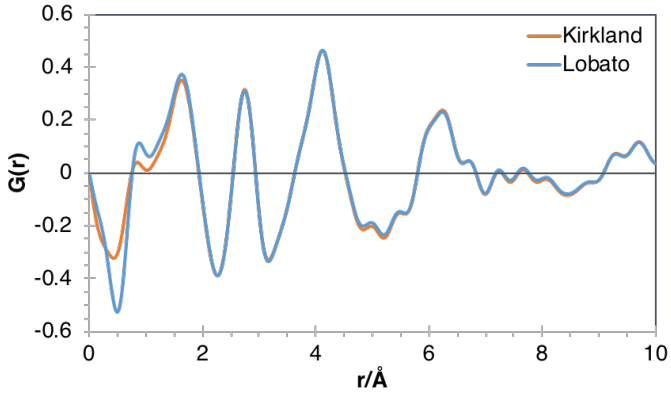

Figure 3.16: RDF curves obtained using automated scattering intensity fitting with Kirkland's and Lobato and van Dyck's parameterised forms of electron atomic scattering factors.

Whilst the automated fit minimises the sum of squared deviation between $I(\boldsymbol{q})_{fitted}$ and $I(\boldsymbol{q})_{experimental}$ (the 'SS' value readout in the software), additional measures of the goodness of fit were considered, including oscillation of the reduced intensity function $\varphi(\boldsymbol{q})$ about zero and minimised unphysical peaks (below 1Å or the first bond length) in the RDF $G(\boldsymbol{r})$. Manual adjustment of the data range (to exclude high noise at large scattering angles as seen in Figure 3.15) and the fitting parameters in Equation 3.16 can be used to obtain a better fit that optimally agrees with the abovementioned measures. An example of this manual adjustment is shown in Figure 3.17.

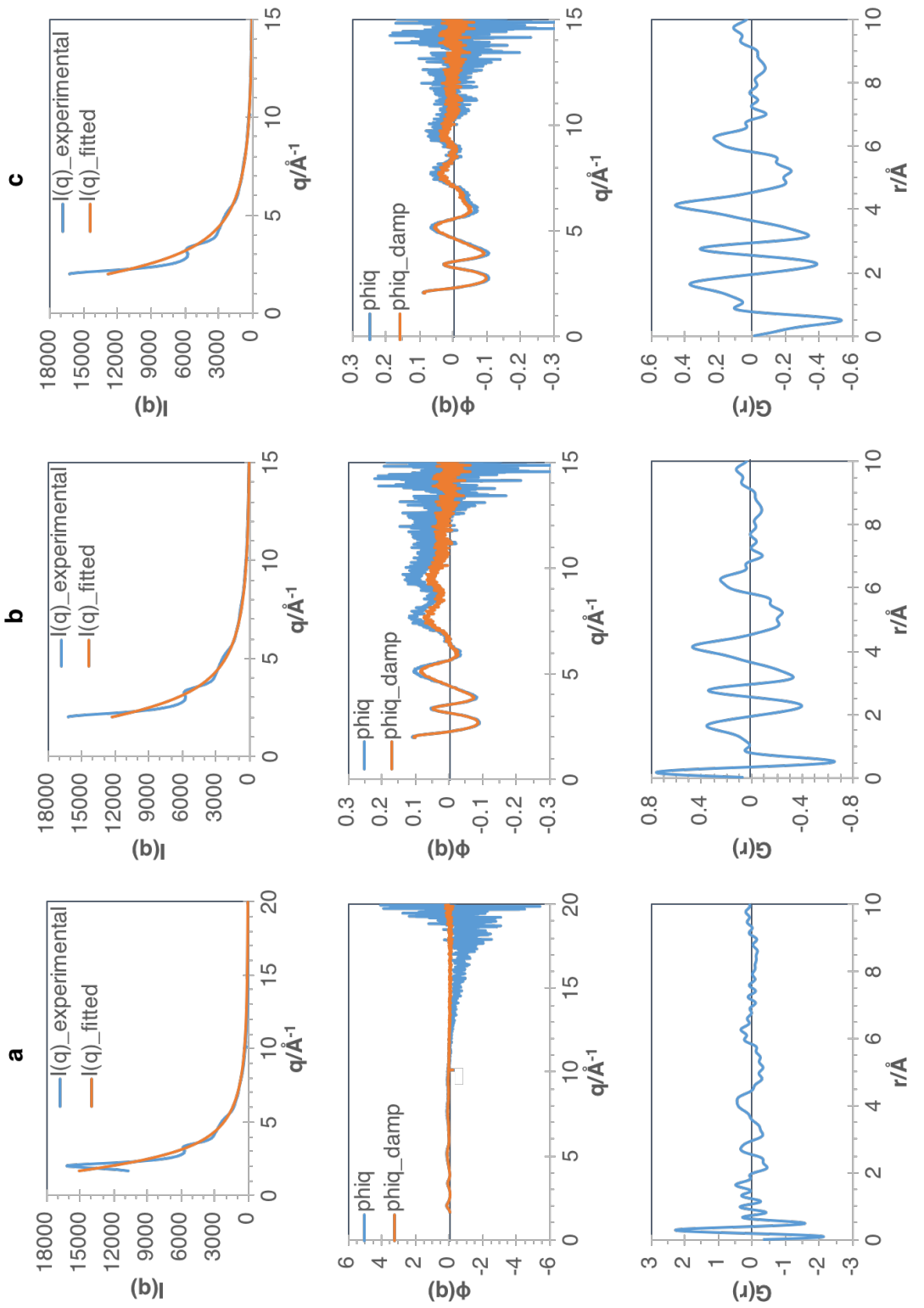

*Figure 3.17: a) Fitting output functions from raw scattered intensity data and b) after excluding data with high noise at large scattering angles. c) By manually increasing the value of N, φ(**q**) oscillates about zero at larger scattering angles and the unphysical RDF peaks below 1Å are minimised.*

3.8.3. Model refinement

Small models of pure $Ge_2Sb_2Te_5$ (108 atoms) and 4% Cr-doped $Ge_2Sb_2Te_5$ (103 atoms) were initially constructed by random dense packing of atoms in a cubic cell with lattice parameters (15.15Å and 14.78Å) corresponding to densities of 5.88g/cm^3 and 5.92g/cm^3 respectively. These density values were based on amorphous pure $Ge_2Sb_2Te_5$ models taken from the literature (Akola & Jones, 2007; Borisenko, Chen, Song, Nguyen-Manh, & Cockayne, 2009; Hegedüs & Elliott, 2008) and the chromium elemental concentration as determined from SEM-EDX analysis.

A molecular dynamics (MD) simulation of cooling from a melt was then performed using a canonical (constant NVT) ensemble and the initially constructed starting models. The models were melted at 2000K for 2ps and gradually cooled to 400K in steps of 200K for 2ps per step. Finally, the structures were equilibrated at 300K for 2ps. The total simulation time was therefore approximately 20ps. The MD simulations were performed using the Perdew-Burke-Ernzerhof (PBE) functional and a 200eV pseudopotential energy cut-off. The energy was sampled at the gamma point of the Brillouin zone only. DFT energy optimisation of the models was also performed using CASTEP code (Clark et al., 2005) with full geometry relaxation under rigid periodic boundary conditions, using a pseudopotential energy cut-off at 300eV.

Limiting factors including the small model size, the short MD simulation period of 20ps (compared to experimental irradiation times of 20s) and the use of rigid periodic boundary conditions in the DFT energy optimisation may have contributed to computational errors in the liquid-quench simulation of these models. As such, the DFT-optimised models were then refined against the experimental RDF data to obtain more accurate representations of the material from which experimental data were

acquired. Scattering intensity components that contributed to peaks below 1Å in the experimental RDF were first removed from the reduced intensity function $\varphi(\boldsymbol{q})$ using a Fourier filter. Calculations of $\varphi(\boldsymbol{q})$ from the models were then compared with and refined against the experimental values of $\varphi(\boldsymbol{q})$ using a Reverse Monte Carlo (RMC) software (Borisenko, Chen, Song, & Cockayne, 2009). The maximum movement of any atom in each Monte Carlo step was limited to 0.02Å and 10000 iterations were calculated for each refinement.

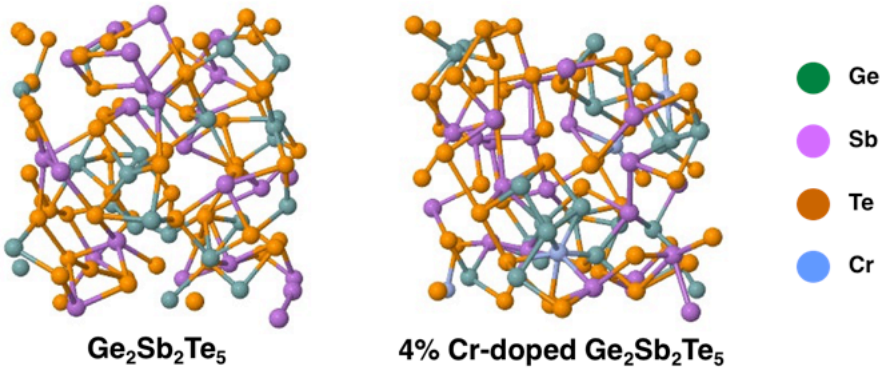

Figure 3.18: Energy-optimised models of amorphous $Ge_2Sb_2Te_5$ and 4% Cr-doped $Ge_2Sb_2Te_5$ visualised using Jmol[2].

A thin film model of 108 atoms was also prepared from the bulk GST model described above and melted at 800K for 2ps, quenched from 800K to 400K in steps of 200K and 2ps per step and equilibrated at 300K for another 2ps. Two further simulations were carried out (using similar quench rates and a total period of 8ps as above) with and without the influence of an electric field applied perpendicular to the film. The magnitude of the electric field was estimated from the laser excitation parameters (calculations in Appendix C).

[2] *Jmol: an open-source Java viewer for chemical structures in 3D*. http://www.jmol.org.

Chapter 4

Optical anisotropy in $Ge_2Sb_2Te_5$ films

4.1. Modification of laser irradiated regions

During preliminary laser excitations, the laser power and duration of irradiation were chosen simply to induce a visible change in the optical reflectivity of a sufficiently large region of the films for subsequent experiments. Whilst such laser-irradiated regions can be distinguished by the naked eye, identification of distinct sub-regions within the irradiated spots requires optical microscopy. This served as a reference for further structural characterisation enabling the study of surface morphology features and site-specific preparation of samples for electron microscopy (Chapter 5).

No appreciable difference in the film appearance was observed when nanosecond laser pulses of relatively low power (< 3mW) were used to irradiate the as-deposited amorphous film for short durations (less than 10s). When the laser power or exposure duration was increased, brighter irradiated regions (with higher optical reflectivity) were observed. Initially, there were difficulties in aligning these laser-irradiated regions (approximately 1 mm in diameter) for optical absorbance measurements. Irradiation of bigger regions was attempted by moving the disc during laser exposure, but this resulted in uneven exposure and damage to the capping layer which appeared as dark dendritic structures on the film surface (Figure 4.1).

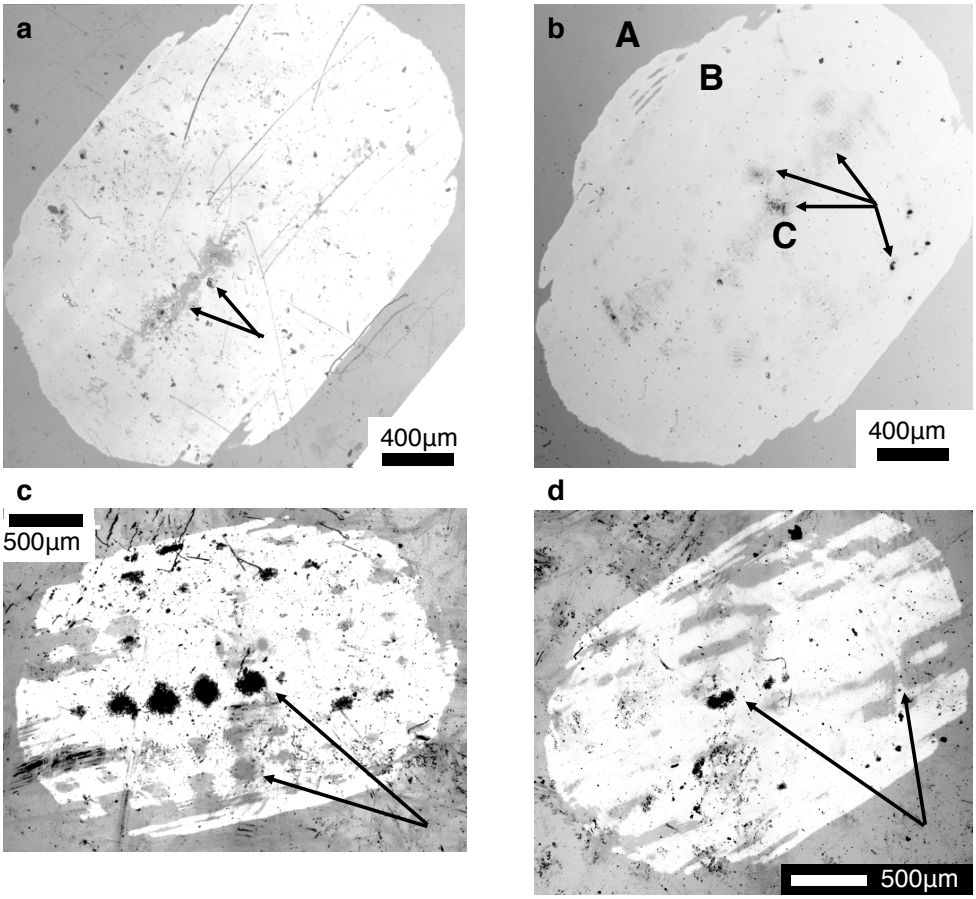

Figure 4.1: Reflected bright-field images of spots irradiated with (a) left circularly polarized light (L-CPL) and (b) right circularly polarized light (R-CPL) on GST, and with (c) L-CPL and (d) R-CPL on N-GST films. Regions with uneven exposure and surface damage are marked by arrows. An approximate laser power of 3.5mW (with 10% energy fluctuation) was used.

Subsequent modification of the optical setup (and an optimised experimental procedure described in Section 3.2) resulted in more homogeneous and larger (2–2.5mm in diameter) laser-irradiated regions. Figure 4.2(a) shows such a region irradiated with low fluence (energy density of 10.2mJ/cm^2) for 20s. The region marked A is the as-deposited amorphous film, whereas region B marks the irradiated region that has presumably undergone a phase transformation to a crystalline state (resulting in higher optical reflectivity). Irradiation with higher laser fluence (11.1mJ/cm^2) resulted in the appearance of a darker central region C (Figure 4.2(b)) that expands in

size with increasing fluence. At an even higher fluence (17.8mJ/cm^2), the middle of the spot becomes almost transparent to the naked eye (region X in Figure 4.2(c & d)).

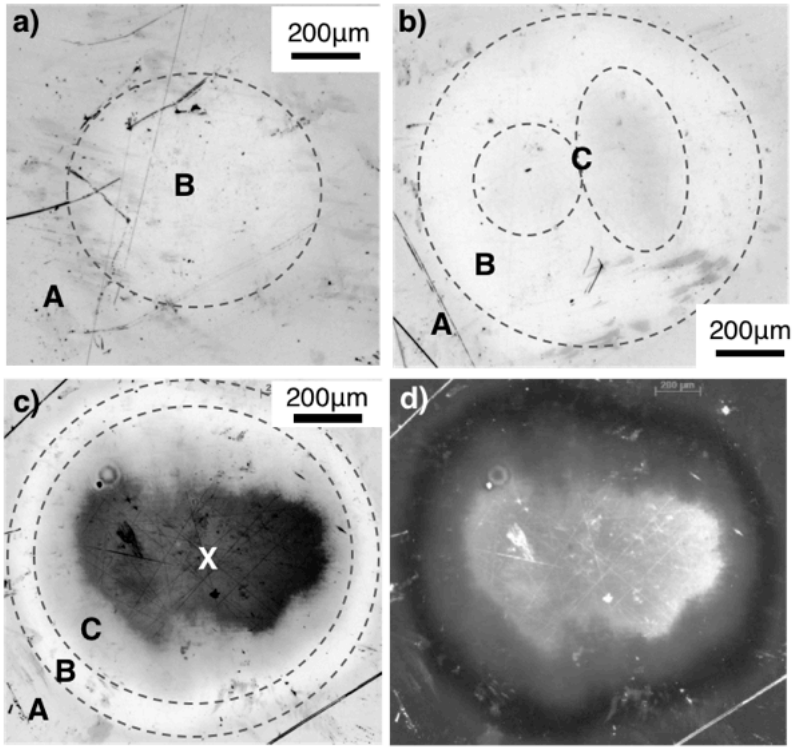

Figure 4.2: Typical change in appearance of regions in a 37nm thick 3% Cr-GST film on LiF substrate irradiated with increasing laser fluence ((a)10.2mJ/cm^2, (b)11.1mJ/cm^2 and (c, d)17.8mJ/cm^2). (a-c) are reflected bright-field images while (d) shows (c) with inverted contrast (where the transparency of region X is evident).

The fluence values for the onset of crystallisation and formation of different sub-regions vary for different film compositions, film thicknesses and substrates on which the film was deposited, due to differences in absorption of the laser irradiation. For example, a series of regions in a 55nm thick GST film on LiF substrate irradiated with a similar range of laser fluence is shown in Figure 4.3, where region C is observed at a lower fluence value than in the previous example.

This evolution of the film appearance in response to laser irradiation with increasing fluence is typical of nanosecond laser pulse excitation, where a melting-solidification/crystallisation phenomenon (Friedrich et al., 2001) leads to a thermal

phase change. The centre of the irradiated spots also experiences higher temperature than the surrounding area, consistent with a temperature profile that follows the Gaussian laser beam profile. Thus, at higher laser fluence, hole-formation can occur at the centre (region X) due to ablation or evaporation of material (Friedrich et al., 2001). Similar formation and growth of distinct regions of different optical reflectivity as a function of laser power have previously been observed by Fu et al. (2012).

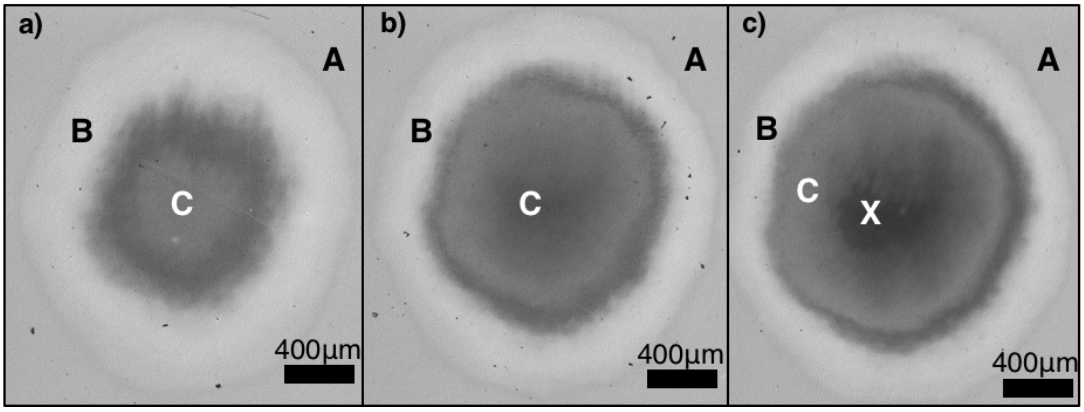

Figure 4.3: Optical images of regions in a 55nm thick GST film on LiF substrate irradiated with increasing laser fluence (a)10.3mJ/cm^2, (b)15.5mJ/cm^2 and (c)19mJ/cm^2.

4.2. Raman spectral analysis and over-irradiation

Raman spectroscopy performed on laser-irradiated regions showed differences between these spectra and those acquired from the surrounding non-irradiated film. Amorphous GST films prepared by sputtering typically have a broad peak at approximately 150cm^{-1} and a weak shoulder at 120cm^{-1}, while crystalline GST spectra have been reported to have sharper peaks at approximately 120cm^{-1} and 140cm^{-1}, with weak shoulders at around 105 – 110cm^{-1} and 150cm^{-1}. Both amorphous and crystalline phases have been reported to have a broad peak at 220cm^{-1}, with an additional peak at approximately 160cm^{-1} for the hexagonal crystalline phase. The vibrations normally ascribed to these peaks are summarised in Table 4.1.

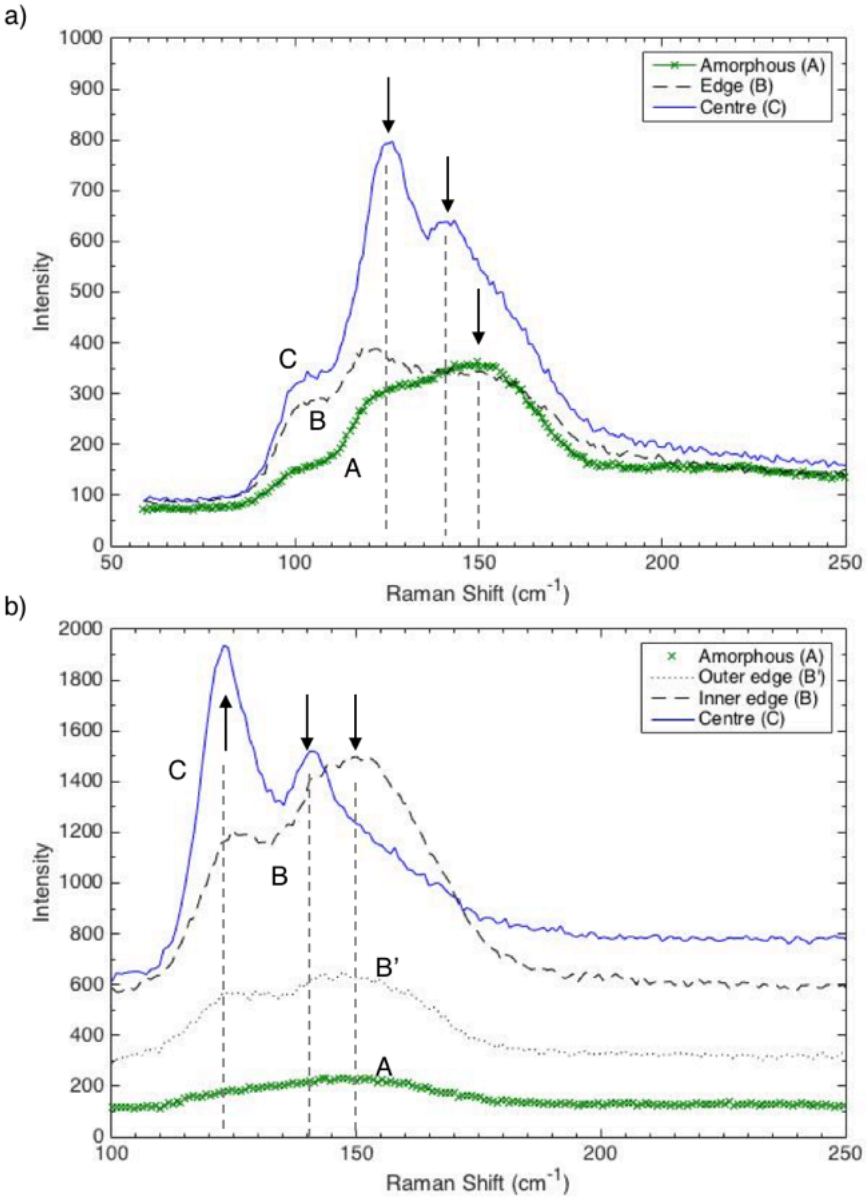

Figure 4.4: Raman spectra of regions A, B and C in laser-irradiated spots in (a) pure GST film (on silica) shown in Figure 4.1(b) and (b) 37nm thick 3% Cr-GST film (on LiF substrate) irradiated with 15mJ/cm^2. Spectra B' and B in (b) are acquired from outer and inner edges of region B respectively.

Figure 4.4(a) shows spectra acquired from a laser-irradiated region, B, of the GST film shown in Figure 4.1(b) and a non-irradiated region, A. The spectrum from region A agrees with that of amorphous GST (broad band around 149cm^{-1}). The spectrum from region B exhibits a peak at ~120cm^{-1}, resembling crystalline GST. The spectrum C acquired from darker spots in the centre (areas with surface damage) shows

more pronounced peaks at ~120cm^{-1} and ~140cm^{-1}, indicating differences in the extent of crystallisation within the irradiated region.

Raman spectra acquired from laser-irradiated regions of doped films exhibited similar characteristics and peak positions, with an amorphous band around 147–149cm^{-1} and crystalline peaks at 119–125cm^{-1} and 137–141cm^{-1}, indicating minimal structural distortion due to the low dopant concentration. Spectra acquired from a region of 3% Cr-GST film irradiated with 15mJ/cm^2 laser fluence is shown in Figure 4.4(b). Changes in the relative intensity of the characteristic peaks indicate a gradual crystallisation from sub-regions B to C.

Fu et al. (2012) have attributed the formation of a darker central region in laser-irradiated spots to over-irradiation, characterised by the emergence of a peak at ~140cm^{-1} that suppressed the crystalline peak at ~160cm^{-1}. However, while a significant peak at ~140cm^{-1} was observed at the irradiated regions, there was no peak at ~160cm^{-1} in spectra recorded from regions B or C. Although this is not conclusive in identifying the crystalline phase (cubic or hexagonal) or over-irradiation of the spots, this spectral analysis does offer a comparison of the sub-regions and shows a gradual change in structure from the unexposed amorphous film through different sub-regions of the irradiated spot. The darker regions within the irradiated spots (i.e. central region C or areas with surface damage) that exhibited pronounced peaks at ~120cm^{-1} were also revealed to be key in subsequent optical anisotropy experiments exhibiting a significant CD signal as described in section 4.3.2.

Table 4.1

Vibrational modes normally ascribed to peaks in Raman spectroscopy of GST in the literature.

Raman Shift	Peak attributes	References
105 – 110 cm^{-1}	Defective octahedral sites partly present in amorphous phase and partly formed from tetrahedral sites during crystallisation; $E_g(2)$ mode of hexagonal Sb_2Te_3	Němec et al., 2012
~ 120 cm^{-1}	A1 modes of corner-sharing Ge-rich $GeTe_{4-n}Ge_n$ (n=0,1,2,3) tetrahedral units containing Ge–Ge bonds; Ge-based defective octahedra	Andrikopoulos, Yannopoulos, Kolobov, Fons, & Tominaga, 2007; Kozyukhin, Veres, Nguyen, Ingram, & Kudoyarova, 2013
~ 140 cm^{-1}	Te–Te bonds (segregation of Te crystalline phases at expense of crystalline Sb_2Te_3)	Fu et al., 2012
~ 150 cm^{-1}	Stretching vibrations of Sb–Te bonds in pyramidal $SbTe_3$ or Sb_2Te_3 units; Defective octahedral coordination of Sb	Fu et al., 2012; Němec et al., 2012; Andrikopoulos et al., 2007
~ 160 cm^{-1}	$A_{1g}(2)$ mode of crystalline Sb_2Te_3; Substitution of Sb atoms at Te atom positions in $(Te_2)Sb\text{-}Sb(Te_2)$	Kozyukhin et al., 2013; Sosso, Caravati, Mazzarello, & Bernasconi, 2011

4.3. Preliminary circular dichroism measurements

4.3.1. Pure and N-doped GST

Preliminary circular dichroism (CD) spectroscopy measurements were performed on amorphous regions (A) and at the centre of spots irradiated at low laser fluence (B) in GST and N-doped GST films (Figure 4.1). Since the CD signal is related to the difference in absorbance between left (L-) and right (R-) circularly polarised light (CPL), as previously described, a positive signal indicates that L-CPL is absorbed to a greater extent than R-CPL.

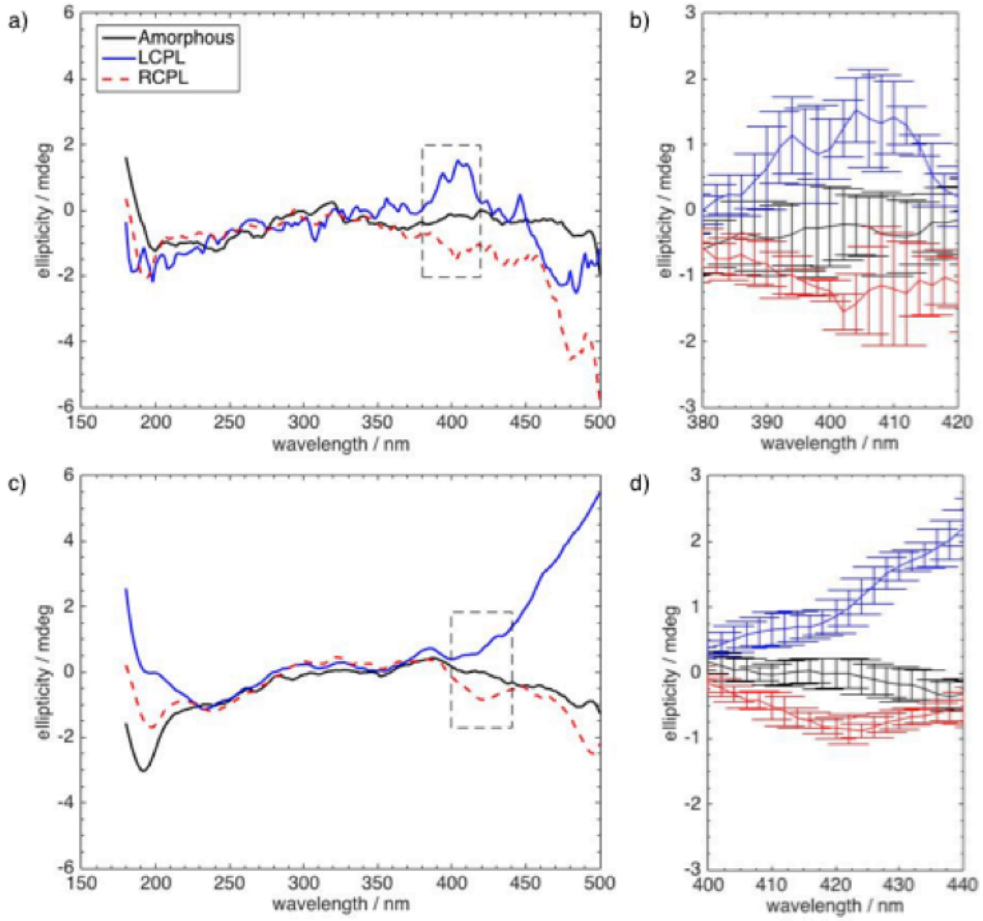

Figure 4.5: Averaged CD spectra obtained using the R1 prism position from regions in (a) pure GST and (c) N-doped GST. The regions within the dashed boxes highlight the signals from the laser-irradiated spots that exhibit a significant near-symmetric deviation from the signal from the amorphous region are shown in (b) and (d) with symmetric error bars (twice the standard deviation from repeated scans).

Figure 4.5(a) shows averaged CD spectra obtained from an amorphous GST film (at R1 prism position). As expected for an achiral material, there is no significant difference in the absorption of L- and R-CPL, resulting in a constant signal close to zero. However, CD spectra from the centre of the laser-irradiated spots show a nearly-symmetric deviation from the amorphous signal between wavelengths of 380 nm to 420 nm. The N-doped GST film (Figure 4.5(c)) shows a similar response, where spots irradiated with L-CPL and R-CPL show differentiated signals in the amorphous region beyond 400 nm.

Within the wavelength range considered (Figures 4.5(b) and (d)), CD spectra measured at film regions irradiated with CPL of different handedness exhibit a mirror symmetry dependence on the handedness. The signals from spots irradiated with L-CPL are positive, corresponding to greater absorption of L-CPL, and similarly, signal from the spots irradiated with R-are negative, corresponding to greater absorption of R-CPL. Differences in the CD signal are more pronounced in the case of N-doped GST at wavelengths between 405nm and 435nm, whereas the difference in pure GST is only significant within the wavelength range of 400nm to 415nm.

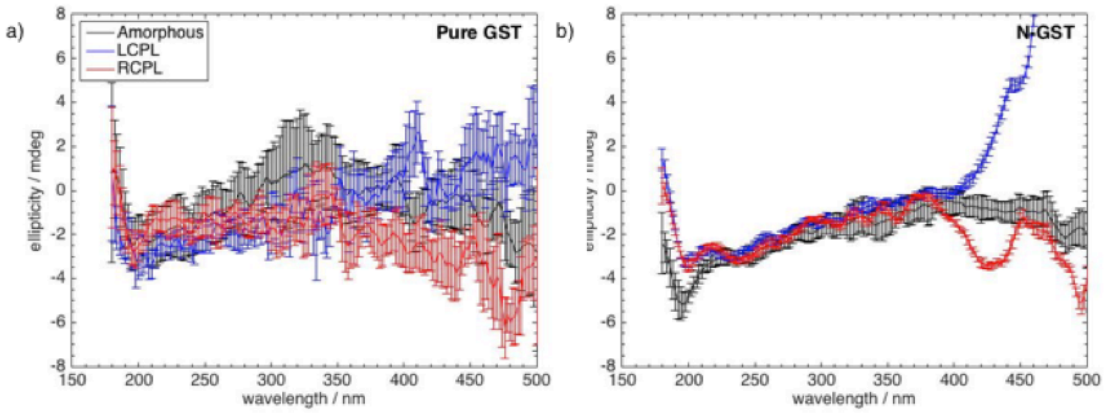

Figure 4.6: Doubled CD signals obtained using the difference in spectra at the R1and R2 prism positions from regions in (a) pure GST and (b) N-doped GST. Higher absorption of the pure GST film gives higher noise in the spectra recorded at the R2 position (due to lower beam intensity and higher PMT voltage levels), leading to higher noise in (a) compared to (b).

This is also illustrated in the effectively doubled CD signals shown in Figure 4.6 (calculated using the difference in signals obtained at the R1 and R2 prism positions as described in Section 3.3.2), where the deviations in the irradiated spectra from the amorphous spectrum in both pure GST and N-GST films are more evident. Although the magnitude of ellipticity observed is only in the order of a few millidegrees, these preliminary results suggest that the handedness of laser light used

to irradiate and induce phase change in amorphous GST films produces mirror symmetry in the CD signal at certain wavelengths.

Differences in the CD signal between laser-irradiated and amorphous regions were more pronounced for N-doped GST than pure GST films, which may suggest that the presence of dopants could be a significant cause of the chirality resulting from the photo-induced phase change. This was tested by depositing GST films doped with other elements at the same concentration as for nitrogen (10 atomic percent), including dopants which have demonstrated enhancement of thermal stability (such as selenium (Vinod, Ramesh, & Sangunni, 2015), titanium (Wei et al., 2011), chromium (Wang et al., 2015) and gold (Prasai & Drabold, 2015), cerium (Huang, Tsai, Wang, & Hsieh, 2012) and indium (Singh, Kaura, Mukul, Singh, & Tripathi, 2014)). Regions in these films were irradiated with left (L-) and right (R-) circularly polarised light (CPL) with similar laser power. The CD spectra obtained from these alternate doped films are shown in figure 4.7.

It is important to note that since the irradiation of regions with L-CPL and R-CPL are separate excitations, the intensity of the CD signal is not necessarily the same for the different handedness, as seen in differences in maximum signal intensity for Ti-GST, Ce-GST and Cr-GST films (Figure 4.7(b), (d) and (f)). Furthermore, possible errors in sample positioning during CD spectroscopy measurements (such that the beam is misaligned and illuminates the edge of the irradiated spot) may result in relatively flat CD spectra resembling those of the amorphous regions. Such errors were subsequently rectified by confirmation of the corresponding PMT voltages (where lower voltages indicate lower absorption and weaker beam intensity at mostly

amorphous regions, as described in Section 3.3.2) and repeating measurements where misalignment was obvious.

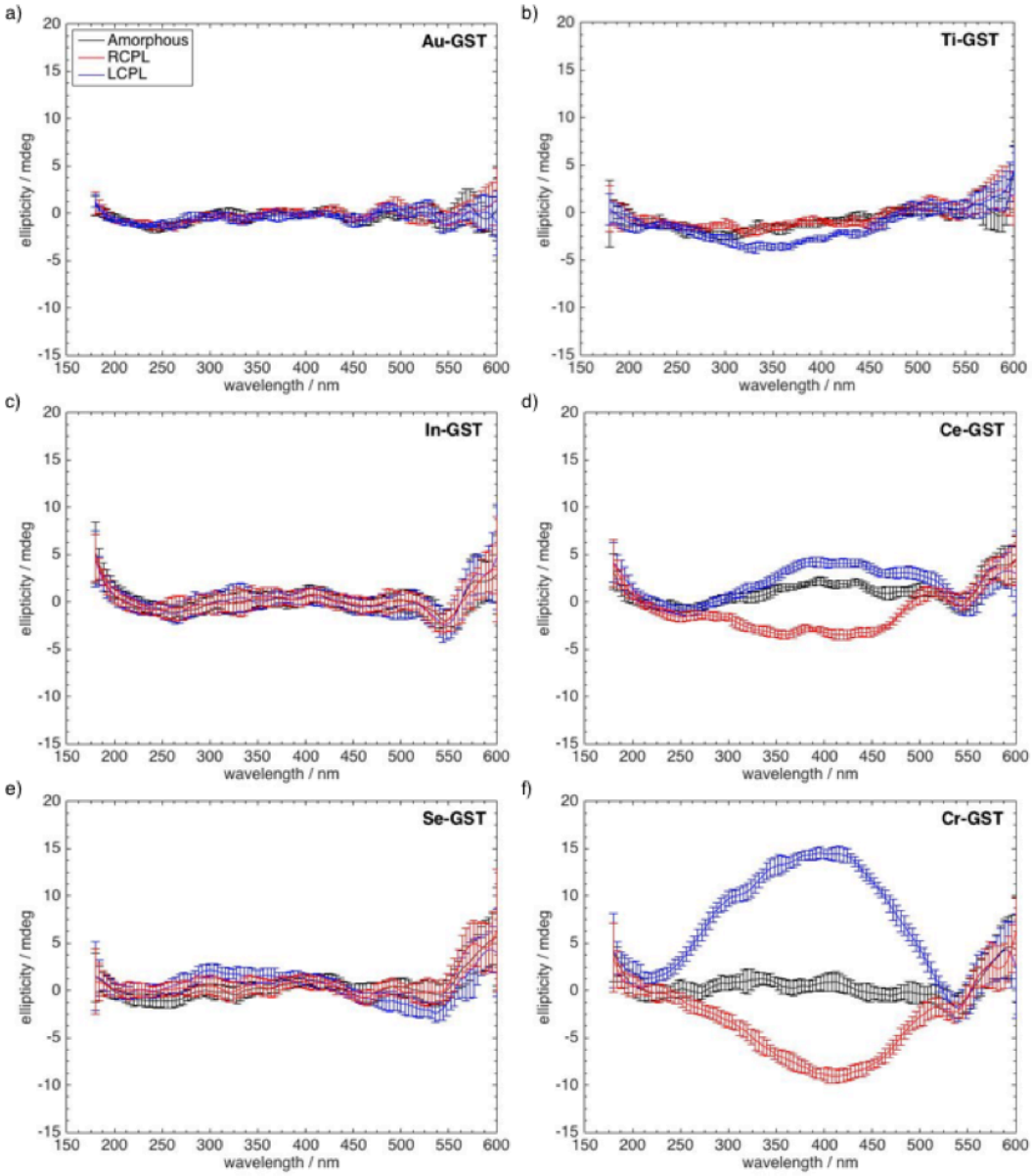

Figure 4.7: Doubled CD signals from GST films with various dopants at (10 at%). (a) Au-GST, (b) Ti-GST, (c) In-GST, (d) Ce-GST, (e) Se-GST and (f) Cr-GST films.

4.3.2. Cr-doped GST

Within the doped GST films measured, significant differences in the CD response were observed in irradiated regions of Ce-doped (Figure 4.7(d)) and Cr-

doped GST (Figure 4.7(f)) films. The largest CD signal (a doubled signal of more than 10 millidegrees) was obtained from laser-irradiated regions in Cr-doped GST. Due to challenges in the storage and maintenance of the Ce target, which cracked without storage in oil (and would have required cleaning before use in film deposition), chromium was selected as the most viable of the dopants for further investigation.

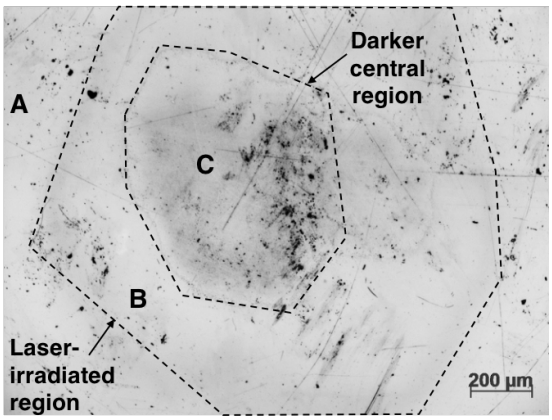

Figure 4.8: Optical image of preliminary laser irradiation of Cr-GST film showing the presence of a darker central region C that was not observed previously in pure and N-GST films.

The formation of a darker central region C (Figure 4.8) was first observed in the irradiated Cr-doped GST. Increasing the laser irradiation power resulted in growth of this region (Figure 4.9), which was also correlated with an increase in CD signal intensity (Figure 4.10). Hence, the presence and growth of the darker central region C was used as a visual indicator of a level of laser irradiation that would subsequently result in the observation of CD effects.

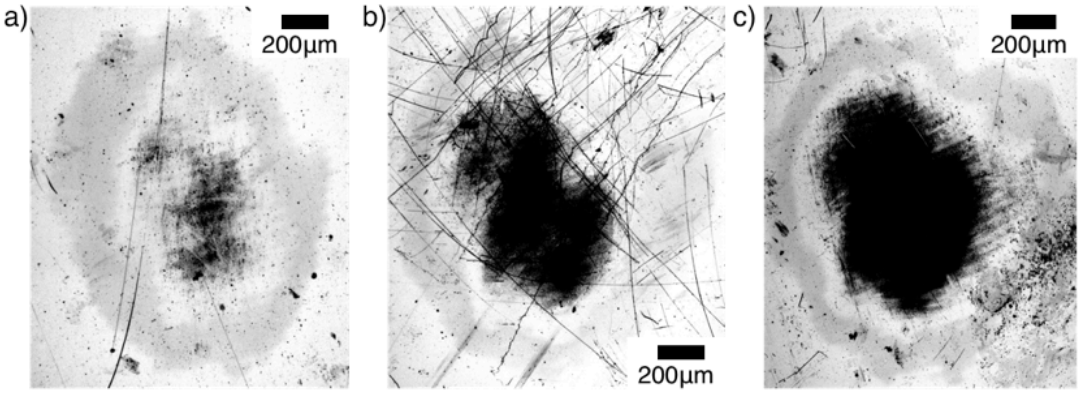

Figure 4.9: Optical images of Cr-GST film irradiated with laser powers of (a) 11.6mJ/cm^2, (b) 12.5mJ/cm^2 and (c) 13.9mJ/cm^2, showing growth of a central darker region with increasing laser power.

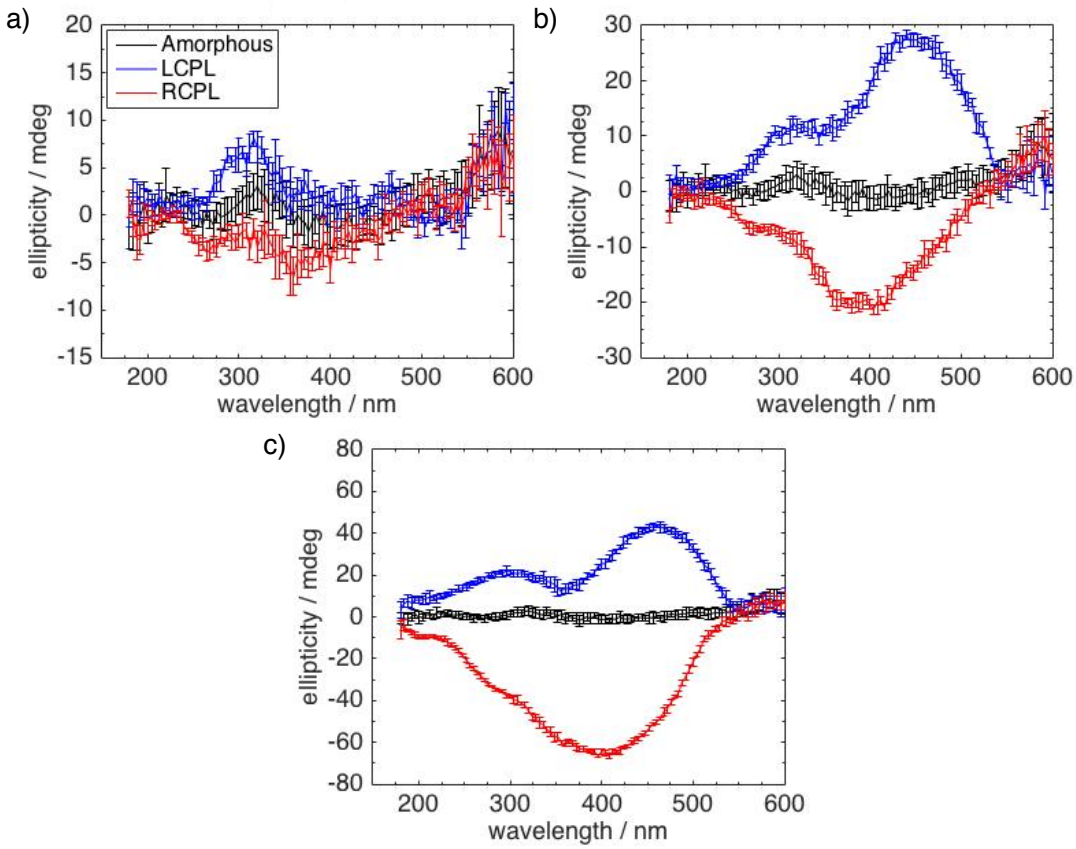

Figure 4.10: CD signals obtained with increases in laser power (a) 11.6mJ/cm^2, b) 12.5mJ/cm^2 and c) 13.9mJ/cm^2) used to irradiate Cr-GST film regions as shown in Figure 4.9.

While naturally occurring organic molecules and compounds exhibit a chiral response of the order of millidegrees of ellipticity, detection of small magnitude signals is difficult in applications such as chiroptical switches and sensors. Therefore, the chiral signal is often enhanced by increasing the film thickness or by incorporating meta-structures for chiral amplification. It follows that for any useful application of this phenomenon as observed in pure or doped GST films, the magnitude of the signal observed in these preliminary results would require improvement. Thus, the effects of various film deposition and laser excitation parameters on the CD response of laser-irradiated film regions were further investigated with the goal of increasing the CD signal observed in these materials. These factors are listed and evaluated in the following sections, with experiments carried out on both pure and Cr-doped GST films since the latter represented the most promising material in terms of the CD signal obtained from the preliminary results.

4.4. Factors affecting the CD signal

The following variables related to thin film deposition and laser excitation were identified as possible factors affecting the CD measurements,

i) The material composition of the thin films in terms of dopant concentration,

ii) The thickness of the films deposited,

iii) Substrates,

iv) The presence of a capping layer on top of the films

v) The laser fluence or energy density used to irradiate regions of the films.

Doubled CD spectra recorded from pure GST and Cr-GST film samples were normalised (as described in Section 3.3.2) by taking the difference between the signals

obtained from regions irradiated with L-CPL and R-CPL and those obtained from amorphous regions. The corresponding error bars for each data point were carried over from the doubled CD spectra before normalisation. Spectra obtained from regions irradiated with linearly polarised light (L-PL) were not considered as these were not distinguishable from those recorded from the amorphous region (Figure 4.11).

Several features in the normalised spectra were identified for further comparative analysis as shown in Figure 4.12(a); the peak signal strength or magnitude (global maximum for L-CPL and minimum for R-CPL) and the peak wavelength (at which the peak signal was recorded). In some cases where the spectra had two significant peaks (Figure 4.12(b)), the next extrema (global minimum for L-CPL and maximum for R-CPL) were also considered. These two sets of extrema tend to occur in the wavelength ranges between 250nm – 350nm and 370nm – 560nm. Artefacts at either end of the scan range (close to 180nm or 600nm) were excluded when considering the positions of these extrema points.

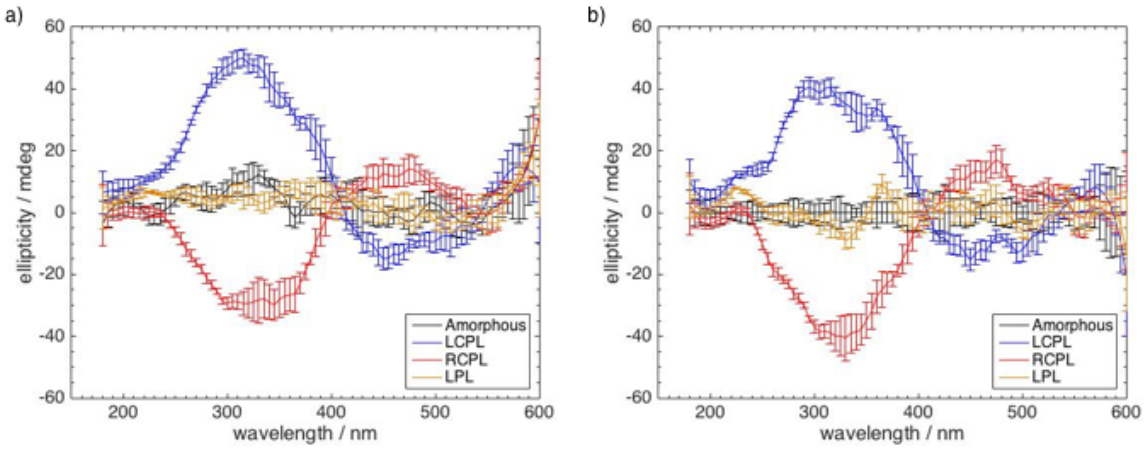

Figure 4.11: Differences between typical L-PL spectra (in brown) and amorphous spectra (in black) compared to L-CPL (in blue) and R-CPL (in red) spectra, shown (a) before and (b) after normalisation with respect to the amorphous spectra (obtained from regions irradiated with laser power of 10mJ/cm^2 on a 55nm thick pure GST film on silica substrate without a capping layer).

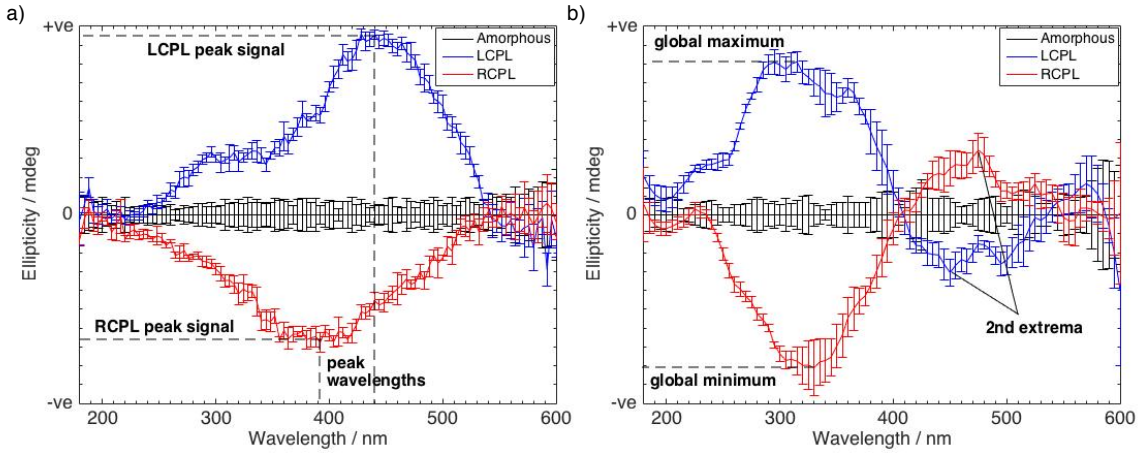

Figure 4.12: Illustration of key characteristic features in CD spectra identified for comparison and analysis of the effects of various experimental factors on the CD spectra. Normalised spectra were obtained from regions irradiated with a laser fluence of 10mJ/cm^2 in (a) a 40nm thick Cr-GST film on silica substrate with a capping layer and (b) a 55nm thick pure GST film on silica substrate without a capping layer.

An overall distribution of the samples discussed in the following sections is shown in Figure 4.13, with the CD spectra measured from each sample represented in terms of their peak signal magnitude and wavelength position.

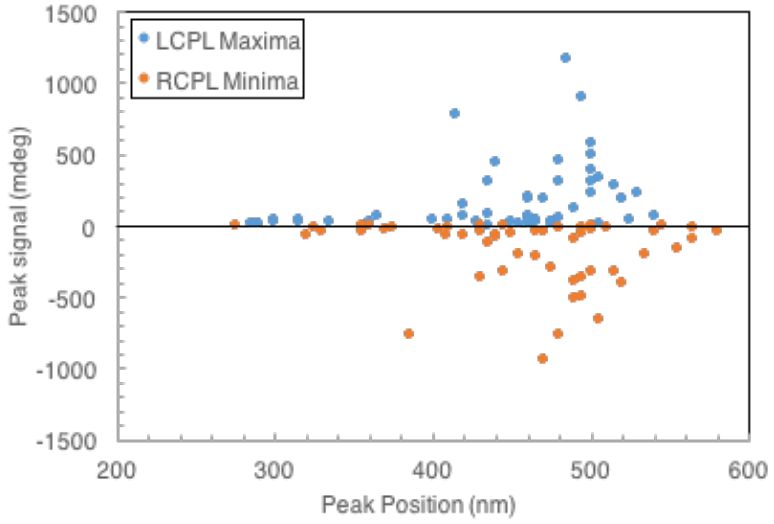

Figure 4.13: Overall distribution of CD spectra, where each datum point represents a single spectrum in terms of its peak signal magnitude and wavelength position as discussed above.

4.4.1. Effect of a capping layer

The presence of a capping layer was shown to be insignificant in the CD measurements. There was negligible difference in the peak signal strength or position of corresponding CD spectra recorded from films of the same thickness and material composition, deposited on the same substrate and excited with the same laser power, but differing in the presence or absence of a capping layer. Figure 4.14 shows an example of a set of CD spectra obtained from irradiated regions of Cr-GST films with and without the capping layer.

Although the capping layer was initially deposited to reduce oxidation of the films, peeling of the surface was observed in SEM images (Figure 4.15). Peeling of the capping layer also meant that the GST layer was exposed after laser irradiation and hence the cap was no longer effective in retarding surface oxidation. In addition, the capping layer obscured the actual morphology of the underlying GST layer, which is important in understanding the origin of the observed CD signal.

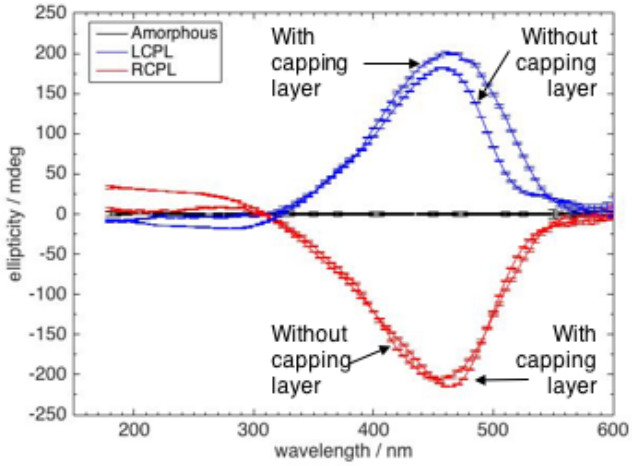

Figure 4.14: Normalised double CD spectra obtained from regions of capped and uncapped Cr-GST films (40 nm thick films deposited on LiF substrates and irradiated with 8mW laser power), showing a similar magnitude in the peak signal and the same peak wavelength position.

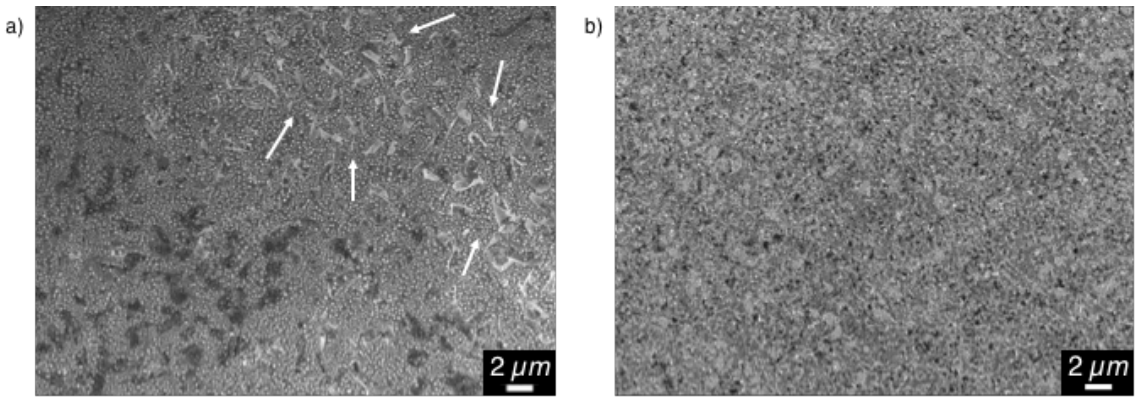

Figure 4.15: SEM images of films irradiated with similar laser power (a) with and (b) without a capping layer. Peeling of the surface capping layer is marked by arrows in (a).

Since the peak CD signal was of comparable magnitude and occurred at similar wavelength for both capped and non-capped films, a capping layer was not deposited during subsequent sample preparation.

4.4.2. Effect of laser fluence

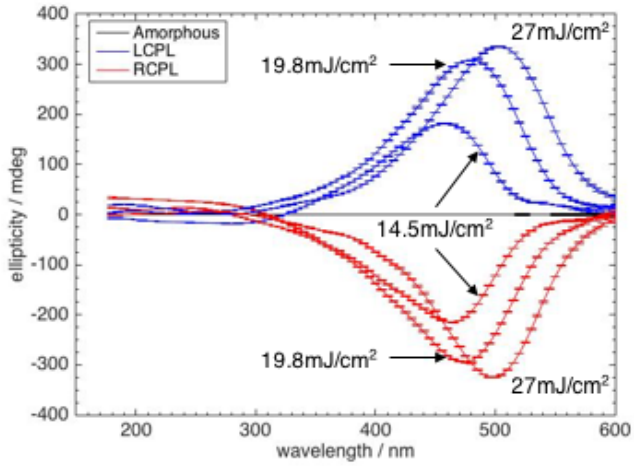

Figure 4.16: An increase in laser fluence used to irradiate regions of a 40nm thick Cr-GST deposited on LiF substrate without capping layer leads to an increase in peak CD signal intensity and a red shift of the peak to higher wavelengths.

The fluence or energy density of the laser excitation used to modify the film was found to have the most significant impact on the maximum signal and peak wavelength of CD spectra. An increase in laser power used to irradiate film regions

typically resulted in an increase in peak signal and a red shift of the peak, as illustrated in Figure 4.16.

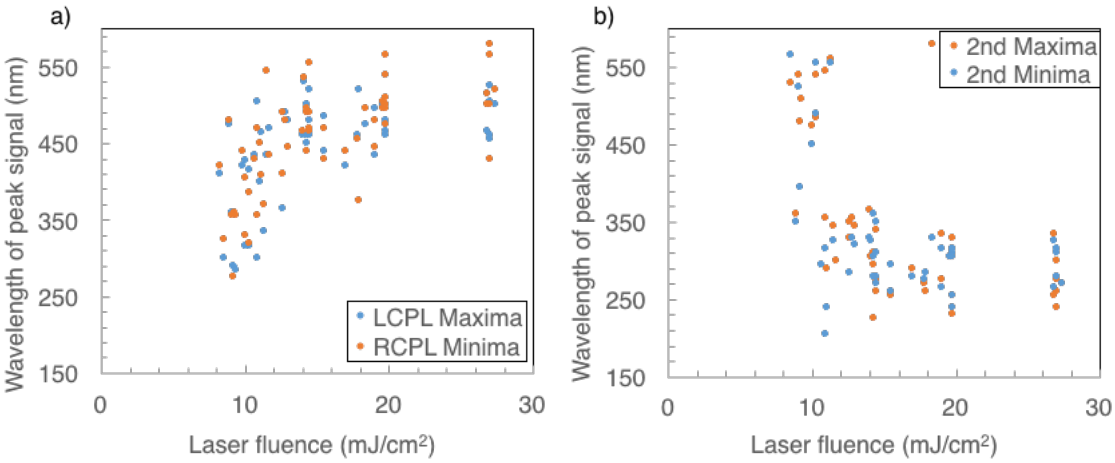

Figure 4.17: The dependence of the wavelengths of peak CD signals ((a) global extrema, (b) 2nd extrema) on laser fluence.

Considering the overall distribution of samples, (Figure 4.17(a)), there is a positive (non-linear) correlation observed between peak wavelength and laser fluence with a red shift of the peak to higher wavelengths with an increase in fluence. Maximum absorption of CPL at longer wavelengths (higher frequency) in films irradiated with higher laser fluence suggests the dominance of lower energy excitations when the CPL interacts with chiral structures in structurally modified regions of the film. An increase in conjugation in molecules, where there is a smaller energy gap between bonding and anti-bonding orbitals, leads to absorption at longer wavelengths compared to molecules with less conjugated bonds. A similar electronic delocalisation (resonance bonding as discussed in Chapter 2) may be responsible for the effects observed in GST films. However, modification of the film under laser irradiation with different powers, and thus, different temperatures and rates of phase change, could also

have led to the presence of different structural units that absorb CPL at different wavelengths.

However, where a second extremum was observed in the CD spectra, these second were blue shifted to shorter wavelengths with an increase in laser fluence. This is most evident in the significant drop in the peak wavelengths beyond 10mJ/cm^2 (Figure 4.17(b)). This could also be interpreted as an effective reversal of the extrema, as illustrated in Figure 4.18. Considering the spectra recorded from the regions irradiated with L-CPL (in blue), the maximum absorption of L-CPL at ~300nm for lower fluence switches to a minimum (indicating greater absorption of R-CPL) for higher fluence, while the minimum observed at ~450nm for lower fluence switches to a maximum for higher fluence. A similar reversal can also be observed in the spectra recorded from regions irradiated with RCPL.

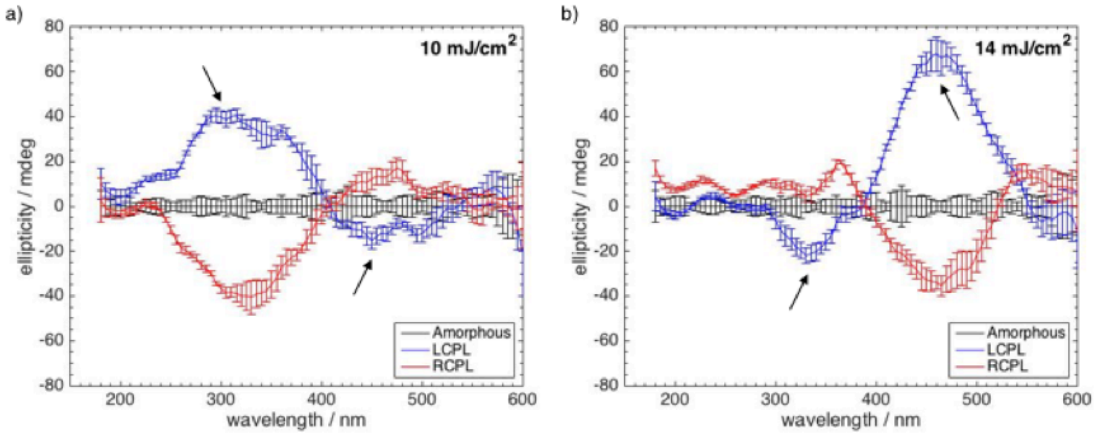

Figure 4.18: Reversal of the 1st and 2nd extrema positions with increased laser fluence (from a) 10 mJ/cm^2 to b) 14 mJ/cm^2) used to irradiate regions of a 55nm thick pure GST film deposited on silica substrate without capping layer. Arrows indicate extrema of the spectra recorded from regions irradiated with L-CPL.

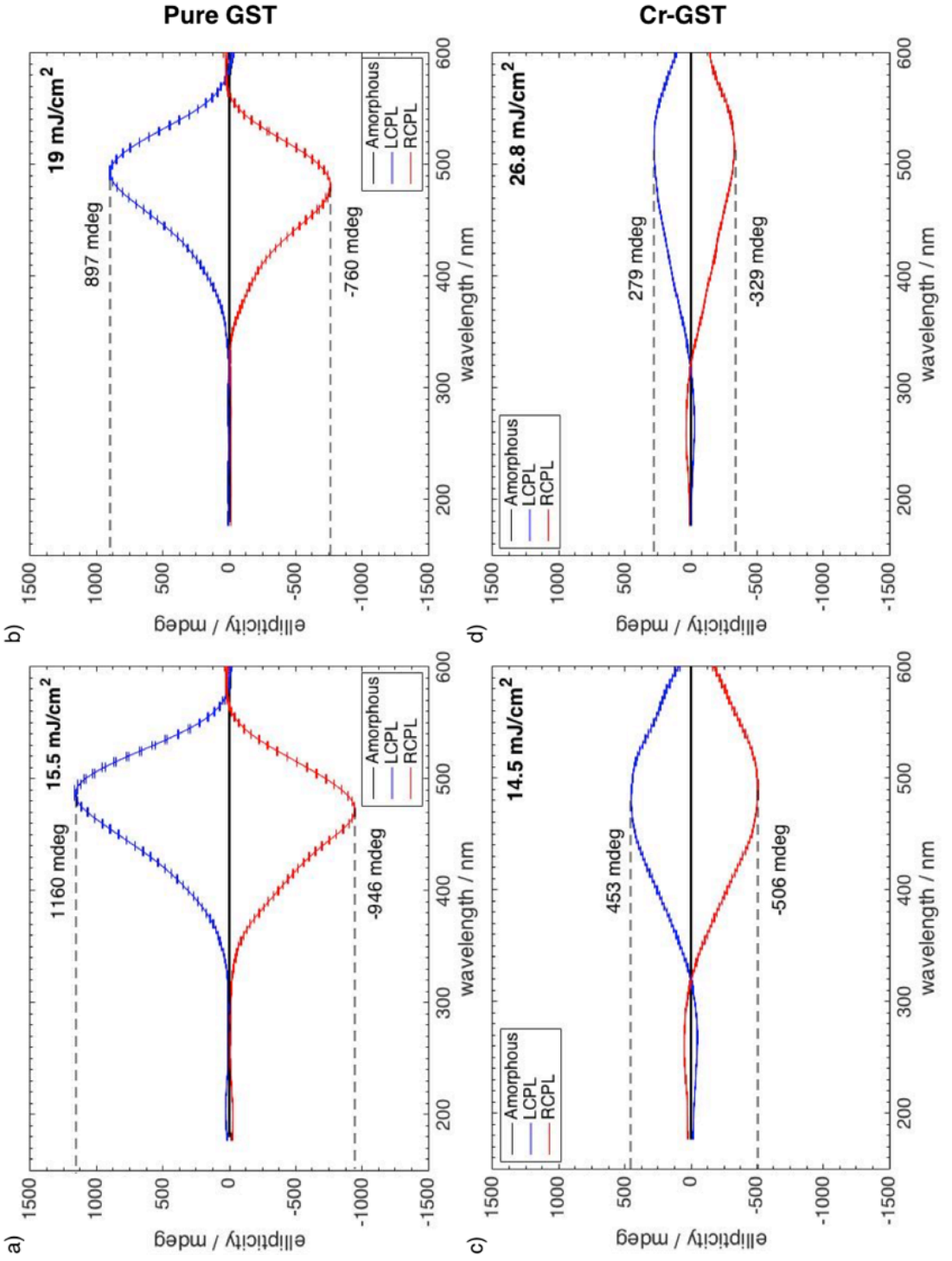

Figure 4.19: Normalised doubled CD spectra measured from regions of a 55nm thick pure GST film (grown on a LiF substrate without a capping layer) irradiated with a) 15.5 mJ/cm^2 (showing the maximum signal of 1160 mdeg obtained for the L-CPL-irradiated spot) and b) 19 mJ/cm^2 (which resulted in a lower peak signal of 897 mdeg). A further decrease in signal with increased fluence is shown in spectra (c) and (d) measured from 60nm thick 3% Cr-doped GST film regions (grown on a LiF substrate without a capping layer).

As already described, this phenomenon may arise due to structural modifications of the film regions under laser irradiation. Chiral structures that exhibit maximum absorption at ~300nm may be dominant in regions irradiated with lower fluence while there is a higher concentration of structures exhibiting maximum absorption at ~500nm in regions irradiated with higher fluence. However, the reversal in CPL absorption may also be explained by the presence of different chiral structures which absorb different handedness of CPL at the same wavelength.

While the largest (doubled) CD signal of 1160 millidegrees was achieved by using 15.5mJ/cm^2 irradiation of pure GST films (Figure 4.19(a)), a decrease in the peak signal was observed with a further increase in laser fluence in both pure GST (Figure 4.19(b)) and Cr-doped GST films (Figure 4.19(c, d)). This could be due to ablation of material from region X at higher fluence (as seen in Figures 4.2 and 4.3), leading to a decrease in the concentration of chiral structures and the corresponding CD signal intensity.

4.4.3. Effect of dopant concentration

The decrease in signal beyond a certain fluence is also illustrated in Figure 4.20, where the distribution of CD signals is categorised by dopant concentration. The largest signals were obtained at approximately 15mJ/cm^2, beyond which a decrease in signal occurs due to increased ablation of material as discussed earlier. The peak CD signal is also suppressed with increased dopant concentration, as evidenced by the decrease in the maximum signal magnitudes. While only films deposited on LiF substrates are shown in Figure 4.20 for clarity, the films grown on silica substrates showed a similar trend.

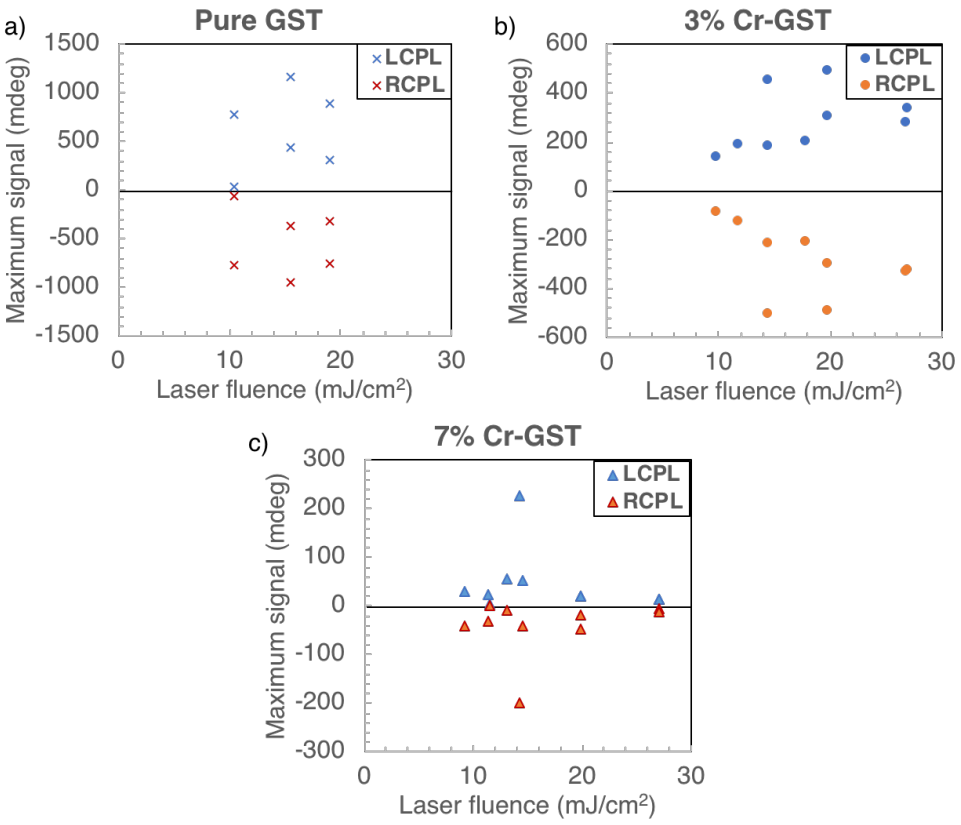

Figure 4.20: Distribution of peak CD signals obtained as a function of laser fluence from (a) undoped GST, (b) 3% Cr-doped GST and (c) 7% Cr-doped GST films, showing signal suppression with increasing dopant concentration. Only measurements from films deposited on LiF substrates are shown. Spread of signal data at the same fluence is due to different film thickness.

Introduction of dopant Cr atoms into the GST lattice may have disrupted the formation of chiral structures under laser irradiation, such that the decrease in concentration of such structures in the film leads to a weaker absorption of CPL and weaker CD signal intensities. However, there is no discernible effect of doping on the peak wavelength positions for L-CPL maxima and R-CPL minima (Figure 4.21), suggesting that any structural changes did not significantly affect the wavelength dependence of CPL absorption.

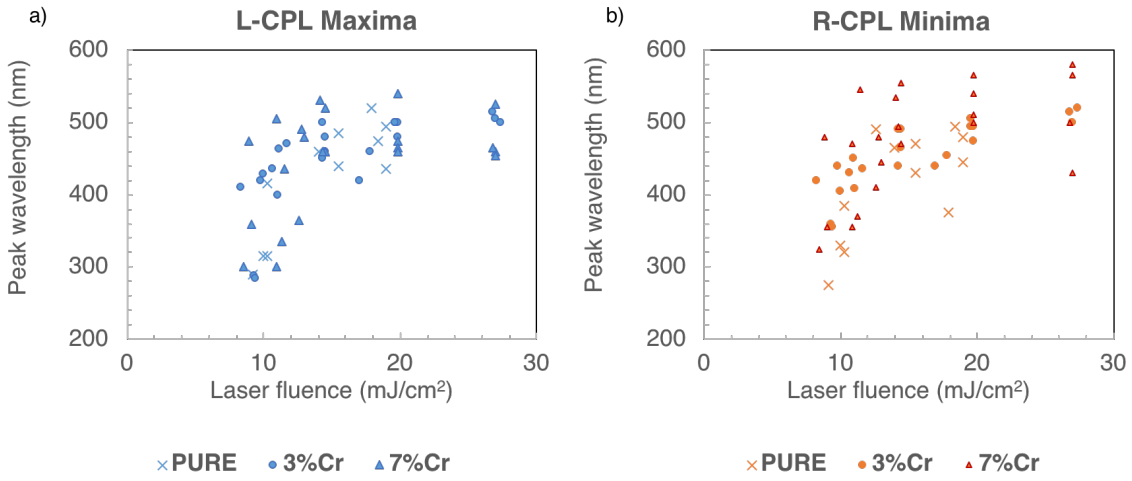

Figure 4.21: Wavelengths of peak CD signals ((a) global L-CPL maxima and (b) R-CPL minima) versus laser fluence used for irradiation, showing no discernible difference due to the dopant concentrations in GST films.

4.4.4. Substrate dependence

Having discussed the effect of laser fluence and dopant concentration on the peak CD signal, the distribution of CD responses categorised by dopant concentration are further analysed according to the substrates on which films were deposited as shown in Figure 4.22.

It is evident from the measurements of pure GST films (Figure 4.22(a)) that the CD signal is suppressed when the films are deposited on silica as compared to lithium fluoride substrates. However, in the case of Cr-doped GST films (Figure 4.22(b, c)), the peak signal magnitude obtained is independent of the substrate. There is no further discernible difference in the wavelength position of the peak CD signals for different substrates (Figure 4.23).

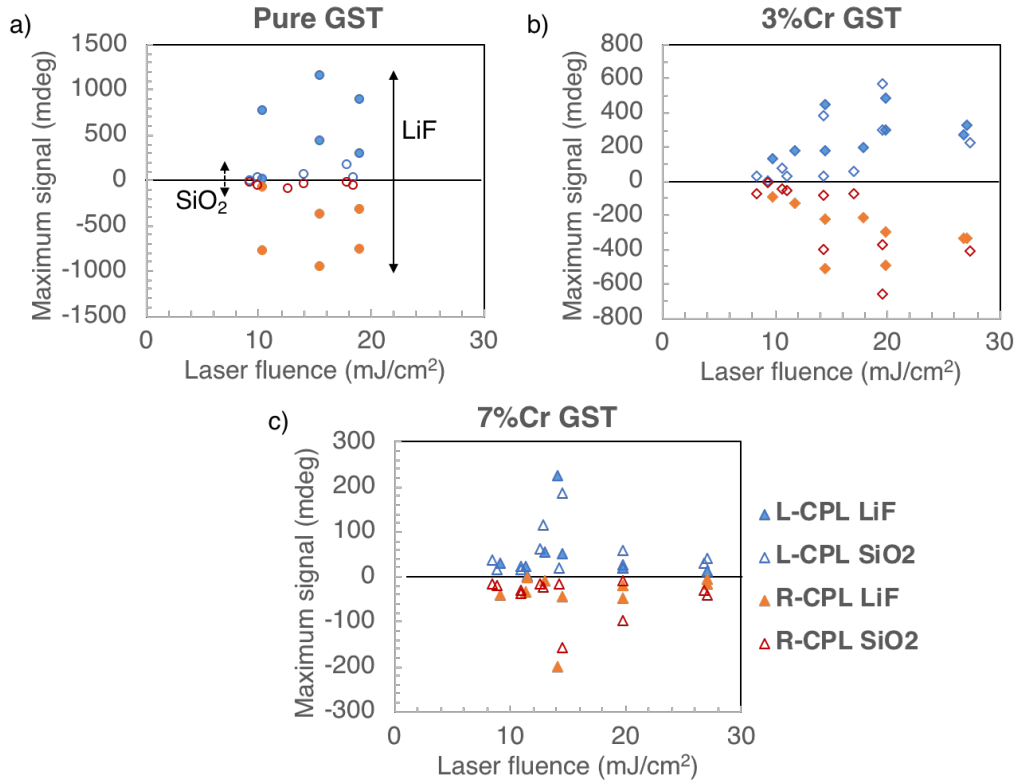

Figure 4.22: Peak CD signals measured as a function of laser fluence from (a) pure GST, (b) 3% Cr-doped GST and (c) 7% Cr-doped GST films. The two different substrates used are differentiated by markers, with open markers representing SiO_2 and filled markers representing LiF substrates.

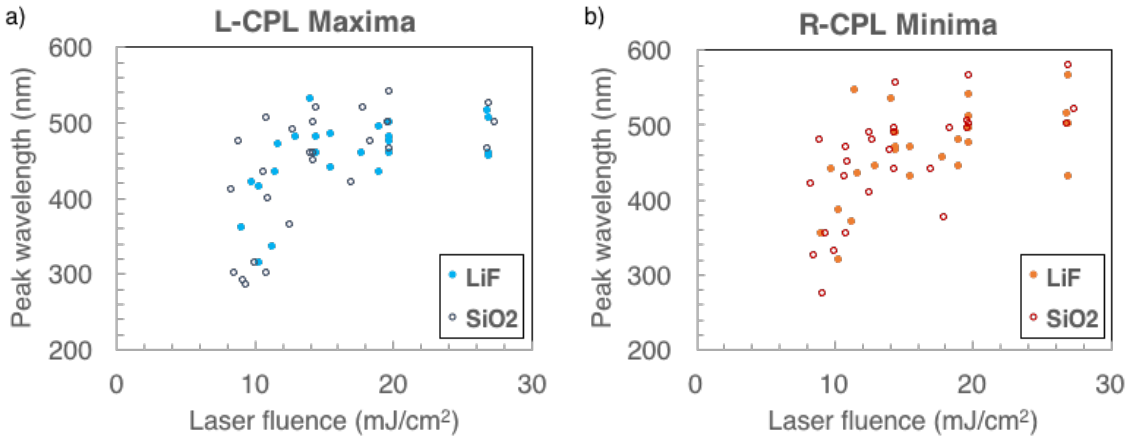

Figure 4.23: Wavelengths of peak CD signals ((a) global L-CPL maxima and (b) R-CPL minima) versus the laser fluence used for irradiation, showing no discernible difference due to the substrates on which films were deposited. Open markers represent SiO_2 while filled markers represent LiF substrates.

4.4.5. Effect of film thickness

For each of the experimental variables discussed thus far, films were deposited at two different thicknesses, 35±3nm (thin) and 55±3nm (thick) as measured by a depth profiler. Figure 4.24 illustrates the tendency of thicker films to exhibit a larger CD signal intensity for all dopant concentrations, suggesting that the CD effects originate throughout the film thickness. Given the strong suppression of the CD signal in pure GST films grown on silica substrates as described previously, Figure 4.24(a) shows only GST films deposited on a lithium fluoride substrate while Cr-doped GST films deposited on both silica and lithium fluoride substrates are included in Figures 4.24(b) and (c).

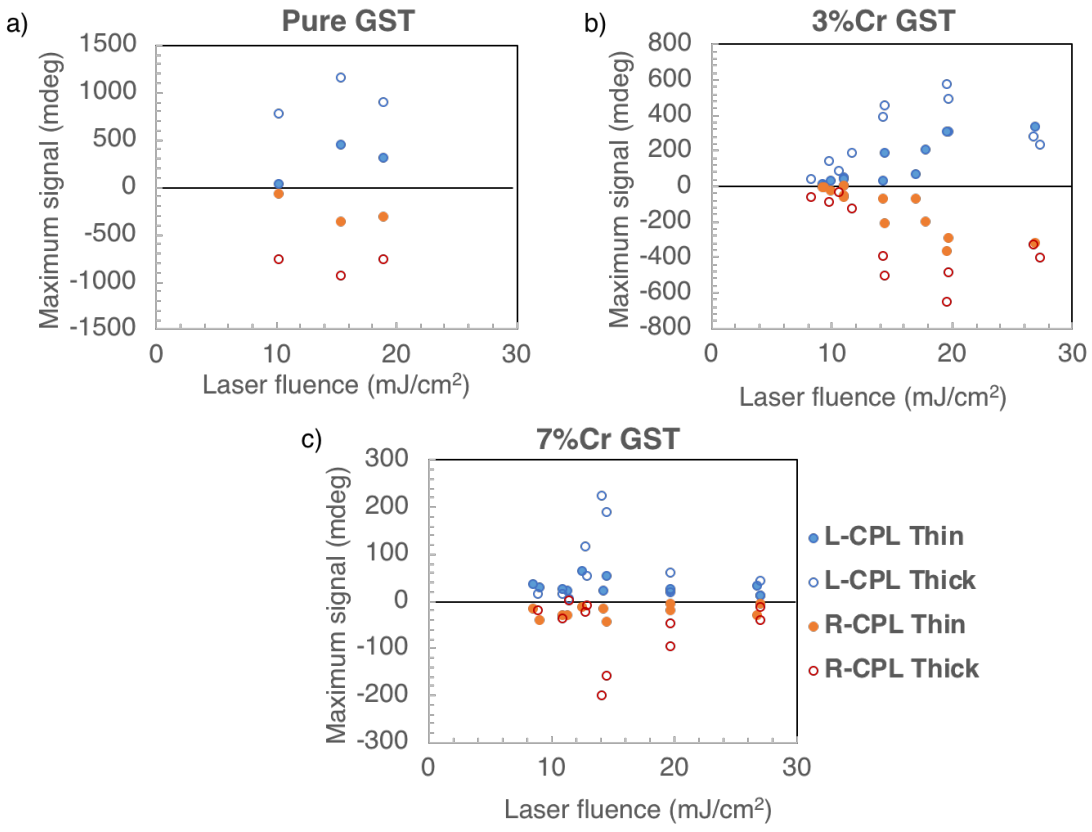

Figure 4.24: Peak CD signals measured as a function of laser fluence for (a) pure GST (on LiF only), (b) 3% Cr-doped GST and (c) 7% Cr-doped GST films. 35nm and 55nm films are represented by filled and open markers respectively.

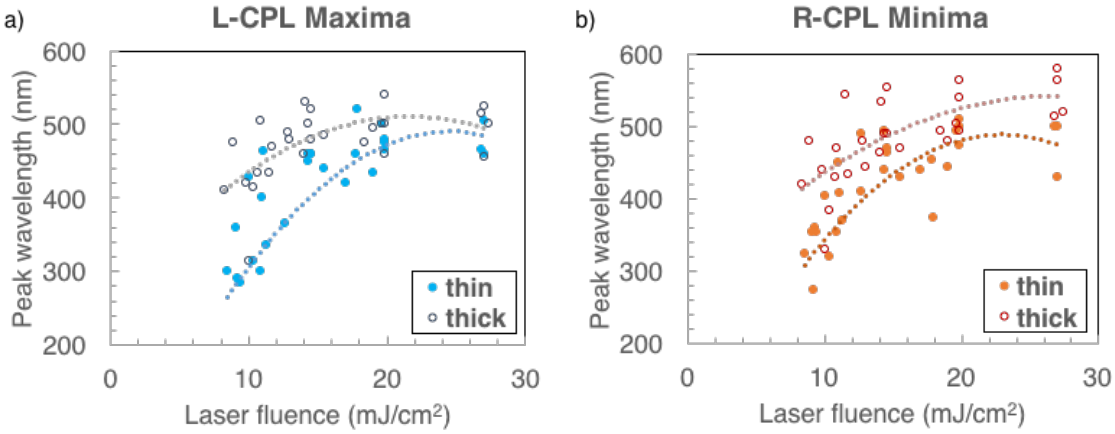

Figure 4.25: Wavelengths of peak CD signals. ((a) global L-CPL maxima and (b) R-CPL minima) versus laser fluence, showing a red shift in peak position with an increase in film thickness (trend lines are included as a guide). Filled and open markers represent 35nm and 55nm films respectively.

In contrast to the effects of earlier variables where different dopant concentrations and substrates had no significant impact on the wavelength position of the peak CD signals, it was found that an increase in film thickness gave rise to a red shift as shown in Figure 4.25. This red shift may be related to an increased fraction of material that had undergone a phase change, which may exhibit absorption of light at a higher wavelength.

4.4.6. Discussion

There are several possible mechanisms for the CD effects and induced chirality observed in the above experiments, one of which is that the electric field component of the light used to induce the phase change influences the direction of crystallisation (along or perpendicular to the polarisation vector). As discussed earlier in Chapter 2, polarisation-dependent mechanisms have been proposed for phase transitions in other materials, e.g. photo-crystallisation of amorphous selenium films (Lyubin et al., 1997; Poborchii et al., 1998; Tikhomirov et al., 1997) and As_2S_3 layered structures (Frumar

et al., 1995), and it is plausible that a similar mechanism is responsible for photo-induced chirality in the GST films. Following CPL illumination and the ensuing phase change, growing crystallites may align along or perpendicular to the polarisation vector of the chiral light, forming a chiral structure as light propagates through the film.

Another possible mechanism involves the formation and alignment of an excess of chiral or charged defects within the film, as observed in other chalcogenide glasses (Elliott & Tikhomirov, 1996). Although the existence of charged defects has not been reported in phase change memory materials such as GST, the presence of nanoscale order (para-crystalline fragments such as even-membered ring motifs) in the amorphous phase (Akola & Jones, 2007; Borisenko, Chen, Song, Nguyen-Manh, et al., 2009) has been suggested as a reason behind fast phase transitions. Rotation or alignment of such crystalline fragments during CPL illumination may lead to the formation of crystallites organized in a chiral structure. For example, helical chains of Ge atoms have been proposed to be responsible for the mirror-symmetric magneto-optical Kerr rotation observed in $[(GeTe)_2(Sb_2Te_3)]_n$ film superlattices (Bang et al., 2015). Similarly, GeN chiral clusters have been identified in atomistic models of N-doped GST refined against electron diffraction experimental data (Borisenko, Chen, Song, & Cockayne, 2009). Hence, it is not unreasonable to expect the formation of similar chiral clusters in the structure of Cr-doped GST films.

There have been some studies on Cr-doped GST reported in the literature (Skelton & Elliott, 2013; Wang et al., 2015; Zhang, Ronneberger, Li, & Mazzarello, 2012). Wang et al., (2015) reported that crystalline Cr-GST inherits the phase structure of GST and that the amorphous phase exhibits improved thermal stability. First

principle simulations (Skelton & Elliott, 2013) have found that Cr atoms occupy both interstitial and octahedral cationic sites usually located next to voids, allowing the host material to accommodate a more flexible range of geometries. Doping of GST with Cr has also been found to introduce ferromagnetic properties (Skelton & Elliott, 2013; Zhang et al., 2012), which may lead to different interactions with the electromagnetic field of chiral illumination.

Although preliminary measurements of N-GST and Cr-GST films exhibited larger CD effects than pure GST films, CD signal suppression in Cr-GST films in subsequent optimised experiments suggests that the introduction of Cr dopants either destroys chirality, perhaps by introducing planes of symmetry such that chiral structures are rendered achiral, or promotes the formation of near-equal amounts of chiral structures that absorb either handedness of CPL such that the smaller difference in CPL absorption results in lower CD signal intensity. Nevertheless, the mechanisms of induced chirality suggested above may still apply to both pure and doped GST films.

While the presence of a capping layer was deemed insignificant, laser fluence had a pronounced effect on the induced CD effects in laser-irradiated film regions. Increasing fluence caused an increase in CD signal strength and a red shift in the peak signal for both L-CPL and R-CPL irradiations. However, this was only true up to a certain threshold, beyond which CD signal intensity decreased for all film compositions. Film thickness also played a role, with thicker films exhibiting larger CD effects and a red shift in peak signal position.

The proposed mechanism involving chiral alignment of crystallite growth is consistent with these results, where a thicker film or an increase in laser power would increase the chiral light-matter interaction, leading to a greater concentration of chiral

structures resulting in a larger CD signal. A further increase in power, however, causes a progression from melting-induced crystallisation to ablation (Zhang et al., 2012) that removes surface material. Removal of matter, equivalent to a thinner film, would then result in a decrease in CD signal. The red shift in peak signal positions may be due to an increased fraction of material in the film that has undergone a phase change in either thicker films or films irradiated with higher fluence, which exhibits stronger absorption of CPL at longer wavelengths than the fraction of material that has not changed structurally. This may also be related to the phenomenon of resonance bonding in the crystalline phase, where increased electronic delocalisation may contribute to the red shift observed.

Deposition of pure GST films on silica substrates also resulted in a suppression of CD signal compared to films deposited on lithium fluoride substrates, whereas Cr-doped GST films showed no such substrate dependence. The substrate may affect the film structure during deposition and influence subsequent crystallisation, but understanding these effects will require further structural investigation.

4.5. Stability of CD effects

4.5.1. Long-term stability

Although multiple spectral scans on each film sample region ensured the repeatability of the results discussed thus far, degradation of the films due to structural relaxation or oxidation could affect the stability of the CD effects observed over time. The long-term stability of the regions exhibiting opposing CD polarity is vital to any potential applications based on their differentiated absorption of CPL. Therefore, CD

spectroscopic measurements were also repeated on multiple occasions using similar instrumental setups and methods.

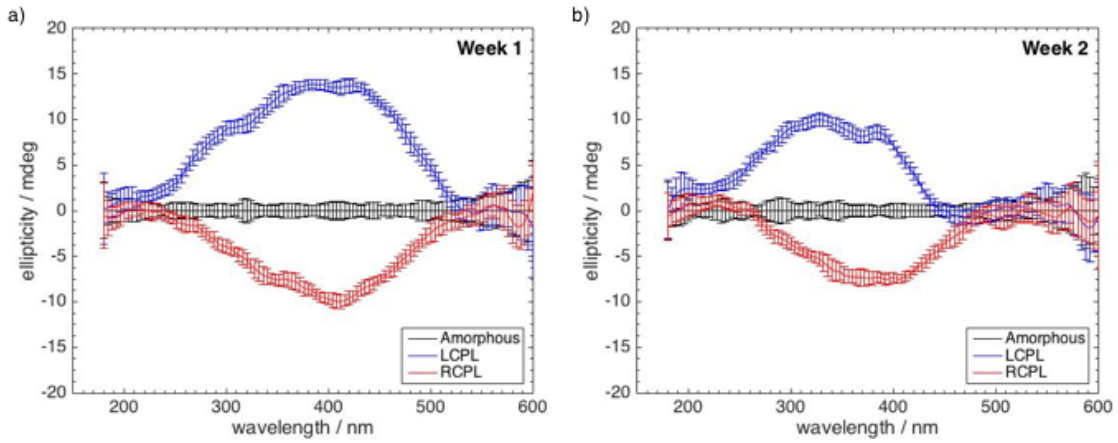

Figure 4.26: Normalised doubled CD spectra of laser-irradiated regions on a 40nm thick 3% Cr-doped GST films deposited on silica without a capping layer, measured (a) 7 days and (b 15 days after laser irradiation at approximately 9mJ/cm^2.

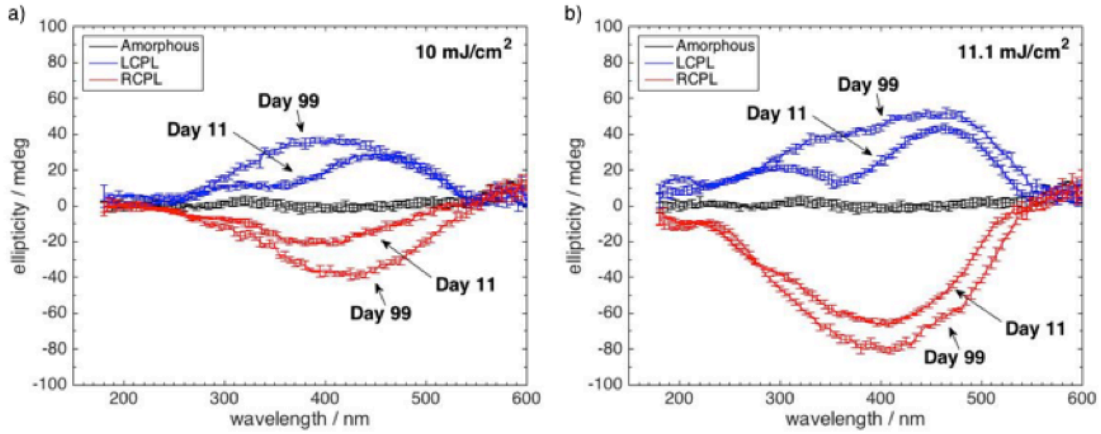

Figure 4.27: Doubled CD spectra of regions on another 40nm thick 3% Cr-doped GST film (deposited on silica without a capping layer, measured (a) 11 days and (b) 99 days after laser irradiation with 10mJ/cm^2 and 11.1mJ/cm^2 respectively.

Figure 4.26 shows the CD spectra of one such film measured a week apart. Laser irradiation on film regions was carried out a week prior to the first measurement. The CD spectra of a similar film irradiated with higher laser fluence and measured three months apart are shown in Figure 4.27. The peak CD signal shows a small decrease in magnitude in the short-term (over a week) and a small increase over a

longer period (of three months). However, it is not possible to describe the time evolution or stability of the CD spectra based on these two examples alone.

Hence, CD spectroscopic measurements were also performed on a thicker film irradiated with higher laser fluence on three different occasions (Figure 4.28), with the first measurement performed a month after laser irradiation and with an interval of approximately one month between each subsequent sets of measurements. As in the previous examples, an initial decrease followed by an increase in CD signal over a longer term is observed in the example shown in Figure 4.28. However, the final magnitude is still lower than that from the first measurement.

Shifts in beam positioning on the film during the different measurements and variations in the spectroscopy instrumentation setup (e.g. PMT detector gain, baseline spectrum and noise) may be responsible for the differences observed in the time-dependent CD response. In addition, Ostwald ripening and structural relaxation of the laser-irradiated regions as well as oxidation of the film may contribute to changes in the CD signal strength.

Despite these variations, the CD spectra recorded are of the same order of magnitude and have proved to be reproducible months after laser irradiation. However, in general samples were stored under vacuum with desiccants to reduce any structural degradation and CD spectroscopic measurements (as discussed in section 4.4) were performed as soon as possible, ranging from a week to a month, after laser irradiation.

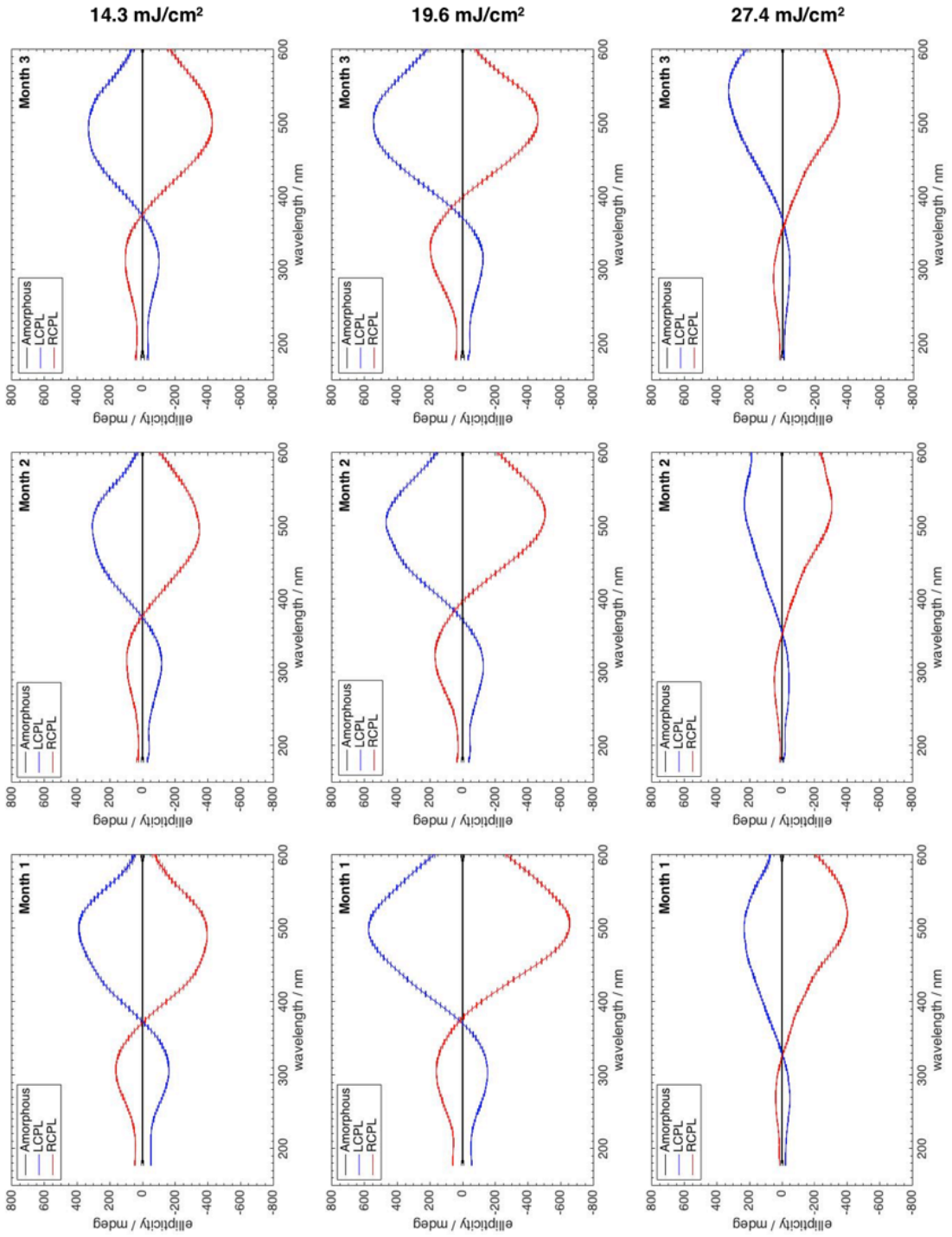

Figure 4.28: Normalised doubled CD spectra of laser-irradiated regions (different laser fluence marked by rows) on a 60nm thick 3% Cr-doped GST film deposited on silica without a capping layer, measured on three different occasions (27, 43 and 68 days respectively after laser irradiation).

4.5.2. Thermal stability

The amorphous phase of GST is known to have high stability (for several decades) at room temperature with respect to crystallisation, which has significance in the data retention characteristics of phase change memory devices. Although any definitive conclusions as to the long-term stability of the CD effects observed in the irradiated regions exhibiting opposing CD polarity would require monitoring over a longer period than the three months of the above study, the evolution of these effects with temperature also provides key insights into their thermal stability. As such, the effect of thermal annealing on the CD effects was investigated by subjecting the same 60nm thick 3% Cr-doped GST film as above to heat treatment.

After measuring the CD at room temperature (T1 ~25 °C), the sample was placed on a hotplate at an approximate temperature of 60°C for 5 minutes to establish thermal equilibrium across the whole sample disk. The temperature of the hotplate was monitored using a thermocouple with readings taken every second, giving an average temperature of 59 ± 0.4°C (T2). The sample was then allowed to cool down to room temperature before performing CD spectroscopic measurements on the various film regions again. This process was then repeated at temperatures of 160°C (T3 = 156 ± 1.3°C) and 360°C (T4 = 346 ± 12.4°C).

The CD spectra obtained from this annealing experiment are plotted in Figure 4.29. The evolution of the peak CD signal magnitude with temperature is also illustrated in Figure 4.30. Thermal annealing of the film showed a general decrease in the peak CD signal magnitude of laser-irradiated regions with increasing temperature. In the case of the lower laser fluence of 14.3mJ/cm^2, the CD signal drops to almost zero after annealing at 360°C, almost indistinguishable from the amorphous film

regions. However, for the regions irradiated with higher fluence, the CD signal increases with annealing temperatures up to 160°C and then decreases after annealing at 360°C.

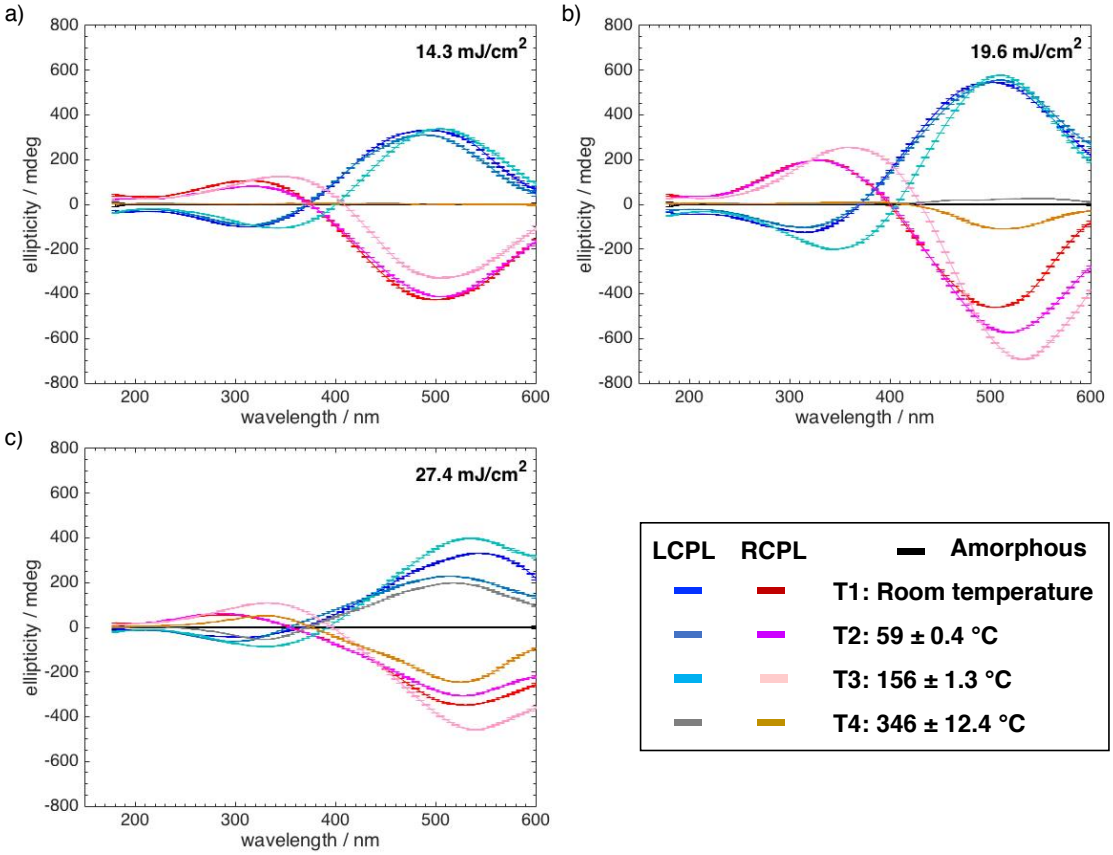

Figure 4.29: Normalized doubled CD spectra of regions irradiated with laser fluences of (a) 14.3mJ/cm^2, (b) 19.6mJ/cm^2 and (c) 27.4mJ/cm^2 following heating of a 60nm thick 3% Cr-doped GST film deposited on silica without a capping layer.

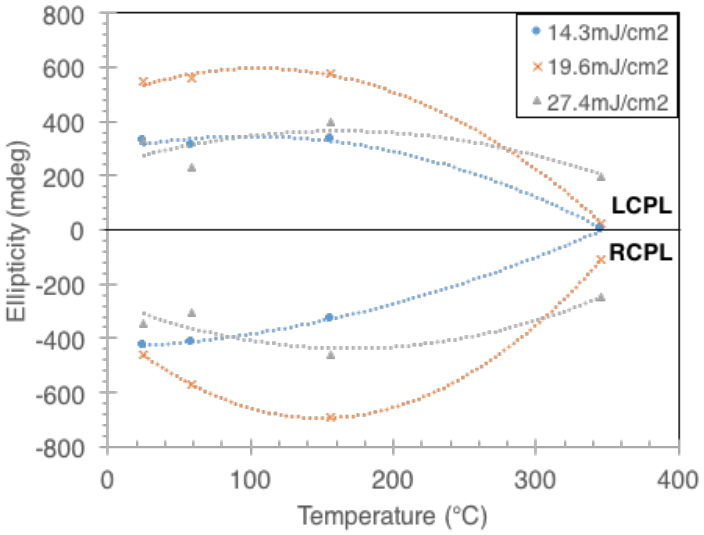

Figure 4.30: Evolution of CD spectra with temperature represented by changes in the peak signal magnitude. Positive signals correspond to global maxima in L-CPL spectra while negative signals correspond to R-CPL minima. Trend lines (2nd order polynomials) are included as a guide.

These results may be explained by a simple thermal mechanism, such as the two-stage process proposed by Poborchii, Kolobov & Tanaka (1999) and described below. When the thin film containing irradiated regions is heated at lower temperatures that are insufficient for melting to occur, the heating promotes growth of existing crystallites that have been preferentially orientated from the earlier laser irradiation, causing an increase in the CD signal similar to that observed for regions irradiated with higher laser power. This form of growth through Ostwald ripening may also be responsible for the time-dependent increase in CD signal as discussed in section 4.5.1. However, when heated to higher temperatures that cause partial melting of the crystallites, the lack of a polarisation influence leads to normal achiral thermal crystallisation, resulting in a reduction in CD response. The decrease in CD signal at the regions irradiated with lower fluence (of 14.3mJ/cm^2) could be due to the formation of almost uniformly sized crystallites during laser irradiation that limits the Ostwald ripening process under heating.

4.6. Switching of CD polarity

Since GST-based non-volatile phase change memory devices operate on the basis of reversible switching between amorphous and crystalline states, the ability to reverse the polarity of the CD effects observed would be beneficial in similar memory devices or chiroptical applications based on material states differentiated by their absorption of CPL. Hence, switching of the CD effects was also explored by irradiating previously irradiated regions by light with a different polarisation.

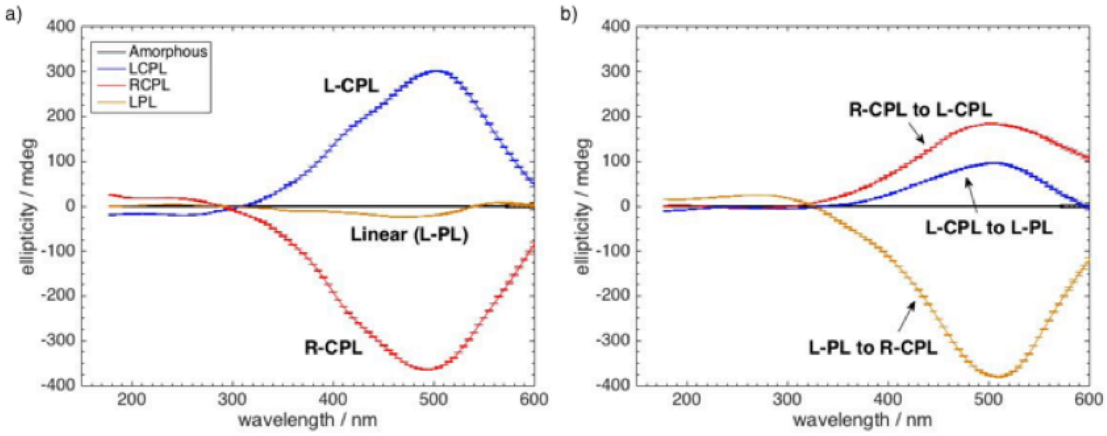

Figure 4.31: (a) Normalised doubled CD spectra of laser-irradiated regions on a 40nm thick 3% Cr-doped GST film deposited on silica without capping layer. Spectra obtained after a second laser irradiation are plotted in (b).

Figure 4.31(a) shows the normalised CD spectra originally measured from a 40nm thick 3% Cr-doped GST film, deposited on a silica substrate without a capping layer, where regions were irradiated with a laser fluence of 19.6mJ/cm^2. The film was then irradiated again, using LPL (linearly polarised light), R-CPL and L-CPL of similar power on regions that were previously irradiated with R-CPL, L-CPL and LPL respectively.

The new measurements are shown in Figure 4.31(b), with spectra plotted in the same colours as the original irradiation in Figure 4.31(a). The second irradiation

caused significant changes in the CD spectra, where importantly the R-CPL to L-CPL transition showed a polarity reversal. The LPL to R-CPL transition exhibits a CD signal comparable in magnitude to the original R-CPL irradiation, while the transition from L-CPL to LPL exhibits a decrease in signal strength. This successfully demonstrates the ability to switch between material states that exhibit different CD signal polarity, which is likely to occur via melting and re-solidification of the irradiated region under the influence of CPL as before. However, the inconsistent recovery of the original signal strength may be due to degradation of the film and further investigation is required to fully understand these switching effects.

4.7. Summary

The results presented in this chapter show that optical anisotropy has been successfully induced in pure and doped GST thin films by irradiation with different handedness of circularly polarised light (CPL). Laser-irradiated regions which have undergone a photo-induced phase change exhibit significant circular dichroism (CD), with consistent mirror-symmetry of opposite handedness and a significant difference from the non-irradiated amorphous regions. It has also been demonstrated that various parameters such as laser fluence, film thickness and dopant concentration influence the CD effects observed. This photo-induced optical anisotropy provides strong evidence of the involvement of non-thermal effects on the phase transition and points towards permanent structural changes in the GST thin films.

Chapter 5

Structural characterisation and analysis

5.1. Surface morphology of laser irradiated regions

Modification of film surfaces due to laser irradiation was characterised by secondary electron imaging in a scanning electron microscope (SEM, as described in Chapter 3). As seen previously, an increase in temperature due to higher fluence leads to the consecutive outward growth of regions B, C and X from the centre of the irradiated spots. These various sub-regions, identified by different optical reflectivity to the unexposed surrounding region A, also differ in terms of surface morphology (Figure 5.1). The variations in surface morphology across the irradiated spots are presented here, as additional means of distinguishing the different sub-regions.

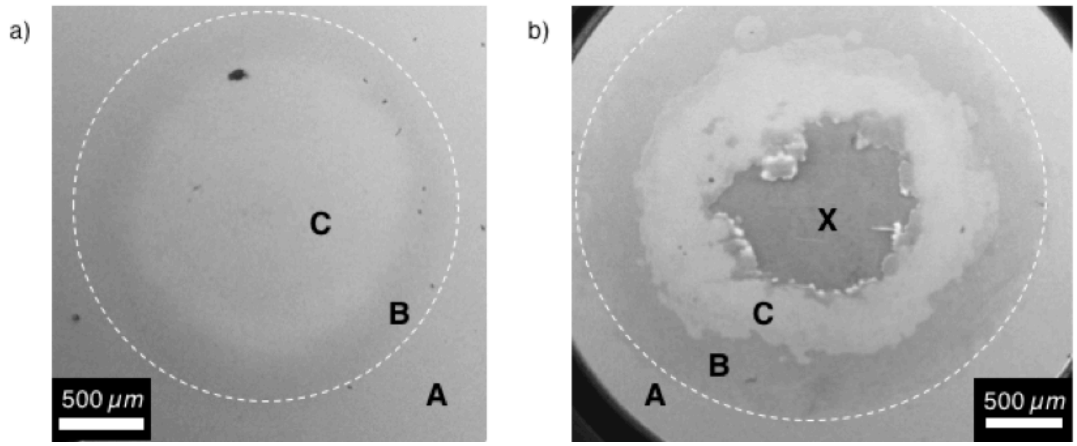

Figure 5.1: Secondary electron SEM images of laser-irradiated regions on (a) 55nm thick pure GST film and (b) 37nm thick 3% Cr-doped GST film, both deposited on LiF substrates. The regions were irradiated with laser fluences of 15.9mJ/cm^2 and 19.8mJ/cm^2 respectively.

Ablation of material at the centre of the irradiated spot at higher laser powers (Figure 5.1(b)) was marked by a brighter contrast at the interface between regions C and X under SEM observation (Figure 5.2). This could be caused by edge effects due to enhanced emission of secondary electrons from the interface (topographical contrast due to thinning of the film), as well as charge accumulation or build-up of electrons in ablated regions due to the underlying insulating substrate. This charging effect is also responsible for streaks and image shifts during image acquisition of heavily ablated regions at higher magnifications (30,000X), that were not observed elsewhere in the film.

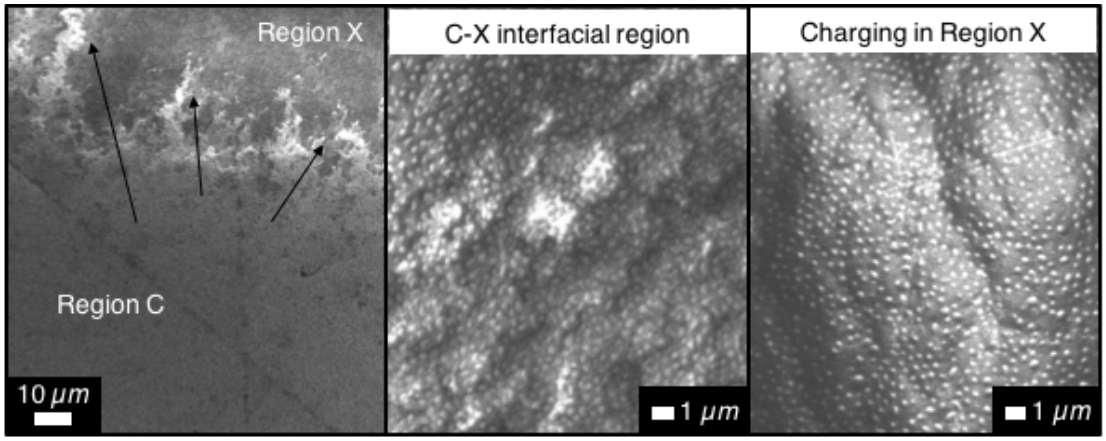

Figure 5.2: Secondary electron SEM images of charging and edge effects (bright regions marked by arrows) visible at the interface between sub-regions C and X due to ablation of the film and exposure of the underlying non-conducting substrate.

The typical evolution in morphology of the film surface is shown in Figure 5.3, where surface features are visible in areas within the laser-irradiated regions. While region B is indistinguishable from region A except for its optical contrast, the size of the surface features increases from the edge towards the centre of region C, contributing to an increasingly rough morphology. Ablation and removal of material

at higher laser fluence may also contribute to this roughness and sharper edges of the surface features at the centre (Region X) of some irradiated spots.

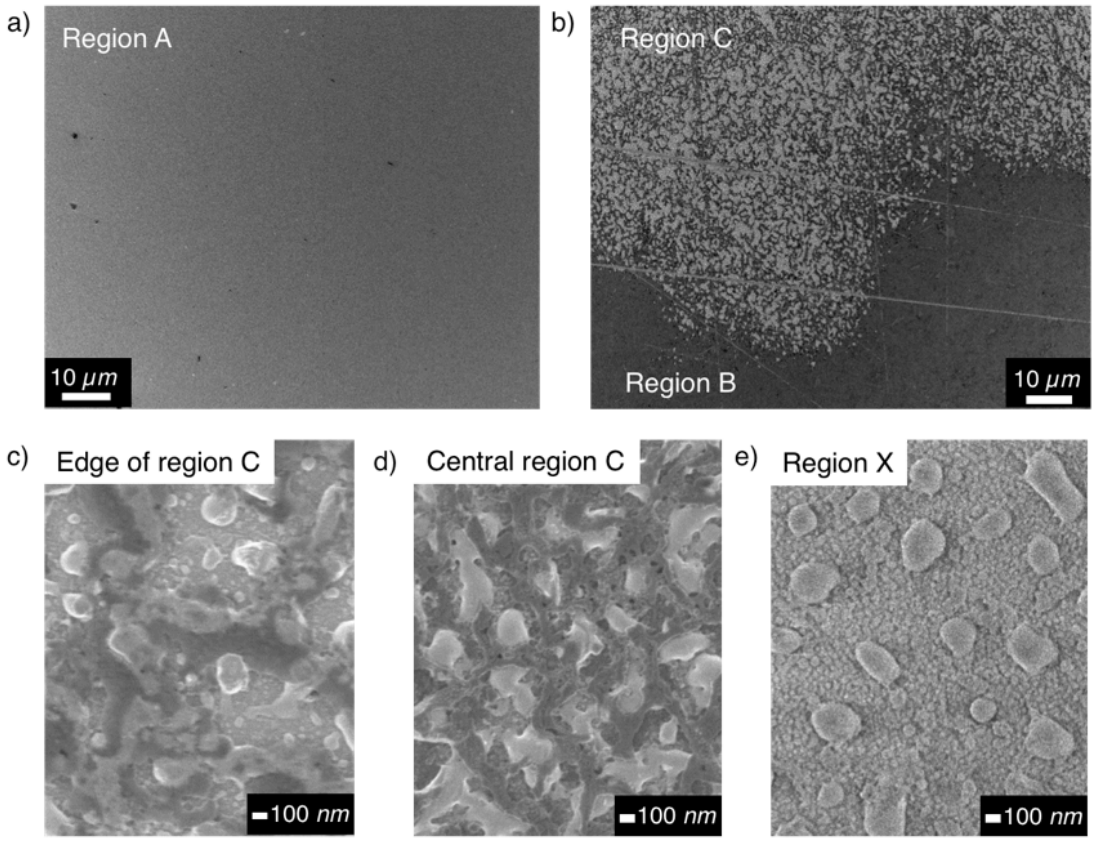

Figure 5.3: Surface morphologies of different sub-regions in a 37nm thick 3% Cr-doped GST film deposited on a LiF substrate without a capping layer and irradiated with a laser fluence of (a – d) 14.5mJ/cm^2 and (e) 19.8mJ/cm^2. (a) The non-irradiated region A is smooth with hardly any distinguishable features. (b) Region B is also featureless under SEM observation but there is a clear boundary between regions B and C. Magnified images in (c) and (d) show the variation in surface morphology between the edge and centre of region C. The ablated central region X from a region irradiated with higher fluence is also shown in (e).

Differences could be observed in the morphology of regions (specifically at region C) irradiated with different polarisation of light (Figure 5.4). Regions irradiated with linearly polarised light (LPL) tend to exhibit directionality of the surface texture that is consistent with the direction of polarisation used during irradiation. The directionality in the LPL-irradiated region is easily discernible from the vertical arrangement of features in the SEM images at the length scale indicated in Figure 5.4.

The calculated power spectrum of the micrograph also shows a horizontal streak, corresponding to the vertical alignment of the features observed in the images. This suggests that the polarisation vector of light used in the irradiation influences the orientation and alignment of features (along the polarisation vector) in the melt. However, this phenomenon was not observed in all LPL-irradiated films, possibly due to masking of the directionality effects by the presence of a capping layer or prolonged melting and rearrangement of the material under a higher laser fluence.

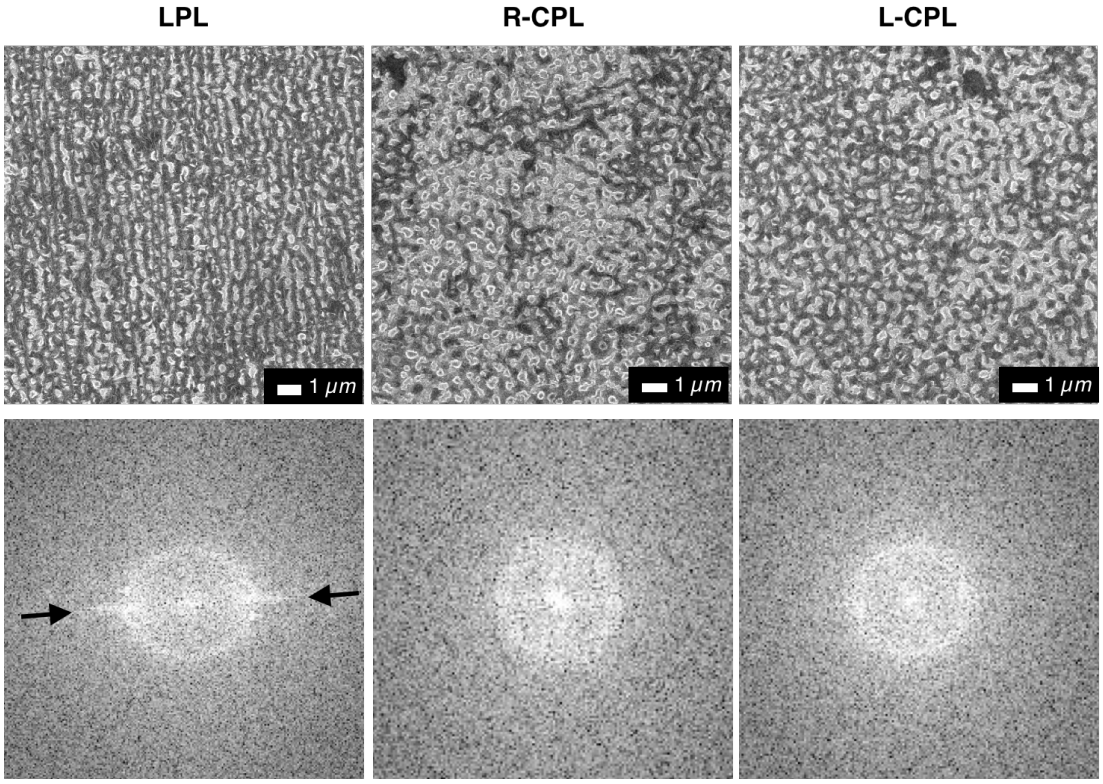

Figure 5.4: Secondary electron SEM images of region C on a 37nm 3% Cr-doped GST film on LiF, irradiated with fluence of 14.5mJ/cm^2 but with different polarisation, and their corresponding 2-dimensional power spectra. Arrows point to the nearly horizontal streak in the LPL power spectrum.

In contrast, no such directionality was observed in film regions irradiated with circularly polarised light (CPL) and the surface morphology of regions irradiated with CPL of two opposing handedness are indistinguishable from one another. However, it

is reasonable that the polarisation might have a similar effect on the orientation of the observed features at the surface or deeper in the film.

5.2. Cross-sectional morphology of irradiated regions

Cross-sectional specimens were prepared from the different sub-regions of irradiated films for further structural characterisation using TEM. Bright-field TEM and dark-field STEM images of the heavily ablated region X showed a decrease in the film thickness (from a deposited thickness of 37nm to approximately 10nm in Figure 5.5) and hemispherical protrusions on the surface of the film that match the size of the surface features observed in the SEM images.

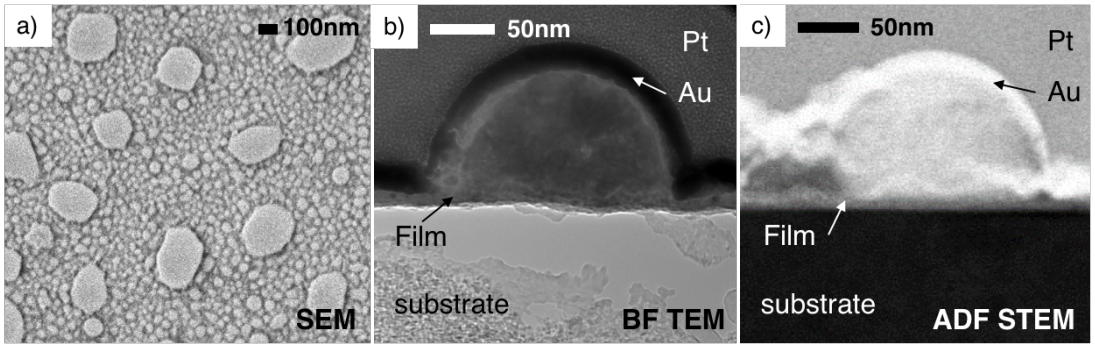

Figure 5.5: Cross-sectional images of a heavily ablated region X of a 3% Cr-doped GST film deposited on LiF substrate with a capping layer and irradiated with a fluence of 19.8mJ/cm^2. (a) SEM image of film surface; (b) Bright-field TEM and (c) high angle annular dark-field (HAADF) STEM images of cross-sectional specimens from the same region. Au and Pt protective layers were deposited during FIB cross-sectioning.

A second film that was irradiated with a lower fluence and exhibited less ablation on the surface showed a smaller decrease in film thickness (from 55nm to a minimum of 40nm at region X in Figure 5.6) and hemispherical protrusions with rougher edges. In contrast, the relatively uniform thickness of the film at the edge of region C indicates a lack of surface modification, consistent with SEM observations.

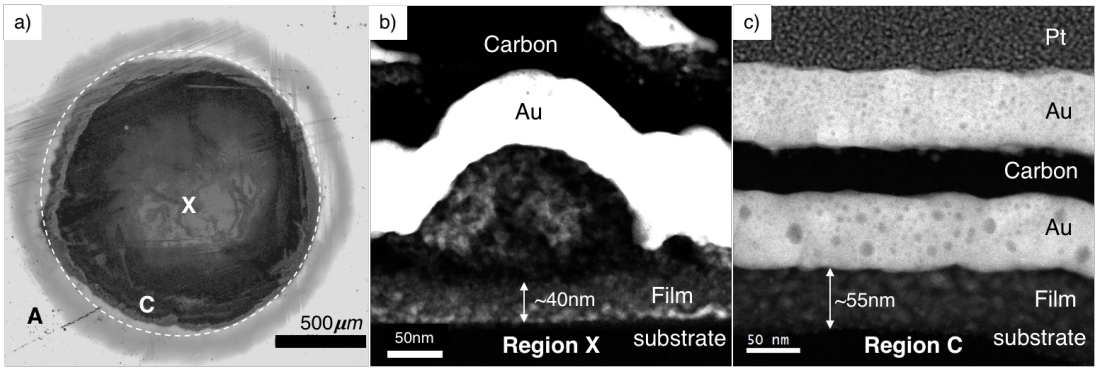

Figure 5.6: Cross-sectional images at Regions C and X of a 7% Cr-doped GST film deposited on silica substrate with a capping layer and irradiated with a fluence of 12.8 mJ/cm^2. (a) Optical image of the irradiated spot. (b) and (c) HAADF STEM images of cross-sectional samples from Region X and Region C respectively as marked in (a). C, Au and Pt protective layers were deposited during FIB cross-sectioning.

While these observations are consistent with a melting phenomenon, where spherical particles form on the molten surface due to surface tension, the laser fluence clearly influences the morphology and film thickness. By analogy with laser surface melting in metal alloys (Draper & Poate, 1985), an increase in fluence would cause an increase in depth of the surface melting, resulting in more molten material near the surface. Rapid resolidification occurs from the liquid-solid interface towards the surface on switching off the laser irradiation, leading to the formation of spherical surface structures (due to surface tension) with a remaining thinner underlying film.

Relating this phenomenon to the increase in CD signal intensity observed with an increase in laser fluence and film thickness (as discussed in Chapter 4) suggests that it is possible that these surface modifications are primarily responsible for the CD signal. However, CD spectroscopic mapping (Figure 5.7) (or imaging (CD*i*) as described in Zinna et al. (2017)) performed by Siligardi and co-workers (personal communication, 2016) at the B23 beamline revealed that the circular dichroism signal was obtained mainly from regions of the irradiated spots excluding the centre, i.e. sub-

regions B and C and an absence of or decrease in CD signal at region X. This might be due to the ablation of material at region X that results in surface features being more spread apart and correspondingly thinner film in areas without those features. Hence, region C, where the highest CD signal intensities were obtained, was considered the most promising for further comparison of irradiation with different polarisations of light.

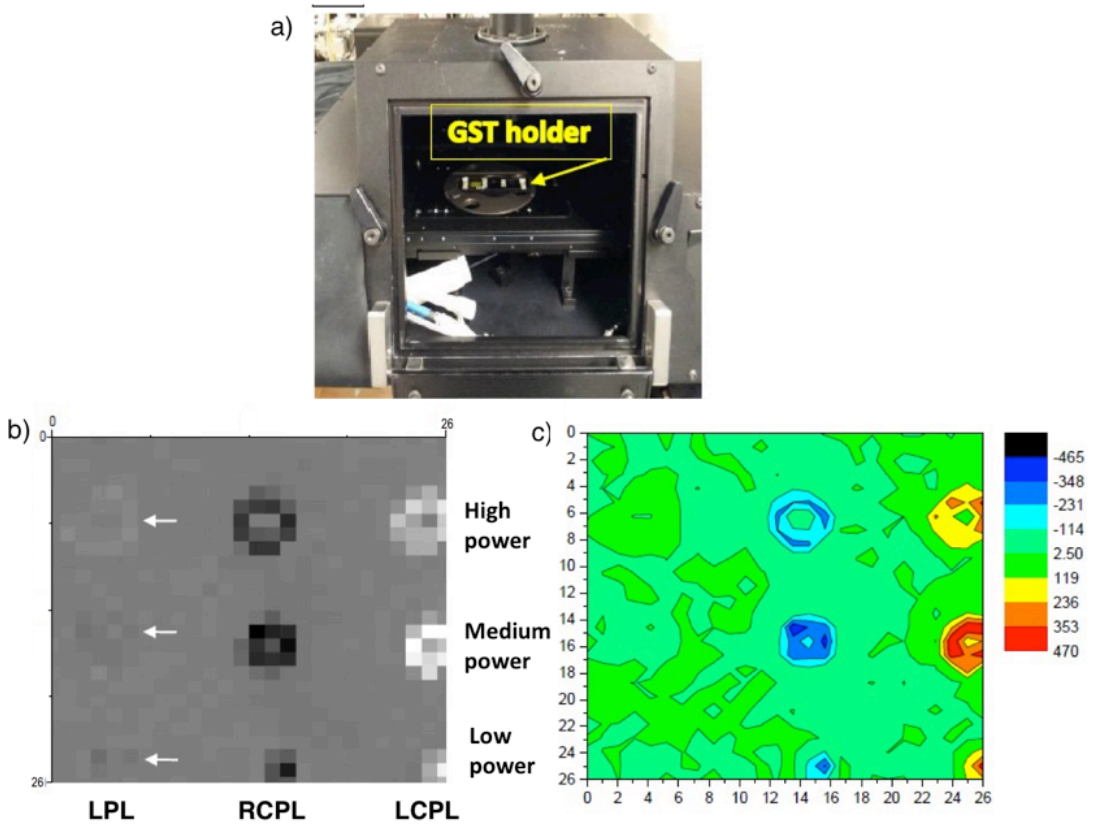

Figure 5.7: (a) Sample holder and stage in Module A at B23 where CD mapping was performed (using a 26-by-26 grid scan at 0.3mm intervals at a wavelength of 450nm) on a 35-nm thick pure GST film deposited on a LiF substrate without a capping layer. (b) Grayscale CD map showing regions of opposing chirality (negative signals in black and positive signals in white). Arrows point to film regions irradiated with linearly polarized light. (c) The same CD map shown in false colour (signal intensities represented by the colour legend).

Figure 5.8 shows cross-sectional specimens prepared from region C for various spots irradiated with a fluence of 15.5 mJ/cm^2 and at an unexposed region A. The film region that was not exposed to laser irradiation (region A) has a uniform thickness whereas the film thickness at regions C in the irradiated spots is highly irregular and uneven due to surface features similar to those observed in region X above. Although no crystalline grains are clearly visible, atomic number (Z) contrast in the STEM images shows segmentation within the surface features at region C, which may be indicative of crystallisation induced by laser irradiation.

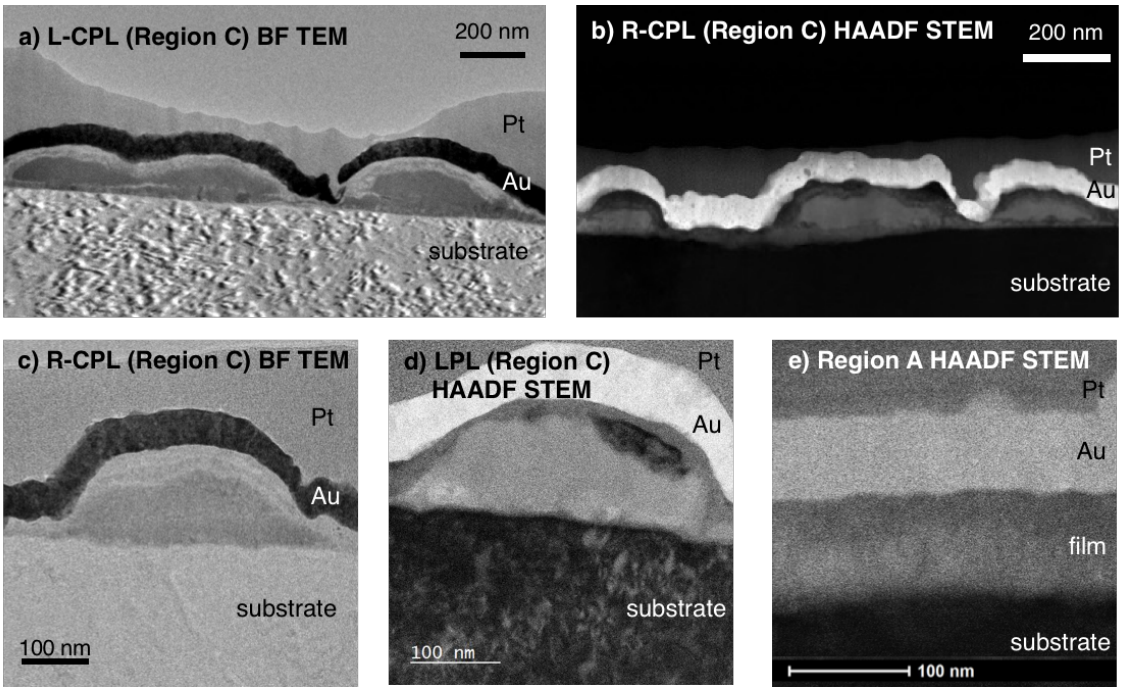

Figure 5.8: Cross-section images of different regions in a 55nm thick pure GST film deposited on LiF substrate without a capping layer and irradiated with a fluence of 15.5 mJ/cm^2. Au and Pt protective layers were deposited during FIB cross-sectioning.

5.3. Film inhomogeneity

5.3.1. Plan-view films

Before analysis of the abovementioned cross-section specimens of irradiated areas, plan-view specimens of the films before irradiation are discussed as a reference. Although as-deposited planar film specimens were amorphous over length scales of over a micron (as seen from the diffuse ring SAED patterns in Figure 5.9 (a) and (c)), occasional clusters of crystalline particles were observed, identified by the mass-thickness contrast in the BF TEM images and diffraction spots in the SAED patterns (Figure 5.9 (b) and (d)).

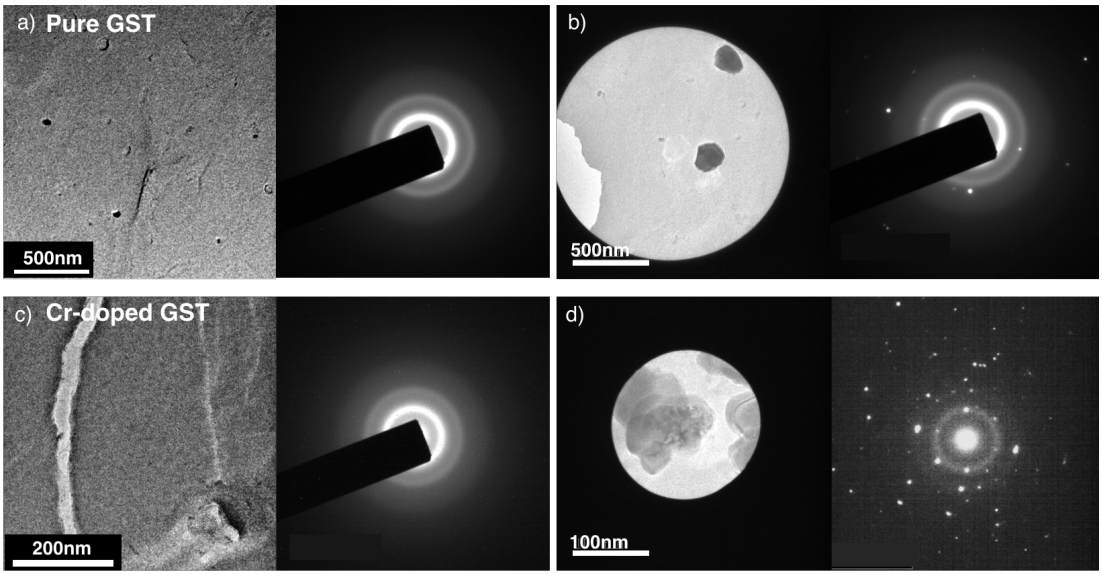

Figure 5.9: TEM BF images and corresponding selected area diffraction patterns recorded from planar specimens of 20 nm thick (a, b) pure GST and (c, d) 3% Cr-doped GST films floated from NaCl substrates. Diffraction patterns in (a), (b) and (c) were obtained with an aperture 1.6 µm in diameter, while the pattern in (d) was obtained with an aperture size of 200 nm.

Energy dispersive X-ray (EDX) spectroscopy recorded from these plan-view films in the TEM revealed that the composition of pure GST was close to that of the target (2 Ge: 2 Sb: 5 Te) used for deposition. EDX line scan analyses from films across

irradiated regions (before cross-sectioning) in the SEM confirmed these measurements (Table 5.1). The ability to resolve the Cr signal by EDX spectroscopy, as opposed to X-ray photoelectron spectroscopy (XPS) where strong overlap of Cr2p and Te3d peaks caused difficulties in quantification (Figure 5.10), allowed a comparison of the compositions of the doped films.

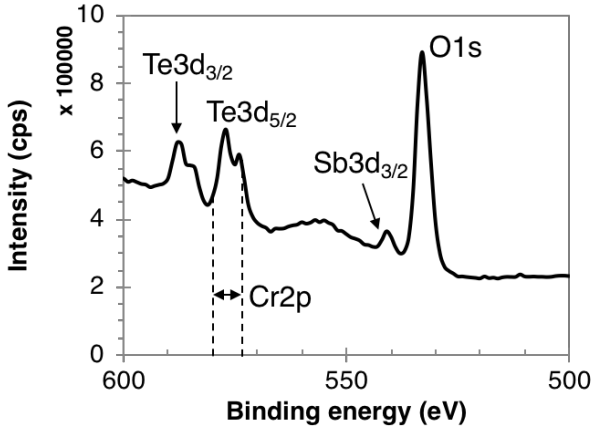

Figure 5.10: Example of an XPS spectrum which shows direct overlap of Te3d and Cr2p peak regions, causing difficulties in the observation and quantification of the Cr signal.

Table 5.1
Average compositions of pure and Cr-doped GST films measured by EDX spectroscopy in the SEM and TEM.

Element	Average Composition (Atomic %)		
	Pure GST	**3% Cr-GST**	**7% Cr-GST**
Ge	28.0 ± 0.5	27.0 ± 0.5	18.0 ± 0.5
Sb	19.0 ± 0.5	22.0 ± 0.5	21.0 ± 0.5
Te	53.0 ± 0.5	48.0 ± 0.5	54.0 ± 0.5
Cr	–	3.0 ± 1.5	7.0 ± 1.5

It is important to note that since EDX quantification was performed without the use of calibration standards, uncontrolled experimental deviations between the specimen and the default standard library in the acquisition software (such as electron probe current and specimen thickness) as well as the presence of native surface

oxidation can lead to inaccuracy in the signal quantification. However, the spread in measurements is reported as experimental error in Table 5.1 and subsequent EDX quantification results.

5.3.2. Cross-sectional specimens

EDX mapping of cross-sectional film specimens showed a relatively homogeneous distribution of the constituent elements in regions without surface modification (Figure 5.11) whereas the surface features exhibited elemental segregation (Figure 5.12). Regions within the hemispherical surface feature were rich in Sb and Te while Ge and Cr were in excess in the underlying thinned film.

Elemental atomic percentages at regions X and B in the 7% Cr-doped GST film (as in Figure 5.6) from these EDX analyses (summarised in Table 5.2) show a similar composition of the film at region B and the underlying film at region X. Simultaneous EELS spectrum image acquisition (Figure 5.13) from the same region as in Figure 5.12 gave similar relative compositions as the EDX results, although overlapping elemental edges posed challenges in the signal quantification.

For example, the overlap of Sb ($M_{4,5}$-edge at 528eV with a delayed maximum) and O (K-edge at 532eV) edges resulted in difficulties in distinguishing the respective signals and led to less accurate quantification. The white lines observed at the Cr-$L_{2,3}$ edges (575eV and 584eV) also caused difficulties while defining the background and signal windows at the Te-$M_{4,5}$ edges (572eV), resulting in lower accuracy in quantification of the Te signal. The Te-M_3 edge (819eV) could be used for quantification instead but this minor edge was less intense and less visible than the major $M_{4,5}$ edges.

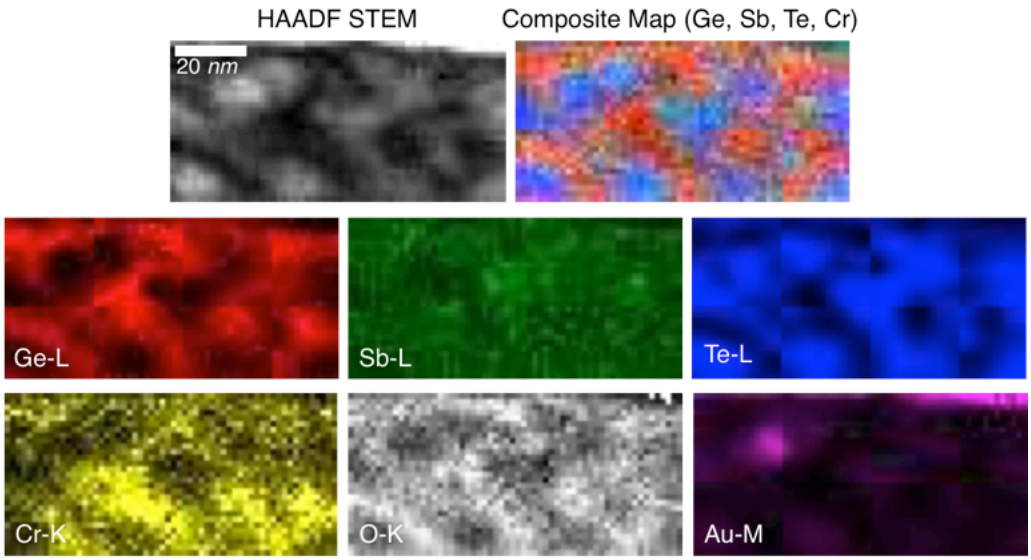

Figure 5.11: Coloured EDX elemental distribution (signal integral) maps and a composite image of cross-sectional specimen from region B of a 7% Cr-doped GST film, corresponding to Figure 5.6(c).

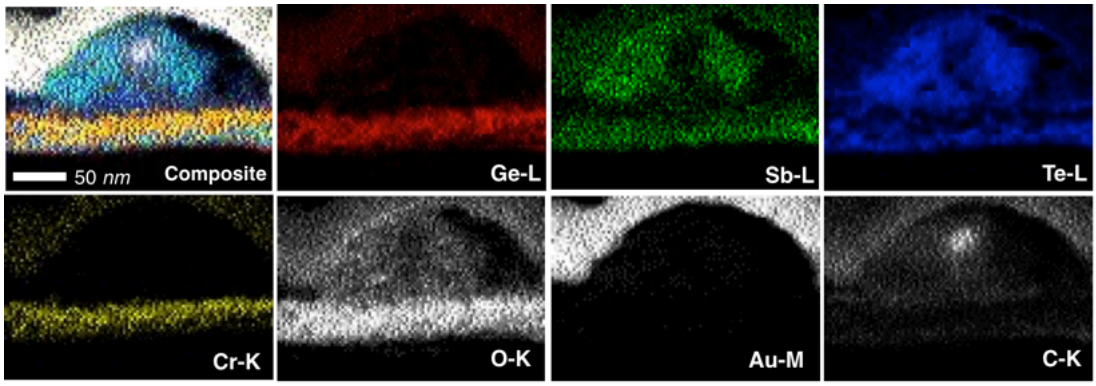

Figure 5.12: Coloured EDX elemental distribution (signal integral) maps and a composite image of cross-sectional specimen from region X of a 7% Cr-doped GST film, corresponding to Figure 5.6(b).

Table 5.2
Elemental atomic percentages quantified from EDX spectrum acquisitions at region B and within the hemispherical surface feature and the underlying film at region X of a 7% Cr-doped GST film (as in Figure 5.12).

Element	Average Composition (Atomic %)		
	Region B	Region X	
		Within hemisphere	Underlying film
Ge	14.0 ± 0.5	–	19.0 ± 0.5
Sb	28.0 ± 0.5	19.5 ± 0.5	21.0 ± 0.5
Te	50.0 ± 0.5	80.5 ± 0.5	52.0 ± 0.5
Cr	8.0 ± 0.5	–	8.0 ± 0.5

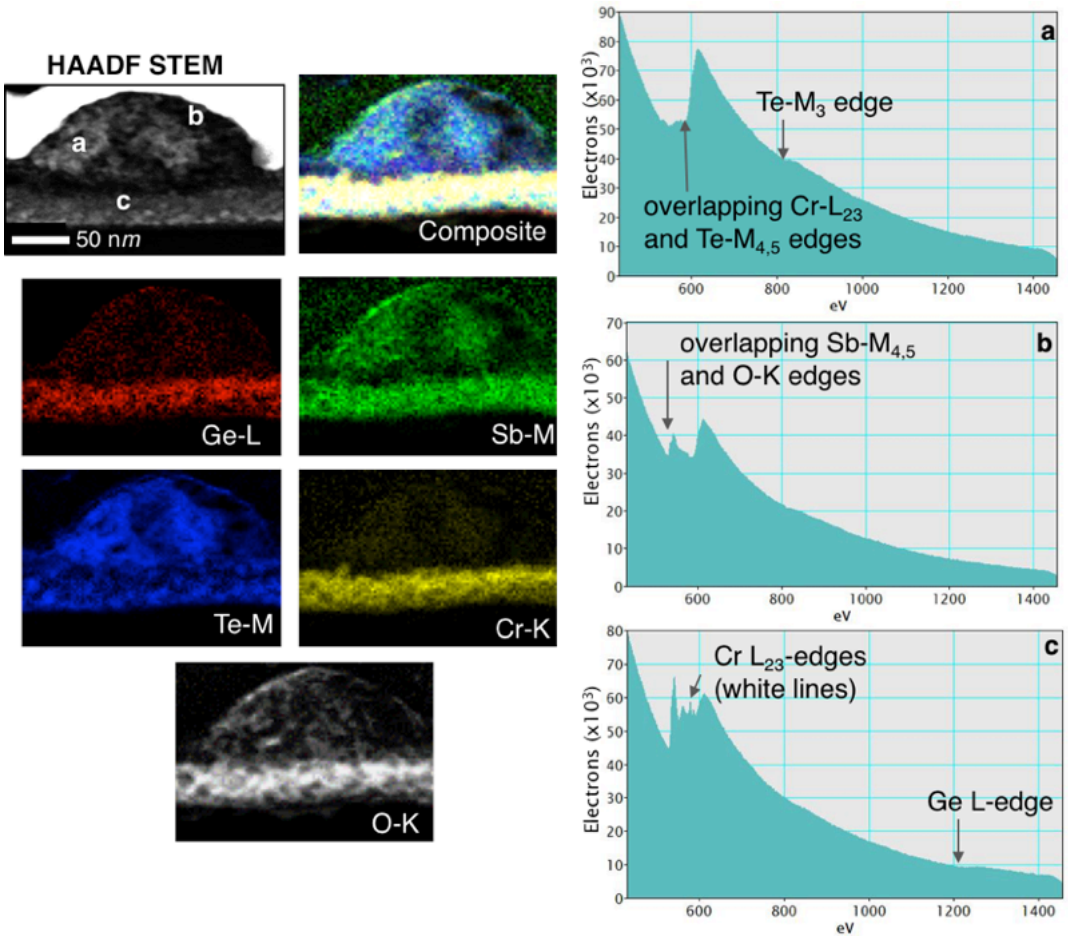

Figure 5.13: Coloured EELS elemental distribution (signal integral) maps and high core-loss spectra extracted from selected areas (a, b and c) within the hemispherical surface feature in region X of a 7% Cr-doped GST film, as identified in the HAADF STEM image (corresponding to Figure 5.6(b)).

Despite these difficulties, the EELS elemental maps correlate well with the EDX maps, confirming the inhomogeneity of the modified films after laser irradiation. The coincident positions of Cr and Ge signals suggest that Cr dopants may occupy positions in the Ge/Sb sub-lattice, as predicted from simulated models by Skelton & Elliot (2013).

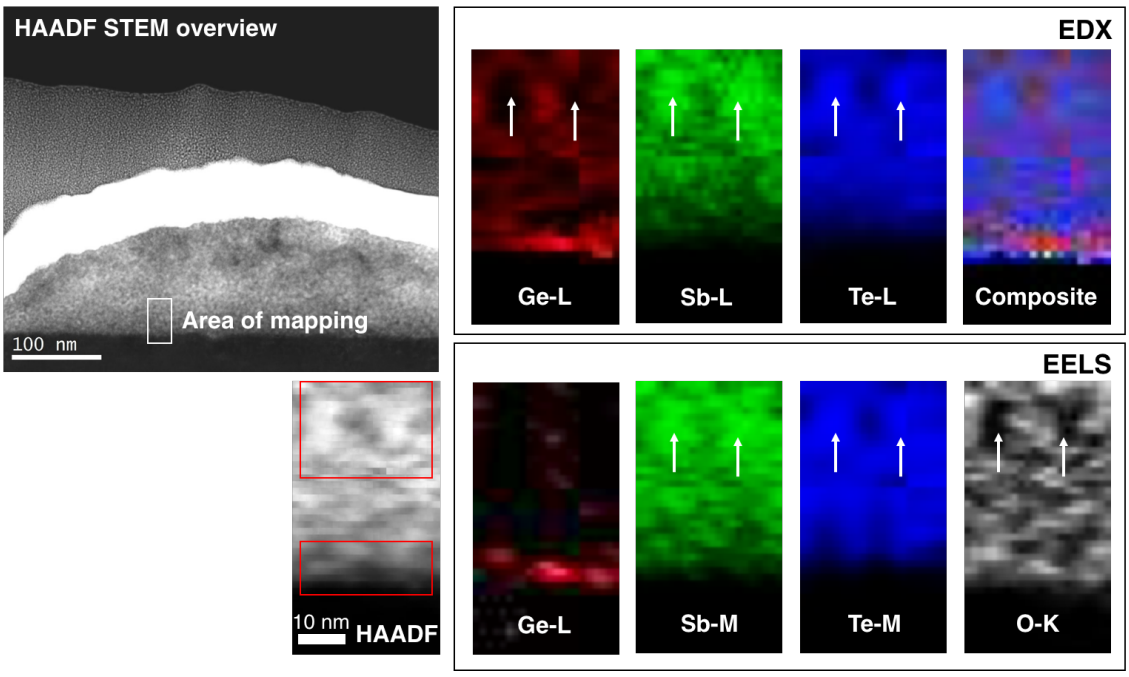

Figure 5.14: EDX and EELS elemental maps and corresponding HAADF STEM images of a cross-sectional specimen at region C of a pure GST film irradiated with L-CPL and a fluence of 15.5mJ/cm^2. White arrows in the maps indicate regions with corresponding high Sb/Te and low Ge/O signals.

Table 5.3
Elemental atomic percentages quantified from EDX and EELS map acquisitions at different sub-regions indicated by the rectangles in the HAADF image shown in Figure 5.14.

Element	Average Composition (Atomic %)		
	EDX	EELS	
		Top half	Bottom edge
Ge	14.5 ± 0.5	-	9.0 ± 0.5
Sb	24.0 ± 0.5	29.0 ± 0.5	43.0 ± 0.5
Te	61.5 ± 0.5	71.0 ± 0.5	48.0 ± 0.5

EDX and EELS compositional analysis of cross-sectional specimens prepared from region C of an irradiated pure GST film (as in Figure 5.8) showed similar results within the hemispherical surface features, although there seemed to be no separate underlying film. Figure 5.14 shows elemental maps obtained from simultaneous EDX and EELS acquisition at one such specimen at region C. The results suggest that the Ge concentration is higher at the substrate interface. Regions with high signal intensities of Sb/Te also seem to correlate to regions with low Ge/O signals, indicating elemental segregation. The average composition at different regions within the analysed area is summarised in Table 5.3.

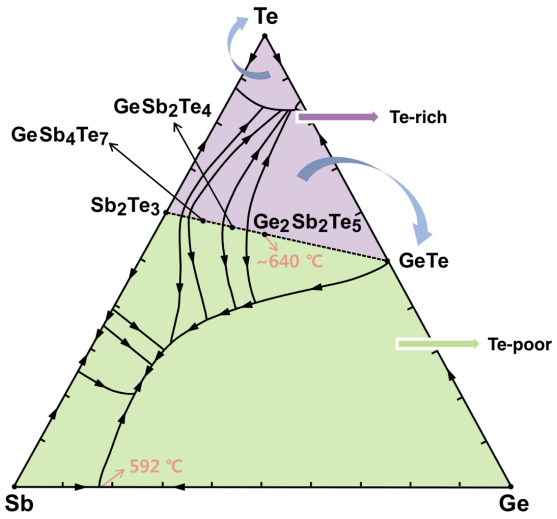

Figure 5.15: The ternary phase diagram of the Ge-Sb-Te liquidus surface (modified from Kang et al. (2009)).

Thermally induced atomic diffusion has been observed in electrically stressed GST devices due to multiple driving forces including electro-migration and thermo-migration (Kang et al., 2009; Yang, Cho, Park, & Joo, 2013; Yang, Park, Kim, & Joo, 2009), resulting in phase separation in the molten state. While Kang et al. (2009) reasoned that GeTe precipitation was most likely to occur if the cooling of molten $Ge_2Sb_2Te_5$ material were to follow a path of thermodynamic equilibrium (based on the

phase diagram of the liquidus surface in the Ge-Sb-Te ternary system (Figure 5.15)), the migration of Te and formation of a Ge/Sb-rich phase has been observed at opposing electrodes (Yang et al., 2009).

However, the influence of the electric field under CPL irradiation is not easily discerned given the constant rotation of the electric field vector in a circularly polarised plane wave. Instead, the observed elemental segregation (in Figure 5.14) may be due to crystallisation-induced or solidification-induced segregation (Debunne et al., 2011) that occurs when different phases solidify at different temperatures.

In contrast to the abovementioned GeTe precipitation or Ge/Sb-rich phase separation, the correlation of the Sb and Te signals implies separation of a Sb/Te-rich phase within the surface features. Further analysis of other areas in the lamella confirm the presence of Ge in the periphery of this Sb/Te-rich phase (Figure 5.16). In addition, since no lattice fringes indicating crystallinity were observed in high resolution STEM images of the irradiated film (Figure 5.17), X-ray and electron diffraction studies were carried out to characterise the phase of these regions.

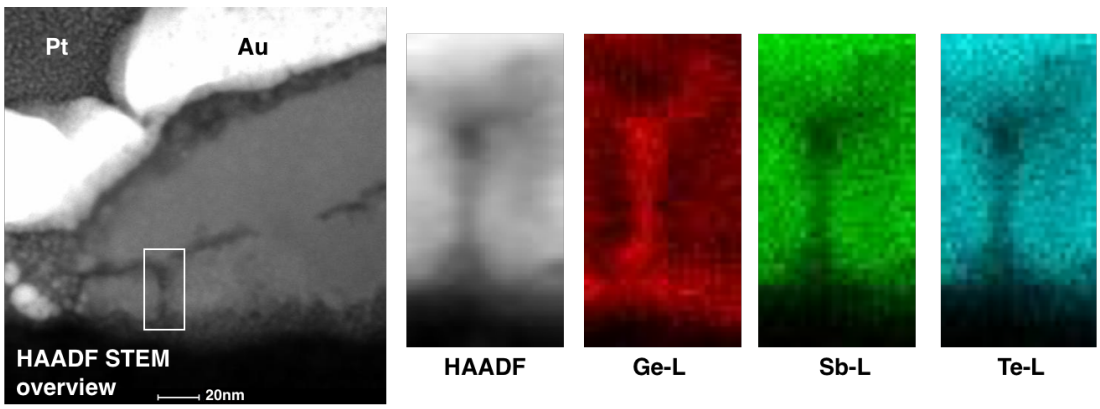

Figure 5.16: Elemental maps of integrated EDX signal intensities of a region in the same irradiated pure GST specimen lamella.

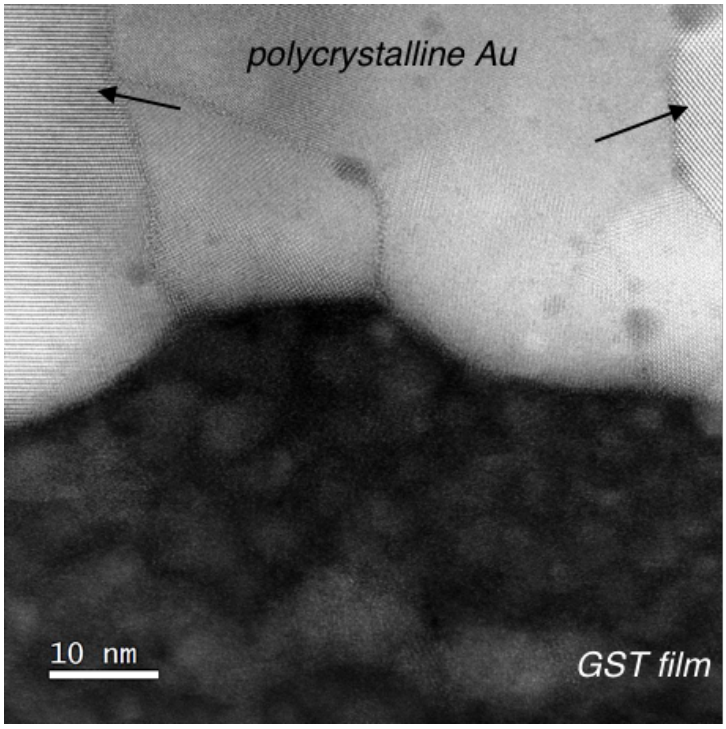

Figure 5.17: No lattice fringes indicating crystallinity were observed in high resolution HAADF STEM images of irradiated GST film regions.

5.4. X-ray diffraction studies

X-ray diffraction patterns recorded from various regions of 60nm thick pure GST thin films deposited on polycrystalline sapphire (Al_2O_3) and amorphous silica (SiO_2) substrates were azimuthally averaged into one-dimensional spectra (Figure 5.18) for comparison. These spectra were referenced against entries of similar materials in a XRD database calibrated to the experimental incident X-ray wavelength (λ = 0.493Å).

Figure 5.19 shows some differences between the azimuthally averaged profiles of the diffraction patterns obtained from different film regions and the exposed Al_2O_3 substrate. Apart from peaks corresponding to those of the Al_2O_3 substrate (sharp diffraction peaks at 16.2º and 23.9º and a smaller peak at 26.3º) (Swanson & Fuyat, 1953), deviations (less intense broad peaks) in the spectra were also observed close to

the *d*-spacings of the cubic (c-GST) and hexagonal (h-GST) phases of GST (Nonaka, Ohbayashi, Toriumi, Mori, & Hashimoto, 2000; Petrov et al., 1968).

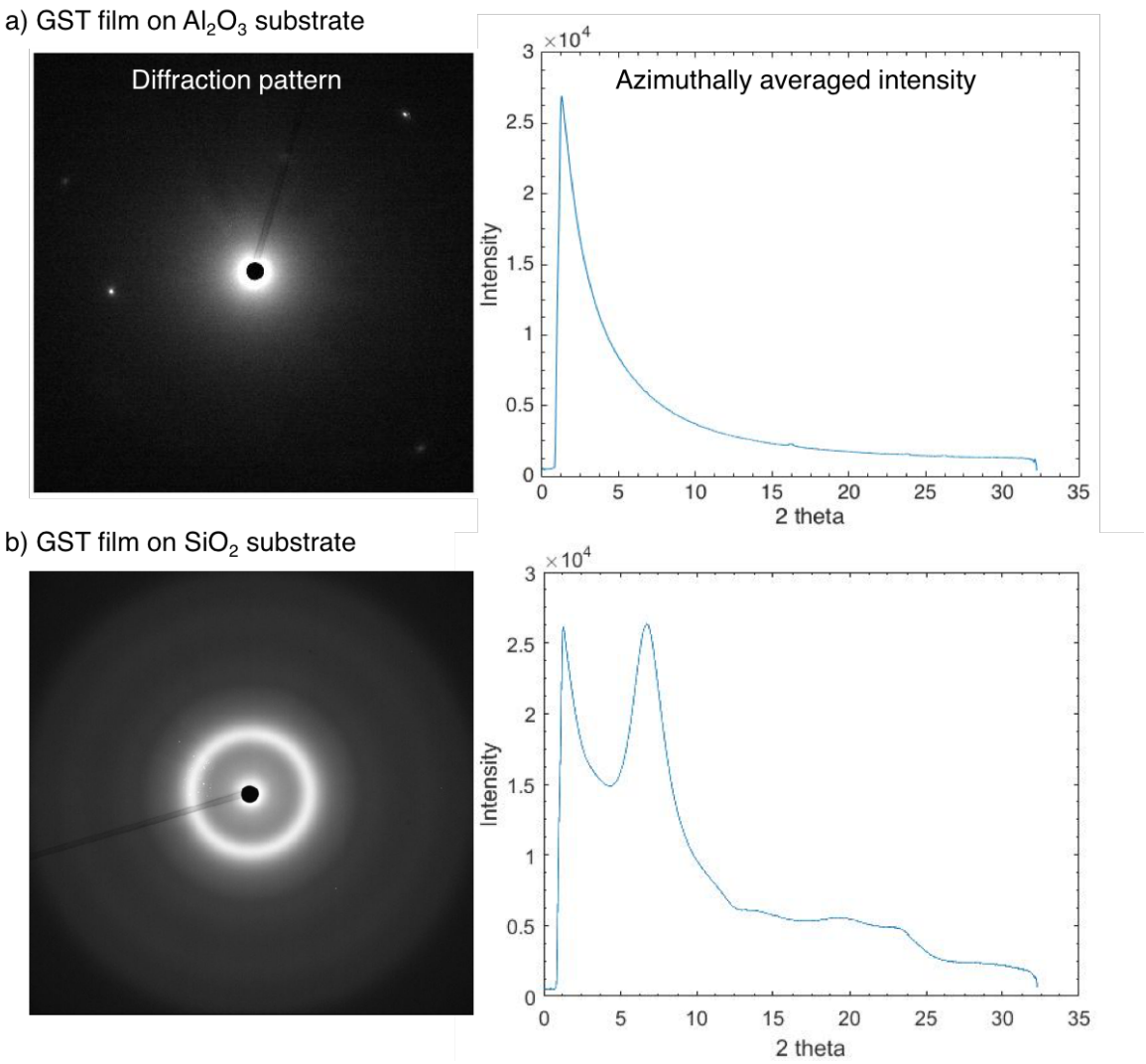

Figure 5.18: X-ray diffraction patterns recorded to a diffraction angle of 2theta (2θ) =32°, or q = ~ 7Å^{-1}, and the one-dimensional azimuthally averaged intensity spectra from GST films deposited on a) Al_2O_3 and b) SiO_2 substrates.

There is some uncertainty in attributing these broad peaks to either crystalline GST phase due to peak position mismatches between the experimental data and the abovementioned literature and their close proximity to the reference peaks of the substrate. For example, the broad peak at approximately 9.3º is close to the reported values of 9.24º and 9.40º for hexagonal and cubic GST phases respectively, where both

values are within the experimental error (spread of data) of ±0.1º. Similarly, the splitting of the peak around 24º could be attributed to the substrate (23.9º), h-GST (24.0º – 24.2º) or c-GST (24.6º).

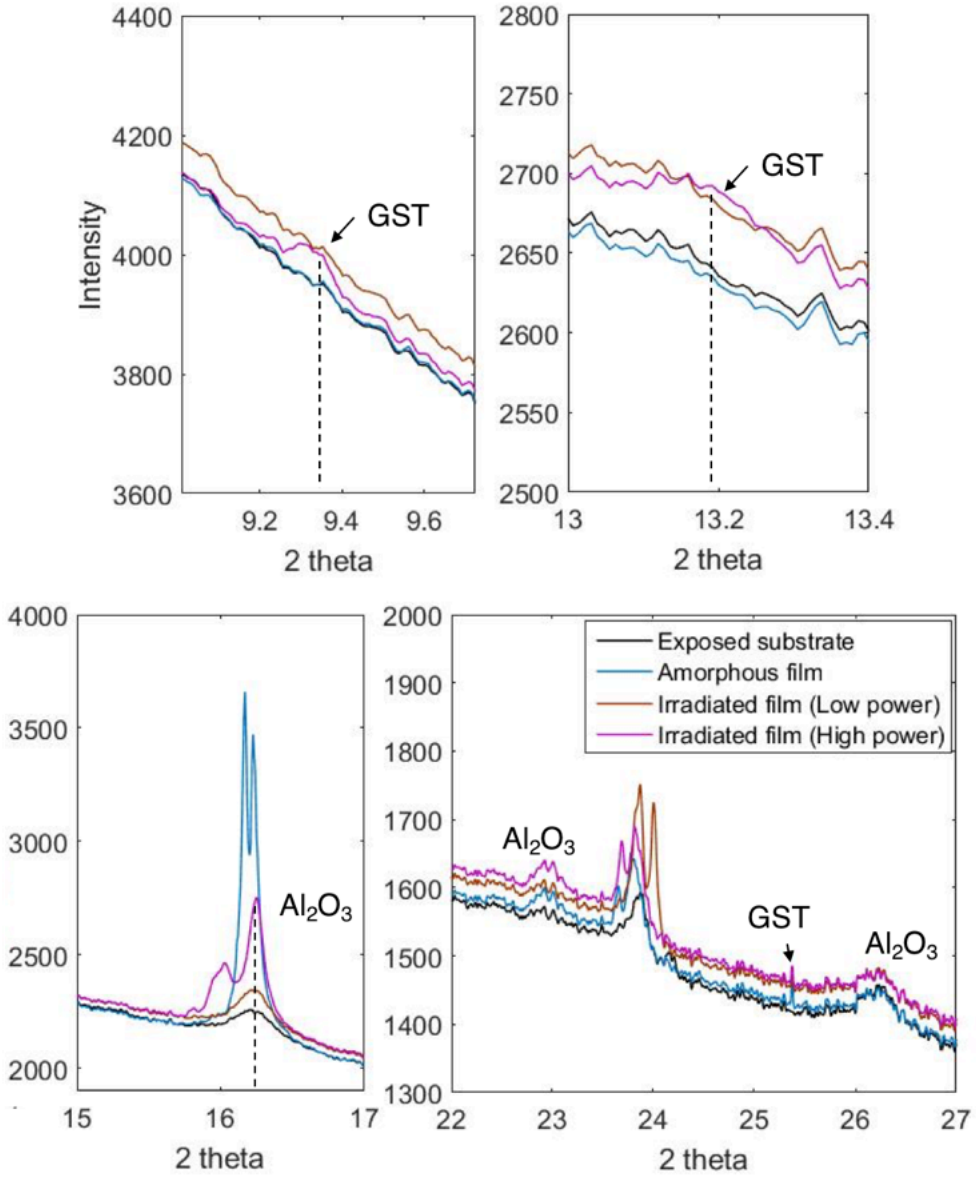

Figure 5.19: Differences in azimuthally averaged X-ray diffraction spectra obtained from different regions on the GST film deposited on a sapphire substrate showing possible crystalline GST peaks.

A summary of experimental peaks matched to the closest reference peaks and possible phase attributions is given in Appendix D.

The lack of concentric circles in the diffraction patterns suggests insufficient numbers of randomly orientated crystallites for good statistics. Thin films are susceptible to preferred orientation effects, especially due to the parallel incident beam used in transmission geometry, where certain diffraction peaks do not show up in the spectra. Although there is a possibility of epitaxial film growth leading to the thin film orientation mirroring that of the substrate, the lower intensity of the broad peaks as compared to the pronounced substrate peaks signify insufficient film thickness, leading to scattering and diffraction mostly by the bulk of the substrate. Peak broadening of these low intensity spectral features may also indicate smaller crystallite sizes relative to the bulk substrate.

5.5. Electron diffraction studies

Electron diffraction analysis was performed on the set of irradiated regions that produced the highest CD signal intensities; in region C of a 55nm thick pure GST film deposited on LiF substrate without a capping layer and irradiated with 15.5mJ/cm^2 fluence (cross-sectional specimen images of which are shown in Figure 5.8). Diffraction patterns were recorded from these specimens under quasi-parallel probe conditions in STEM mode in the Titan (as described in Chapter 3).

Figure 5.20 shows examples of diffraction patterns recorded at two regions within the modified surface features distinguished from their contrast. The diffraction patterns in (a) and (c) are amorphous while those in (b) and (d) are amorphous with crystalline speckles. Multiple patterns recorded from each of these two areas were averaged and the azimuthally averaged intensity spectra used for RDF analysis. This procedure was repeated at several areas in each specimen from region C of spots

irradiated with L-CPL and R-CPL, and the results are presented in the following section 5.6.

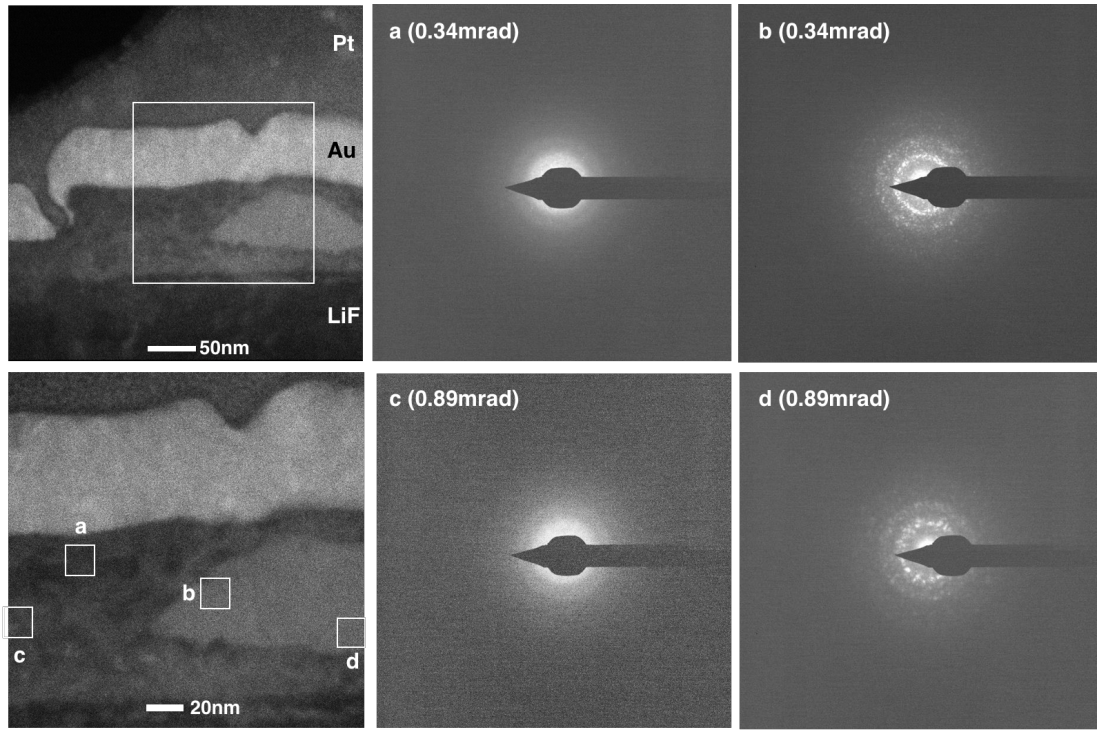

Figure 5.20: HAADF STEM images of a section of the lamella prepared from region C of a pure GST film irradiated with R-CPL and a fluence of 15.5mJ/cm^2 and diffraction patterns recorded using near-parallel probe conditions ((a) and (b) with convergence semi-angle of 0.34mrad, and (c) and (d) with 0.89mrad and estimated probe sizes of <10nm and 4-5nm respectively) from areas indicated in the HAADF STEM images.

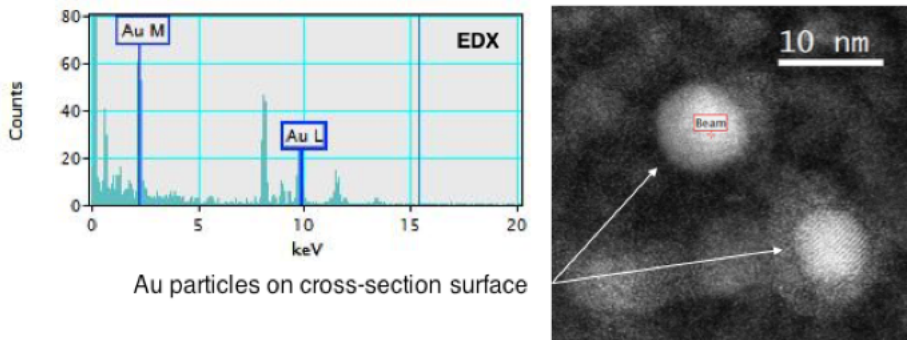

Figure 5.21: Gold particles on the surface of the GST film cross-section, just below the gold capping layer.

Gold particles were found on the cross-sectioned film surface, just below the protective capping layer, as an artefact of FIB milling. Despite the low spatial

resolution of the near-parallel probes, these particles could be distinguished by their brighter scattered intensity in STEM images (and confirmed by EDX compositional analysis (Figure 5.21)). Gold capping layers from deeper within the lamellae also interfered with the analysis of material close to the substrate interface or edges of the surface features. As such, these regions were avoided during the acquisition of diffraction data.

Other diffraction data collected from the cross-sectional specimens of the spot irradiated with L-PL and the amorphous region of the film were unusable due to oxidation and damage of the lamellae before microscopy analysis. Therefore, reference diffraction data was also recorded from the planar amorphous GST films using selected area diffraction (SAED), TEM nanobeam diffraction (NBD) and quasi-parallel probe diffraction in STEM mode.

5.6. RDF Analysis

Reduced density functions (RDF) were extracted from the azimuthally averaged intensity of the recorded electron diffraction patterns using *eRDF Analyser* (Shanmugam et al., 2017). As described in Chapter 3 (Section 3.8), the atomic scattering background ($I(\boldsymbol{q})_{fitted}$) was initially fitted to the azimuthally averaged experimental scattered intensity ($I(\boldsymbol{q})_{experimental}$) using an automated fit function. This was followed by manual adjustments of the various fitting parameters to obtain better fitting through the lower angle oscillations and at higher scattering angles as well as the oscillation of the reduced intensity function $\varphi(\boldsymbol{q})$ about zero, and to minimise the unphysical peaks (below 1Å or the first known bond length) in the RDF $G(\boldsymbol{r})$. The scattering vector ($\boldsymbol{q}$) was calibrated using diffraction data recorded from

polycrystalline aluminium films or gold layers in the cross-sectional specimens under the same beam conditions as for the GST specimens.

5.6.1. Selected area diffraction

RDFs extracted from selected area diffraction data recorded from 20nm thick amorphous GST and 3% Cr-doped GST films using an aperture of 700nm diameter are shown in Figure 5.22. The positions of peaks $\boldsymbol{r}_1$, $\boldsymbol{r}_2$ and $\boldsymbol{r}_3$, describing average interatomic distances between nearest neighbours, next-nearest neighbours and beyond are also summarised in Table 5.4. The experimental error in RDF peak positions results from errors in the determination of the centre of the diffraction patterns during azimuthal averaging (deviation of ±2 pixels due to ellipticity), which contributes to errors in the calibration of the scattering vector ($d\boldsymbol{s} = \pm 10^{-6}$ Å^{-1}/pixel), as well as errors in the fitting of the atomic scattering background.

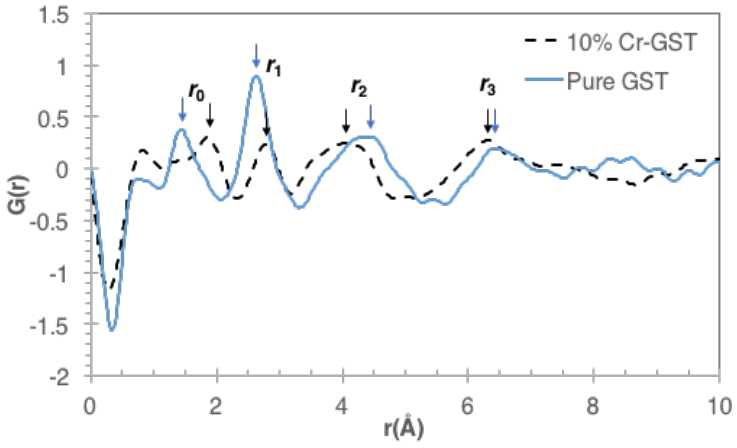

Figure 5.22: RDF curves obtained for 20nm thick amorphous GST (in black) and 3% Cr-doped GST films (in dashed blue) from SAED data recorded using an aperture of 700nm in diameter.

Table 5.4
RDF peak positions from SAED data of 20nm thick amorphous GST and 3% Cr-doped GST films (as in Figure 5.22).

Film	Peak positions (Å)		
	r_1	r_2	r_3
Pure GST	2.63 ± 0.02	4.43 ± 0.04	6.48 ± 0.04
3% Cr-GST	2.79 ± 0.02	4.02 ± 0.04	6.31 ± 0.04

Since these films were floated off in water, the r_0 peaks (< 2Å) observed could be due to native surface oxidation. Although efforts were taken to reduce beam damage by using low beam current (< 1pA) and acquiring over shorter durations to reduce carbon build-up and surface contamination while ensuring sufficient scattering intensity at higher scattering angles (q), beam-induced changes in the local order in the film cannot be excluded. In addition to pre-existing crystallites in the film (as observed using TEM imaging), a combination of beam-induced modification, surface contamination and native oxidation may be responsible for the deviations of the observed r_1, r_2 and r_3 values for pure GST from those reported in the literature (2.68Å, 4.01Å and 6.20Å in Borisenko, Chen, Song, Nguyen-Manh, & Cockayne (2009); 2.67Å, 4.14Å and 6.66Å in Park et al. (2007); ~2.7Å, ~4.2Å, ~6.3Å in Lang, Song, Nguyen-Manh, & Cockayne (2007)).

The r_1 peak in Cr-GST is shifted to a longer interatomic distance than in pure GST while r_2 and r_3 are shifted to shorter distances. This suggests longer dominant bonds between nearest neighbour atoms and a different local geometry due to the Cr dopant. There is no literature on Cr-doped GST RDF available for comparison with the present experimental data, but analysis of the refined DFT structural models may provide some insight into the differences between the local geometries of pure and doped GST material.

Figure 5.23 shows RDF curves extracted from SAED data recorded from another 20nm amorphous GST film where a region of the film was intentionally crystallised under prolonged and intense electron beam exposure (Figure 5.24), with the peak positions summarised in Table 5.5. Differences between this data and the earlier amorphous one shown in Figure 5.22 show the variation in short range order in the deposited films upon phase transformation. An additional peak at ~5.3Å ($\boldsymbol{r}_c$) and peak splitting of the $\boldsymbol{r}_3$ peak is seen in crystalline GST. The first three peak positions ($\boldsymbol{r}_1$, $\boldsymbol{r}_2$ and $\boldsymbol{r}_c$) of the beam-crystallised region are close to those of an ideal NaCl-type crystal (with lattice constant $\boldsymbol{a}$ = 6.02Å, following calculations similar to those by Ruan, Murooka, Raman, & Murdick (2007)). The first three interatomic distances corresponding to edge, face diagonal and solid diagonal distances in the ideal crystalline cubic lattice are included in the figure.

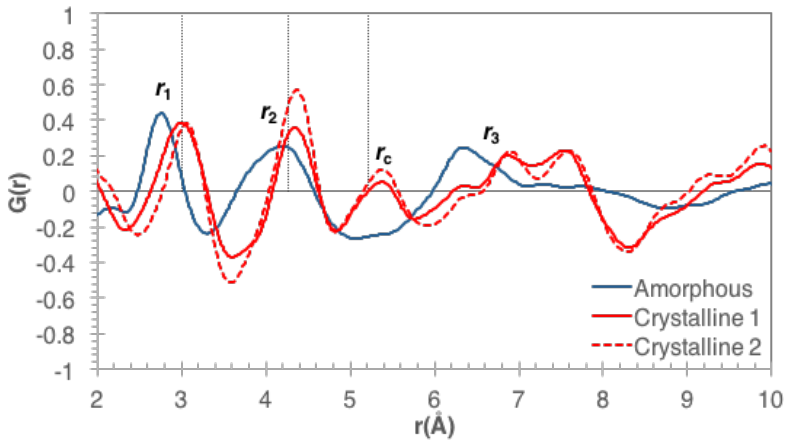

Figure 5.23: RDF curves obtained from SAED data of a 20nm thick amorphous GST film (in dark blue) and a region crystallised under the electron beam (in red). Vertical lines represent the first three interatomic distances (at 3.01Å, 4.26Å and 5.21Å) in an ideal NaCl crystal with lattice constant 6.02Å.

Table 5.5
RDF peak positions measured from SAED data of a 20nm thick amorphous GST film and beam-induced crystalline regions (as in Figure 5.23).

Data	Aperture size (Ø)	Peak positions (Å)			
		r_1 (± 0.02)	r_2 (± 0.04)	r_c (± 0.04)	r_3 (± 0.04)
Amorphous	1.6µm	2.75	4.20	-	6.35
Crystalline 1	1.6µm	2.99	4.34	5.37	6.87 / 7.54
Crystalline 2	200nm	3.06	4.37	5.38	6.89 / 7.59

Diffraction data was acquired from the crystalline region using two different apertures of 1.6µm ('Crystalline 1') and 200nm ('Crystalline 2') in diameter. The lack of complete rings in the diffraction pattern acquired from the 'Crystalline 2' region signifies an insufficient number of crystallites for good particle statistics as compared to data averaged over a larger area ('Crystalline 1') with more randomly orientated crystallites (Figure 5.24). A shift in the RDF peak positions to slightly longer interatomic distances at the 'Crystalline 2' region (Table 5.5) also implies a different local order.

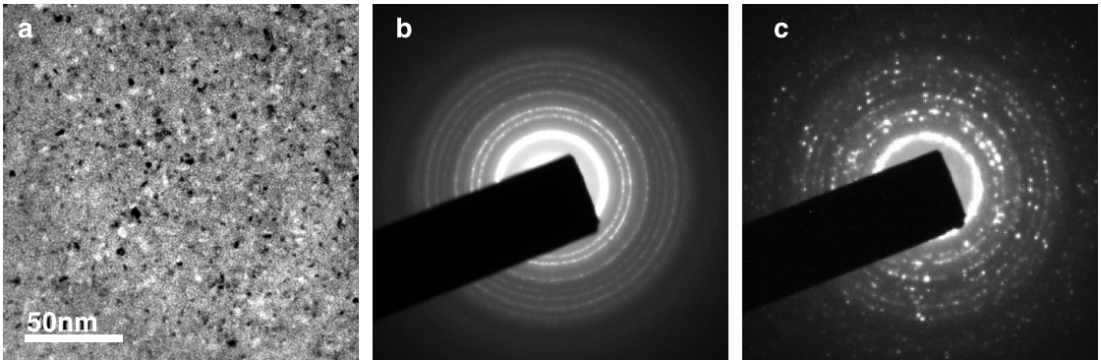

Figure 5.24: a) Region of GST film crystallised under the electron beam and diffraction patterns of the region acquired with a selected area aperture of b) 1.6µm and c) 200nm in diameter.

5.6.2. Nanobeam and quasi-parallel probe diffraction

Amorphous GST

RDFs extracted from TEM nanobeam diffraction (NBD in both microprobe (μP) and nanoprobe (nP) modes) and quasi-parallel STEM probe diffraction data recorded from a 20nm thick amorphous GST film are shown in Figure 5.25. The estimated beam sizes and the RDF peak positions are also summarised in Table 5.6.

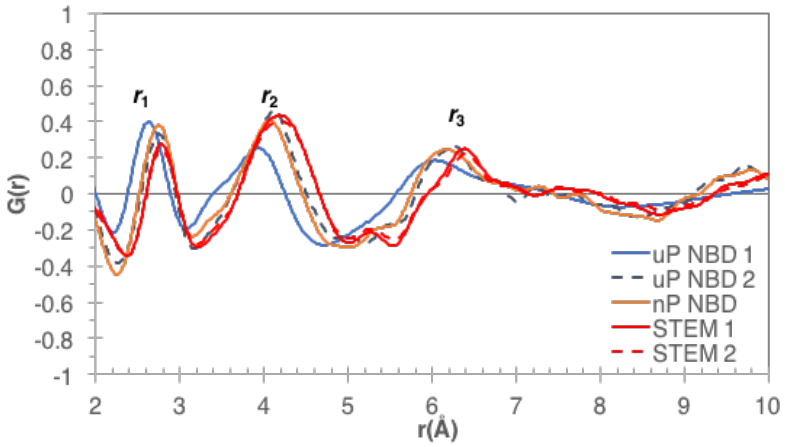

Figure 5.25: RDF curves obtained from TEM (μP and nP) NBD and quasi-parallel STEM diffraction data of a 20nm thick amorphous GST film.

Table 5.6
RDF peak positions for various diffraction data of a 20nm thick amorphous GST film (as in Figure 5.25).

RDF curve	Estimated beam size (Ø)	Peak positions (Å)		
		r_1 (± 0.02)	r_2 (± 0.04)	r_3 (± 0.04)
μP NBD 1	1.3μm	2.63	3.93	6.17
μP NBD 2	< 90nm	2.75	4.12	6.25
nP NBD	< 50nm	2.75	4.08	6.17
STEM 1	< 10nm	2.78	4.19	6.38
STEM 2	4-5nm	2.79	4.12	6.41

Note: NBD data are obtained in parallel TEM mode while STEM data are obtained from a summation of 10 acquisitions each with convergence angles of 0.34mrad (STEM 1) and 0.89mrad (STEM 2).

Only data up to $\boldsymbol{q}$ = 12.2Å^{-1} was used in order to obtain the best fit to the experimental scattering data from 'μP NBD 1', which could have led to increased truncation effects, evident from the smoother RDF curve and peaks compared to the other curves for which data up to $\boldsymbol{q}$ = 15.5Å^{-1} were used in the fitting.

However, the difference in quasi-parallel STEM probe sizes seems to have a negligible effect on the positions of the RDF peaks of diffraction data obtained at convergence semi-angles of 0.34mrad ('STEM 1' with estimated probe size of < 10nm) and 0.89mrad ('STEM 2' with estimated probe size of 4-5nm). Due to the low scattering intensity, even with exposure durations of up to a minute, data was summed over 10 or more acquisitions (over an estimated square area of 300nm by 300nm) by positioning the beam at fresh locations without overlap and avoiding the surrounding radius of surface contamination at previous positions.

Irradiated GST regions

Since μP and nP TEM diffraction data still had contributions from the substrate and protective capping layers, only quasi-parallel STEM probe diffraction data were used in the analysis of irradiated GST regions with hemispherical surface features (at region C). Given the variation in composition within these features, the atomic scattering intensity background ($I(\boldsymbol{q})_{fitted}$) was fitted to the azimuthally averaged experimental diffraction data ($I(\boldsymbol{q})_{experimental}$) using relative Ge:Sb:Te atomic compositions of 2:2:5 and 0:2:5 (corresponding to atomic fractions p_i in Equation 3.7).

As described in Chapter 3 (Section 3.8), the difference in intensity between the two curves gives rise to oscillations in the reduced intensity function or structure factor ($\varphi(\boldsymbol{q})$), such that minor differences in fitting due to the different atomic fractions only

result in a marginal change in peak heights but not the peak positions in the RDF curve. Multiple and inelastic scattering may also affect the scattering intensity background fitting and the RDF peak positions. While the absolute peak heights are useful for the quantification of atomic coordination (which requires analysis of partial distribution functions such as Ge-Te or Sb-Te pairs), this work is more concerned with changes in the overall RDF peak positions. Hence, the atomic composition $Ge_2Sb_2Te_5$ was used for all subsequent analyses.

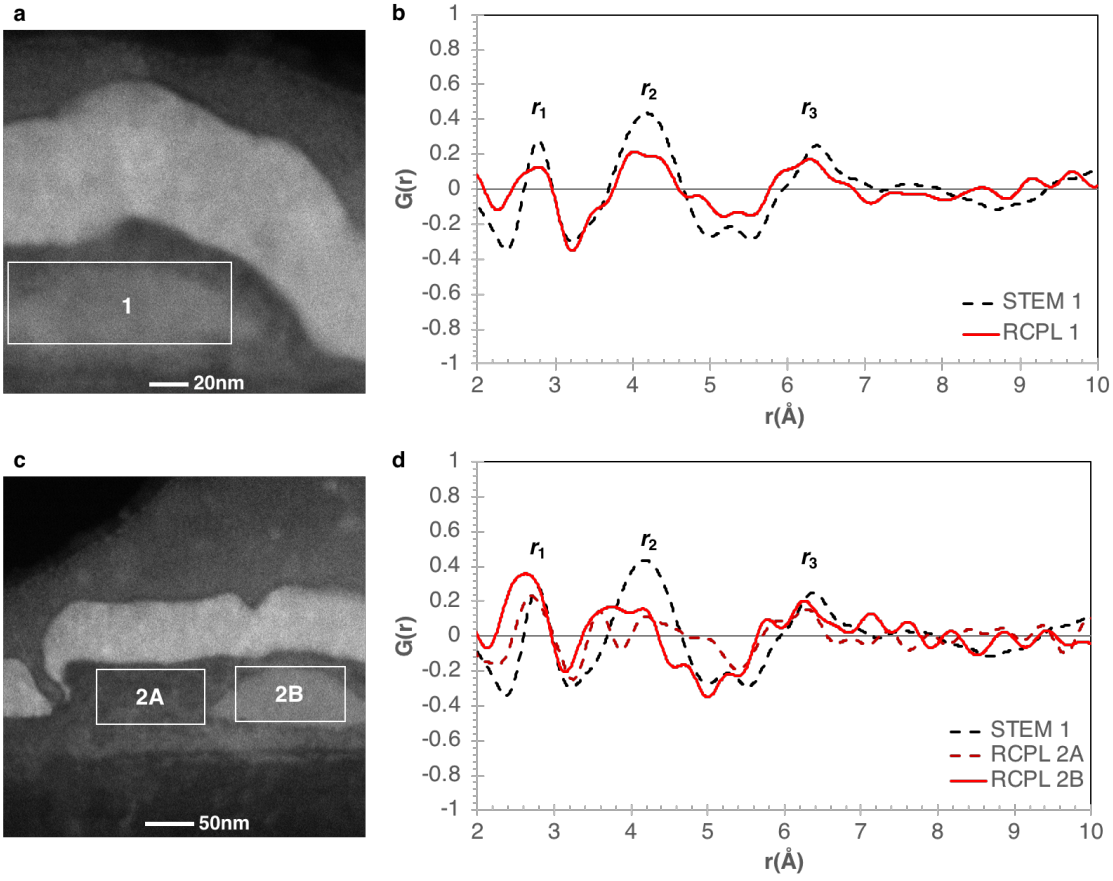

Figure 5.26: RDF curves extracted from STEM probe diffraction data recorded from (a, b) surface features in RCPL-irradiated region C and (c, d) areas of different contrast within such features. Amorphous RDF 'STEM 1' is also included in both plots.

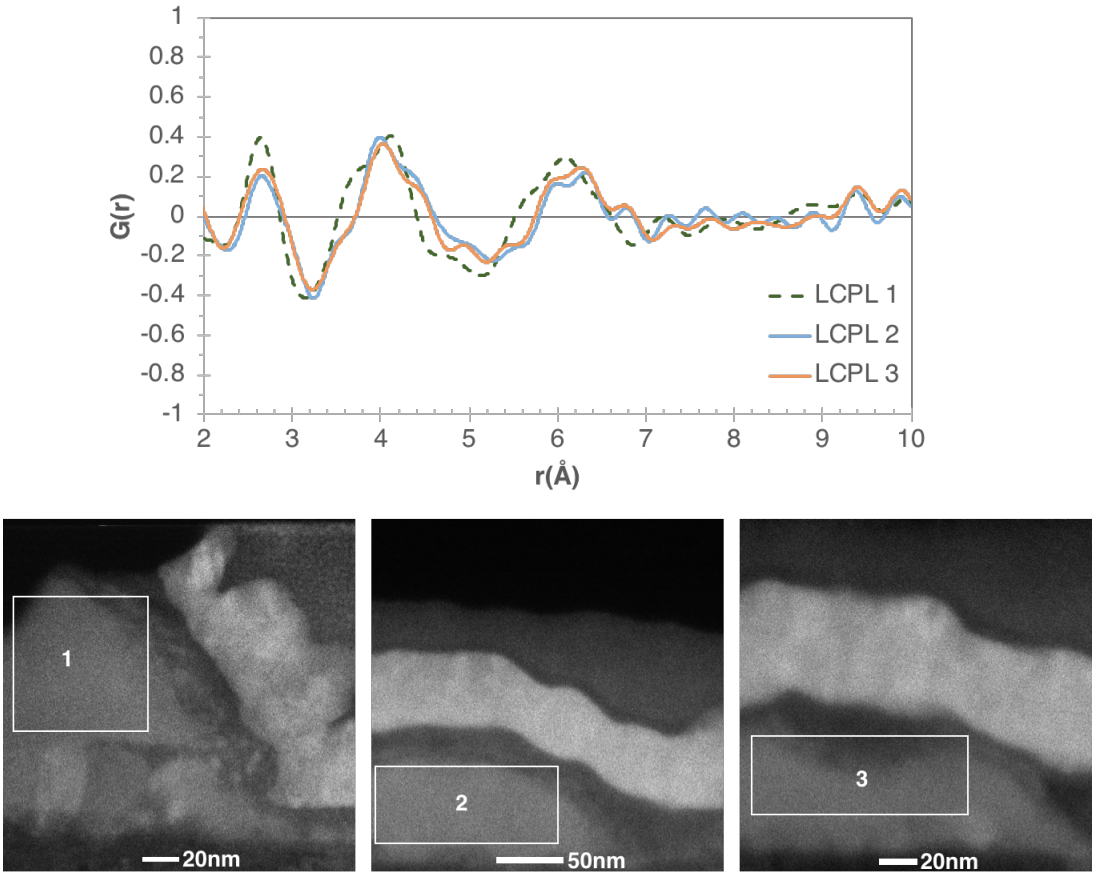

Figure 5.27: RDF curves extracted from STEM probe diffraction data recorded from surface features in LCPL-irradiated region C, as indicated in the HAADF STEM images.

Comparing the irradiated region RDF curve 'RCPL 1' with the amorphous RDF curve 'STEM 1' obtained with a similar probe size, it is evident that the irradiated regions are mostly amorphous (Figure 5.26(b)). The peak positions of RDF curves from different LCPL-irradiated region C feature areas (Figure 5.27) are also similar to those of the amorphous RDF. The broadening and splitting of the peaks in the RDF curves of 'RCPL 2A' and '2B' (Figure 5.26(d)) as well as the variations in r_2 and r_3 peak shoulders in RDF curves from different feature areas in LCPL-irradiated regions ('LCPL 1','2' and '3') indicate greater local disorder and a larger spread of nearest and next-nearest neighbour distances.

Table 5.7
RDF peak positions for various diffraction data from LCPL and RCPL irradiated region C of the GST film (as in Figures 5.26 and 5.27).

RDF curve	Peak positions (Å)		
	r_1 (± 0.02)	r_2 (± 0.04)	r_3 (± 0.04)
RCPL 1	2.79	4.02	6.29
RCPL 2A	2.70	3.59 / 4.20	6.30
RCPL 2B	2.79	4.19	5.79 / 6.26
LCPL 1	2.64	4.10	6.08
LCPL 2	2.65	3.99	6.31
LCPL 3	2.66	4.02	6.27

Note: Double values represent positions of split peaks.

Due to the poorer signal-to-noise ratio of diffraction data summed over a smaller number of acquisitions (a smaller area each), these RDF curves are of a lower quality (with high-frequency oscillations more apparent beyond 5Å) than the amorphous RDF curve. In contrast to the expected crystallisation of the laser-irradiated regions, the similarity of the peak positions of the RDF curves obtained from laser-irradiated regions to those from amorphous regions indicate that both the LCPL and RCPL irradiated regions probed are mostly amorphous.

It is possible that sub-region C in the irradiated film regions may have been initially crystallised by the laser irradiation and then melt-quenched into an amorphous state during the subsequent cooling process. Some melt-quenched regions may still retain some crystalline fragments, as suggested by the proximity of the saddle point at ~5Å in the 'RCPL 2A' RDF curve (Figure 5.26) to the characteristic crystalline r_c peak at 5.21Å (as seen in Figure 5.23). A local maximum is also observed at ~5.2Å in the 'STEM 1' amorphous RDF curve, which exhibits longer interatomic distances than other amorphous values in literature (Borisenko, Chen, Song, Nguyen-Manh, et al.,

2009; Lang et al., 2007; Park et al., 2007) possibly due to the presence of nanocrystallites.

Although the r_1 peak in the LCPL RDF curves occurs at up to 0.15Å shorter interatomic distance than that observed in the RCPL and amorphous RDF curves from diffraction data collected with similar beam sizes (Table 5.7), the peak position is closer to the interatomic distance obtained from the 'μP NBD 1' amorphous data (Table 5.6) and values reported in literature (Borisenko, Chen, Song, Nguyen-Manh, et al., 2009; Lang et al., 2007; Park et al., 2007). The shifting of the r_1 peak position towards shorter distances may be attributed to the shortening of the dominant Ge-Te and Sb-Te bonds due to increased electron localisation, indicating a more amorphous nature of the LCPL region probed (Borisenko, Chen, Song, Nguyen-Manh, et al., 2009). Since diffraction analysis (on areas within a total lamellae length of approximately 10 microns) is localised with respect to the entire irradiated spot or even sub-region C, the deviation in r_1 peak position may also be attributed to an artefact of the variations in local order as seen in the amorphous RDFs obtained with different beam sizes.

5.7. Liquid quench simulations

5.7.1. Structural models of pure GST

Refinement of structural models against the experimental data presented above and analysis of the local bond distribution may provide further insight into the local geometry. The bond type and bond angle distributions in the starting structural models of pure GST obtained through molecular dynamics (MD) liquid quench simulation

('Starting bulk' model) and subsequent DFT energy-optimisation ('Energy optimised' model) as described in Chapter 3 are summarised in Figures 5.28 and 5.29.

As expected, Ge-Te and Sb-Te bonds are predominant in the models, with up to about 25% of the total bonds consisting of homonuclear (Ge-Ge, Sb-Sb and Te-Te) and Ge-Sb bonds that have a low probability of occurrence in crystalline structures. The mean bond angle decreased from 101.2º (±23.7º) in the starting bulk model to 96.9º (±18.5º) in the energy-optimised model, closer to the ideal octahedral 90º bond angle. Non-planar closed ring structures were observed in these models, with 4-membered rings (such as Ge(Sb)-Te-Ge(Sb)-Te) being the most common with a few 5-membered and 3-membered rings also identified (Figure 5.30).

The bond type and bond angle type distributions show that differences between the starting MD model and the DFT energy-optimised model are small, and thus, any errors or inaccuracy in computation due to the limitations discussed in section 3.8.3 are minimal.

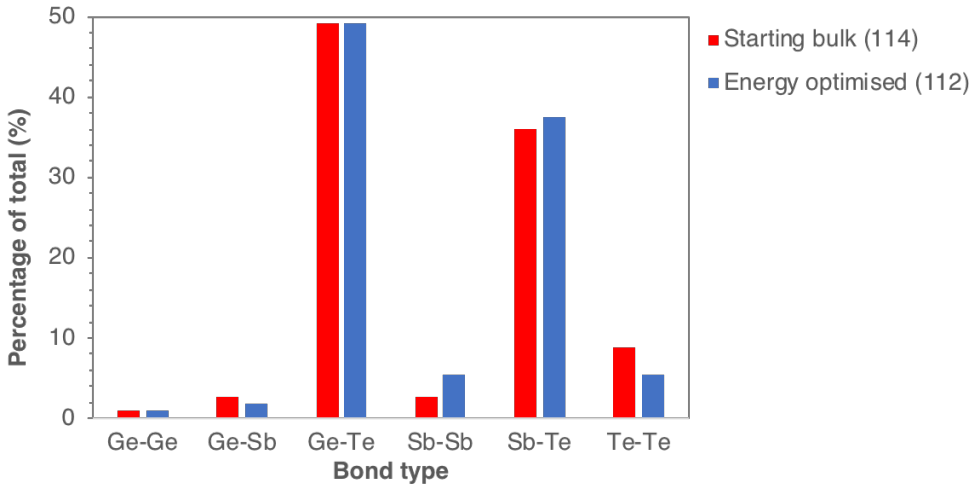

Figure 5.28: Bond type distributions in the starting MD model (red) and DFT energy-optimised model (blue), expressed as percentages of the total number of bonds (in brackets).

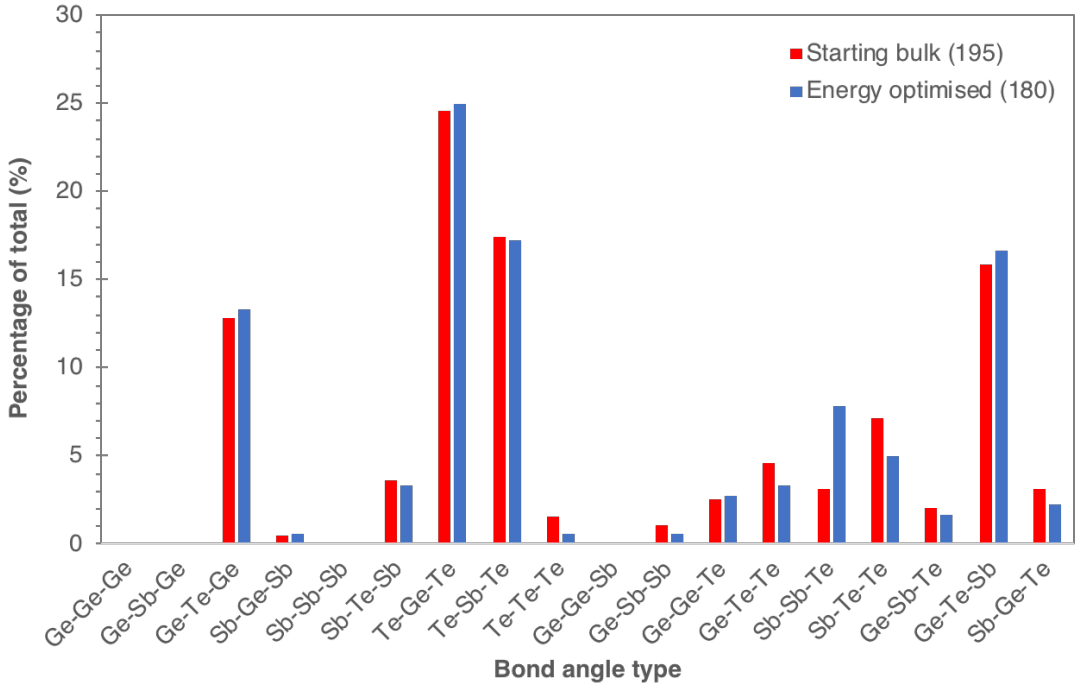

Figure 5.29: Bond angle distributions in the starting MD model (red) and DFT energy-optimised (blue) model, expressed as percentages of the total number of bond angles (in brackets).

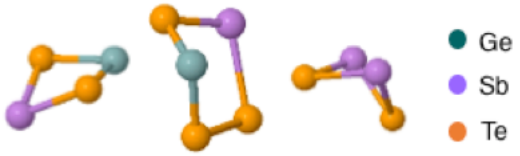

Figure 5.30: Examples of closed rings present in the structural models of pure GST.

Refinement against experimental data

Reverse Monte Carlo (RMC) refinements of the energy-optimised bulk model were carried out against experimental RDF data. 'uP NBD 1' and 'STEM 2' RDF data were selected to exhibit the range of local order in the amorphous GST films (Figure 5.31). The model was also refined against selected experimental RDF data from irradiated regions ('LCPL 3', 'RCPL 2A' and 'RCPL 2B') (Figure 5.32).

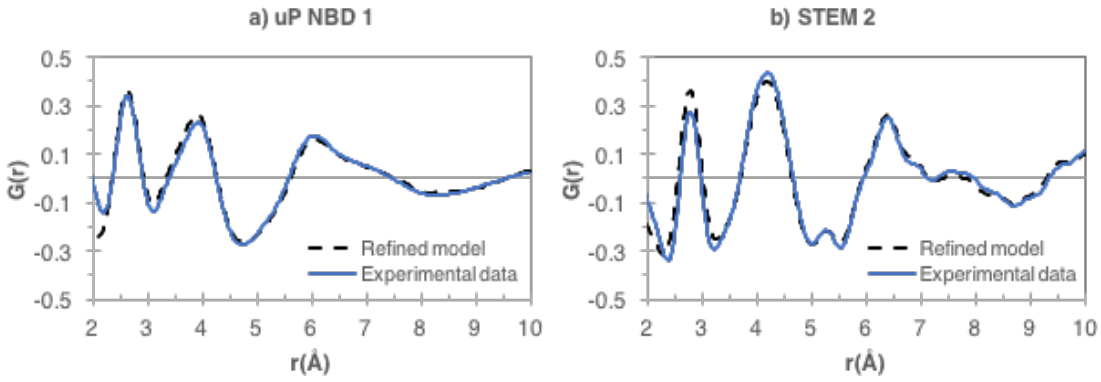

Figure 5.31: RDFs of models (dashed black) refined against amorphous RDF data (a) uP NBD 1 and b) STEM 2) (blue).

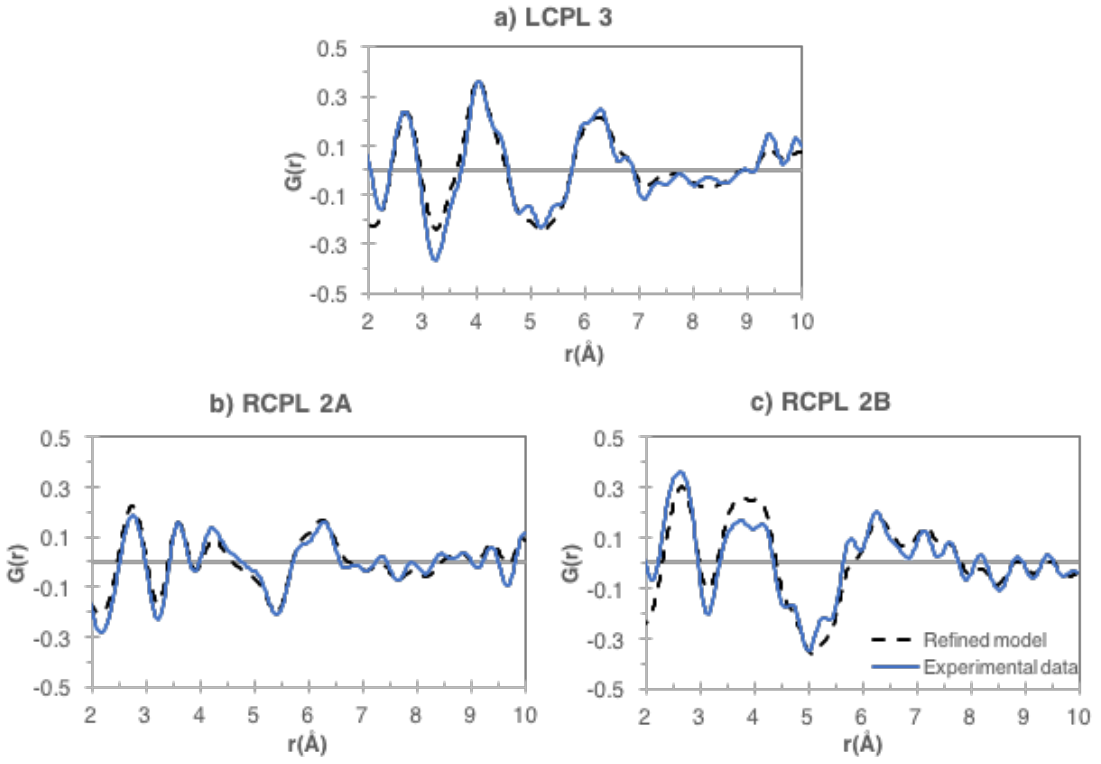

Figure 5.32: RDFs of models (dashed black) refined against amorphous RDF data (a) LCPL 3, b) RCPL 2A and c) RCPL 2B) (blue).

Distributions of bond and bond angle types (not shown) were largely similar between the refined models of amorphous and irradiated regions, which also followed the distribution in the unrefined models. While differences in the r_1 peak position in the experimental data are mostly correlated with the average lengths of the dominant

Ge-Te bonds (2.62Å – 2.77Å) in the refined models, these nearest-neighbour distances are spread over a range of values (standard deviations of up to 0.2Å). The difference in r_1/r_2 peak ratio has previously been attributed to differences in bond lengths of dominant Ge-Te and Sb-Te bonds (Borisenko, Chen, Song, Nguyen-Manh, et al., 2009).

The mean bond angles in the refined models (Table 5.8) are higher than the ideal octahedral 90º bond angle, indicating the presence of defective octahedral bond sites or tetrahedral bond angles (ideally 109.5º). The total coordination numbers for Ge, Sb and Te are much lower than values reported for amorphous GST (Caravati et al., 2007) but as discussed earlier in section 5.6.2, errors in the atomic scattering background fitting may lead to errors in the RDF peak height and inaccurate quantification of atomic coordination.

Table 5.8
Mean bond angles and coordination numbers of Ge, Sb and Te atoms in the various refined models.

Refined model	**Mean bond angle**	**Coordination number** (± 0.05)		
		Ge	**Sb**	**Te**
µP NBD 1	97.3º ± 15.1º	2.3	1.9	1.7
STEM 2	98.7º ± 16.3º	2.5	1.8	1.6
LCPL 3	100.6º ± 18.3º	2.5	2.1	1.7
RCPL 2A	96.3º ± 19.4º	2.3	2.2	1.7
RCPL 2B	99.0º ± 15.4º	2.4	2.0	1.7

Since the RDF describes the average material structure and is less sensitive to variations in local order, it must be noted that the refined structural models are not unique and more than one structural configuration can be fitted to the experimental data. As such, the results of the model refinements and structural analysis presented

above only present some possible representations that agree with the experimental data observed.

5.7.2. Cr-doped structural models

The bond type and bond angle distributions in the starting bulk and energy-optimised structural models of Cr-doped GST were also analysed. While Ge-Te and Sb-Te bonds are still dominant over other bond types, Cr-Te bonds were the most common in the dopant bond pairs, followed by Cr-Ge, then Cr-Sb (Figure 5.33). This agrees with Skelton & Elliott's simulations (2013) where Cr dopants were found to bond preferentially with Te in crystalline GST.

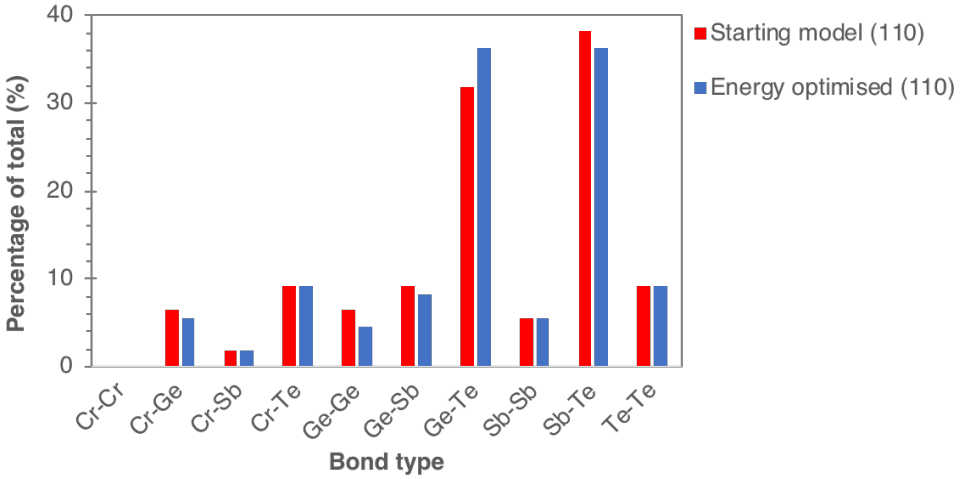

Figure 5.33: Bond type distributions in the starting MD model (red) and DFT energy-optimised model (blue), expressed as percentages of the total number of bonds (in brackets).

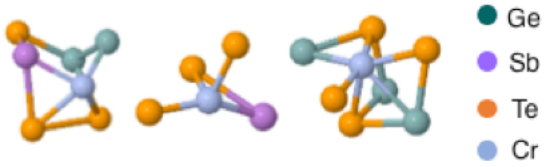

Figure 5.34: Examples of Cr coordination geometry and ring structures in the models.

The mean bond angle in both models (98.3º with a standard deviation of 24.9º for the starting model and 22.9º for the energy-optimised model) was comparable to that of the energy-optimised pure GST model (96.9º ± 18.5º). Snapshots of the Cr coordination geometry (with higher coordination than any of the other elements) in the energy-optimised model are shown in Figure 5.34.

The energy-optimised model was refined against the amorphous 3% Cr-doped GST experimental RDF data. The refined model had a lower total number of bonds than before refinement and a decrease in homonuclear bonds as well as Sb-Te bonds relative to Ge-Te bonds (Figure 5.35). The refined model had a mean bond angle of 98.6º ± 21.7º.

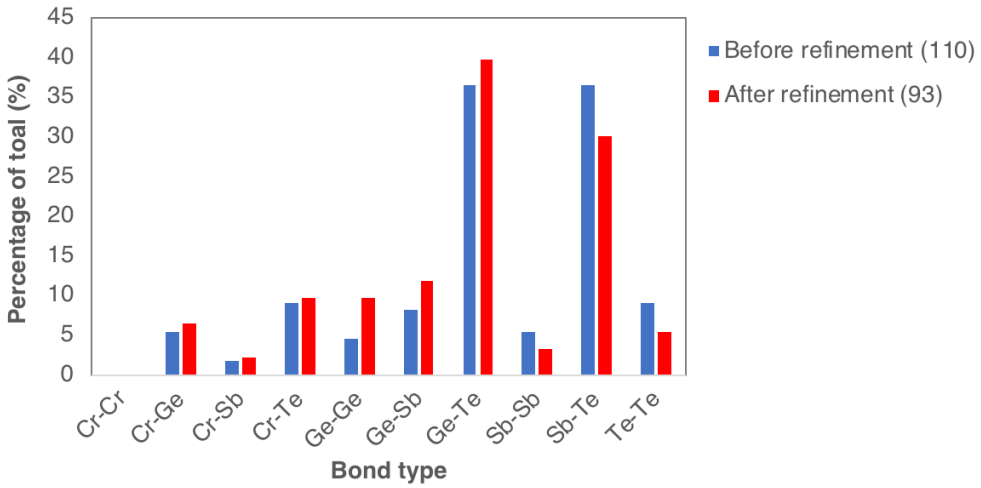

Figure 5.35: Bond type distributions in the refined model (red) and energy-optimised model before refinement (blue), expressed as percentages of the total number of bonds (in brackets).

5.7.3. Annealing under the influence of an electric field

The influence of an applied electric field was studied by comparing the thin film models of pure GST annealed with and without an electric field applied perpendicular to the film, as described in Chapter 3 (Section 3.8.3). The electric field model exhibited a lower total number of bonds compared to the model simulated

without a field and an increase in dominant Ge-Te and Sb-Te bonds at the expense of homopolar bonds (Figure 5.36). This was also reflected in the distribution of related bond angles (Figure 5.37).

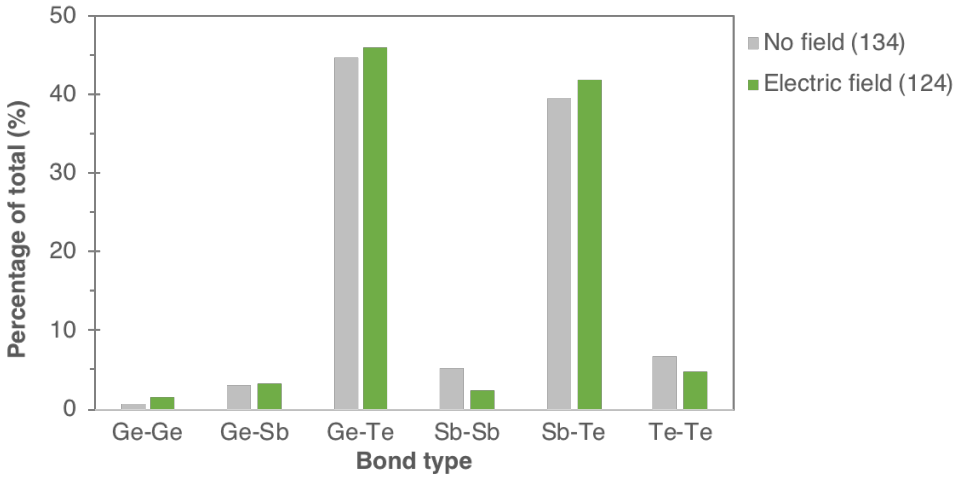

Figure 5.36: Bond type distributions in the models annealed with (green) and without (grey) an electric field, expressed as percentages of the total number of bonds (in brackets).

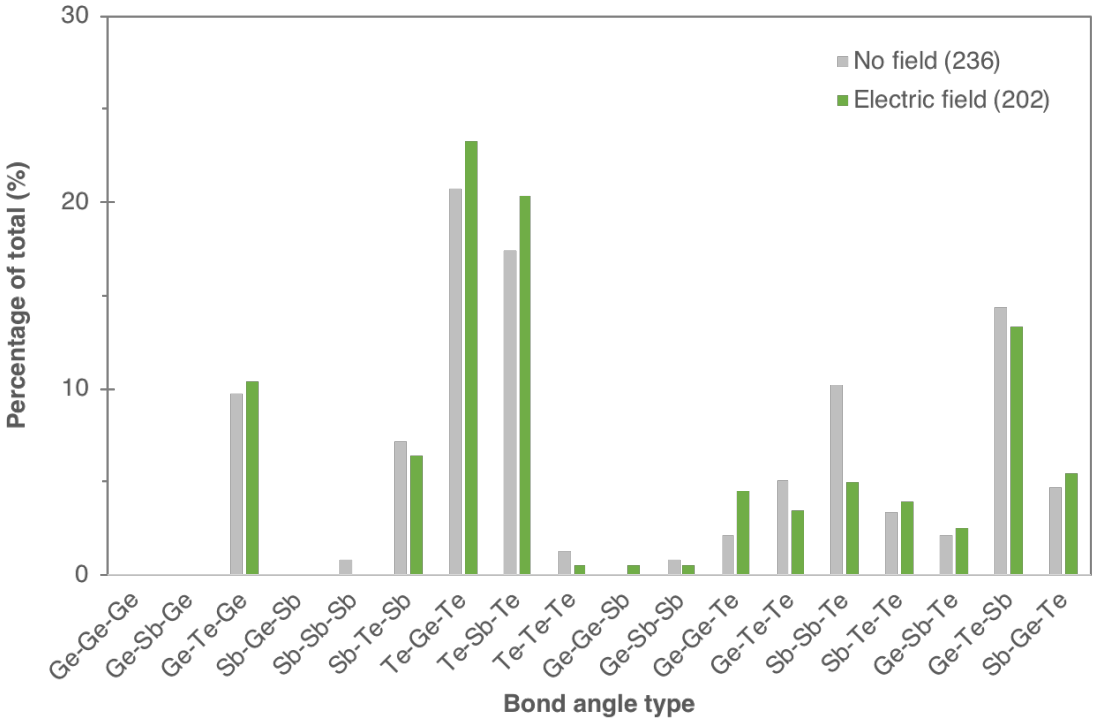

Figure 5.37: Bond angle type distributions in the models annealed with (green) and without (grey) an electric field, expressed as percentages of the total number of bonds (in brackets).

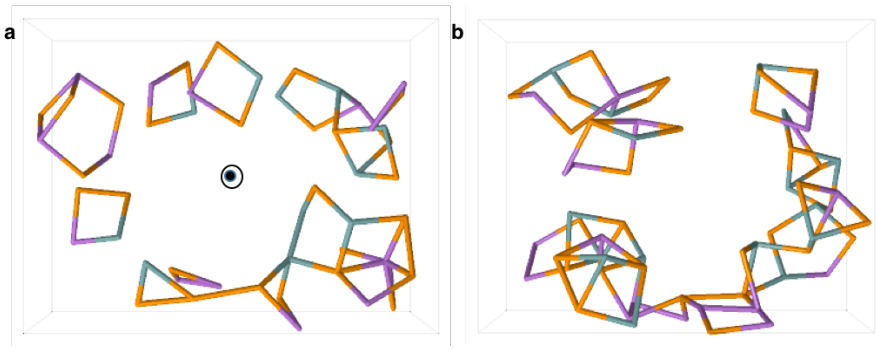

Figure 5.38: Top view of the thin film models annealed (a) with and (b) without an electric field (direction as indicated in (a)) showing only closed ring structures.

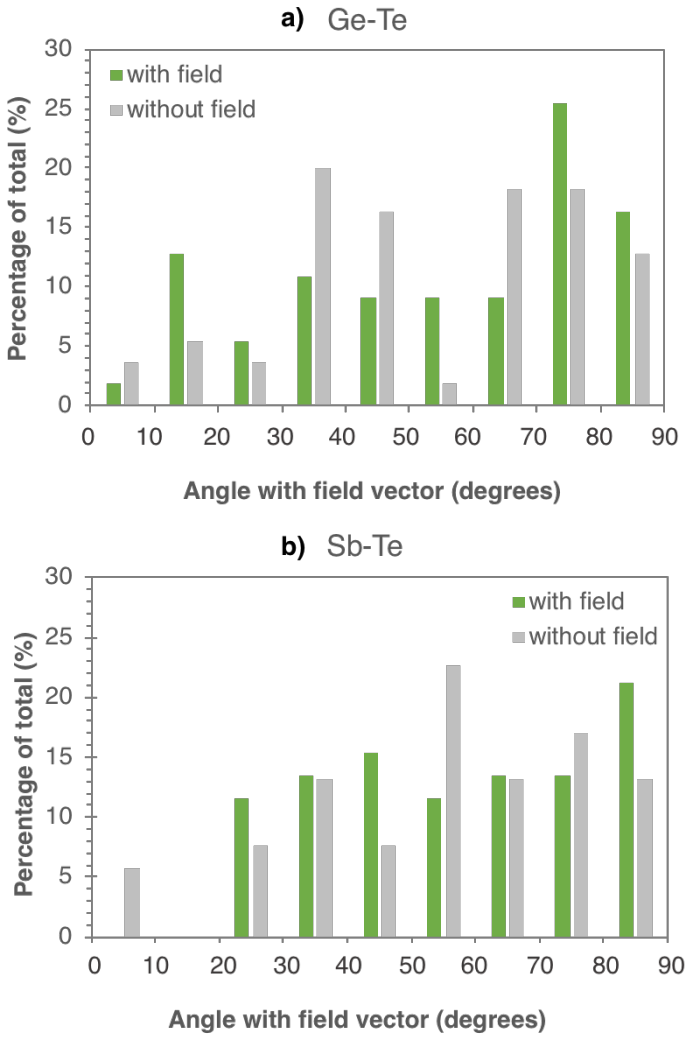

Figure 5.39: Distribution of a) Ge-Te and b) Sb-Te bond angles respective to the electric field unit vector in the thin film models annealed with and without the field. The model with an applied field exhibits an increase in Ge-Te bonds perpendicular (70° -90°) to the vector and a decrease in Sb-Te bonds parallel (0° -20°) to the vector compared to the model without a field.

The annealing process employed in the liquid quench simulations resulted in cross-linked structures in both models, including predominantly 4-membered rings but also a few 3 and 5-membered rings, and a couple of 6-membered rings in the model quenched under an electric field.

However, the extent of cross-linking seems to be reduced in the electric field model (Figure 5.38) due to the decrease in homonuclear Sb-Sb and Te-Te bonds, resulting in an increase in ring structures and chains formed through Ge-Te and Sb-Te bonds. Comparison of the distribution of bond angles with respect to the electric field vector (Figure 5.39) in both thin film models also suggests preferential alignment of Ge-Te and Sb-Te bonds perpendicular to the field vector under the influence of the electric field. There is no apparent phase segregation observed in the electric field model but this may be due to the extremely short time scale of the simulations (in the order of picoseconds) as compared to the total experimental irradiation of 20s.

5.8. Discussion

Given the lack of conclusive results regarding the structure of the irradiated regions from X-ray powder diffraction experiments and the impracticality of surveying an irradiated spot in its entirety using highly localised TEM characterisation, representative specimens were prepared from sub-region C of irradiated regions in pure GST films that exhibited the highest CD signal intensity. However, as seen from the RDF analyses, these irradiated regions are surprisingly mostly amorphous in nature, as opposed to being crystalline with chiral structures expected to give rise to the CD signal observed. A clearer picture of the laser-induced material changes in the film is sought by correlating the optical and SEM observations of the surface

morphology with Raman spectroscopy results and diffraction studies of the cross-sectional specimens.

In films initially irradiated at low laser power, differences between the Raman spectra of the non-exposed film (Region A outside the spot) and the irradiated spot (brighter region B with higher optical reflectivity) confirms the crystallinity of the latter. Increasing the laser power leads to melting of the material at the centre of the irradiated spot and subsequent rapid cooling once the laser pulses are switched off, which results in the modification of the film surface (hemispherical surface features). Lateral dissipation of heat allows this melt region to grow in size, as observed with the increase in laser fluence. Formation of the darker sub-region C is attributed to a melt-quench transition from crystalline back to an amorphous state, while retaining a brighter crystalline ring (region B) at the periphery of the spot. A further increase in laser power then leads to melt-ablation (region X) at the centre of the spot. This explanation of laser-induced changes in the material is related to core-ring structure patterning by laser lithography (Chu et al., 2010), where the centre (dark core) of the irradiated spots are melt-quenched into an amorphous state while the brighter edge (ring) is crystalline.

The amorphous nature of the film regions which exhibit the highest circular dichroism (CD) signal intensity then poses a conundrum. While it is possible that the film underlying the hemispherical features could be crystalline (similar to the crystalline bases of etched core-ring structures as reported by Chu et al. (2010) , there was little or no GST material observed underlying the surface features in some of the regions probed. The analysis of such a region was often encumbered by interference from folding over of the crystalline substrate or gold capping layers from deeper within

the lamella, and there was insufficient evidence from high-resolution STEM imaging to confirm any such crystallinity of the GST material close to the interface.

In light of these observations, it is possible that the interpretation of the X-ray diffraction results may reflect a mostly amorphous structure with some minor crystalline peaks. Speckles in the electron diffraction patterns acquired from the interior of the hemispherical surface features also indicate the presence of para-crystallites dispersed amongst a mostly amorphous material. The RDF peak positions of both amorphous and irradiated regions were typically at longer interatomic distances than values reported for amorphous GST in literature as discussed earlier, with the shift towards longer crystalline distances implying increased local order. Although the shortening of the r_1 peak position in LCPL-irradiated RDF curves and the differences in the r_1/r_2 peak ratio attributed to increased electron localisation detract from a resonantly bonded crystalline structure (with increased electron delocalisation), local extrema observed in the RCPL-irradiated RDF curves close to the crystalline r_c peak also support the presence of small crystallites.

While the results of the RDF analysis and refinements of melt-quench simulation models against the experimental data demonstrate the variation in local order, it is difficult to draw any further conclusions on the structural differences due to laser irradiation with different handedness of CPL. However, the observation of chain cross-linking and ring structures in the refined models support the presence of motif structures in melt-quenched material that may contribute to increased local order. While preferential alignment of the dominant Ge-Te and Sb-Te bonds perpendicular to an applied electric field (akin to a linear polarised laser irradiation) has been

observed, discerning the effects of a rotating field vector in the case of circularly polarised light is complicated.

Asymmetry in these cross-linked structures and rings (chiral centres or asymmetry of plane) may be responsible for increased chirality in the laser-irradiated material as compared to the as-deposited amorphous material, in which similar ring motifs have also been observed. If these chiral structures are responsible for the CD signal intensity observed, the higher absorption of CPL at melt-quenched amorphous region C compared to region B may be explained by the increase in material depth at modified surface features. An increased concentration of chiral structures would then result in greater CPL absorption and a higher CD signal intensity at region C as observed.

A possible additional mechanism may involve the arrangement of the surface features, related to the directionality of the features observed in spots irradiated with linearly polarised light (LPL). If film regions irradiated with CPL exhibited an arrangement of the surface features similar to metamaterial layer assembly (where surface features act as chiral structures) or laser induced periodic surface structures (Bonse, Hohm, Kirner, Rosenfeld, & Kruger, 2017; van Driel, Sipe, & Young, 1982; Wang & Guo, 2006), such a phenomenon could be responsible for increased chirality and CD signal at regions with bigger surface structures than regions with lesser extent of surface modification.

Chapter 6

Conclusion

6.1. Summary and discussion

This thesis set out to explore the athermal factor in the amorphous-to-crystalline phase change in $Ge_2Sb_2Te_5$ thin films by employing circularly polarised laser light (CPL) to induce this phase transition. Photo-induced optical anisotropy, which was studied by measurements of circular dichroism (CD) or differential absorption of opposite handedness of CPL, indicated the significant influence of polarisation on the optical absorption of the laser-irradiated film regions. The effect of various parameters such as the presence of a capping layer, substrate on which films were deposited, film thickness, dopant concentration (of chromium in particular) and laser fluence on the CD signals observed, as well as their long-term and thermal stability were also investigated to understand the effects of this photo-induced phase change further.

The observed optical anisotropic effect provided strong new evidence of non-thermal effects on the phase transition of $Ge_2Sb_2Te_5$ that are not transient (as observed in optical dissociation studies (Waldecker et al., 2015)), but instead, leads to a photo-induced structural change with increased chirality and accompanying changes in optical absorption. The characterisation of morphological as well as compositional changes in the film revealed a graduated modification of the film surface (differentiated by sub-regions). However, contrary to the expected amorphous-to-crystalline phase transition, X-ray and electron diffraction results indicated a mostly

amorphous structure in the sub-region with the highest CD signals observed. This raised a question as to the origin of the significant CD signals observed at the laser-irradiated film regions as compared to the as-deposited amorphous regions. Further analysis of the electron diffraction data, including crystalline speckles in addition to the diffused rings characteristic of amorphous material and differences in RDF peak positions, suggested the presence of small para-crystallites induced by the laser irradiation.

An explanation of these results has been proposed, whereby laser irradiation of the amorphous film would induce crystallisation (at sub-region B as observed from Raman measurements) but irradiation at higher fluence and the subsequent cooling could result in a melt-quenched amorphous structure with crystalline fragments or relics preserved, that aligns with the literature (Akola et al., 2011; Chu et al., 2010). However, given that $Ge_2Sb_2Te_5$ is not known to typically crystallise in any of the Sohncke space groups, an alternative explanation involving the arrangement of modified surface features acting as a chiral assembly in a meta-layer may be viable.

Although the results of the RDF analysis and structural model refinements demonstrated the variation in local order amongst the film regions, it is difficult to draw any further conclusions on the influence of irradiation with different handedness of CPL based on the localised structural characterisation through electron diffraction studies. While the results of the electric field simulation (annealing of the thin film model under the influence of an applied electric field) suggested preferential alignment of certain bonds perpendicular to the electric field vector that could lead to chiral structures or motifs, an extrapolation of the effects of a rotating electric field vector in the case of CPL would require further study.

6.2. Potential research directions

The present structural characterisation work is admittedly limited in its scope of study due to typical time constraints of a DPhil thesis, having looked at highly localised areas within the irradiated sub-regions where the highest CD signals were observed. Hence, a more extensive study of representative areas within all the irradiated sub-regions would be beneficial towards gaining a better understanding of the phenomenon observed. While the liquid quench simulations and refinements of the structural models complement the results of the experimental RDF analysis in this thesis, further structural characterisation carried out with X-ray and electron diffraction studies may elucidate differences in the structural representations of material irradiated with different polarisations of light. This would call for a refinement of techniques in X-ray diffraction measurements for signal collection from the thin films (for instance, by using grazing incidence angles or reflection-mode instead of transmission-mode geometry) and sequential acquisition of electron diffraction data from many large areas (e.g. using serial mapping).

Automated serial mapping using pencil beam illumination in STEM on a double-corrected JEOL Atomic Resolution Microscope (JEM-ARM300CF "Grand ARM") and a counting mode Merlin Medipix detector (which eliminates dark noise and dead time between frames for accurate and faster readouts) has become recently available and it has been attempted on cross-section specimens with the preliminary results now in processing. This technique offers great promise and significant advantage in data acquisition since overview STEM images and pixel-by-pixel diffraction data can be recorded simultaneously at fast speeds, allowing for more efficient acquisition of large datasets under the same probe conditions. Although

falling outside of the scope of this thesis, such mapping is a future direction of structural investigation to understand the origin of the induced chirality in the studied materials.

In any case, the use of multiple experimental datasets as input for Reverse Monte Carlo (RMC) model refinements can lead to more accurate results with a better agreement between the structural models and the experimental data. The employment of additional refinement constraints, such as the types of bond pairs allowed in the model, minimum bond lengths and the range of bond angles for the various bond pairs, or hybrid RMC methods which minimise both the deviation in structure factors and the potential energy may be helpful in narrowing down the configurational possibilities.

The effect of the various parameters in the simulation and refinement of the models (e.g. pseudopotential energy cut-off, periodic boundary conditions and bond tolerance) on the resulting configurations (bond type and angle distributions) also merits further investigation. Although the size of the models used in this work were considered reasonable given the statistical averaged description that RDF provides, the use of larger models may be useful in extracting partial distribution functions of the various bond pairs and may lead to a more accurate quantification of atomic coordination numbers and bond distributions.

On a longer term, it might be insightful to carry out molecular dynamics liquid quench simulations of such models over a longer quench period and a time-step experiment with rotation of the electric field vector at each step to simulate the influence of circular polarisation. Although such a simulation would be computationally intensive (the liquid quench simulations presented in this thesis took

approximately three months per model), it may be beneficial for the study of phase transitions in material systems for potential photonics and chiroptical applications or even theoretical structures and metastable intermediate states that may not be experimentally accessible.

6.3 Implications and practical applications

The findings of the current work have demonstrated the ability to record the helicity of CPL in $Ge_2Sb_2Te_5$ thin films for the first time. While the origin of the photo-induced chirality has not been conclusively determined as yet, the ability to create additional differentiated states based on their optical absorption of CPL holds great promise in increasing the data storage density of phase change memory devices, perhaps enabled by new architecture.

Given the nature of the optical chirality that has been observed in this work, the technique of recording helicity presented may have potential applications in plasmonics and metamaterials by creating chiral layers in other phase-change materials or inorganic films e.g. for use as spectral filters that can be tuned to selectively absorb different wavelengths of CPL (Plum & Zheludev, 2017). This capability may also be harnessed in optoelectronics applications, perhaps as a chiroptical switch that controls and allows the flow of information in a photonics-based circuit. However, such an application would require enhancement of the CD signal observed in the material, which implies development of new materials with even higher CD response.

Appendix A

Sohncke space groups

Table A.1
Three-dimensional Sohncke space group types that chiral structures are known to crystallise in (as described in Chapter 2.3.3)

Crystal system	**Space groups (in Hermann-Mauguin notation)**
Triclinic	P1
Monoclinic	P2, $P2_1$, C2
Orthorhombic	P222, $P222_1$, $P2_12_12$, $P2_12_12_1$, C222, $C222_1$, F222, I222, $I2_12_12_1$
Tetragonal	P4, $P4_1$, $P4_2$, $P4_3$, I4, $I4_1$, P4222, $P42_12$, $P4_122$, $P4_12_12$, $P4_222$, $P4_22_12$, $P4_322$, $P4_32_12$, I422, $I4_122$
Trigonal	P3, $P3_1$, $P3_2$, R3, P312, P321, $P3_112$, $P3_121$, $P3_212$, $P3_121$, R32
Hexagonal	P6, $P6_1$, $P6_5$, $P6_2$, $P6_4$, $P6_3$, P622, $P6_122$, $P6_522$, $P6_222$, $P6_422$, $P6_322$
Cubic	P23, F23, I23, $P2_13$, $I2_13$, P432, $P4_232$, F432, $F4_132$, I432, $P4_332$, $P4_132$, $I4_132$

Appendix B

Quasi-parallel beam condition in Titan

With the specimen placed at the eucentric height i.e. the z-height at which the image of the specimen remains stationary when tilted about its axis, in TEM mode and the largest C2 aperture inserted, the illumination was switched to STEM mode and the default nanoprobe setting changed to microprobe. The diffraction disk was aligned at the centre of the high-angle annular dark field (HAADF) detector and the HAADF-STEM image was approximately focused and stigmated. Switching from diffraction to imaging mode, direct beam alignments (beam shift and beam tilt pivot points) were carried out at a high magnification. The C2 aperture was then switched to the smallest available 10μm aperture and centred. Finally, in diffraction mode, activating free lens control allowed the selection of a large convergence semi-angle range. The convergence semi-angle can be adjusted by fine-tuning the C2 and C3 lenses, such that an additional intermediate image of the source is created between the two lenses, allowing more flexibility and a larger range of convergence angles when switching from 'normal' to 'large' angle range (Table B.1).

Table B.1
Minimum convergence semi-angles using a 10μm C2 aperture under different illumination settings in microprobe (μP) and nanoprobe (nP) STEM mode in the Titan and the corresponding probe sizes (diameter) estimated from polycrystalline aluminium film HAADF-STEM image resolutions

Illumination	Angle range	Convergence semi-angle	Probe size
μP (MC on)	Large	0.12mrad	< 15nm
	Normal	0.48mrad	< 5nm
nP (MC off)	Large	0.34mrad	< 10nm
	Normal	0.89mrad	< 3nm

Appendix C

Calculation of the electric field strength

The Poynting vector $\vec{\boldsymbol{S}} = \vec{\boldsymbol{E}} \times \vec{\boldsymbol{H}}$ is the energy flux vector (per unit area per unit time) that describes the instantaneous power flow of electromagnetic energy. In optics, intensity (or irradiance) is given by the time averaged power density $\langle|\boldsymbol{S}|\rangle$.

For a propagating sinusoidal uniform plane wave, the Poynting vector always aligns with the direction of propagation while oscillating in magnitude, with an electric field $\vec{\boldsymbol{E}}$ and a magnetic field $\vec{\boldsymbol{H}}$ in phase and perpendicular to one another (transverse to direction of propagation). The condition for the wave solution is given by $= \frac{\boldsymbol{E}}{\eta}$, where η is the intrinsic impedance of the transmission medium. The time averaged power density (or intensity) is then given by $I = \frac{1}{2}|\boldsymbol{E}||\boldsymbol{H}| = \frac{1}{2}\frac{|\boldsymbol{E}|^2}{\eta}$, where a factor of ½ is introduced to correct for the average power flow since $|\boldsymbol{E}|$ and $|\boldsymbol{H}|$ are amplitudes of peak fields.

Solving for $|\boldsymbol{E}|$ then gives a peak electric field value;

$$E = \sqrt{2I\eta}$$

Given an average laser power of 5.9mW (which has a pulse energy density of 15.5mJ/cm^2 according to the calculations in section 3.2), the averaged laser intensity per pulse (with 8ns duration) is estimated by assuming a rectangular top-hat pulse shape as follows.

$$I_{avg} = Power\ density_{avg} = \frac{\text{Energy density}_{pulse}}{\text{Pulse duration } \tau_p}$$

$$= 15.5 \times 10^{-3} \text{ J cm}^{-2} / 8 \times 10^{-9} \text{ s}$$

$$= 1.94 \times 10^{6} \text{ W/cm}^2$$

$$= 1.94 \times 10^{10} \text{ W/m}^2$$

Using impedance in free space ($\eta_0 = 120\pi\ \Omega$), the peak electric field value is calculated as;

$$E = \sqrt{2 I_{avg} \eta_0} = 3.83 \times 10^{6} \text{ V/m}$$

However, the value for a Gaussian pulse would differ by a factor of 2, since the effective area in a Gaussian beam is given by $\pi r^2/2$ (where *r* is the beam radius) as compared to πr^2 in a top-hat beam. Hence, the peak electric field value is estimated to be 7.6×10^{6} V/m.

Appendix D

X-ray diffraction peaks

Table D.1

Comparison of experimental and reference diffraction peaks

Experimental Peaks (2 *theta*)			**Literature Values (2 *theta*)**		
Exposed substrate	**Amorphous regions**	**Irradiated regions**	**Al_2O_3**	**c-GST**	**h-GST**
		5.20 5.87 **(MH)**			4.9981
		6.23 **(M)**			6.6657
		~9.3 **(MH)**		**9.4078**	**9.2444**
			11.0858		**12.6817**
		13.20 – 13.23 **(MH)**	**13.5794**	**13.3197**	**13.4819**
14.628		14.49	14.3867		
		15.86 **(H)**			
	16.07 – 16.17	16.02 – 16.11			
16.20	16.20 – 16.25	16.20	16.2886	**16.3318**	
	17.05	~17.70 **(H)**	**17.7137**		17.6935
22.91			22.9512		
	23.69 – 23.80	23.65 – 23.8 **(MH)**			23.7943
23.88		23.84 – 23.87	23.9140		
	24.00	23.95 – 24.12 **(LM)**			24.0025 24.1976 24.2718
		24.59		24.6035	
	25.37	25.37	25.3022		25.1846 25.5219
26.30	26.30	26.30	26.3102		26.2818

Experimental peaks are obtained from various regions of a 60nm thick GST film on Al_2O_3 substrate while the reference peaks are values reported in literature (Al_2O_3 (Swanson & Fuyat, 1953), cubic $Ge_{1.6}Sb_{1.6}Te_4$ (Nonaka et al., 2000) and hexagonal $Ge_2Sb_2Te_5$ (Petrov et al., 1968)) that have been calibrated for the incident X-ray wavelength.

Major reference peaks for each material are indicated in bold, while rows of cells shaded in grey indicate possible phase attributions. 'L', 'M' and 'H' in brackets indicate the laser power (low, medium or high respectively) used to irradiate the spots from which the experimental peaks were observed.

Bibliography

Akola, J., & Jones, R. (2007). Structural phase transitions on the nanoscale: The crucial pattern in the phase-change materials Ge2Sb2Te5 and GeTe. *Physical Review B*, *76*(23), 235201. https://doi.org/10.1103/PhysRevB.76.235201

Akola, J., Larrucea, J., & Jones, R. O. (2011). Polymorphism in phase-change materials: melt-quenched and as-deposited amorphous structures in Ge2Sb2Te5 from density functional calculations. *Physical Review B*, *83*(9), 94113. https://doi.org/10.1103/PhysRevB.83.094113

Andrikopoulos, K. S., Yannopoulos, S. N., Kolobov, A. V., Fons, P., & Tominaga, J. (2007). Raman scattering study of GeTe and Ge2Sb2Te5 phase-change materials. *Journal of Physics and Chemistry of Solids*, *68*(5–6), 1074–1078. https://doi.org/10.1016/j.jpcs.2007.02.027

Bang, D., Awano, H., Tominaga, J., Kolobov, A. V., Fons, P., Saito, Y., … Murakami, S. (2015). Mirror-symmetric magneto-optical Kerr rotation using visible light in [(GeTe)2(Sb2Te3)1]n topological superlattices. *Scientific Reports*, *4*(1), 5727. https://doi.org/10.1038/srep05727

Becke, A. D. (1993). A new mixing of Hartree–Fock and local density- functional theories. *The Journal of Chemical Physics*, *98*(2), 1372–1377. https://doi.org/10.1063/1.464304

Bonse, J., Hohm, S., Kirner, S. V., Rosenfeld, A., & Kruger, J. (2017). Laser-Induced Periodic Surface Structures— A Scientific Evergreen. *IEEE Journal of Selected Topics in Quantum Electronics*, *23*(3). https://doi.org/10.1109/JSTQE.2016.2614183

Borisenko, K. B., Chen, Y., Cockayne, D. J. H., Song, S. A., & Jeong, H. S. (2011). Understanding atomic structures of amorphous C-doped Ge2Sb2Te5 phase-change memory materials. *Acta Materialia*, *59*(11), 4335–4342. https://doi.org/10.1016/j.actamat.2011.03.057

Borisenko, K. B., Chen, Y., Song, S. A., & Cockayne, D. J. H. (2009). Nanoscale phase separation and building blocks of Ge2Sb2Te5N and Ge2Sb2Te5N2 thin films. *Chemistry of Materials*, *21*(21), 5244–5251. https://doi.org/10.1021/cm9022612

Borisenko, K. B., Chen, Y., Song, S. A., Nguyen-Manh, D., & Cockayne, D. J. H. (2009). A concerted rational crystallization/amorphization mechanism of Ge2Sb2Te5. *Journal of Non-Crystalline Solids*, *355*(43–44), 2122–2126. https://doi.org/10.1016/j.jnoncrysol.2009.06.029

Cao, T., Zhang, L., Simpson, R. E., Wei, C., & Cryan, M. J. (2013). Strongly tunable circular dichroism in gammadion chiral phase-change metamaterials. *Optics Express*, *21*(23), 27841–27851. https://doi.org/10.1364/OE.21.027841

Caravati, S., Bernasconi, M., Kühne, T. D., Krack, M., & Parrinello, M. (2007). Coexistence of tetrahedral- and octahedral-like sites in amorphous phase change materials. *Applied Physics Letters*, *91*(17), 171906.

https://doi.org/10.1063/1.2801626

Caravati, S., Colleoni, D., Mazzarello, R., Kühne, T. D., Krack, M., Bernasconi, M., & Parrinello, M. (2011). First-principles study of nitrogen doping in cubic and amorphous Ge2Sb2Te5. *Journal of Physics. Condensed Matter : An Institute of Physics Journal*, *23*(26), 265801. https://doi.org/10.1088/0953-8984/23/26/265801

Caravati, S., Sosso, G. C., Bernasconi, M., & Parrinello, M. (2013). Density functional simulations of hexagonal Ge2Sb2Te5 at high pressure. *Physical Review B*, *87*(9), 94117. https://doi.org/10.1103/PhysRevB.87.094117

Chen, Y., Cockayne, D. J. H., Borisenko, K. B., & Song, S. A. (2011). *Reduction of spherical aberration effects on selected area electron diffraction data from cross-sectional samples*. Unpublished manuscript.

Chu, C. H., Da Shiue, C., Cheng, H. W., Tseng, M. L., Chiang, H.-P., Mansuripur, M., & Tsai, D. P. (2010). Laser-induced phase transitions of Ge2Sb2Te5 thin films used in optical and electronic data storage and in thermal lithography. *Optics Express*, *18*(17), 18383. https://doi.org/10.1364/OE.18.018383

Clark, S. J., Segall, M. D., Pickard, C. J., Hasnip, P. J., Probert, M. I. J., Refson, K., & Payne, M. C. (2005). First principles methods using CASTEP. *Zeitschrift Für Kristallographie - Crystalline Materials*, *220*(5/6), 567–570. https://doi.org/10.1524/zkri.220.5.567.65075

Cockayne, D. J. H., Chen, Y., Li, G., & Borisenko, K. B. (2010). The technique of RDF of nanovolumes using electron diffraction. *Journal of Physics: Conference Series*, *241*, 12006. https://doi.org/10.1088/1742-6596/241/1/012006

Cockayne, D. J. H., & McKenzie, D. R. (1988). Electron diffraction analysis of polycrystalline and amorphous thin films. *Acta Crystallographica Section A*, *44*(6), 870–878. https://doi.org/10.1107/S0108767388004957

Coombs, J. H., Jongenelis, A. P. J. M., van Es-Spiekman, W., & Jacobs, B. A. J. (1995). Laser-induced crystallization phenomena in GeTe-based alloys. I. Characterization of nucleation and growth. *Journal of Applied Physics*, *78*(8), 4906. https://doi.org/10.1063/1.359779

Da Silva, J. L. F. (2011). Effective coordination concept applied for phase change (GeTe) m (Sb2 Te3) n compounds. *Journal of Applied Physics*, *109*(2). https://doi.org/10.1063/1.3533422

Da Silva, J. L. F., Walsh, A., Wei, S.-H., & Lee, H. (2009). Atomistic origins of the phase transition mechanism in Ge2Sb2Te5. *Journal of Applied Physics*, *106*(11), 113509. https://doi.org/10.1063/1.3264883

Debenedetti, P. G. (1996). *Metastable liquids : concepts and principles*. Princeton University Press.

Debunne, A., Virwani, K., Padilla, A., Burr, G. W., Kellock, A. J., Deline, V. R., … Jackson, B. (2011). Evidence of crystallization–induced segregation in the phase change material Te-rich GST. *Journal of The Electrochemical Society*, *158*(10), H965. https://doi.org/10.1149/1.3614508

DiVincenzo, D. P. (1988). Nonlinear optics as a probe of chiral ordering in amorphous semiconductors. *Physical Review B*, *37*(3), 1245–1261. https://doi.org/10.1103/PhysRevB.37.1245

Doyle, P. A., & Turner, P. S. (1968). Relativistic Hartree–Fock X-ray and electron scattering factors. *Acta Crystallographica Section A*, *24*(3), 390–397. https://doi.org/10.1107/S0567739468000756

Draper, C. W., & Poate, J. M. (1985). Laser surface alloying. *International Metals Reviews*, *30*(1), 85–108. https://doi.org/10.1179/imtr.1985.30.1.85

Elliott, S., & Tikhomirov, V. (1996). Vectoral and scalar photoinduced effects in chalcogenide glasses. *Journal of Non-Crystalline Solids*, *198–200*, 669–674. https://doi.org/10.1016/0022-3093(96)00002-6

FEI. (2010). *Appendix A*. *True Crystal Strain Analysis: A step-by-step manual*. FEI Company.

Filik, J., Ashton, A. W., Chang, P. C. Y., Chater, P. A., Day, S. J., Drakopoulos, M., … Wilhelm, H. (2017). Processing two-dimensional X-ray diffraction and small-angle scattering data in DAWN 2. *Journal of Applied Crystallography*, *50*(3), 959–966. https://doi.org/10.1107/S1600576717004708

Flack, H. D. (2003). Chiral and achiral crystal structures. *Helvetica Chimica Acta*, *86*(4), 905–921. https://doi.org/10.1002/hlca.200390109

Fons, P., Osawa, H., Kolobov, A. V., Fukaya, T., Suzuki, M., Uruga, T., … Tominaga, J. (2010). Photoassisted amorphization of the phase-change memory alloy Ge2Sb2Te5. *Physical Review B*, *82*(4), 41203. https://doi.org/10.1103/PhysRevB.82.041203

Friedrich, I., Weidenhof, V., Lenk, S., & Wuttig, M. (2001). Morphology and structure of laser-modified Ge2Sb2Te5 films studied by transmission electron microscopy. *Thin Solid Films*, *389*(1–2), 239–244. https://doi.org/10.1016/S0040-6090(01)00891-4

Friedrich, I., Weidenhof, V., Njoroge, W., Franz, P., & Wuttig, M. (2000). Structural transformations of Ge2Sb2Te5 films studied by electrical resistance measurements. *Journal Of Applied Physics*, *87*(9), 4130–4134. https://doi.org/10.1063/1.373041

Fritzsche, H. (1995). Optical anisotropies in chalcogenide glasses induced by band-gap light. *Physical Review B*, *52*(22), 15854–15861.

Frumar, M., Firth, A. P., & Owen, A. E. (1995). Optically induced crystal-to-amorphous-state transition in As2S3. *Journal of Non-Crystalline Solids*, *192–193*, 447–450. https://doi.org/10.1016/0022-3093(95)00426-2

Fu, J., Shen, X., Xu, Y., Wang, G., Nie, Q., Lin, C., … Wang, R. (2012). Structural evolution of Ge2Sb2Te5 films under the 488nm laser irradiation. *Materials Letters*, *88*, 148–151. https://doi.org/10.1016/j.matlet.2012.08.051

Gammer, C., Mangler, C., Rentenberger, C., & Karnthaler, H. P. (2010). Quantitative local profile analysis of nanomaterials by electron diffraction. *Scripta Materialia*, *63*(3), 312–315. https://doi.org/10.1016/j.scriptamat.2010.04.019

Ganesh, K. J., Kawasaki, M., Zhou, J. P., & Ferreira, P. J. (2010). D-STEM: A parallel electron diffraction technique applied to nanomaterials. *Microscopy and Microanalysis*, *16*(5), 614–621. https://doi.org/10.1017/S1431927610000334

Gholipour, B., Zhang, J., MacDonald, K. F., Hewak, D. W., & Zheludev, N. I. (2013). An all-optical, non-volatile, bidirectional, phase-change meta-switch. *Advanced Materials*, *25*(22), 3050–3054. https://doi.org/10.1002/adma.201300588

Goulon, J., Goulon-Ginet, C., Rogalev, A., Benayoun, G., Brouder, C., & Natoli, C. R. (2000). X-ray natural circular dichroism and chiral-EXAFS in gyrotropic crystals. *Journal of Synchrotron Radiation*, *7*, 182–188. https://doi.org/10.1107/S0909049598016628

Hegedüs, J., & Elliott, S. R. (2008). Microscopic origin of the fast crystallization ability of Ge-Sb-Te phase-change memory materials. *Nature Materials*, *7*(5), 399–405. https://doi.org/10.1038/nmat2157

Huang, B., & Robertson, J. (2010). Bonding origin of optical contrast in phase-change memory materials. *Physical Review B - Condensed Matter and Materials Physics*, *81*(8), 081204(R). https://doi.org/10.1103/PhysRevB.81.081204

Huang, Y.-J., Tsai, M.-C., Wang, C.-H., & Hsieh, T.-E. (2012). Characterizations and thermal stability improvement of phase-change memory device containing Ce-doped GeSbTe films. *Thin Solid Films*, *520*(9), 3692–3696. https://doi.org/10.1016/j.tsf.2011.12.014

Hussain, R., Jávorfi, T., & Siligardi, G. (2012). Circular dichroism beamline B23 at the Diamond Light Source. *Journal of Synchrotron Radiation*, *19*(1), 132–135. https://doi.org/10.1107/S0909049511038982

Jóvári, P., Kaban, I., Steiner, J., Beuneu, B., Schöps, A., & Webb, M. A. (2008). Local order in amorphous Ge2Sb2Te5 and GeSb2Te4. *Physical Review B*, *77*(3), 35202. https://doi.org/10.1103/PhysRevB.77.035202

Kalb, J. A., Wuttig, M., & Spaepen, F. (2007). Calorimetric measurements of structural relaxation and glass transition temperatures in sputtered films of amorphous Te alloys used for phase change recording. *Journal of Materials Research*, *22*(3), 748–754. https://doi.org/10.1557/jmr.2007.0103

Kaminsky, W. (2000). Experimental and phenomenological aspects of circular birefringence and related properties in transparent crystals. *Reports on Progress in Physics*. https://doi.org/10.1088/0034-4885/63/10/201

Kang, D., Lee, D., Kim, H.-M., Nam, S.-W., Kwon, M.-H., & Kim, K.-B. (2009). Analysis of the electric field induced elemental separation of Ge2Sb2Te5 by transmission electron microscopy. *Applied Physics Letters*, *95*(1), 11904. https://doi.org/10.1063/1.3168517

Kastner, M. (1972). Bonding bands, lone-pair bands, and impurity states in chalcogenide semiconductors. *Physical Review Letters*, *28*(6), 355–357. https://doi.org/10.1103/PhysRevLett.28.355

Khulbe, P. K., Wright, E. M., & Mansuripur, M. (2000). Crystallization behavior of as-deposited, melt quenched, and primed amorphous states of Ge2Sb2.3Te5 films. *Journal of Applied Physics*, *88*(7), 3926. https://doi.org/10.1063/1.1289811

Kim, Y., Jang, M. H., Jeong, K., Cho, M.-H., Do, K. H., Ko, D.-H., … Kim, M. G. (2008). Investigation of phase transition of Ge2Sb2Te5 and N-incorporated Ge2Sb2Te5 films using x-ray absorption spectroscopy. *Applied Physics Letters*, *92*(6), 61910. https://doi.org/10.1063/1.2844878

Kirkland, E. J. (1998). *Advanced Computing in Electron Microscopy*. Boston, MA: Springer US. https://doi.org/10.1007/978-1-4757-4406-4

Kirkland, E. J. (2010). Appendix C Atomic Potentials and Scattering Factors. In *Advanced Computing in Electron Microscopy* (2nd ed., Vol. 40, pp. 243–260). Boston, MA: Springer US. https://doi.org/10.1007/978-1-4419-6533-2

Kitamura, N., Katsumata, Y., Morita, T., Hira, T., & Saiki, T. (2012). Optical anisotropy in amorphous GeSbTe thin films induced by nonthermal phase change with femtosecond pulse excitation. In *11th European Phase Change and Ovonics Science Symposium (E*PCOS)*. Tampere, Finland.

Koch, C. T., & Garofalini, S. H. (2006). Determining the radial pair-distribution function within intergranular amorphous films by numerical nanodiffraction. *Ultramicroscopy*, *106*(4–5), 383–8. https://doi.org/10.1016/j.ultramic.2005.11.005

Kohara, S., Kato, K., Kimura, S., Tanaka, H., Usuki, T., Suzuya, K., … Takata, M. (2006). Structural basis for the fast phase change of Ge2Sb2Te5: Ring statistics analogy between the crystal and amorphous states. *Applied Physics Letters*, *89*(20), 201910. https://doi.org/10.1063/1.2387870

Kohn, W., & Sham, L. J. (1965). Self-consistent equations including exchange and correlation effects. *Physical Review*, *140*(4A), A1133–A1138. https://doi.org/10.1103/PhysRev.140.A1133

Kolb, U., Gorelik, T., Kübel, C., Otten, M. T., & Hubert, D. (2007). Towards automated diffraction tomography: Part I—Data acquisition. *Ultramicroscopy*, *107*(6–7), 507–513. https://doi.org/10.1016/j.ultramic.2006.10.007

Kolobov, A. V., Fons, P., Frenkel, A. I., Ankudinov, A. L., Tominaga, J., & Uruga, T. (2004). Understanding the phase-change mechanism of rewritable optical media. *Nature Materials*, *3*(10), 703–708. https://doi.org/10.1038/nmat1215

Kolobov, A. V., Fons, P., & Tominaga, J. (2014). Athermal amorphization of crystallized chalcogenide glasses and phase-change alloys. *Physica Status Solidi (B)*, *251*(7), 1297–1308. https://doi.org/10.1002/pssb.201350146

Kolobov, A. V., Fons, P., Tominaga, J., Frenkel, A. I., Ankudinov, A. L., Yannopoulos, S. N., … Uruga, T. (2005). Why phase-change media are fast and stable: A new approach to an old problem. *Japanese Journal of Applied Physics*, *44*(5B), 3345–3349. https://doi.org/10.1143/JJAP.44.3345

Kolobov, A. V., Fons, P., Tominaga, J., & Hase, M. (2014). Excitation-assisted disordering of GeTe and related solids with resonant bonding. *The Journal of Physical Chemistry C*, *118*(19), 10248–10253. https://doi.org/10.1021/jp412412j

Kolobov, A. V., Krbal, M., Fons, P., Tominaga, J., & Uruga, T. (2011). Distortion-triggered loss of long-range order in solids with bonding energy hierarchy. *Nature Chemistry*, *3*(4), 311–316. https://doi.org/10.1038/nchem.1007

Kolobov, A. V., & Tominaga, J. (2012). Fundamentals of amorphous semiconductors. In *Chalcogenides* (Vol. 164, pp. 3–34). Springer, Berlin, Heidelberg. https://doi.org/10.1007/978-3-642-28705-3

Kooi, B. J., & De Hosson, J. T. M. (2002). Electron diffraction and high-resolution transmission electron microscopy of the high temperature crystal structures of GexSb2Te(3+x) (x=1,2,3) phase change material. *Journal of Applied Physics*, *92*(7), 3584–3590. https://doi.org/10.1063/1.1502915

Kooi, B. J., Groot, M. G., & De Hosson, J. T. M. (2004). In situ transmission electron microscopy study of the crystallization of Ge2Sb2Te5. *Journal of Applied Physics*, *95*(3), 924. https://doi.org/10.1063/1.1636259

Kosyakov, V. I., Shestakov, V. A., Shelimova, L. E., Kuznetsov, F. A., & Zemskov, V. S. (2000). Topological characterization of the Ge-Sb-Te phase diagram. *Inorganic Materials*, *36*(10), 1004–1017. https://doi.org/10.1007/BF02757976

Kozyukhin, S., Veres, M., Nguyen, H. P., Ingram, A., & Kudoyarova, V. (2013). Structural changes in doped Ge2Sb2Te5 thin films studied by Raman spectroscopy. *Physics Procedia*, *44*, 82–90. https://doi.org/10.1016/j.phpro.2013.04.011

Krbal, M., Kolobov, A. V., Fons, P., Tominaga, J., Elliott, S. R., Hegedus, J., & Uruga, T. (2011). Intrinsic complexity of the melt-quenched amorphous Ge2Sb2Te5 memory alloy. *Physical Review B*, *83*(5), 54203. https://doi.org/10.1103/PhysRevB.83.054203

Krbal, M., Kolobov, A. V., Fons, P., Tominaga, J., Elliott, S. R., Hegedus, J., … Uruga, T. (2012). Crystalline GeTe-based phase-change alloys: Disorder in order. *Physical Review B*, *86*(4), 45212. https://doi.org/10.1103/PhysRevB.86.045212

Kwon, M.-H., Lee, B.-S., Bogle, S. N., Nittala, L. N., Bishop, S. G., Abelson, J. R., … Kim, K.-B. (2007). Nanometer-scale order in amorphous Ge2Sb2Te5 analyzed by fluctuation electron microscopy. *Applied Physics Letters*, *90*(2), 21923. https://doi.org/10.1063/1.2430067

Lang, C., Song, S. A., Nguyen-Manh, D., & Cockayne, D. J. H. (2007). Building blocks of amorphous Ge2Sb2Te5. *Physical Review B*, *76*(5), 54101. https://doi.org/10.1103/PhysRevB.76.054101

Lankhorst, M. H. R. (2002). Modelling glass transition temperatures of chalcogenide glasses. Applied to phase-change optical recording materials. *Journal of Non-Crystalline Solids*, *297*(2–3), 210–219. https://doi.org/10.1016/S0022-3093(01)01034-1

Lee, J., Shin, J.-H., Lee, G.-H., & Lee, C.-H. (2016). Two-dimensional semiconductor optoelectronics based on van der Waals heterostructures. *Nanomaterials*, *6*(12), 193. https://doi.org/10.3390/nano6110193

Lencer, D., Salinga, M., & Wuttig, M. (2011). Design rules for phase-change materials in data storage applications. *Advanced Materials (Deerfield Beach, Fla.)*, *23*(18), 2030–58. https://doi.org/10.1002/adma.201004255

Li, T. T., Darmawikarta, K., & Abelson, J. R. (2013). Quantifying nanoscale order in amorphous materials via scattering covariance in fluctuation electron microscopy. *Ultramicroscopy*, *133*, 95–100. https://doi.org/10.1016/j.ultramic.2013.06.017

Li, X.-B., Liu, X. Q., Han, X. D., & Zhang, S. B. (2012). Role of electronic excitation in phase-change memory materials: A brief review. *Physica Status Solidi (B)*, *249*(10), 1861–1866. https://doi.org/10.1002/pssb.201200380

Liu, X. Q., Li, X. B., Zhang, L., Cheng, Y. Q., Yan, Z. G., Xu, M., … Ma, E. (2011). New structural picture of the Ge2Sb2Te5 phase-change alloy. *Physical Review Letters*, *106*(2), 25501. https://doi.org/10.1103/PhysRevLett.106.025501

Lobato, I., & van Dyck, D. (2014). An accurate parameterization for scattering factors, electron densities and electrostatic potentials for neutral atoms that obey all physical constraints. *Acta Crystallographica Section A Foundations and Advances*, *70*(6), 1–13. https://doi.org/10.1107/S205327331401643X

Lotnyk, A., Bernütz, S., Sun, X., Ross, U., Ehrhardt, M., & Rauschenbach, B. (2016). Real-space imaging of atomic arrangement and vacancy layers ordering in laser crystallised Ge2Sb2Te5 phase change thin films. *Acta Materialia*, *105*, 1–8. https://doi.org/10.1016/j.actamat.2015.12.010

Lu, Y., Stegmaier, M., Nukala, P., Giambra, M. A., Ferrari, S., Busacca, A., … Agarwal, R. (2017). Mixed-mode operation of hybrid phase-change nanophotonic circuits. *Nano Letters*, *17*(1), 150–155. https://doi.org/10.1021/acs.nanolett.6b03688

Lucovsky, G., & White, R. M. (1973). Effects of resonance bonding on the properties of crystalline and amorphous semiconductors. *Physical Review B*, *8*(2), 660–667. https://doi.org/10.1103/PhysRevB.8.660

Lyubin, V., Klebanov, M., Mitkova, M., & Petkova, T. (1997). Polarization-dependent, laser-induced anisotropic photocrystallization of some amorphous chalcogenide films. *Applied Physics Letters*, *71*(15), 2118. https://doi.org/10.1063/1.119354

Lyubin, V. M., & Tikhomirov, V. K. (1991). Novel photo-induced effects in chalcogenide glasses. *Journal of Non-Crystalline Solids*, *135*(1), 37–48. https://doi.org/10.1016/0022-3093(91)90440-H

Matsunaga, T., Yamada, N., & Kubota, Y. (2004). Structures of stable and metastable Ge2Sb2Te5, an intermetallic compound in GeTe-Sb2Te3 pseudobinary systems. *Acta Crystallographica Section B*, *60*(6), 685–691. https://doi.org/10.1107/S0108768104022906

McGreevy, R. L., & Pusztai, L. (1988). Reverse Monte Carlo simulation: A new technique for the determination of disordered structures. *Molecular Simulation*, *1*(6), 359–367. https://doi.org/10.1080/08927028808080958

Miller, T. A., Rudé, M., Pruneri, V., & Wall, S. (2016). Ultrafast optical response of the amorphous and crystalline states of the phase change material Ge2Sb2Te5. *Physical Review B*, *94*(2), 24301. https://doi.org/10.1103/PhysRevB.94.024301

Mitchell, D. R. G., & Petersen, T. C. (2012). RDFTools: A software tool for quantifying short-range ordering in amorphous materials. *Microscopy Research and Technique*, *75*(2), 153–163. https://doi.org/10.1002/jemt.21038

Moshe, H., Vanbel, M., Valev, V. K., Verbiest, T., Dressler, D., & Mastai, Y. (2013). Chiral thin films of metal oxide. *Chemistry*, *19*, 10295–10301. https://doi.org/10.1002/chem.201300760

Mu, X., Wang, D., Feng, T., & Kübel, C. (2016). Radial distribution function imaging by STEM diffraction: Phase mapping and analysis of heterogeneous nanostructured glasses. *Ultramicroscopy*, *159*, 84–86. https://doi.org/10.1016/j.ultramic.2016.05.009

Müller, U. (2016). Molecular Symmetry. In *International Tables for Crystallography Vol. A Chapter 3.2* (pp. 772–776).

Němec, P., Nazabal, V., Moreac, a., Gutwirth, J., Beneš, L., & Frumar, M. (2012). Amorphous and crystallized Ge-Sb-Te thin films deposited by pulsed laser: Local structure using Raman scattering spectroscopy. *Materials Chemistry and Physics*, *136*(2–3), 935–941. https://doi.org/10.1016/j.matchemphys.2012.08.024

Nishiyama, Z. (1978). *Martensitic Transformation.* Elsevier Science.

Nonaka, T., Ohbayashi, G., Toriumi, Y., Mori, Y., & Hashimoto, H. (2000). Crystal structure of GeTe and Ge2Sb2Te5 meta-stable phase. *Thin Solid Films*, *370*(1–2), 258–261. https://doi.org/10.1016/S0040-6090(99)01090-1

Opletal, G. (2017). Hybrid Reverse Monte Carlo (HRMC). CSIRO. https://doi.org/10.4225/08/59dab19e0c3d8

Park, G.-S., Kwon, J.-H., Kim, M., Yoon, H. R., Jo, W., Kim, T. K., … Khang, Y. (2007). Crystalline and amorphous structures of Ge–Sb–Te nanoparticles. *Journal of Applied Physics*, *102*(1), 13524. https://doi.org/10.1063/1.2752550

Pernice, W. H. P., & Bhaskaran, H. (2012). Photonic non-volatile memories using phase change materials. *Applied Physics Letters*, *101*(17), 1–5. https://doi.org/10.1063/1.4758996

Petersen, T. C., McBride, W., McCulloch, D. G., Snook, I. K., & Yarovsky, I. (2005). Refinements in the collection of energy filtered diffraction patterns from disordered materials. *Ultramicroscopy*, *103*(4), 275–83. https://doi.org/10.1016/j.ultramic.2005.01.002

Petrov, I. I., Imamov, R. M., & Pinsker, Z. G. (1968). Electron-diffraction determination of the structures of Ge2Sb2Te5 and GeSb4Te7. *Soviet Physics Crystallography*, *13*(3), 339–342.

Plum, E., & Zheludev, N. (2017). Chiral Optics of Planar Metamaterials. In *The 8th International Conference on Metamaterials, Photonic Crystals and Plasmonics*. Seoul, Korea, Republic of.

Poborchii, V. V., Kolobov, A. V., & Tanaka, K. (1998). An in situ Raman study of polarization-dependent photocrystallization in amorphous selenium films. *Applied Physics Letters*, *72*(10), 1167–1169. https://doi.org/10.1063/1.121002

Poborchii, V. V., Kolobov, A. V., & Tanaka, K. (1999). Photomelting of selenium at low temperature. *Applied Physics Letters*, *74*(2), 215–217. https://doi.org/10.1063/1.123297

Prasai, B., & Drabold, D. A. (2015). Transition metals in phase-change memory materials: Impact upon crystallization (pp. 511–524). Springer, Cham. https://doi.org/10.1007/978-3-319-15675-0_19

Privitera, S., Rimini, E., & Zonca, R. (2004). Amorphous-to-crystal transition of nitrogen- and oxygen-doped Ge2Sb2Te5 films studied by in situ resistance measurements. *Applied Physics Letters*, *85*(15), 3044–3046. https://doi.org/10.1063/1.1805200

Raoux, S., Ielmini, D., Wuttig, M., & Karpov, I. (2012). Phase change materials. *Materials Research Science Bulletin*, *37*(February), 118–123. https://doi.org/10.1557/mrs.2012.357

Raoux, S., Xiong, F., Wuttig, M., & Pop, E. (2014). Phase change materials and phase change memory. *MRS Bulletin*, *39*(8), 703–710. https://doi.org/10.1557/mrs.2014.139

Raty, J.-Y., Bichara, C., Mazzarello, R., Rausch, P., Zalden, P., & Wuttig, M. (2012). Comment on "New Structural Picture of the Ge2Sb2Te5 Phase-Change Alloy." *Physical Review Letters*, *108*(23), 239601. https://doi.org/10.1103/PhysRevLett.108.239601

Ríos, C., Stegmaier, M., Hosseini, P., Wang, D., Scherer, T., Wright, C. D., … Pernice, W. H. P. (2015). Integrated all-photonic non-volatile multi-level memory. *Nature Photonics*, *9*(11), 725–732. https://doi.org/10.1038/nphoton.2015.182

Robbie, K., Brett, M. J., & Lakhtakia, A. (1996). Chiral sculptured thin films. *Nature*, *384*, 616. https://doi.org/doi:10.1038/384616a0

Robertson, J., & Huang, B. (2012). Bonding and optical contrast in phase change memory materials. *Physica Status Solidi (B)*, *249*(10), 1867–1873. https://doi.org/10.1002/pssb.201200361

Ross, U., Lotnyk, A., Thelander, E., & Rauschenbach, B. (2014). Direct imaging of crystal structure and defects in metastable Ge2Sb2Te5 by quantitative aberration-corrected scanning transmission electron microscopy. *Applied Physics Letters*, *104*(12), 121904. https://doi.org/10.1063/1.4869471

Ruan, C.-Y., Murooka, Y., Raman, R. K., & Murdick, R. A. (2007). Dynamics of Size-Selected Gold Nanoparticles Studied by Ultrafast Electron Nanocrystallography. *Nano Letters*, *7*(5), 1290–1296. https://doi.org/10.1021/nl070269h

Schellman, J. A. (1975). Circular dichroism and optical rotation. *Chemical Reviews*, *75*(3), 323–331. https://doi.org/10.1021/cr60295a004

Shanmugam, J., Borisenko, K. B., Chou, Y.-J., & Kirkland, A. I. (2017). eRDF Analyser: An interactive GUI for electron reduced density function analysis. *SoftwareX*, *6*, 185–192. https://doi.org/10.1016/j.softx.2017.07.001

Shportko, K., Kremers, S., Woda, M., Lencer, D., Robertson, J., & Wuttig, M. (2008). Resonant bonding in crystalline phase-change materials. *Nature Materials*, *7*(8), 653–658. https://doi.org/10.1038/nmat2226

Singh, G., Kaura, A., Mukul, M., Singh, J., & Tripathi, S. K. (2014). Theoretical and experimental investigations of the properties of Ge2Sb2Te5 and indium-doped Ge2Sb2Te5 phase change material. *Applied Physics A*, *117*(3), 1307–1314. https://doi.org/10.1007/s00339-014-8542-9

Skelton, J. M., & Elliott, S. R. (2013). In silico optimization of phase-change materials for digital memories: a survey of first-row transition-metal dopants for $Ge_2Sb_2Te_5$. *Journal of Physics. Condensed Matter : An Institute of Physics Journal*, *25*(20), 205801. https://doi.org/10.1088/0953-8984/25/20/205801

Song, S. A., Zhang, W., Sik Jeong, H., Kim, J.-G., & Kim, Y.-J. (2008). In situ dynamic HR-TEM and EELS study on phase transitions of Ge2Sb2Te5 chalcogenides. *Ultramicroscopy*, *108*(11), 1408–19. https://doi.org/10.1016/j.ultramic.2008.05.012

Sosso, G. C., Caravati, S., Mazzarello, R., & Bernasconi, M. (2011). Raman spectra of cubic and amorphous Ge2Sb2Te5 from first principles. *Physical Review B*, *83*(13), 1–8. https://doi.org/10.1103/PhysRevB.83.134201

Sosso, G. C., Miceli, G., Caravati, S., Behler, J., & Bernasconi, M. (2012). Neural network interatomic potential for the phase change material GeTe. *Physical Review B*, *85*(17), 174103. https://doi.org/10.1103/PhysRevB.85.174103

Sun, Z., Zhou, J., & Ahuja, R. (2006). Structure of phase change materials for data storage. *Physical Review Letters*, *96*(5), 55507. https://doi.org/10.1103/PhysRevLett.96.055507

Sundaram, S. K., & Mazur, E. (2002). Inducing and probing non-thermal transitions in semiconductors using femtosecond laser pulses. *Nature Materials*, *1*(4), 217–224. https://doi.org/10.1038/nmat767

Swanson, H. E., & Fuyat, R. K. (1953). Standard X-Ray Diffraction Powder Patterns. *Natl. Bur. Stand. (U.S.), Circ. 539*, *II*, 20.

Tikhomirov, V. K., Hertogen, P., Glorieux, C., & Adriaenssens, G. J. (1997). Oriented crystallization of amorphous Se induced by linearly polarized light. *Physica Status Solidi (a)*, *162*(2), R1–R2. https://doi.org/10.1002/1521-396X(199708)162:2<R1::AID-PSSA99991>3.0.CO;2-J

Tran, D. T., Svensson, G., & Tai, C.-W. (2017). SUePDF: a program to obtain quantitative pair distribution functions from electron diffraction data. *Journal of Applied Crystallography*, *50*(1), 304–312. https://doi.org/10.1107/S160057671601863X

Treacy, M. M. J., & Borisenko, K. B. (2012). The local structure of amorphous silicon. *Science*, *335*(6071), 950–953. https://doi.org/10.1126/science.1214780

Treacy, M. M. J., & Gibson, J. M. (1996). Variable Coherence Microscopy: a rich source of structural information from disordered materials. *Acta Crystallographica Section A Foundations of Crystallography*, *52*(2), 212–220. https://doi.org/10.1107/S0108767395012876

Treacy, M. M. J., Gibson, J. M., Fan, L., Paterson, D. J., & McNulty, I. (2005). Fluctuation microscopy: a probe of medium range order. *Reports on Progress in Physics*, *68*(12), 2899–2944. https://doi.org/10.1088/0034-4885/68/12/R06

Tuma, T., Pantazi, A., Le Gallo, M., Sebastian, A., & Eleftheriou, E. (2016). Stochastic phase-change neurons. *Nature Nanotechnology*, *11*(8), 693–699. https://doi.org/10.1038/nnano.2016.70

van Driel, H. M., Sipe, J. E., & Young, J. F. (1982). Laser-Induced Periodic Surface Structure on Solids: A Universal Phenomenon. *Physical Review Letters*, *49*(26), 1955–1958.

Vinod, E. M., Ramesh, K., & Sangunni, K. S. (2015). Structural transition and enhanced phase transition properties of Se doped Ge2Sb2Te5 alloys. *Scientific Reports*, *5*(1), 8050. https://doi.org/10.1038/srep08050

Voyles, P. M., Gibson, J. M., & Treacy, M. M. J. (2000). Fluctuation microscopy: a probe of atomic correlations in disordered materials. *Journal of Electron Microscopy*, *49*(2), 259–266. https://doi.org/10.1093/oxfordjournals.jmicro.a023805

Voyles, P. M., & Muller, D. A. (2002). Fluctuation microscopy in the STEM. *Ultramicroscopy*, *93*(2), 147–159. https://doi.org/10.1016/S0304-3991(02)00155-9

Waldecker, L., Miller, T. A., Rudé, M., Bertoni, R., Osmond, J., Pruneri, V., … Wall, S. (2015). Time-domain separation of optical properties from structural transitions in resonantly bonded materials. *Nature Materials*, *14*(10), 991–5. https://doi.org/10.1038/nmat4359

Wang, J., & Guo, C. (2006). Permanent recording of light helicity on optically inactive metal surfaces. *Optics Letters*, *31*(24), 3641. https://doi.org/10.1364/OL.31.003641

Wang, Q., Liu, B., Xia, Y., Zheng, Y., Huo, R., Zhang, Q., … Feng, S. (2015). Cr-doped Ge2Sb2Te5 for ultra-long data retention phase change memory. *Applied Physics Letters*, *107*(22), 222101. https://doi.org/10.1063/1.4936847

Wei, S. J., Zhu, H. F., Chen, K., Xu, D., Li, J., Gan, F. X., … Li, G. H. (2011). Phase change behavior in titanium-doped Ge2Sb2Te5 films. *Applied Physics Letters*, *98*(23), 231910. https://doi.org/10.1063/1.3597617

Weidenhof, V., Friedrich, I., Ziegler, S., & Wuttig, M. (2001). Laser induced crystallization of amorphous Ge2Sb2Te5 films. *Journal of Applied Physics*, *89*(6), 3168. https://doi.org/10.1063/1.1351868

Wełnic, W., Pamungkas, A., Detemple, R., Steimer, C., Blügel, S., & Wuttig, M. (2005). Unravelling the interplay of local structure and physical properties in phase-change materials. *Nature Materials*, *5*(1), 56–62. https://doi.org/10.1038/nmat1539

Wuttig, M., & Yamada, N. (2007). Phase-change materials for rewriteable data storage. *Nature Materials*, *6*(11), 824–32. https://doi.org/10.1038/nmat2009

Yamada, N., & Matsunaga, T. (2000). Structure of laser-crystallized Ge2Sb(2+x)Te5 sputtered thin films for use in optical memory. *Journal of Applied Physics*, *88*(12), 7020–7028. https://doi.org/10.1063/1.1314323

Yamada, N., Ohno, E., Akahira, N., Nishiuchi, K., Nagata, K., & Takao, M. (1987). High Speed Overwritable Phase Change Optical Disk Material. *Japanese Journal of Applied Physics*, *26*(S4), 61. https://doi.org/10.7567/JJAPS.26S4.61

Yan, A., Sun, T., Borisenko, K. B., Buchholz, D. B., Chang, R. P. H., Kirkland, A. I., & Dravid, V. P. (2012). Multi-scale order in amorphous transparent oxide thin films. *Journal of Applied Physics*, *112*(5), 54907. https://doi.org/10.1063/1.4750025

Yang, T.-Y., Cho, J.-Y., Park, Y.-J., & Joo, Y.-C. (2013). Driving forces for elemental demixing of GeSbTe in phase-change memory: Computational study to design a durable device. *Current Applied Physics*, *13*(7), 1426–1432. https://doi.org/10.1016/j.cap.2013.04.030

Yang, T.-Y., Park, I.-M., Kim, B.-J., & Joo, Y.-C. (2009). Atomic migration in molten and crystalline Ge2Sb2Te5 under high electric field. *Applied Physics Letters*, *95*(3), 32104. https://doi.org/10.1063/1.3184584

Zhang, K., Li, S., Liang, G., Huang, H., Wang, Y., Lai, T., & Wu, Y. (2012). Different crystallization processes of as-deposited amorphous Ge2Sb2Te5 films on nano- and picosecond single laser pulse irradiation. *Physica B: Condensed Matter*, *407*(13), 2447–2450. https://doi.org/10.1016/j.physb.2012.03.044

Zhang, W., Ronneberger, I., Li, Y., & Mazzarello, R. (2012). Magnetic properties of crystalline and amorphous phase-change materials doped with 3d impurities. *Advanced Materials*, *24*(32), 4387–4391. https://doi.org/10.1002/adma.201201507

Zinna, F., Resta, C., Górecki, M., Pescitelli, G., Di Bari, L., Jávorfi, T., … Siligardi, G. (2017). Circular dichroism imaging: Mapping the local supramolecular order in thin Films of chiral functional polymers. *Macromolecules*, *50*(5), 2054–2060. https://doi.org/10.1021/acs.macromol.6b02590